Spin-Orbit Coupling Effects and Magnetism of the Topological Edge States of Graphene

Dissertation
zur Erlangung des Doktorgrades
an der Fakultät für Mathematik, Informatik und Naturwissenschaften
Fachbereich Physik
der Universität Hamburg

vorgelegt von

Thorben Schmirander

Hamburg

2021

Eidesstattliche Versicherung

Hiermit versichere ich an Eides statt, die vorliegende Dissertationsschrift selbst verfasst und keine anderen als die angegebenen Hilfsmittel und Quellen benutzt zu haben. Die eingereichte schriftliche Fassung entspricht der auf dem elektronischen Speichermedium. Die Dissertation wurde in der vorgelegten oder einer ähnlichen Form nicht schon einmal in einem früheren Promotionsverfahren angenommen oder als ungenügend beurteilt.

Hamburg, den 15. September 2021

Abstract

The discovery of a new class of materials, the so-called topological insulators with conducting edges and insulating bulk, leads to a topological classification of materials with unprecedented electrical properties. Graphene is a time-reversal symmetric topological insulator exhibiting the quantum spin Hall effect. This effect can be described by the Kane-Mele model, which attributes the resulting quantized spin Hall conductance to the existence of helical edge states localized at the zigzag edges of the graphene honeycomb lattice. A multi-orbital tight-binding model can be used for the description of edge states in graphene nanoribbons. Such a model permits to discuss the electrical properties of the edge states in graphene nanoribbons under realistic experimental conditions, such as a sample deformation, and by considering electronic interactions in half-filled or doped samples. In this work a mean-field approach is used to describe the two magnetic phases occurring in half-filled graphene nanoribbons with zigzag edges. The energy gap of the magnetic ground state and first exited state of a single-orbital model comprised of the carbon p_z-orbitals is compared to that of a multi-orbital model, which respects the electronic interactions due to the finite occupation of the $3d$-orbitals. A non-magnetic phase is found for different amounts of hole and electron doping and the qualitative changes due to the inclusion of the $3d$-orbitals are examined. The $2s$- and other $2p$-orbitals of graphene become important when deformations of the honeycomb lattice cause a coupling of the in-plane σ- and out-of-plane π-bands. This leads to a deformation-induced spin-orbit coupling, which competes with the intrinsic spin-orbit coupling to determine the spin-alignment of the edge states in bent samples. Using an effective tight-binding model comprised of $2s$-, $2p_x$-, $2p_y$- and $2p_z$-orbitals, this competition is analyzed numerically and analytically and a dominance of bending-induced spin-orbit coupling over the intrinsic spin-orbit coupling of the $2p$-orbitals is found for moderate bending strengths. A difference occurs, when this competition is considered in an effective 9-orbital model, additionally including the 5 $3d$-orbitals of carbon. The $3d$-orbitals couple directly to the $2p_z$-orbitals due to the lattice geometry and therefore the intrinsic spin-orbit coupling of the $3d$-orbitals has a larger influence of the spin-orientation of the edge states, than the intrinsic spin-orbit coupling of the $2p$-orbitals. As a central result of this work, the description of edge states in deformed samples is found to require both σ- and $3d$-bands. Especially for measuring the strength of the intrinsic $3d$-orbital spin-orbit coupling, a quantity which is not precisely known in graphene, a better understanding of the processes behind the spin alignment of the edge states under realistic experimental conditions is of great importance.

Zusammenfassung

Die Entdeckung einer neuen Materialklasse, den sogenannten Topologischen Isolatoren, welches einen Isolator mit elektrisch leitenden Randzuständen darstellt, führte zu einer topologischen Klassifizierung von Materialen mit beispiellosen elektrischen Eigenschaften. Graphen ist ein topologischer Isolator mit Zeitumkehrsymmetrie, welcher den Quanten Spin Hall Effekt zeigt. Dieser Effekt kann mittels des Kane-Mele Modells beschrieben werden, welches die quantisierte Spin Hall Leitfähigkeit der Existenz von helikalen Randzuständen zuschreibt, die sich an den Zigzag-Rändern des Graphen Honigwabengitters bilden. Ein Viel-Orbital Modell stark gebundener Elektronen kann für die Beschreibung von Randzuständen in Graphen Nanoribbons verwendet werden. Ein solches Modell erlaubt es, die elektrischen Eigenschaften der Randzustände in Graphen unter experimentell realistischen Bedingungen zu betrachten, wie zum Beispiel Deformationen oder Elektronen-Wechselwirkungen in halb gefüllten oder dotierten Proben. In dieser Arbeit wird ein Selbstkonsistenz-Ansatz für die Elektronen-Wechselwirkung verwendet, um die zwei entstehenden magnetischen Phasen in halbgefüllten Graphen Nanoribbons mit Zigzag-Rändern zu beschreiben. Die Energielücke zwischen dem magnetischen Grund- und dem ersten angeregten Zustand innerhalb des Ein-Orbital Modells für die p_z-Orbitale von Kohlenstoff wird mit dem eines Viel-Orbital Modells verglichen, welches auch die Elektronen-Wechselwirkungen aufgrund der endlichen $3d$-Orbital Besetzung berücksichtigt. Überdies wird eine nicht-magnetische Phase für Dotierung mit Elektronen oder Löchern gefunden und die qualitativen Unterschiede durch die Berücksichtigung der $3d$-Orbitale werden untersucht. Die $2s$- und übrigen $2p$-Orbitale in Graphen werden wichtig, wenn Deformation des regelmäßigen Honigwabengitters ein Koppeln der σ-Bänder innerhalb der Graphenebene und der π-Bänder orthogonal zur Ebene verursachen. Dies führt zu einer Deformations-induzierten Spin-Bahn-Kopplung, welche mit der intrinsischen Spin-Bahn-Kopplung um die Spinausrichtung der Randzustände in diesen deformierten Proben konkurriert. Mithilfe eines weiteren effektiven Modells stark-gebundener Elektronen, bestehend aus $2s$-, $2p_x$-, $2p_y$- und $2p_z$-Orbitalen, wird dieser Wettbewerb analytisch und numerisch beschrieben und es stellt sich die Dominanz der Deformations-induzierten Spin-Bahn-Kopplung bereits für kleine Deformationen heraus. Dies ändert sich, wenn das Konkurrieren der unterschiedlichen Terme in einem 9-Orbital Modell betrachtet wird, welches zusätzlich die 5 $3d$-Orbitale von Kohlenstoff berücksichtigt. Die $3d$-Orbitale koppeln direkt an die $2p_z$-Orbitale aufgrund der Gittergeometrie und daher ist der Einfluss der intrinsischen Spin-Bahn-Kopplung der $3d$-Orbitale größer, als der der $2p$-Orbitale. Ein zentrale Ergebnis dieser Arbeit ist, dass die Beschreibung der Randzustände in deformierten Graphenproben sowohl σ-, als auch d-Bänder benötigt. Insbesondere für das Verständnis des Einflusses der $3d$-Orbital Spin-Bahn-Kopplung, dessen Stärke in Graphen weiterhin schwierig zu bestimmen ist, ist ein besseres Verständnis der Prozesse hinter der Spinausrichtung der Randzuständen unter realistischen experimentellen Bedingungen von großer Wichtigkeit.

Contents

1. Introduction

The development of the band theory of solids [1] in the early days of the formulation of quantum mechanics [2–4], has provided physicists with an arsenal of new methods to discover and describe phenomena with previously unknown depth and accuracy. The exploration of the theoretical framework has lead to understanding a whole range of material classes, such as superconductors [5, 6] or semiconductors [7, 8], which are still active research subjects today and enjoy application in many technological areas [9–19]. Despite the great success of band theory, however, it took almost a century to identify and harness an underlying structure, hidden in the symmetries of the band structures of solids. It lead to the formulation of *topological band theory* [20]. Topology is one of the central branches of modern mathematics and deals with the classification of sets, by allowing the definition of closed and open subsets [21]. This has far-reaching consequences, for example it allows to relate different sets with each other via very general features, the so-called topological invariants. These invariants depend only on the structure of the sets, rather than the individual objects they are comprised of. One area for the application of topology is geometry, where topological invariants may be assigned to manifolds at the example of the Euler characteristic [22], corresponding to the number of holes of this manifold. A torus, a representative of a manifold with Euler characteristic 1, is therefore topologically equivalent to a cup, because of their identical topological invariant. In the same way a ball is topologically equivalent to a bottle, a pretzel to a t-shirt and the written Arabian number eight to a pair of pants. Both a pretzel and a t-shirt can be continuously deformed to a flat sheet with three holes, see Fig. 1.1. During this stretching and compressing, the number of holes does not change. Thus the number of holes can be considered an invariant that identifies equivalence classes of objects.

The key discovery required for the specification of topological band theory was the assignment of topological invariants to the band structure of solids, creating equivalence classes of their Hamiltonians with gapped and gapless spectra [23]. In this case the phase space of states of these Hamiltonians takes the role of the manifold and topological invariants are assigned in a similar manner [24]. In this context they are called *TKNN invariant* [25] or Z_2-*index* [26]. The definition of these invariants makes use of the symmetries of the systems, such as time-reversal symmetry or charge conjugation and differentiate between a topological and trivial insulator [20].

While Landau theory [27] has provided good explanations for the phase transitions that were encountered until recently, the discovery of a new kind of phase transition required the underlying structure given by the topological invariants, which serves as explanation for the existence of different topological phases. The classical Hall effect was discovered in 1879 by
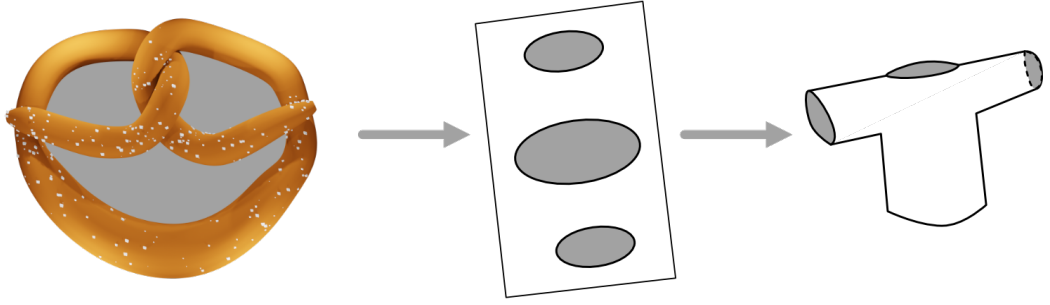
FIGURE 1.1.: Both a pretzel and a t-shirt contain three holes and are thus topologically equivalent to each other, according to the Euler characteristic.

Edwin Hall, who found that a voltage perpendicular to a current within a two-dimensional conductor is created by a transversal magnetic field [28]. The charge building up at different edges of the conductor compensates for the Lorentz force caused by the magnetic field and thus, no topological classification was required for understanding this phenomenon. The quantum Hall effect on the other hand, discovered by Klaus von Klitzing [29], revealed a surprising addition to the theory of the classical effect, because at high magnetic fields and low temperatures, the Hall conductance becomes quantized. An intricate plateau structure was found, that was astonishingly robust with respect to the geometry or quality of the sample. The quantization of the Hall conductance by integer multiples of the constant e^2/h lead to precise measurement of the electrical resistance, but required the development of a geometric interpretation, such that it could be linked to a topological invariant [30].

A theoretical model later proposed by Haldane [31], which exhibits the quantum anomalous Hall effect, relies on a periodic magnetic field with zero magnetic flux through the unit cell of graphene. Because it occurs without the splitting in Landau levels, this type of quantum Hall effect is referred to as "anomalous". The Hall conductance becomes quantized in this model, because of broken time-reversal symmetry. Thus, it is a realization of a Chern insulator [32] and the Chern number in this context is the TKNN invariant. There are different types of Chern insulators, where the Chern number assumes integer values and other types, where it assumes fractional values. This results in the integer quantum Hall effect (QHE) [25] or the fractional QHE [33]. In both types of Chern insulators the topological nature is manifesting in a bulk topological invariant and an edge topological invariant, which are identical [20] - a principle known as the *bulk-boundary correspondence* [34].

The above types of Hall effects have in common, that they are all related to transport mechanisms of the particle charges at the sample edges. Another range of effects describe the spin transport at the edges of a sample and are thus called spin Hall effects [35–37] in analogy to the classical Hall effect. They refer to a spin current in a system subject to an electric field [38]. This effect can also be realized in two-dimensional semiconductors and manifests in a vanishing charge Hall conductance, but a finite spin Hall conductance.

The quantum mechanical analogue to the spin Hall effect is the quantum spin Hall effect, where the spin Hall conductance becomes quantized at low temperatures [39]. Time-reversal symmetry is required for this effect to occur [40] and since the Chern number is only defined in time-reversal broken systems, the TKNN invariant has to be replaced by a Z_2-index, as Kane and Mele found out [26, 41]. The model proposed for the quantum spin Hall effect, can effectively be described by two copies of the Haldane model linked by spin-orbit coupling [31] - one model for each type of spin. This way the time reversal-symmetry is maintained and the spin-up electrons feature a chiral integer quantum Hall effect, while the spin-down electrons exhibit an anti-chiral integer quantum Hall effect - both with opposing TKNN invariant - and thus the total TKNN invariant is zero. Since this system is time-reversal symmetric, it is called a topological insulator, rather than a Chern insulator [23, 42, 43]. Bernevig, Hughes and Zhang have introduced a model, alternative to Kane and Mele, in order to explain the quantum spin Hall effect via strain in the graphene lattice, which gives rise to an effective magnetic field [44, 45]. Similar to the Chern insulator, where the Hall conductance can be quantized according to fractional or integer values, also the spin Hall conductance of the topological insulator can be quantized in both manners [46–48]. All of the aforementioned topologically non-trivial insulators have in common, that there exists a metallic state at the interface to a material with different topological order [49, 50].

The first experimental realization of a topological insulator was in HgTe quantum wells [45, 51] and shortly after, a realization of a three-dimensional topological insulators has been found in $Bi_{1-x}Sb_x$ [52, 53]. These days the quantum spin Hall effect and topological insulator are studied rather ubiquitously [54, 55]. Additionally, more exotic types of topological insulators are being realized, such as photonic topological insulators [56–59] or candidates with exciton-polaritons [60] instead of electrons or photons. Such quasi-particles are a product of strongly coupled quantum-well excitons and cavity photons, which condense in a chiral edge mode of a microcavity. A magnetic topological insulator, another type of non-trivial insulators, but with magnetic order in addition to an intriguing band topology, has recently been found in the layered van-der-Waals compound $MnBi_2Te_4$ [61]. Topological insulators are of primary interest in the area of spintronics [62, 63], because the mechanisms for spin transport are expected to lead to more efficient electronic devices [40] with much lower power consumption [64, 65].

Parallel to the discovery and theoretical predictions in the field of topological insulators, a compound with peculiar characteristics emerged as an interesting research subject [66, 67]. Graphene is an allotrope of carbon, with a two-dimensional bipartite lattice structure known as the honeycomb lattice [68, 69]. While the initial description of the band structure of graphite date back until the middle of the 20th century [70–72] and graphene has already been theorized at the time [31], it took until very recently to synthesize and measure its characteristics [73–76]. Graphene has been identified as a candidate for hosting topological edge states at zigzag edges, because the models for explanation of the quantum spin Hall effect are based on the honeycomb lattice structure of graphene [26].

In Fig. 1.2 a) the two types of edges for the honeycomb lattice are shown, the armchair
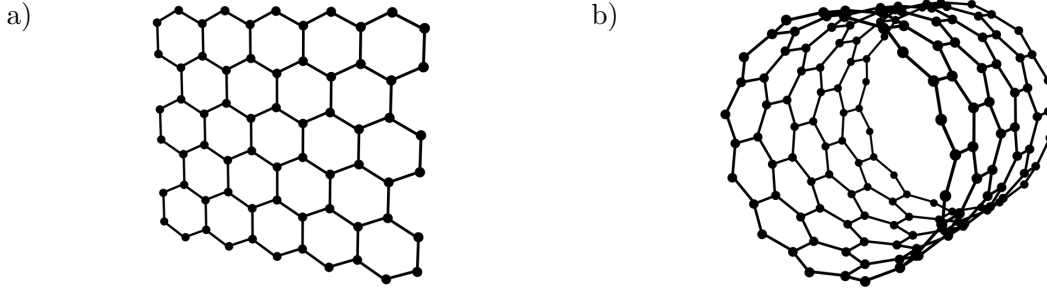
FIGURE 1.2.: a) Zigzag and armchair edges in a flat sample of graphene. b) A graphene nanotube with zigzag edges.

and zigzag edges. Due to symmetry of the Brillouin zone of graphene, the gap crossing edge states can only occur at the zigzag-type [77]. In b) a carbon nanotube with zigzag edge is given, which is also a candidate for hosting edge states. In this case the curvature of the system, gives rise to deformation-induced spin-orbit coupling, which competes with the intrinsic spin-orbit coupling of the carbon atoms and determines the electric properties of such samples [78].

For a realization of a topological insulator, the time-reversal invariant intrinsic spin-orbit coupling is of significance, because it lends a helicity to the conduction channels, which is required for the spin transport at the edges [79]. In graphene, the intrinsic spin-orbit coupling is found to be very small [80, 81], however. Attempts to increase the spin-orbit coupling in graphene have been made via deformation [82] of the crystal lattice, via hydrogenation [83], fluorination [84], by plasmonic excitations [85] or by increasing it with proximity effects. For this the graphene sample is placed on a substrate, such as transition-metal dichalcogenides (TMDC) [86] or WS_2 [87].

Ab-initio calculations of the band structure of graphene have revealed that the band gap of graphene is mainly given by the intrinsic spin-orbit coupling in the *d*-orbitals. A common practice is the formulation of a tight-binding model [88], which describes the π-bands of the hexagonal crystal lattice via nearest-neighbor hopping. The higher-in-energy orbitals are often times included by next-nearest-neighbor hopping [80], but another approach is the inclusion of the *d*-orbital states in the Hilbert space directly. This leads to a multi-orbital tight-binding model of graphene. It has many advantages to depart from an effective treatment of the additional orbitals, because other influences to the graphene sample, such as strain and bending of the lattice, can be treated in a direct way, rather than implementing each effectively. A prime example is the computation of electronic interactions. A multi-orbital tight-binding model allows the formulation of an extended Hubbard model, which includes Coulomb interactions due to the additional orbitals. This leads to a more refined description of the effect of the electronic interactions on the band structure of graphene. Other methods for the computations of ground states of interacting systems, such as dy-

namical mean-field theory (DMFT) [89], density functional theory (DFT) [90, 91] or the Green's function (GF) method for computing the transport properties of graphene [92], can provide a more accurate picture of the relevance of correlations in the graphene sample. The interactions are not expected to play a dominant role, however, and therefore the reduced computational effort of treating the extended Hubbard model in the mean-field approximation provides more flexibility in the choice of system sizes and is less involved than other computational methods, which is altogether beneficial to computation speed.

In this thesis a multi-orbital tight-binding model of graphene is formulated with the aim to compute the magnetic ground state of zigzag nanoribbons under different interaction strengths and sample sizes. The internal energies of different magnetic phases are compared. The topologies of the ground state and first excited state are analyzed and the influence of the Coulomb interaction strengths in different orbitals is discussed. Additionally, a non-magnetic phase is treated and analyzed with respect to electron or hole doping. The results obtained from the single-orbital model are compared to those of the multi-orbital model by analyzing the d-orbital occupation and internal energy contribution due to the more sophisticated implementation of the Coulomb interaction.

As spin-orbit coupling is a necessary factor for the helicity of the edge states in graphene, the effect of intrinsic and Rashba-type spin-orbit coupling on the edge state dispersion is analyzed without electronic interactions and their topology and spin textures are studied. Deformation of the regular graphene lattice leads to Rashba-type spin-orbit coupling due to the broken inversion symmetry of the sample. After an understanding of the Rashba-type spin-orbit coupling both on bulk graphene and on the gap crossing edge states has been gained, the occurrence of deformation-induced spin-orbit coupling is examined in detail. For this purpose the multi-orbital tight-binding model is extended to include the sp^2- in addition to the d-orbitals. A perturbative treatment of the intrinsic spin-orbit coupling among p- and d-orbitals leads to a detailed understanding of the spin-alignment of the edge states in bent ribbons. Using different bending profiles, localized bulk states are found, which localize mostly around points of extremal deformation curvature.

Together, the results of the mean-field and spin-orbit coupling considerations lead to a refined understanding of the topological characteristics of the gap crossing edge states in graphene nanoribbons with zigzag edges under realistic experimental conditions. This may help to understand the measurements of edge states magnetic moments in graphene samples, which is still elusive. It also underpins the importance of the d-orbital intrinsic spin-orbit coupling in the analysis of deformation-induced spin-orbit coupling, which has not found detailed consideration in the literature as of yet.

As a first step the origin of spin-orbit coupling is discussed in Chapter 2 and how it arises naturally from a fully relativistic treatment of a fermion under the influence of an electric field via the Dirac equation. In the next step the role of symmetries in crystals is discussed and how group theory may be used to compute effective spin-orbit coupling terms arising from specific symmetries. For this $k \cdot p$-theory is briefly touched. This type of perturbation theory allows to use symmetry groups to find the relevant states for the description of the dispersion

relation at different points in the Brillouin zone of solids. Furthermore, Löwdin perturbation theory is discussed, which permits the reduction of an extended Hilbert space to a subspace of more influential states, that regard the effect of other weakly coupled states perturbatively. These theories are then used to discuss two types of effective spin-orbit coupling terms, the *Dresselhaus*- and *Rashba*-type - both arising to different broken symmetries of the crystal lattice. Lastly the current experimental and theoretical status regarding the analysis of the spin-orbit coupling strength in graphene is presented.

For the formulation of a multi-orbital tight-binding model of graphene, matrix elements in the Slater-Koster approximation are derived in Chapter 3. It follows a treatment of Rashba-type spin-orbit coupling, as it is arising from the finite overlap of the sp^2-hybridized orbitals and the π-bands as a consequence of the broken inversion symmetry with respect to the direction perpendicular to the graphene plane. The trigonal warping at the Dirac points of bulk graphene is a consequence of the Rashba-type spin-orbit coupling. It is discussed by means of the sublattice spin expectation values, which are tightly connected to the topology of graphene and encoded in these features of the bulk Hamiltonian. The four relevant states for the description are then treated analytically with an effective 2×2-model, allowing for the computation of the sublattice spin expectation values and winding numbers. They are compared to numerical results.

In Chapter 4 the properties of graphene as a time-reversal invariant topological insulator are discussed via the Kane-Mele model. Once the qualities of zigzag graphene nanoribbons as a model system for hosting helical edge states are established, their dispersion relation is discussed in the context of a multi-orbital tight-binding model. The influence of Rashba-type spin-orbit coupling, as well as that of a magnetic field and intrinsic spin-orbit coupling, is presented by analyzing the helicity and gap crossing behavior of these edge states.

In Chapter 5 the Coulomb interaction among different orbitals is derived in the form of a multi-orbital Hubbard model, which is then approximated by the mean-field approach.

The three edge phases are presented in Chapter 6 and their topological characteristics are discussed. In a next step the magnetic properties of the antiferromagnetic and ferromagnetic edge phases are compared and the influence of the nanoribbon size on their dispersion relations is treated. The ground state in the single-orbital Hubbard model, only comprised of p_z-orbitals, as well as the first excited magnetic state, is obtained. A non-magnetic phase is analyzed with respect to electron or hole doping. This analysis is then extended to the multi-orbital Hubbard model, where the effect of additional interaction strengths in the d-orbitals are examined.

The occurrence of Rashba-type spin-orbit coupling due to the deformation of the regular graphene lattice in a non-interacting tight-binding model is discussed in Chapter 7. The theory for including distortion of the planar graphene lattice via the Slater-Koster approximation is presented. The tight-binding model is extended to contain sp^2-orbitals. Then deformations with constant curvature along and perpendicular to the zigzag edges are applied and the effect on the edge state dispersion and band structure is assessed. The spin textures of the edge states are computed and the alignment of the spin at the edges as a

result of the induced Rashba-type spin-orbit coupling of the sp^2-orbitals is compared to that of the d-orbitals. For deformations with varying curvature, bulk localized states are found, which occur due to the existence of bending-induced gauge potentials in these ribbons.

In Chapter 8 the results are summarized and opportunities for future exploration are stated.

2. Spin-orbit Interaction

2.1. Origin of Spin-orbit Coupling

Spin-orbit coupling is an effect of relativistic origin, which couples the motional degree of freedom of an electron to one of its intrinsic properties, the spin [93]. Due to the motion of the electron, static electric fields in a laboratory system are perceived as magnetic fields in its rest frame. The spin of the electron causes a magnetic dipole moment that couples to this magnetic field. The atomic or *intrinsic spin-orbit coupling* originates from the electric field generated by a positively charged nucleus. Other types of spin-orbit coupling arise due to electric fields of other origins, such as in a sample that is being placed on a substrate. This resulting asymmetry of the periodic crystal potential within said sample gives rise to spin-orbit coupling effects which can be described by the respective point group symmetries of such external factors [94]. One example is the *Dresselhaus*-type spin-orbit coupling, which occurs when a crystals does not exhibit a center of inversion [95]. Another example is the *Rashba*-type spin-orbit coupling, occurring when the system lacks a broken mirror symmetry along a high-symmetry axis [96]. Spin-orbit coupling due to strain of the crystal lattice or curvature is also possible, both of which may break symmetries in other ways and thus introduce gaps in the crystal band structure [78, 82]. In the following, a general introduction of the relativistic origin and description of spin-orbit coupling is given. It is discussed how the Dirac equation leads to a spin-orbit coupling term in the non-relativistic Pauli equation. Then examples of the spin splitting of Rashba- and Dresselhaus-type spin-orbit coupling are given and their symmetry properties are discussed. Lastly, the current experimental status of measuring spin-orbit coupling in graphene is described.

2.1.1. Relativistic Description of Spin-orbit Coupling

It is a central result of electrodynamics that an electric field in a stationary frame of reference induces a magnetic field in a frame of reference with relative velocity. Such a situation arises when electrons orbit the positively charged nucleus of an atom, such that the nuclear electric potential induces a magnetic field in the rest frame of the electron, which couples to its spin [97]. Such an interaction is known as *spin-orbit coupling*. Generally, a magnetic field $\vec{B}$ couples to a particle with the spin $\vec{S}$ via [98]

$$\hat{H} = -\hat{\vec{\mu}}_S \cdot \vec{B}, \tag{2.1}$$

where $\hat{\vec{\mu}}_S = -\frac{g_s \mu_B}{\hbar} \hat{\vec{S}}$ is the spin magnetic dipole moment, $g_s = 2$ is the spin-g-factor for the electron and $\mu_B = \frac{e\hbar}{2m}$ the Bohr magneton. For an external electric field $\vec{E}$ in the laboratory system, the magnetic field $\vec{B}'$ in a frame moving with the velocity $\vec{v}$, is given in good approximation by [98]

$$\vec{B}' \approx -\frac{1}{c^2} \vec{v} \times \vec{E}, \tag{2.2}$$

where c is the speed of light. The spin magnetic moment $\hat{\vec{\mu}}_S$ is responsible for a torque $\hat{\vec{\tau}}' = \hat{\vec{\mu}}_S \times \vec{B}' = \left(\frac{d\hat{\vec{S}}}{dt}\right)_{\text{rest}}$ in the rest frame of the electron. Computing the spin-orbit coupling strength by inserting Eq. 2.2 in Eq. 2.1 will result in a wrong magnetic field, because kinematic effects change the apparent spin and magnetic field in the rest frame of the electron. A vector in a moving coordinate system will appear differently when observed from different frames of reference, in particular from rotating ones. The spin $\hat{\vec{S}}$ of the electron is such a vector in a rotating frame of reference, which depends on the vector $\vec{S}$ itself, as well as the axis of rotation $\frac{\vec{\omega}}{|\omega|}$. The temporal derivatives in the two systems are related by [99]

$$\left(\frac{d\hat{\vec{S}}}{dt}\right)_{\text{lab}} = \left(\frac{d\hat{\vec{S}}}{dt}\right)_{\text{rest}} + \vec{\omega} \times \hat{\vec{S}}. \tag{2.3}$$

Here, the $\left(\frac{d}{dt}\right)_{\text{rest}}$ derivative is the change in the rotating rest frame of the electron and the $\left(\frac{d}{dt}\right)_{\text{lab}}$ derivative corresponds to that in the laboratory system. The rest frame of the electron is not an inertial system, because it is orbiting the atomic nucleus and is thus accelerated in different directions. For any given moment in time, the orbital motion of the electron with angular velocity $\vec{\omega}$ can be taken as a linear velocity $\vec{v}$ during a time interval δt in very good approximation [99, 100]. Due to the motion of the electron, $\vec{v}$ will not be collinear to the velocity during the following time step. Thus, more than one Lorentz-transformation is required for transforming from the laboratory system to the rest frame of the electron and in general, two consecutive Lorentz boosts will not only result in another boost, but in a boost and a rotation. It is assumed that the relative speed $\Delta\vec{v}$ of the two rest frames along the electrons path for each time step is small compared to their speed difference to the laboratory system. Furthermore, both velocities are assumed to be significantly smaller than the speed of light. Therefore the angle of the rotation after two Lorentz transformations is $\Delta\Omega = -(\gamma - 1)\frac{\vec{v} \times \Delta\vec{v}}{v^2}$ [99] and for each time step δt, together with $\gamma \approx 1 + \frac{1}{2}\frac{v^2}{c^2}$,

$$\vec{\omega} = \frac{1}{2c^2}\left(\dot{\vec{v}} \times \vec{v}\right) \tag{2.4}$$

is the *Thomas precession frequency*. This is the frequency of the spin magnetic moment precessing around the magnetic field vector as a consequence of the motion of the rest frame

of the electron. Following [101], Eq. 2.4 is inserted in Eq. 2.3 and the torque in the laboratory frame becomes

$$\left(\frac{d\hat{\vec{S}}}{dt}\right)_{\text{lab}} = \hat{\vec{\mu}}_S \times \left(\vec{B}' - \frac{m}{e}\vec{\omega}\right).$$

(2.5)

This is known as *Thomas precession*. The acceleration in the Thomas precession frequency is expressed as $\dot{\vec{v}} = \frac{e}{m}\vec{E}$ and thus, even though there is no magnetic field in the laboratory system, the spin of the electron is subject to a torque $\hat{\vec{\tau}} = \left(\frac{d\hat{\vec{S}}}{dt}\right)_{\text{lab}}$ with an effective magnetic field

$$\vec{B} = -\frac{1}{2c^2}\vec{v} \times \vec{E},$$

(2.6)

due the relativistic transformations to a rotating frame of reference. A central potential $V(\vec{r})$, generated by an atomic nucleus for example, causes a radially symmetric electric field $\vec{E}$ in the laboratory system, which allows the apparent magnetic field to be characterized by the angular momentum $\hat{\vec{L}}$ of the electron. Substituting $e\vec{E}(r) = -\frac{dV}{dr}\frac{\vec{r}}{r}$ and the definition of the angular momentum operator $\hat{\vec{L}} = \hat{\vec{r}} \times \hat{\vec{p}}$ in the magnetic field Eq. 2.6, the interaction Eq. 2.1 becomes

$$\hat{H} = \frac{1}{2m^2c^2}\frac{1}{r}\frac{dV(\vec{r})}{dr}\hat{\vec{L}} \cdot \hat{\vec{S}}.$$

(2.7)

2.1.2. The Pauli Equation and the Dirac Equation

The *Pauli equation* is the non-relativistic limit of the *Dirac equation* [98] and describes part of the Dirac 4-spinor subject to electric and magnetic fields. It contains the spin-orbit coupling term Eq. 2.7 as a natural consequence of the Dirac equation describing a relativistic spin-1/2 fermion in an electric field, even though this fact is not obvious in the latter. The Dirac equation describes a fermion, which has the relativistic energy

$$E^2 = c^2 p^2 + m^2 c^4,$$

(2.8)

where m and p are its mass and momentum, c is the speed of light. For a quantum mechanical system, a 4×4-matrix equation can be formulated, such that it is linear in the 4-component spinor wave function and fulfills Eq. 2.8. Then, each of the spinor components have energies $+E$ or $-E$. The Dirac equation for the wave function $|\Psi\rangle$ is

$$\left(i\hbar\frac{\partial}{\partial t} - \hat{H}_D\right)|\Psi\rangle = 0,$$

(2.9)

where the Dirac Hamiltonian H_D for a particle with charge e and mass m in an electromagnetic field, defined by scalar potential ϕ and vector potential $\vec{A}$, reads

$$\hat{H}_D = c\hat{\vec{\alpha}} \cdot \left(\hat{\vec{p}} + e\vec{A}\right) + \hat{\beta}mc^2 - e\phi. \tag{2.10}$$

Here, the 4×4 Dirac matrices $\hat{\vec{\alpha}} = (\hat{\alpha}_x, \hat{\alpha}_y, \hat{\alpha}_z)^T$ and $\hat{\beta}$ are given by

$$\hat{\alpha}_\mu = \begin{pmatrix} 0 & \hat{\sigma}_\mu \\ \hat{\sigma}_\mu & 0 \end{pmatrix} \qquad \text{and} \qquad \hat{\beta} = \begin{pmatrix} \hat{\sigma}_0 & 0 \\ 0 & \hat{\sigma}_0 \end{pmatrix}. \tag{2.11}$$

The components $\hat{\sigma}_\mu$ of $\hat{\alpha}_\mu$ are the Pauli matrices $\hat{\sigma}_x$, $\hat{\sigma}_y$ and $\hat{\sigma}_z$, while $\hat{\sigma}_0$ is the identity matrix in two dimensions. The doubly degenerate solutions of Eq. 2.9 with positive energy correspond to the electron, while those with negative energy to its anti-particle, the positron. These particles are described by the wave functions ψ and χ for the electron and positron, respectively, and include an additional degree of freedom, the spin, which arises due to the four-components of the Dirac equation. Hence, the total wave function has the four components $|\Psi\rangle = (\psi_\uparrow, \psi_\downarrow, \chi_\uparrow, \chi_\downarrow)$. For the free particle, neither the angular momentum operator, nor the spin operator commute with the Dirac Hamiltonian [98]. The sum of $\hat{\vec{J}} = \hat{\vec{S}} + \hat{\vec{L}}$, however, is a conserved quantity, as well as the squares of the individual parts $\hat{S}^2$ and $\hat{L}^2$. The Pauli equation, which can be derived from the Dirac equation in the non-relativistic limit for a particle in a magnetic field, contains a term with these operators. The Pauli equation only considers the states from the four-component spinor describing the particle and does not describe their anti-particle counterparts. The two components are called big and small component of the total wave function $|\Psi\rangle$. If the small component is considered non-relativistic, the coupling between both components can be simplified, such that the equations for both components can be decoupled in second order. Then,

$$\hat{H}_P|\psi\rangle = \left(E - mc^2\right)|\psi\rangle \tag{2.12}$$

becomes the eigenvalue equation for the large component $|\psi\rangle = (\psi_\uparrow, \psi_\downarrow)$ and therefore the Pauli Equation is a 2×2-matrix equation. The Pauli-Hamiltonian is given as

$$\hat{H}_P = \frac{1}{2m}\{(\hat{\vec{p}} + e\vec{A}) \cdot \hat{\vec{\sigma}}\} \cdot \{(\hat{\vec{p}} + e\vec{A}) \cdot \hat{\vec{\sigma}}\} - e\hat{\sigma}_0\phi. \tag{2.13}$$

It can be expressed in a form similar in appearance as the Schrödinger equation

$$\hat{H}_P = \left(\frac{1}{2m}\left(\hat{\vec{p}} + e\vec{A}\right)^2 - e\phi\right) \cdot \hat{\sigma}_0 + \frac{e\hbar}{2m}\hat{\vec{\sigma}} \cdot \vec{B}. \tag{2.14}$$

The magnetic moment coupling to a magnetic field is identified as $\hat{\vec{\mu}}_S = -\frac{g_s\mu_B}{\hbar}\hat{\vec{S}}$ and the last term is of the form of Eq. 2.7, but with an incorrect factor. The origin of the spin-orbit

coupling term in Eq. 2.14 is $\vec{B} = \vec{\nabla} \times \vec{A}$, which describes a magnetic field in the laboratory system. In the case of intrinsic spin-orbit coupling, however, there is no magnetic field in the rest frame, but only the radially symmetric nuclear electric potential. As discussed in the previous section, the transformation between rotating frames of reference leads to an effective magnetic field coupling to the spin magnetic moment reduced by half, when compared to that stated in Eq. 2.14. If one would decouple the big and small components in higher order, the non-relativistic treatment of the Dirac equation would exhibit additional terms and account for the factor of the spin-orbit coupling term correctly as well.

2.2. Spin-orbit Coupling and Crystal Symmetries

The momentum space of solids is commonly described around high-symmetry points, such that group theoretical arguments can be used to formulate couplings between groups of wave functions. They are characterized by irreducible representations of point groups. One such procedure is the $k \cdot p$- theory [7, 102]. With this method the behavior of energy bands away from high-symmetry points can be obtained perturbatively by considering a fixed crystal momentum vector $\mathbf{k}$ and the momentum vector $\mathbf{p}$. The resulting models can become very difficult to solve, because at high symmetry points of the lattices, very many states must be considered, increasing the dimension of the problem. For reducing this complexity, *Löwdin perturbation theory* [103] may be used, where the Hamiltonian describing the interactions among many bands is reduced to a Hamiltonian acting on only a subspace. More weakly coupled bands are included perturbatively, leading to effective expressions for the description of spin-orbit couplings in these types of systems. The description of the zinc blende crystal structure by Dresselhaus [95] via the $k \cdot p$- method has brought forward a spin splitting due to *bulk inversion asymmetry*, called *Dresselhaus-type* spin-orbit coupling [104]. It is rooted in the fact that zinc blende does not feature a point of inversion in the Brillouin zone, due to the two different species of atoms in the diamond crystal lattice T_d. For the wurtzite structure Sheka and Rashba [96] used the same approach to derive another type of momentum-dependent splitting, originating from a missing mirror symmetry of the wurtzite crystal lattice $C_{6\nu}$ [105], called the *Bychkov-Rashba-type* or *Rashba-type* spin-orbit coupling. Today, spin-orbit coupling due to *structure inversion asymmetry* is generally called *Rashba-type* spin-orbit coupling [106]. In this section, the symmetry analysis of a Hamiltonian is discussed and the $k \cdot p$ - method and Löwdin perturbation theory are briefly summarized. Then, effective expressions of the *Dresselhaus-* and *Rashba-type* spin-orbit coupling are derived.

2.2.1. The Role of Symmetries

Time-reversal Symmetry

This paragraph is based on [34]. The Hamiltonian H is invariant under the operation of time-reversal symmetry $\hat{\mathscr{T}}$ if [20]

$$\hat{\mathscr{T}}\hat{H}(\mathbf{k})\hat{\mathscr{T}}^{-1} = \hat{H}(-\mathbf{k}). \tag{2.15}$$

There are two types of time-reversal symmetry in a system with an internal symmetry, such as the spin, namely with the properties $\hat{\mathscr{T}}^2 = \pm 1$. The case $\hat{\mathscr{T}} = -i\hat{\sigma}_y \hat{K}$, where $\hat{K}$ is the operation of complex conjugation, leads to the antisymmetric time-reversal operation with $\hat{\mathscr{T}}^2 = -1$. It is required for the description of spin-1/2 particles [34] and ensures a symmetry in the energy spectrum of $\hat{H}$, also known as Kramers degeneracy [107, 108]. If a pair of eigenstates of the Hamiltonian is related by the time-reversal operation, it follows from the antiunitary time-reversal operation, that these two states are orthogonal.

Time reversal symmetry accounts for the invariance of the Hamiltonian under reversal of the direction of time [109] and thus in the Brillouin zone $\mathbf{k} \to -\mathbf{k}$. Momenta, which are invariant under inversion of the Brillouin zone are called *time-reversal invariant momenta*. Due to the symmetry of the Hamiltonian, eigenstates related by time-reversal symmetry have identical energy and thus eigenenergies of the Hamiltonian at time-reversal invariant momenta are at least doubly degenerate. The spin as internal degree of freedom is also reversed by the time-reversal operation, such that the Kramers degeneracy for the energy E and states with spin $\uparrow$ or $\downarrow$ amounts to

$$E(\mathbf{k})_\uparrow = E(-\mathbf{k})_\downarrow \qquad \text{and} \qquad E(\mathbf{k})_\downarrow = E(-\mathbf{k})_\uparrow. \qquad (2.16)$$

If the Hamiltonian is not only time-reversal invariant, but also symmetric under spatial inversion, the energy spectrum additionally shows

$$E(\mathbf{k})_\uparrow = E(-\mathbf{k})_\uparrow \qquad \text{and} \qquad E(\mathbf{k})_\downarrow = E(-\mathbf{k})_\downarrow. \qquad (2.17)$$

In that case, all energies are spin degenerate [107]. A class of materials known as time-reversal symmetric topological insulators, which will be discussed in a later chapter, relate their topological properties to the conservation of time-reversal symmetry [26, 41]. In graphene in particular, the intrinsic spin-orbit interaction allows to open a gap in the energy spectrum at the time-reversal invariant momenta while the Kramers degeneracy is not lifted. The mirror-symmetry along the out-of plane axis of the graphene crystal structure is the reason, why the spectrum remains spin degenerate [110].

Point Group Symmetries of Crystal Lattices and their Representations

Before discussing how the knowledge of group theory is used to find models for band structure calculation, an overview of point groups and their representations is given, which is based on [111]. A set of elements together with an operation (a *product* operation) forms a group, if they fulfill a number of conditions. First, the product of any two elements is also an element of the group. Second, the product operation is associative. Third, a unit element exists and fourth, an inverse to each of the group elements as a member of the group exists. A *representation* of an abstract group is another group of square matrices, homomorphic to said abstract group, such that for each two group elements A and B in the abstract group, matrices $D(A)$ and $D(B)$ exist with $D(AB) = D(A)D(B)$, where $D(AB)$ is uniquely determined by the element AB. If there exists a similarity transformation[1], which reduces every element of the representation group to block form, the representation is reducible. The trace of a representation is called *character*, which is invariant under a similarity transformation. If a block within a such matrix or the representation itself is not decomposable[2],

---

[1]Two $n \times n$-matrices F and G are called *similar*, if there exist an invertible $n \times n$-matrix S, such that $F = SGS^{-1}$ [112], relating them by a similarity transformation.

[2]Relating a representation to a number of *irreducible representations*, is called *decomposition*. A representation can be brought into block-diagonal form, where each block can be treated individually, when its character is a linear combination of characters for *irreducible representations* of the group [111].

it forms an *irreducible representation.* In the analysis of physical models with respect to their symmetries, the dimensionality of each irreducible representation is connected to the degeneracy of the energy levels of the system. If a perturbation is applied to the system, it may cause a reduction of the symmetry and consequently the degeneracy of the energy levels decreases. It is common practice to list the irreducible representations of point groups around high-symmetry points in the Brillouin zone for different types of crystal lattices [113, 114]. Graphene has the point group symmetry D_{6h} at the Γ- and D_{3h} at the K-point [115].

Application of Group Theory to the Computation of Band Structures

One of the first to recognize the importance of symmetries in solid state physics was Wigner [116]. Group theoretical structures are increasingly important when the models for such systems, i.e. in the computation of band structures, become more complex. The quantum mechanical adaption of group theory was tightly connected to the development of the theory of point groups [113, 117]. The more general space groups still find application in the discussion of band structures in recent times [118, 119]. As recognized in the literature [120–123], spin-orbit coupling effects arising from specific types of symmetries play a central role in the description of the energy bands and it can be the source of very complex spin structures. Therefore, spin-orbit coupling is commonly described by using symmetry analysis [124, 125], which will be done in the following sections. In this section, a possible formulation of the symmetry analysis is briefly summarized for the purpose of describing different types of spin-orbit coupling in later sections. A popular application of the perturbative description of energy bands in the vicinity of high-symmetry points was done by Dresselhaus, Kip and Kittel (DKK) [126]. They formulated a $k \cdot p$ - model for three-bands on the diamond lattice and obtained the energies in the spinless case for the three degenerate orbitals $\{d_{xy}, d_{yz}, d_{xz}\}$. The latter form a basis of the Γ_{25}^{+} irreducible representation of the symmetry group T_d at the Γ-point of the diamond lattice [102]. The $k \cdot p$ - method starts with the idea that instead of solving the Schrödinger equation for the wave function $\psi_{n,\boldsymbol{k}}(\mathbf{r})$ with band index n and vector $\mathbf{k}$, the Bloch ansatz $\psi_{n,\boldsymbol{k}}(\mathbf{r}) = u_{n,\boldsymbol{k}}(\mathbf{r}) e^{i\boldsymbol{k}\cdot\boldsymbol{r}}$ is made and the problem is rewritten for $u_{n,\boldsymbol{k}}(\mathbf{r})$, such that the extra terms coming from the exponential part can be treated as a perturbation [111]. Then, the corresponding Schrödinger equation including spin-orbit coupling has the form[3] [93, 104, 127]

$$\left[\frac{\hat{\mathbf{p}}^2}{2m} + V(\mathbf{r}) + \frac{\hbar}{4m^2c^2}\hat{\mathbf{p}}\cdot\left(\hat{\vec{\sigma}}\times\vec{\nabla}V\right) + \frac{\hbar}{m}\mathbf{k}\cdot\hat{\pi}\right]u_{n,\boldsymbol{k}}(\mathbf{r}) = \left(E_n(\mathbf{k}) - \frac{\hbar^2\mathbf{k}^2}{2m}\right)u_{n,\boldsymbol{k}}(\mathbf{r}).$$

$$(2.18)$$

It is defined $\hat{\pi} = \hat{\mathbf{p}} + \frac{\hbar}{4mc^2}\hat{\vec{\sigma}}\times\vec{\nabla}V$, where $V(\mathbf{r})$ is the potential and $\hat{\mathbf{p}} = \frac{\hbar}{i}\nabla$ is the momentum operator. The vector $\hat{\vec{\sigma}}$ contains the Pauli spin matrices. The last term on the left hand side of Eq. 2.18, $\frac{\hbar}{m}\mathbf{k}\cdot\hat{\pi}$, is considered the perturbation, which describes how a variation of

---

[3]The factor of the spin-orbit coupling is due to the convention in [95] of using $\vec{\sigma}$, instead of the spin $\vec{S} = \frac{\hbar}{2}\vec{\sigma}$.

k affects the function $u_{n,\boldsymbol{k}}(\mathbf{r})$ at the Γ point. The expansion can also be performed around other points $\mathbf{k}_0$ in the Brillouin zone, by substituting $\mathbf{k} \to \mathbf{k} - \mathbf{k}_0$. To highlight the use of symmetry arguments, the above form of Eq. 2.18 of the Hamiltonian, without including the spin-orbit coupling term, can be rewritten into the DKK model [102]. The result is a second-order perturbation theory formulation in the $k \cdot p$-method

$$H_{rs} = \langle r|H(\mathbf{k})|s\rangle = \frac{\hbar^2}{m^2} \sum_{i,j} k_i k_j \sum_{l,\nu,\alpha \neq \Gamma} \frac{\langle r|p_i|l\alpha\nu\rangle\langle l\alpha\nu|p_j|s\rangle}{E_\Gamma - E_{l\alpha}}, \tag{2.19}$$

where r and s are basis functions transforming according to the Γ_{25}^+ irreducible representation of T_d. This sum contains the states of the representation α in band l, where ν states may be degenerate with the same energy $E_{l\alpha}$. The momentum operator matrix elements $\langle r|p_i|l\alpha\nu\rangle$ obey certain symmetry relations. Many matrix elements depend on each other and some are zero, when the A_1 representation is not being contained in the character decomposition of their transformation behavior [27]. As a result, all matrix elements can be reduced to a number of independent ones - three in this case - which are specific to the three-band model of the diamond lattice. This symmetry analysis and subsequent reduction of complexity highlights the power of this approach and illustrates why it is widely used for band structure calculations. By including the spin in the three-band model, it becomes a six-band model with states in the basis $|J, m_J\rangle$, labeled by $J = L + S$, because neither L nor S is a good quantum number anymore - as a consequence of the inclusion of the spin-orbit coupling term in Eq. 2.18 [102]. The six-band model describes the light and heavy holes, as well as the spin-orbit split-off bands in diamond below the Fermi energy. It was treated in very similar fashion by a number of different authors [102, 122, 123, 128, 129]. More elaborate models, such as the 8×8- Kane model or the 14×14- Kane model [104, 128, 130–133], are generally used to describe the bands of a wide range of semiconductors around their Fermi level in more detail. The group theoretical analysis of graphene with the $k \cdot p$- method started by considering graphite [72], because a monolayer of this material was not discovered at the time and it is still subject of active research [115, 134].

2.2.2. Löwdin Perturbation Theory

In larger Hilbert spaces, where a group of states is only weakly interacting with another group of states, it can be beneficial to treat both groups separately and include their interaction only effectively. Löwdin perturbation theory [103] is a method for computing a modified Hamilton operator acting only on a subspace of the larger Hamilton operator. It separates the whole Hilbert space into group A, for which the equations are solved exactly, and group B, which are included as additional interactions for group A. This process is called *downfolding* and it must be solved approximately, because it contains the energies of the possibly degenerate states of A, which are not known prior to solving the eigensystem, but are required for its formulation. As an approximation, these energies are usually substituted by known expressions, close

to the actual value. Then, the Hamiltonian for the combined system $A + B$ is expressed as a Hamiltonian U^A, only for the subspace of system A, where B is accounted for via renormalization, resulting in [103]

$$U_{mn}^A = H_{mn} + \sum_{\alpha \in B} \frac{H_{m\alpha}\left(1 - \delta_{m\alpha}\right) H_{\alpha n}\left(1 - \delta_{\alpha n}\right)}{E - H_{\alpha\alpha}} + \sum_{\alpha,\beta \in B} \frac{H_{m\alpha}\left(1 - \delta_{m\alpha}\right) H_{\alpha\beta}\left(1 - \delta_{\alpha\beta}\right) H_{\beta n}\left(1 - \delta_{\beta n}\right)}{\left(E - H_{\alpha\alpha}\right)\left(E - H_{\beta\beta}\right)} + \cdots$$

(2.20)

Here the indices m and n range only over the states of the system A.

2.2.3. Dresselhaus-type Spin-orbit Coupling: Bulk Inversion Asymmetry

Dresselhaus [95] used $k \cdot p$-theory to determine band splittings of semiconductors with diamond structure due to spin-orbit coupling. First they derived secular equations in the basis of degenerate unperturbed functions that would transform according to various irreducible representations of the double point group T_d of zinc blende [122, 123]. In a following step, the degenerate functions are then subject to spin-orbit coupling, which incorporates the symmetry of the lattice by symmetries of its matrix elements. Spin splittings occur when along high-symmetry lines the previously degenerate functions reorder according to the irreducible representation of the point groups across the Brillouin zone. The main difference of the zinc blende structure to the diamond structure is the lack of inversion symmetry, as a consequence of the two different types of elements in the crystal. Dresselhaus found that the lower conduction band Γ_6 of zinc blende is spin-split by [95, 135]

$$E = C_0 k^2 \pm C_1 [k^2 \left(k_x^2 k_y^2 + k_y^2 k_z^2 + k_z^2 k_x^2\right) - 9k_x^2 k_y^2 k_z^2]^{1/2},$$

(2.21)

with two material constants C_0 and C_1. This splitting is the central feature of the linear and cubic Dresselhaus-type spin-orbit coupling effect and a result of the absence of inversion symmetry. Using the theory of invariants, one can derive the Hamiltonian for the conduction electrons [102, 104, 135] and one can construct the following invariant Hamiltonian in the $\{|\uparrow\rangle, |\downarrow\rangle\}$ space

$$\hat{H}_k^{6c6c} = \gamma_c \left(\left[k_x \left(k_y^2 - k_z^2\right)\right] \hat{s}_x + \text{c.p.}\right).$$

(2.22)

Here, c.p. stands for cyclic permutation. This Hamiltonian results in the same splitting as in Eq. 2.21. For two dimensions, Eq. 2.22 is modified by $k_z \to \langle k_z \rangle = 0$ and $k_z^2 \to \langle k_z^2 \rangle \neq 0$ and by using the notation $k_\pm = k_x \pm i k_y$ it becomes

$$\hat{H}_{6c6c}^b = b \begin{pmatrix} 0 & \frac{1}{4} k_- \left(k_+^2 - k_-^2\right) - k_+ \langle k_z^2 \rangle \\ \frac{1}{4} k_+ \left(k_-^2 - k_+^2\right) - k_- \langle k_z^2 \rangle & 0 \end{pmatrix},$$

(2.23)

where b is a material constant. In a two-dimensional system it can be rewritten into the linear Dresselhaus term [136–140]

$$\hat{H}_D^{\text{lin}} = -\langle k_z^2 \rangle \left(\hat{s}_x k_x - \hat{s}_y k_y \right) \tag{2.24}$$

and the cubic Dresselhaus term

$$\hat{H}_D^{\text{cub}} = k_x k_y \left(k_y \hat{s}_x - k_x \hat{s}_y \right). \tag{2.25}$$

These two effective forms of the Dresselhaus spin-orbit coupling are encountered in models with explicitly broken inversion symmetry in general. In fact, operators invariant under the D_{2d} point group as in Eqs. 2.24 and 2.25 are referred to as Dresselhaus-type, because of their identical transformation behavior.

2.2.4. Rashba-type Spin-orbit Coupling: Structure Inversion Asymmetry

Rashba and Sheka have computed the energy bands of the wurtzite structure and proceeded in similar fashion to Dresselhaus and employed $k \cdot p$-theory to the wurtzite structure point group $C_{6\nu}$ [141]. Only terms $\sim k^2$ in the momentum are retained in the Löwdin perturbative treatment and the spin-splitting of the Γ_7^6 valence band becomes [96]

$$E_{1,2} = ak_\parallel^2 + bk_\perp^2 + \varepsilon \pm \alpha k_\parallel, \tag{2.26}$$

using constants a, b, ε and α, with the in-plane momentum $k_\parallel$ and out-of-plane momentum $k_\perp$. Then, an extremum of the energy splitting for both solutions is located on a circle with radius $k_\parallel \sim |\frac{\alpha}{2a}|$. This feature of Eq. 2.26 occurs in situations, when a crystal exhibits a single high-symmetry axis of at least threefold rotational symmetry [142]. Let such an axis be parallel to the cartesian z-coordinate. In a two-dimensional system perpendicular to said axis, an effective Hamiltonian [106]

$$\hat{H}_{\text{R}} = \alpha \left(\hat{\boldsymbol{s}} \times \boldsymbol{k} \right)_z = \alpha \left(\hat{s}_x k_y - \hat{s}_y k_x \right) \tag{2.27}$$

can be formulated, which has the same qualitative feature of the spin-splitting discussed above [143]. Causes for the Rashba-type spin-orbit coupling can be electric fields [107, 144, 145], which reduce the symmetry of the system, leading to lifted degeneracies [146] as a consequence of the Stark effect [80]. In graphene, spin-flip terms due to Rashba-type spin-orbit coupling connect π-bonds, made up of p_z-orbitals, which are symmetric along the z-axis, to the s-, p_x- and p_y-orbitals from the σ-bonds. DFT calculations have shown, that the spin-orbit coupling from the p_x- and p_y-orbitals is much weaker than that of the d-orbitals [110]. Other DFT calculations have shown, that in-plane deformations may enhance the Rashba-type spin-orbit coupling strongly [147].

2.2.5. Symmetry Properties of Spin-orbit Coupling

The Rashba Hamiltonian in Eq. 2.27, similar to the linear Dresselhaus Hamiltonian Eq. 2.24, is formulated in a specific coordinate system. In order to discuss such a transformation behavior, it needs to be known how the individual components transform. This is presented in the appendix A.1. For a Hamiltonian to be invariant under point group symmetries, it needs to transform according to the A_1 irreducible representation of that group[4]. Otherwise, a similarity transformation may be used to show that the Hamiltonian is not invariant under the point group operations, even if it transforms according to any number of irreducible representations of that group other than A_1 [148]. As an example, the rows of the tables A.7, A.8 and A.9 in the appendix may be used to construct Dresselhaus- and Rashba-type Hamiltonians and possible choices for basis functions are listed there. They transform according to the respective irreducible representations. These products of basis functions are set apart from each other by their transformation behavior according to different irreducible representations of the corresponding point groups, as well as their specific choice of coordinates. This is generally expressed in the theory of invariants, which constructs interaction terms according to their transformation behavior [104]. A possible formulation of the linear Dresselhaus Hamiltonian is $\hat{s}_y k_x + \hat{s}_x k_y \sim \left(x^2 + y^2 \right) z$ [149] in a given choice of basis. It does not transform as a basis function of the A_1 irreducible representation of the group D_{2d}. For this particular symmetry, the group actions are defined in a coordinate system rotated by 45° with respect to the above Dresselhaus-type Hamiltonian. For rotating the Hamiltonian by 45°, the coordinates need to be changed as $k_x \to k_x + k_y$, $\hat{s}_y \to \hat{s}_x + \hat{s}_y$ etc. Then

$$\hat{s}_y k_x + \hat{s}_x k_y \to \hat{s}_x k_x - \hat{s}_y k_y, \tag{2.28}$$

which transforms according to xyz - a cubic basis function of the irreducible representation A_1 of D_{2d}. The result has the form of Eq. 2.24. The Rashba part in Eq. 2.27 transforms according to $\left(x^2 - y^2 \right) z$. It is a basis function of the irreducible representation A_1 of the group $C_{2\nu}$. As stated above, terms with similar transformation behavior can be used to create effective Hamilton operators of the same type, but with different orders in which the coordinates occur or in different coordinate choices. For example by considering higher-than-linear orders (as the cubic Dresselhaus term, Eq. 2.25) or by swapping $k_x \leftrightarrow \hat{\tau}_z \hat{\sigma}_x$ and $k_y \leftrightarrow \hat{\sigma}_y$, with the Pauli matrices in sublattice spin space $\hat{\sigma}_i$, the explicit form of the terms can be changed, while their transformation behavior is maintained. By using the formulation in sublattice spin rather than momentum, a lower-than-linear order used in low energy approximation is achieved [150]. For a discussion of the identical symmetry transformation of these terms, also see appendix A.1.

---

[4]The A_1 irreducible representation is a one-dimensional representation, where the characters of each class of the group elements are $+1$.

2.3. Strength of Spin-orbit Coupling in Graphene

In this section, an overview is given on the status of theoretical and experimental assessment of the spin-orbit coupling strength in graphene. Today, the spin-orbit coupling gap may be measured with electron spin resonance, detected via resistivity measurements with graphene in Hall bar geometry in a magnetic field [151]. The application of a magnetic field on the carriers in the sample will align the spin magnetic moments to the field direction. If a photon with an energy matching the resonance frequency starts to interact with a carrier and is thus allowed to bridge the Zeeman-splitting gap, a spin flip of the carrier can be induced [152]. This spin flip is facilitated by the polarization of the magnetic field vector of the incident photon perpendicular to the quantization axis of the carriers. Such condition allows for a finite transition probability to the spin-flip state of the carrier, if additionally the precession frequency and the photon frequency are in resonance. The sample resistivity is changed, because holes in the valence and mobile carriers in the conduction band are created by such an excitation. This measurement technique enables the measurement of the g-factor of graphene and also the zero-field splitting. Application of this measurement technique results in direct access of the intrinsic spin-orbit coupling gap, being measured as $\Delta E = 42.2(8)\,\mu\text{eV}$ [151], as well as another closely matching result [153]. Van-der-Waals heterostructures may provide a controlled environment to systematically induce and measure spin-orbit coupling effects in graphene [154].

The spin-orbit interaction is responsible for a quantum interference effect, weak antilocalization (WAL) [87, 155–158], caused by self-interference of electronic wave functions along closed paths [75, 159]. The presence of spin-orbit coupling locks the momentum of a carrier to its spin. Consequently counter-propagating carriers are phase-locked and prone to destructive interference. This suppresses backscattering and results in a higher conductivity at zero magnetic field [94, 160]. In graphene, the chirality of the charge carriers is responsible for the phase shift, that would otherwise be caused by strong spin orbit coupling [152]. Thus, in this particular case, the system exhibits weak antilocalization, despite rather weak spin-orbit coupling. Weak localization (WL) on the other hand is an effect of similar quantum mechanical origin as WAL. At low temperatures, the conductivity of a degenerate electron gas decreases, due to elastic scattering at impurities of the solid, despite the expected intrinsic conductivity. This is caused by long-range coherence of electronic wave-functions, causing constructive interference and an increased backscattering. The consequence is lower conductivity at zero magnetic field [157, 161]. The difference between WL and WAL is precisely the phase locking of spin and propagation, in the case of strong spin-orbit coupling. The strength of Rashba-type spin-orbit coupling in graphene-on-WS$_2$-type van-der-Waals heterostructures is measured on the order of $5\,\text{meV}$ [87] or up to $10\,\text{meV} - 15\,\text{meV}$ [154]. For Bilayer-graphene on WSe$_2$, the induced Rashba-type spin-orbit coupling is measured by Landau level structure obtained from electrical transport measurements and a spin-orbit coupling strength of around $15(5)\,\text{meV}$ is found [162]. Another type of spin-orbit coupling, the Ising spin-orbit coupling [163], is fitted to have a magnitude of $2.2(1)\,\text{meV}$ in this exper-

iment. Ising spin-orbit coupling is a type of Dresselhaus-type spin-orbit coupling, arising in non-centrosymmetric solids, such as monolayer transition-metal dichalcogenides (TMDCs) [163]. It can be understood as a Zeeman splitting, which preserves time-reversal symmetry, by exhibiting a spin-splitting of opposite sign on the two valleys in the Brillouin zone [162, 164]. The modification of graphene band structure in heterostructures other than TMDCs are possible, for example with Pb and Au [165] or Pb and Ir [166], causing a proximity-induction of the large spin-orbit coupling. In this case, the hybridization of graphene with the heavy Pb atoms causes a very large spin-orbit coupling strength of 80 meV [165], which is observed using non-local signals in resistivity measurements and confirmed via WL signals from fitting to magnetoconductivity data. Other types of metals, such as Cu [167], also result in proximity-induced spin-orbit couplings of 20 meV.

Other methods for increasing the spin-orbit coupling in graphene may be the preparation of a sample with adatoms, such as fluorine or hydrogen. In this case, the adatom locally distorts the two-dimensional structure of graphene, such that the following three-dimensional hybridization is a direct cause for the increased spin-orbit coupling strength. In the case of hydrogen it amounts to 2.5 meV [83]. For fluorinated graphene, not only the distortion of the lattice, but also the large spin-orbit coupling of the F atoms themselves is suspected to be responsible for the 9 meV increase of the spin-orbit coupling strength over a pristine graphene sample or the hydrogenated one [168].

Not only experiments have dealt with the characterization of spin-orbit coupling in graphene, but also theoretical assessments have been performed. Kane and Mele have estimated the intrinsic spin-orbit coupling strength of graphene, resulting in a gap at the Dirac points on the order of 0.1 meV [41]. By fitting a similar tight-binding model to band structures obtained by ab-initio computations, spin-orbit coupling gaps of around $1\,\mu$eV are obtained [81]. For the Rashba spin-orbit coupling strength for a typical electric field of $1.7 \times 10^{-1}\,\mathrm{V\,nm^{-1}}$, these models obtained $43\,\mu$eV and $11\,\mu$eV, respectively. Other studies have found results for the intrinsic spin-orbit coupling strength on the order of 4 meV, while the resulting gap at the Dirac point is $1\,\mu$eV [169]. These numbers were obtained by comparing density-functional theoretical calculations (DFT), featuring the local density approximation of the exchange-correlation potential, to tight-binding models that include both σ- and π-bands of graphene. In this model, the cause of spin-orbit coupling is attributed to the interaction of the σ-bonds of one atom with the p_z-orbital of its neighboring atom. Using other types of DFT calculations with more sophisticated all-electron potentials [170] instead of pseudo-potentials as in [169], a value of $50\,\mu$eV is obtained [171], where a stability of the result with respect to different types of local-density approximation computation is attested. The value for the spin-orbit splitting of the σ-band at the Γ-point of 9 meV is similar to the one in [169], however. More rigorous tight-binding model calculations predict a spin-orbit coupling mostly due to the d-orbitals in graphene, where a gap at the Dirac points of around $23\,\mu$eV is attributed to the interactions of the π-band with the d-orbitals rather than to the σ-band states [80].

Other types of spin-orbit coupling can be systematically dissected by symmetry analysis of the underlying Hamiltonians. In this case, group theoretical arguments for different forms

of the Hamiltonians are used to discuss a hierarchy of hopping and spin-flipping terms that could arise in corresponding tight-binding models and exhibit different characteristics.

One type of spin-orbit coupling is the 'pseudospin-inversion-asymmetry'-induced spin-orbit coupling (PIA) [124, 139]. It is of similar origin as the Rashba-type spin-orbit coupling, coming from a system with broken mirror symmetry along an axis perpendicular to the graphene plane. However, in rippled graphene, the underlying symmetry group D_{3d} prevents nearest-neighbor hopping with a simultaneous spin-flip. As a consequence, only next-nearest neighbor hopping with a spin-flip is occurring, which has a different symmetry than the Rashba-type spin-orbit coupling and exhibits $C_{6\nu}$-symmetry [124]. By using DFT calculations, the strength of these types of spin-orbit couplings can also be estimated by comparison to tight-binding models. This way, the spin-orbit coupling strength of graphene on TMDCs, such as MOS_2 and WSe_2 is computed [139]. In this setup, intrinsic spin-orbit coupling strengths on the order of $0.2\,meV$ and Rashba-type spin-orbit coupling of $0.13\,meV$ (MOS_2), up to $0.36\,meV$ (WS_2) are computed, as well as PIA spin-orbit coupling strengths of $-2.23\,meV$ and $-3.81\,meV$. A theoretical observation of adatoms on graphene leads to the conclusion - again via fitting of a tight binding-computation against DFT computations - that the sp^3-hybridization of a hydrogen adatom is the main source for the enhancement of the intrinsic spin-orbit coupling of graphene [172]. For fluorine however, the hybridization of the fluorine p-orbitals with the carbon p-orbitals is an order of magnitude larger than what would be otherwise expected for sp^3-hybridization alone, because of the strong fluorine spin-orbit coupling.

Even though much work has been invested so far in the precise determination of the spin-orbit coupling gap in graphene, a clear and definite answer is yet to be found. While the overall order of magnitude of the interaction parameter seems to be backed by enough theoretical evidence, in experiments, results are still elusive due to the weak spin-orbit coupling in pristine graphene. Thus, it is expected that in the future different methods of increasing the spin-orbit interactions will be proposed in order to obtain experimental verification of various other aspects of spin physics in graphene.

3. Tight-binding Model

3.1. Introduction

The band structure computation of solids is a common task in theoretical condensed matter physics and over time many different methods have emerged [173, 174]. One of the first steps towards the band structure computation of graphene were taken with the formulation of a tight-binding model for graphite [70]. Today, much is known about graphene [88] and the tight-binding model is used for the description of a wide selection of solids, whereas the parameters of the model are usually fitted against other first principle calculations [80]. For the purpose of this thesis, a sample of graphene will be described by a multi-orbital tight-binding model, which consists of several orbitals per lattice site, as well as a spin degree of freedom. The zone-folding technique is applied, where a unit cell of several atoms is considered periodic in one or two directions [88, 175]. Two-dimensional periodic boundary conditions may be used to describe bulk graphene, whereas only one-dimensional periodic boundary conditions introduce edges in the system. The dangling bonds of the carbon atoms at the edges will be assumed to be terminated by hydrogen bonds, similar in electronegativity to carbon, and therefore the electrons of the sp^2-hybridized orbitals do not contribute to the band structure [50, 176, 177]. Consequently, the electronic states can be separated into in-plane and out-of-plane states, which do not couple among each other, even at the edges. The in-plane σ-band states are mostly responsible for the lattice geometry, while the out-of-plane π-band states determine the electronic properties, as long as the hexagonal structure of the sample is not perturbed. Therefore the $2p_x$-, $2p_y$- and $2s$-orbitals do not need to be regarded for most computations discussed in this thesis. For the description of external factors, such as an electric field, which may lead to Rashba-type spin-orbit coupling, the sp^2-hybridized orbitals become relevant, however. In order to reduce the number of orbitals in the model, an effective term describing the Rashba-type spin-orbit coupling originating from an external electric field will be introduced, because it may describe the effect on the π-bands accurately, without the required complexity of the added σ-states in the system. On the other hand the higher-energy d-orbitals are important for spin-orbit coupling effects. This will influence the electronic properties of the π-bands and therefore the d-orbitals are included in the tight-binding model without making use of effective terms. Graphene nanoribbons with a zigzag edge are metallic in general, because of the flat bands crossing the gap, which belong to the states residing at these edges. Bulk graphene is a semiconductor with a tiny gap arising from intrinsic-spin orbit coupling that is easily overcome by doping [80, 178].

A multi-orbital tight-binding model in the mean-field approximation provides a flexible

method, such that many of these features may be obtained accurately [179].

3.2. Definition of a Multi-band Tight-binding Model

3.2.1. The Geometry of Graphene

Graphene is an atomically flat two-dimensional allotrope of carbon, which forms a hexagonal lattice structure via sp^2-hybridized orbitals. Carbon has six electrons, where two electrons are contained in the $1s$ states and the other four in the $2s$ and $2p$-orbitals. In the sp^2-hybridization, the $2s$-, $2p_x$- and the $2p_y$-orbitals form three bonding and three anti-bonding σ-orbitals, that extend in $120°$ angles in a plane from each atomic site. The electrons in the inner-most shell, the $1s$ state of carbon, are not influenced by the hybridization and therefore each atom contributes three electrons to the three sp^2-hybridized orbitals, filling the σ-states. Then one electron per atomic site is left, which occupies the next energetically low-lying p_z-orbitals. Thus graphene has half-filled π-bonds. Due to symmetry, the p_z-orbitals do not interact with the orbitals forming the σ-bonds. The resulting lattice structure is the so-called *honeycomb lattice*, which can be described as two super-imposed triangular lattices. In the following it is considered a triangular lattice with a two-atomic basis, such that each atom in graphene can be attributed to either sublattice A or B. The resulting structure is shown in Fig. 3.1 a) with the two sublattices displayed in black and red. Then the Bravais lattice is spanned by the vectors

$$\boldsymbol{a}_1 = \sqrt{3}a\,(1,0) \qquad\qquad \boldsymbol{a}_2 = \frac{\sqrt{3}a}{2}\left(1,\sqrt{3}\right), \qquad (3.1)$$

where $a = 1.42\,\mathrm{nm}$ is the lattice constant of graphene [69]. The vectors pointing from one site to its nearest neighbors are denoted by the vectors

$$\boldsymbol{\delta}_1 = \frac{a}{2}\left(\sqrt{3},1\right) \qquad \boldsymbol{\delta}_2 = \frac{a}{2}\left(-\sqrt{3},1\right) \qquad \boldsymbol{\delta}_3 = -a\,(0,1)\,. \qquad (3.2)$$

The two atoms in the unit cell are non-equivalent, and consequently the resulting Brillouin zone also exhibits a triangular shape, with two non-equivalent so-called *Dirac points*. These points coincide with the crystallographic K and K'-points of the honeycomb lattice, see Fig 3.1 b).

3.2.2. The Tight-binding Approximation for a Single Band

The general assumption of the tight-binding approximation is that electrons in the crystal are tightly localized around a specific atomic nucleus, while they interact with the nuclei of the surrounding atoms perturbatively [93]. Let the atoms be located at positions $\mathbf{R}$, then the Hamilton operator H for an electron is expressed as

$$H = \frac{\mathbf{p}^2}{2m} + \sum_{\mathbf{R}'} V\left(\mathbf{r} - \mathbf{R}'\right) \qquad (3.3)$$

$$= H_{\mathbf{R}} + \sum_{\mathbf{R}'\neq\mathbf{R}} V\left(\mathbf{r} - \mathbf{R}'\right), \qquad (3.4)$$
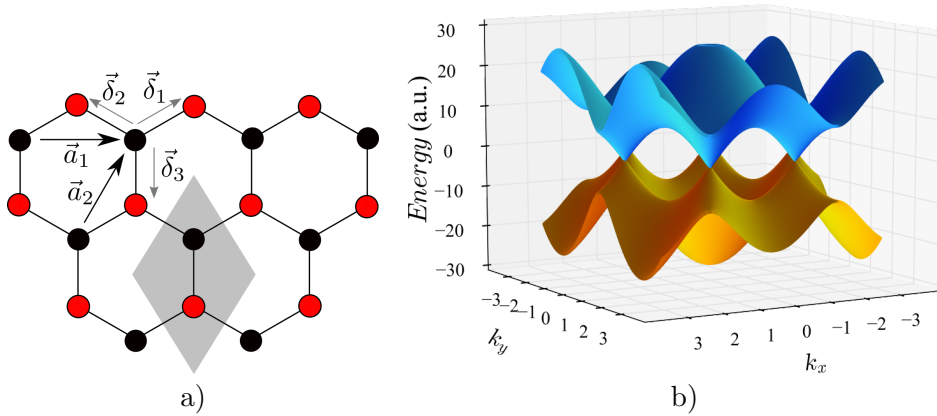
FIGURE 3.1.: a) The honeycomb lattice of graphene with two super-imposed triangular lattices A and B and the lattices vectors. The primitive two-atomic unit cell is marked in gray. b) The dispersion relation of graphene around the Fermi energy $E = 0$.

where the second part of the sum in Eq. 3.4 is the perturbation to the atomic Hamiltonian $H_{\mathbf{R}}$, due to the crystal lattice surrounding site $\mathbf{R}$. This problem can be solved, when a localized basis at each atomic site is considered, such as the localized Wannier states [93]. Then the tight-binding model is described by a transition matrix element t, the *hopping*, from one site to one of its neighbors. Due to the strong localization of the basis states around a specific lattice site, it is a valid approximation to only consider nearest neighbor-hopping matrix elements. Matrix elements among sites located further apart are considered to be negligibly small. As an approximation to the localized Wannier states, atomic orbitals $\varphi_n(\mathbf{r})$ with a set of quantum numbers n are often used [80, 93, 150]. In the atomic orbital basis, states located at different lattice sites are not orthogonal, in contrast to the Wannier states, such that the finite overlap among these basis states must be respected during the solution of the eigenvalue problem. Comparisons of the tight-binding model with DFT computations have shown, however, that this overlap may be neglected for the low-energy description of graphene [80]. Thus a single-orbital tight-binding model in real space with atomic orbitals as basis states may be formulated as [50]

$$H = t \sum_{\mathbf{R}} \sum_{i=1}^{3} \hat{a}_{\mathbf{R}}^{\dagger} \hat{b}_{\mathbf{R}+\boldsymbol{\delta}_i} + \text{h.c.}, \tag{3.5}$$

where the operators $\hat{a}_{\mathbf{R}}^{\dagger}$ and $\hat{b}_{\mathbf{R}+\boldsymbol{\delta}_i}^{\dagger}$ create an electron in the unit cell at position $\mathbf{R}$ and $\mathbf{R} + \boldsymbol{\delta}_i$ and their adjoint annihilates an electron at these positions. They satisfy the fermion anticommutation relations, respectively [50]. The coordinate system has been chosen as in Fig. 3.1 a), such that each $\mathbf{R}$ coincides with the lattices A. The transition matrix element t

for nearest neighbors is usually obtained from fitting the tight-binding model to experimental data [88]. Most of these results are on the order of $|t| = 3\,\mathrm{eV}$ and this value will be used throughout this thesis [150]. The tight-binding model may also be used to fit a larger portion of the Brillouin zone, but then next-nearest-neighbor hopping must be included for more accurate results. This description will be extended towards a multi-orbital tight-binding model and only a nearest-neighbor approximation will be used. For the representation of the Hamiltonian in reciprocal space, the creation and annihilation operators in Eq. 3.5 are Fourier transformed via [50]

$$\hat{a}_{\mathbf{R}} = \frac{1}{\sqrt{N}} \sum_{\mathbf{k}} e^{i\mathbf{k}\mathbf{R}} \hat{\alpha}_{\mathbf{k}} \qquad\qquad \hat{b}_{\mathbf{R}} = \frac{1}{\sqrt{N}} \sum_{\mathbf{k}} e^{i\mathbf{k}\mathbf{R}} \hat{\beta}_{\mathbf{k}} \qquad\qquad (3.6)$$

and the corresponding creation operators in analogy. The number of unit cells is given as N. Then a single-band tight-binding model in reciprocal space at point $\mathbf{k}$ can be formulated, resulting in [50, 80, 93]

$$H_{\mathbf{k}} = t \sum_{i=1}^{3} e^{-i\boldsymbol{\delta}_i \mathbf{k}} \hat{\alpha}_{\mathbf{k}}^{\dagger} \hat{\beta}_{\mathbf{k}} + \mathrm{h.c..} \qquad\qquad (3.7)$$

3.2.3. The Low-energy Description of Graphene

From the single-band Hamiltonian in Eq. 3.7 one can obtain a 2×2-model in the basis of the A and B sublattices, by first rewriting the sum of phase factors $\sum_{i=1}^{3} e^{-i\boldsymbol{\delta}_i \mathbf{k}}$ in terms of the lattices vectors $\boldsymbol{a}_1$ and $\boldsymbol{a}_2$, such that

$$\gamma_{\mathbf{k}} := 1 + e^{-i\mathbf{k}\boldsymbol{a}_2} + e^{-i\mathbf{k}(\boldsymbol{a}_2 - \boldsymbol{a}_1)} \qquad\qquad (3.8)$$

can be defined. The phase due to $e^{-i\mathbf{k}\boldsymbol{\delta}_3}$ can be absorbed into the creation and annihilation operators. Then the Hamilton operator can compactly be written as

$$H_{\mathbf{k}} = t \begin{pmatrix} 0 & \gamma_{\mathbf{k}}^* \\ \gamma_{\mathbf{k}} & 0 \end{pmatrix}. \qquad\qquad (3.9)$$

The basis states are those states located at the two sublattices A and B. Solving $H_{\mathbf{k}}$ in the Brillouin zone results in the dispersion relation depicted in Fig. 3.1 b). This model is a good approximation around the two Dirac points, the points where conduction and valence band become degenerate. Thus, Eq. 3.9 can approximated by a low-energy description, applicable for the close vicinity of these points. For that, $\gamma_{\mathbf{k}}$ is approximated around the Dirac points $K^{(')} = (\pm\frac{4\pi}{3\sqrt{3}}, 0)$, resulting in the low-energy Hamiltonian

$$H_0 = -v_F \hbar (\hat{\tau}_z \hat{\sigma}_x k_x + \hat{\sigma}_y k_y). \qquad\qquad (3.10)$$

Real-valued Functions $\mathcal{R}_l^\lambda$	Complex Functions ϕ_l^m	Linear Combination
$s = \frac{1}{\sqrt{4\pi}}$	$s = \frac{1}{\sqrt{4\pi}}$	$Y_{00} = \quad s \quad = \quad Y_0^0$
$p_z = \sqrt{\frac{3}{4\pi}}\frac{z}{r}$	$p_0 = \sqrt{\frac{3}{4\pi}} \cdot \frac{z}{r}$	$Y_{1,0} = \quad p_z \quad = \quad Y_1^0$
$p_x = \sqrt{\frac{3}{4\pi}}\frac{x}{r}$	$p_{-1} = \frac{1}{\sqrt{2}}\sqrt{\frac{3}{4\pi}}\frac{(x-iy)}{r}$	$Y_{1,1} = \quad p_x \quad = \quad \sqrt{\frac{1}{2}}\left(Y_1^{-1} - Y_1^1\right)$
$p_y = \sqrt{\frac{3}{4\pi}}\frac{y}{r}$	$p_1 = -\frac{1}{\sqrt{2}}\sqrt{\frac{3}{4\pi}}\frac{(x+iy)}{r}$	$Y_{1,-1} = \quad p_y \quad = \quad i\sqrt{\frac{1}{2}}\left(Y_1^{-1} + Y_1^1\right)$
$d_{z^2} = \sqrt{\frac{5}{16\pi}}\frac{(3z^2-r^2)}{r^2}$	$d_0 = \sqrt{\frac{5}{16\pi}}\frac{(3z^2-r^2)}{r^2}$	$Y_{2,0} = \quad d_{z^2} \quad = \quad Y_2^0$
$d_{xz} = \sqrt{12}\sqrt{\frac{5}{16\pi}}\frac{xz}{r^2}$	$d_1 = -\sqrt{6}\sqrt{\frac{5}{16\pi}}\frac{(x+iy)z}{r^2}$	$Y_{2,1} = \quad d_{xz} \quad = \quad \sqrt{\frac{1}{2}}\left(Y_2^{-1} - Y_2^1\right)$
$d_{yz} = \sqrt{12}\sqrt{\frac{5}{16\pi}}\frac{yz}{r^2}$	$d_{-1} = \sqrt{6}\sqrt{\frac{5}{16\pi}}\frac{(x-iy)z}{r^2}$	$Y_{2,-1} = \quad d_{yz} \quad = \quad i\sqrt{\frac{1}{2}}\left(Y_2^{-1} + Y_2^1\right)$
$d_{x^2-y^2} = \sqrt{3}\sqrt{\frac{5}{16\pi}}\frac{(x^2-y^2)}{r^2}$	$d_2 = \sqrt{\frac{3}{2}}\sqrt{\frac{5}{16\pi}}\frac{(x+iy)^2}{r^2}$	$Y_{2,2} = \quad d_{x^2-y^2} \quad = \quad \sqrt{\frac{1}{2}}\left(Y_2^{-2} + Y_2^2\right)$
$d_{xy} = \sqrt{12}\sqrt{\frac{5}{16\pi}}\frac{xy}{r^2}$	$d_{-2} = \sqrt{\frac{3}{2}}\sqrt{\frac{5}{16\pi}}\frac{(x-iy)^2}{r^2}$	$Y_{2,-2} = \quad d_{xy} \quad = \quad i\sqrt{\frac{1}{2}}\left(Y_2^{-2} - Y_2^2\right)$

TABLE 3.1.: Real and complex valued atomic orbitals [181]. The cartesian wave functions are real-valued functions and denoted $\mathcal{R}_l^\lambda(\boldsymbol{x}) := Y_{l\lambda}$ and identified with the naming convention p_z, d_{xz} etc. The conversion to the complex spherical coordinates $\phi_l^m(\boldsymbol{x}) := Y_l^m$ as eigenfunctions to the angular momentum operators $\hat{L}^2$ and $\hat{L}_z$ with quantum numbers l and m are given. The spherical harmonics are defined in Eq. 3.17.

The components k_x and k_y are regarded in close vicinity to the Dirac points via the approximation $\mathbf{k} \approx K^{(')} + (k_x, k_y)$. The constant $v_F = -\frac{3ta}{2\hbar} \approx 1 \times 10^6\,\mathrm{m\,s^{-1}}$ is the Fermi velocity. In order to write Eq. 3.10, the valley isospin $\hat{\tau}_z = \pm 1$ is introduced, which specifies the Dirac cone for which the Hamiltonian is formulated, as it is originating from the relative sign of K and K'. The two sublattices obtain a sublattice spin $\hat{\sigma}_z = \pm 1$, compactly expressing the two-dimensional basis from Eq. 3.9 for states at lattices A and B. The physical description of the sublattice spin is different to that of the real spin $\hat{s}$, because of its transformation behavior [180]. For details regarding the transformation of real and sublattice spin, refer to the appendix A.1.

The Slater-Koster Approximation

The *Slater-Koster approximation* [182] reduces the computation of matrix elements of neighboring sites among different orbitals to a geometrical problem. In this approximation, the interaction matrix elements are reduced to two-center integrals, which only depend on the relative displacement of the atomic sites in the model. These expressions are then formulated via polynomials in the displacement vectors and material-specific constants. The symmetry of the d-orbitals requires several material parameters in order to correctly account for their relative orientation. The contribution from the d- to the p_z-orbitals is mediated via $V_{pd\pi}$,

while the d-orbitals among each other couple via $V_{dd\delta}$ and $V_{dd\pi}$ [80], shown in Fig. 3.2 a). A choice of basis states widely used in tight-binding computations, due to their alignment along the cartesian coordinate axes, is the real-valued cubic harmonics $\mathcal{R}_l^\lambda(\boldsymbol{x}) := Y_{l\lambda}$ [181]. In this definition the index λ denotes the different orbitals for each angular momentum quantum number l. The Slater-Koster approximation makes use of the symmetries of the spherical orbitals and relates them to the matrix elements of the cartesian orbitals. The radially symmetric and complex spherical harmonics $\phi_l^m(\boldsymbol{x}) := Y_l^m$ have the angular momentum quantum number l and its z-projection m. There are different conventions found in the literature regarding the complex phase of the orbital wave functions and two sets of wave functions are stated in Tab. 3.1. Matrix elements between the real-valued orbitals are computed by first expressing the real valued orbitals as linear combinations of complex ones. This is done via a unitary transformation $U_{\mathfrak{lmn}}$, such that

$$\left(U_{\mathfrak{lmn}}\mathcal{R}_l^\lambda\right)(\boldsymbol{x}) = \sum_m b_{m\lambda}^l(\mathfrak{lmn})\phi_l^m(\boldsymbol{x}), \tag{3.11}$$

where appropriate and site-dependent coefficients $b_{m\lambda}^l(\mathfrak{lmn})$ are defined. $U_{\mathfrak{lmn}}$ and these coefficients depend on the local coordinate system at each lattice site. The three indices $\mathfrak{lmn}$ are the so-called directive cosines, which define a vector spanning in the direction from one site to one of its neighbors with unit length, see Fig. 3.2 b). The two vectors of each tripod, tangential to the graphene plane, are obtained by fixing the direction from a site to one of its nearest neighbors by the vector $\boldsymbol{d} = (\mathfrak{l}, \mathfrak{m}, \mathfrak{n})$. The other tangential vector is perpendicular to that direction and the normal vector is perpendicular to both tangential vectors and parallel to the surface normal. This tripod defines the local coordinate system at each site and the x-axis is given by the direction of $\boldsymbol{d}$. Using the above considerations the interaction of a cartesian orbital λ with quantum number l_1 and at another orbital ν at distance $\boldsymbol{R}$ with l_2 is given by [183]

$$\left(\mathcal{R}_{l_1}^\lambda(\boldsymbol{x}+\boldsymbol{R})V(\boldsymbol{x}+\boldsymbol{R})\mathcal{R}_{l_2}^\nu(\boldsymbol{x})\right) = 2\sum_{m>0}^{\min(l_1,l_2)} O_{l_1,l_2}^m\{\mathrm{Re}\left[\bar{b}_{m\lambda}^{l_1}(\mathfrak{lmn})b_{m\nu}^{l_2}(\mathfrak{lmn})\right]\}, \tag{3.12}$$

where $V(\boldsymbol{x}+\boldsymbol{R})$ is the crystal potential of the atoms surrounding site ν. In this definition $O_{l_1 l_2}^m$ are the material parameters in the two-center approximation - e.g. $O_{12}^1 = V_{pd\pi}$ - stated by the matrix elements using the complex atomic orbitals,

$$\delta_{ip}O_{jk}^p = \left(\phi_j^i(\boldsymbol{x}+\boldsymbol{R})V(\boldsymbol{x}+\boldsymbol{R})\phi_k^p(\boldsymbol{x})\right). \tag{3.13}$$

Thus, each interaction matrix element is reduced to a polynomial of the coefficients arising in the unitary transformation between the real and complex valued atomic orbitals. The matrix element connecting the p_z-orbitals on two neighboring sites becomes independent of direction of the relative displacement, due to the radial symmetry of the p_z-orbitals. However, the material parameter $V_{pp\pi}$ in the corresponding matrix element may change, if the relative
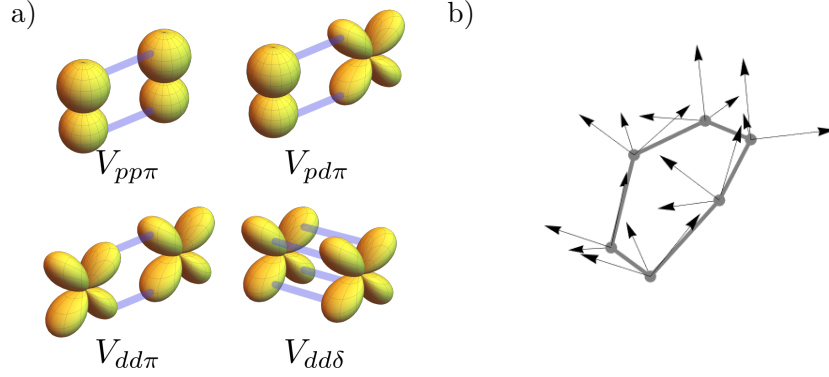
FIGURE 3.2.: a) The interactions among p_z and d-orbitals stated as the material-specific Slater-Koster parameters. b) A hexagon of the graphene lattice in curved space with a tripod of local coordinate axis shown for each site.

distance of neighboring atoms deviates from the lattice constant a. Such a situation would describe strain in graphene, which will not be considered in this work. The interaction parameter $V_{pp\pi}$ directly relates to t in the single-band model Eq. 3.9. Polynomials for the interaction of p_z- and d-orbitals for the case of a flat graphene lattice can be found in the literature [80]. Slater-Koster parameters specific to graphene can be found in [69, 80] and given in Tab. 3.2.

3.2.4. A Multi-orbital Tight-binding model of Graphene

For a multi-orbital tight-binding model, the basis of the Hamiltonian in Eq. 3.5 is extended, such that states with different quantum numbers are included for each site. In that case, hopping among nearest neighbors is possible in a variety of ways, depending on the orbital of the two sites in each case and their relative orientation. Consequently the transition matrix element is written with indices μ and ν for the atomic orbital basis states p_z, d_{xz}, d_{yz}, d_{xy}, $d_{x^2-y^2}$ and d_{z^2} [80]. Due to orthogonality of the basis states, no hopping among different orbitals on the same lattice site is possible. Thus, transitions between these states are not given unless spin-orbit coupling is also considered, which will be discussed in the following sections. In that case real spin degree of freedom will also be required. As discussed above, computing the hopping matrix elements among the d-orbitals, requires the displacement vector from one site to the next. The tight-binding Hamiltonian for the multi-orbital model in reciprocal space is formulated as [80]

$$H_{\mathbf{k}} = \sum_{\mu\nu} E_\mu \delta_{\mu\nu} (\hat{\alpha}_{\mathbf{k}}^{\mu\dagger} \hat{\alpha}_{\mathbf{k}}^{\nu} + \hat{\beta}_{\mathbf{k}}^{\mu\dagger} \hat{\beta}_{\mathbf{k}}^{\nu}) + \sum_{\mu\nu} \sum_{i=1}^{3} e^{-i\boldsymbol{\delta}_i \mathbf{k}} t^{\mu\nu} (\boldsymbol{\delta}_i/a) \hat{\alpha}_{\mathbf{k}}^{\mu\dagger} \hat{\beta}_{\mathbf{k}}^{\nu} + \text{h.c.} \tag{3.14}$$

a)

b)
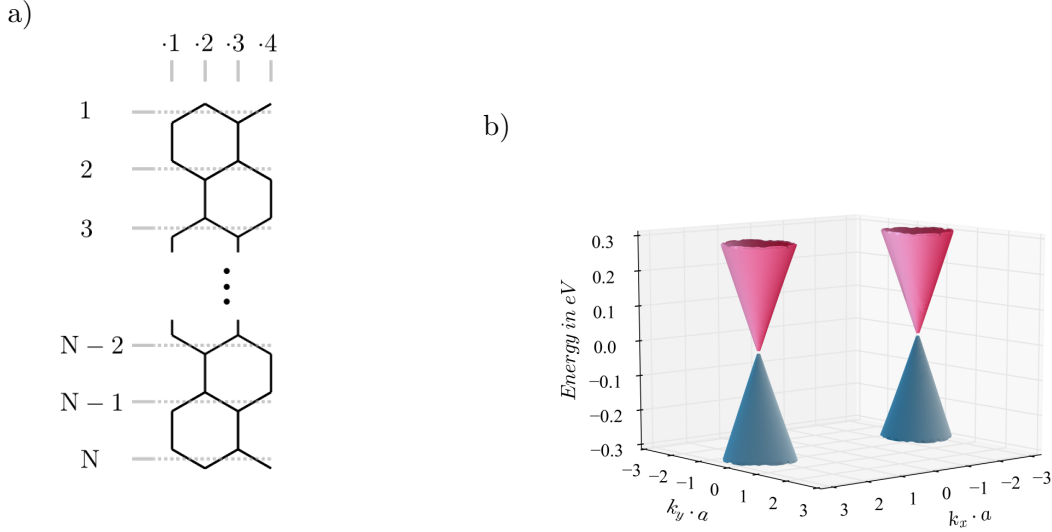
FIGURE 3.3.: a) An example of the numbering of the sites of the tight-binding model. The rows are labeled 1 to N and there are four columns. This results in a rectangular unit cell. b) Low-energy spectrum of the tight-binding model around the two Dirac points. The band gap at the Dirac point is overemphasized.

It is important to note, that $t^{\mu\nu}(\boldsymbol{\delta}_i/a)$ is used for a transition from one site to the neighboring site displaced by $\boldsymbol{\delta}_i$, whereas $t^{\mu\nu}(-\boldsymbol{\delta}_i/a)$ is used for the opposite direction. The lattice constant is denoted a as in the previous case. Additionally the energy of the p_z-orbitals is fixed as $E_p := 0\,\text{eV}$ and the energy of the d-orbitals as $E_d := 12\,\text{eV}$, see Tab. 3.2. This energy is included as on-site contribution in Eq. 3.14 for the d-orbitals of each sublattice separately. The tight-binding model will be used to describe edge states in the following chapters and a larger unit cell comprised of more than two sites will be employed. The geometry used in the model is depicted in Fig. 3.3 a). It consists of N rows of atoms, arranged with two zigzag edges at the top and bottom of the ribbon. The number of columns will be set to 4, but it can be extended if needed. Furthermore, the tight-binding model includes periodic boundary conditions along the x-direction, parallel to the zigzag edge. The Hamiltonian of the nanoribbon with zigzag edges, which is used in this thesis, is given in the appendix, see Eq. B.3. For the description of bulk graphene the periodic boundary conditions can also be closed along y, such that the Hamiltonian in Eq. B.3 leads to Eq. 3.14. The two-dimensional dispersion relation obtained from Eq. 3.14 is shown in Fig. 3.3 b). Here the rectangular shape of the unit cell is reflected in the shape of the Brillouin zone and only two Dirac points are depicted. Per site there are a total of 12 states, one p_z-orbital and the five d-orbital states, each with two spin components. Due to their symmetry, only the d_{xz}- and d_{yz}-states

$V_{pp\pi}$	$V_{pd\pi}$	$V_{dd\pi}$	$V_{dd\delta}$	$V_{pp\sigma}$	$V_{pd\sigma}$	$V_{dd\sigma}$	E_d	E_p
$-3\,\text{eV}$	$-0.69\,\text{eV}$	$-0.3\,\text{eV}$	$2.25\,\text{eV}$	$-8.1\,\text{eV}$	$3.6\,\text{eV}$	$3.3\,\text{eV}$	$12\,\text{eV}$	$0\,\text{eV}$

TABLE 3.2.: The tight-binding parameters for graphene as used in the Slater-Koster approximation.

couple to the p_z-states. The energetic separation of the d-orbitals from the Fermi energy by $12\,\text{eV}$, causes them to be only sparsely populated. Even though the intrinsic spin-orbit coupling, as will be discussed in a later section, couples various d-orbitals with each other, it is advantageous to only consider the d_{xz}- and d_{yz}-states in the calculations. The occupation of the $d_{x^2-y^2}, d_{xy}$- and d_{z^2}-orbitals arising only due to intrinsic spin-orbit coupling can be neglected, because their inclusion does not affect the numerical results of the band structure at the Dirac- or Γ-points on the μeV-scale.

The Density of States

The density of states is an important quantity for determination of the electric properties of solids. For each k-value, the spectrum of the Hamiltonian is computed and the number of energies that are located in a specific energy interval is counted. This binning procedure is using Gaussian bins, that have a small width, such that they approximate δ-distributions [184]. By choosing $\omega_E = 1 \times 10^{-3}t$ and sampling the energy range in steps of $1 \times 10^{-3}t$ the association

$$\delta(E - E_i) \sim \frac{1}{\sqrt{2\pi\omega_E^2}} e^{-\frac{(E-E_i)^2}{2\omega_E^2}} \tag{3.15}$$

is used. The index i covers the states of the Hilbert space and k the different points of the reciprocal space. Due to finite k-space sampling, the discrete nature of the energy bands is depicted as small variations in the density of states. The density of states is defined as

$$\rho(E) = \frac{1}{N_{tot}} \sum_{k,i} \delta(E - E_{k,i}), \tag{3.16}$$

but system sizes with $N \geq 40$ rows have shown to not display the aforementioned variations anymore, see Fig. 3.4, for a non-interacting system with $N = 40$ and d_{xz}- and d_{yz}-orbitals and one-dimensional closed periodic boundary conditions parallel to the zigzag edge. The edge states close to $E = 0$ result in a pronounced peak in the density of states. For the results presented in this thesis, the reciprocal space is sampled by 801 points within $[-\frac{4\pi}{3}, \frac{4\pi}{3})$ for practical reasons, because the number of states becomes very large, especially if d-orbitals are considered.
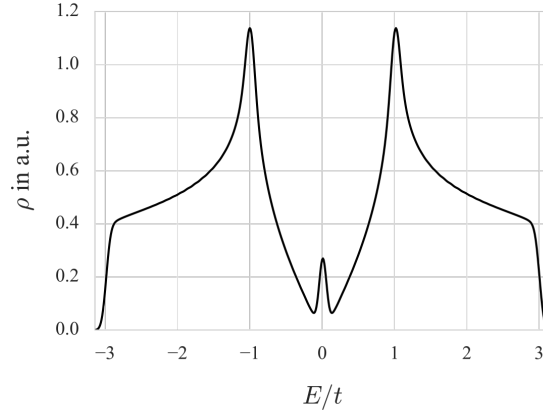
FIGURE 3.4.: The density of states ρ for the energy E in units of t for a system with one-dimensional periodic boundary conditions along the zigzag edge with $N = 40$ and d_{xz}- and d_{yz}-orbitals. A peak around $E/t = 0$ originates from the states localized at the sample edges.

3.3. Intrinsic Spin-orbit Coupling

The derivation of the intrinsic spin-orbit coupling interaction in matrix representation is similar to [80, 82]. From the solution of the angular part of the Schrödinger equation for the hydrogen atom, the spherical harmonics may be obtained, which will be used here. These are given in the Condon-Shortley phase convention [185, 186] as

$$Y_l^m(\theta, \phi) = \sqrt{\frac{(2l+1)(l-m)!}{4\pi(l+m)!}} P_{lm}(\cos\theta) e^{im\phi}, \tag{3.17}$$

where the associated Laguerre Polynomials are defined by [187]

$$P_l^m(x) = \frac{(-1)^m}{2^l l!} \left(1 - x^2\right)^{m/2} \frac{d^{l+m}}{dx^{l+m}} \left(x^2 - 1\right)^l. \tag{3.18}$$

The $Y_l^m(\theta, \phi)$ are eigenfunctions to the $\hat{L}^2$ and $\hat{L}_z$ operators with eigenvalues $\hat{L}_z Y_l^m = \hbar m Y_l^m$ and $\hat{L}^2 Y_l^m = \hbar^2 l(l+1) Y_l^m$, as they have been used in Sec. 3.2.3. In this basis, the spin is included via direct product, e.g. $|p_z, \uparrow\rangle = |p_z\rangle \otimes |\uparrow\rangle$, etc. For an angular momentum operator $\hat{J}$, the matrix elements in the basis $|j, m\rangle$ are derived [188] via

$$\begin{aligned}
\langle j', m' | \hat{J}_x | j, m \rangle &= \langle j', m' | \frac{\hat{J}_+ + \hat{J}_-}{2} | j, m \rangle \\
&= \frac{\hbar}{2} \{ \delta_{jj'} \delta_{m',m+1} \left[(j-m)(j+m+1)\right]^{1/2} \\
&\quad + \delta_{jj'} \delta_{m',m-1} \left[(j+m)(j-m+1)\right]^{1/2} \}
\end{aligned} \tag{3.19}$$

and with

$$\langle j', m' | \hat{J}_y | j, m \rangle = \langle j', m' | \frac{\hat{J}_+ - \hat{J}_-}{2i} | j, m \rangle$$
$$= \frac{\hbar}{2i} \{ \delta_{jj'} \delta_{m',m+1} \left[(j - m)(j + m + 1) \right]^{1/2}$$
$$- \delta_{jj'} \delta_{m',m-1} \left[(j + m)(j - m + 1) \right]^{1/2} \}. \tag{3.20}$$

Using Eqs. 3.19 and 3.20 and the elements of the Hilbert space $|l, m\rangle$ on the space of the $l = 1$ quantum number, the different parts of the operator $\hat{\vec{L}}$ are derived as

$$\hat{L}^+ = \begin{pmatrix} 0 & \sqrt{2} & 0 \\ 0 & 0 & \sqrt{2} \\ 0 & 0 & 0 \end{pmatrix} \qquad \hat{L}^- = \begin{pmatrix} 0 & 0 & 0 \\ \sqrt{2} & 0 & 0 \\ 0 & \sqrt{2} & 0 \end{pmatrix} \qquad \hat{L}_z = \begin{pmatrix} 1 & 0 & 0 \\ 0 & 0 & 0 \\ 0 & 0 & -1 \end{pmatrix} \tag{3.21}$$

and for the spin $\hat{\vec{S}}$, they are the Pauli matrices $\hat{s}_x$, $\hat{s}_y$ and $\hat{s}_z$. Using Eqs. 3.19 and 3.20, the Hamiltonian for the spin-orbit coupling can be written in terms of the ladder operators

$$\hat{\vec{L}} \cdot \hat{\vec{S}} = \left[\frac{\hat{L}^+ \hat{S}^- + \hat{L}^- \hat{S}^+}{2} + \hat{L}_z \hat{S}_z \right]. \tag{3.22}$$

In atoms, the cartesian atomic orbitals p_x, p_y and p_z may be expressed via the complex spherical harmonics [181], which were discussed in Sec. 3.2.3 and stated in Tab. 3.1. They are no eigenfunctions of the angular momentum operator $\hat{L}_z$. If the linear combinations in terms of the spherical harmonics are respected, the representation of the spin-orbit coupling operator in the basis $\{|p_x, \uparrow\rangle, |p_x, \downarrow\rangle, |p_y, \uparrow\rangle, |p_y, \downarrow\rangle, |p_z, \uparrow\rangle, |p_z, \downarrow\rangle\}$ is [80]

$$H_{\text{SOC}}^{\text{P}} = \xi_p \begin{pmatrix} 0 & -i\hat{s}_z & i\hat{s}_y \\ i\hat{s}_z & 0 & -i\hat{s}_x \\ -i\hat{s}_y & i\hat{s}_x & 0 \end{pmatrix} \tag{3.23}$$

and in the same compact notation, in the basis of directed d-orbitals with both spin components and ordered as $\{d_{xy}, d_{x^2-y^2}, d_{xz}, d_{yz}, d_{z^2}\}$, the intrinsic spin-orbit coupling operator becomes

$$H_{\text{SOC}}^{\text{D}} = \xi_d \begin{pmatrix} 0 & 2i\hat{s}_z & -i\hat{s}_x & i\hat{s}_y & 0 \\ -2i\hat{s}_z & 0 & i\hat{s}_y & i\hat{s}_x & 0 \\ i\hat{s}_x & -i\hat{s}_y & 0 & -i\hat{s}_z & i\sqrt{3}\hat{s}_y \\ -i\hat{s}_y & -i\hat{s}_x & i\hat{s}_z & 0 & -i\sqrt{3}\hat{s}_x \\ 0 & 0 & -i\sqrt{3}\hat{s}_y & i\sqrt{3}\hat{s}_x & 0 \end{pmatrix}. \tag{3.24}$$

Here the parameters for the spin-orbit coupling strengths are denoted ξ_p and ξ_d, respectively. Due to the term $\delta_{jj'}$ in Eqs. 3.19 and 3.20, there is no spin-orbit coupling matrix element between $l = 1$ and $l = 2$ states. In order to discuss the splitting of the π-bands at the Dirac cones, the intrinsic spin-orbit coupling Eq. 3.24, is reduced to a low-energy form, on the basis $\{|A\uparrow\rangle, |A\downarrow\rangle, |B\uparrow\rangle, |B\downarrow\rangle\}$ of the p_z-orbitals. In analogy to the Rashba Hamiltonian Eq. 2.27, it leads to the form [26]

$$H_{\mathrm{SOC}} = \xi_d \hat{\tau}_z \hat{s}_z \hat{\sigma}_z. \tag{3.25}$$

This reduced form of the intrinsic spin-orbit coupling Hamiltonian may be used to compute the gap at the Dirac points and a gap of $2\lambda_I = 9\frac{V_{pd\pi}^2}{E_d^2}\xi_d = 26\,\mu\mathrm{eV}$ is obtained for a parameter of $\xi_d = 0.8\,\mathrm{meV}$ [80].

3.4. Rashba-type Spin-orbit Coupling

Rashba-type spin-orbit coupling originates from breaking the mirror symmetry along an axis perpendicular to the graphene plane, which has at least three-fold symmetry [106]. Such a structure-inversion asymmetry leads to a form of spin-momentum-locking [142, 145, 189, 190], resulting ultimately in a spin-orbit coupling term of the form Eq. 2.27. This spin-orbit coupling causes a so-called *trigonal warping*, an effect that splits each Dirac cone at the K and K' point into 4 distinct cones. Before this particular effect of the Rashba-type spin-orbit coupling is discussed in the following sections, an effective term in the low-energy representation is stated. In the basis of directed orbitals in spherical coordinates the Stark effect, due to an electric field perpendicular to the flat graphene plane, introduces matrix elements among states located at identical lattice sites, such that integrals of the type

$$\langle \varphi_i | \hat{z} | \varphi_j \rangle = \int \varphi_i^*(\mathbf{r}) \, r \, \cos\theta \, \varphi_j(\mathbf{r}) \mathrm{d}^3 r \tag{3.26}$$

have to be solved, where e.g. $i = p_z$ and $j = s$ denote the different quantum numbers of the hydrogen orbitals φ_i and φ_j. The interaction couples either on-site s- and p_z-orbitals, p_y- and d_{yz}-orbitals, p_x- and d_{xz}-orbitals or d_{z^2}- and p_z-orbitals, due to the symmetry of the atomic wave functions. In this case the dominant contribution to the π-bands is due to the on-site coupling of s- and p_z-orbitals [145], while the influence of the d-orbital coupling via the Stark effect is small in comparison and can be neglected [80]. The finite overlap of the p_z-orbitals with the sp^2-orbitals at each lattice site can lead to a transition from the π-bands to the sp^2-hybridized bands, followed by a hopping to the sp^2-orbitals at a neighboring site. There, the intrinsic spin-orbit coupling in the p-orbitals allows an electron to return to the π-bands with a spin flip [82]. This is depicted in Fig. 3.5. Such an interaction may be cast into an effective term, describing hopping among p_z-orbitals, together with a spin-flip. It can be derived via Löwdin partitioning, where the influence of the hopping in the sp^2-orbitals and the intrinsic spin-orbit coupling may be expressed effectively via a a term in the subspace of sublattice and real spin states of only the p_z-orbitals. The resulting real-space representation of the effective Rashba-type spin-orbit coupling among the p_z-orbitals is given as [26, 150]

$$\hat{H}_R = i\lambda_R \sum_{\langle ij \rangle} \hat{c}_i^\dagger (\hat{\mathbf{s}} \times \mathbf{d}_{ij})_z \hat{c}_j. \tag{3.27}$$

In this notation the operators $\hat{c}_i$ represent either $\hat{a}_i$ or $\hat{b}_i$ similar to Eq. 3.5, depending on the sublattice at the sites i or j. The vector $\boldsymbol{d}_{ij}$ is the vector pointing from site i to site j and $\hat{\boldsymbol{s}}$ is the vector containing the Pauli spin matrices. λ_R is the parameter denoting Rashba-type spin-orbit coupling strength. A full expression is discussed by Rakyta et al. [191]. It may first be Fourier decomposed and then expanded around the Dirac points. This leads to an interaction matrix in the basis $\{\psi_{A\uparrow}, \psi_{B\uparrow}, \psi_{A\downarrow}, \psi_{B\downarrow}\}$ at the K-point, where the p_z-orbitals
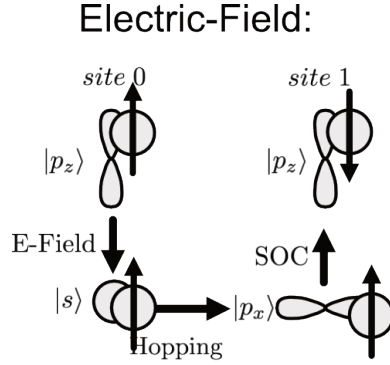
Electric-Field:

FIGURE 3.5.: A schematic overview of the effective term of the Rashba-type spin-orbit coupling originating from an electric field. The z-component of the real spin is indicated by an arrow at each orbital.

located at sublattices A or B with their respective spin indicated, are of the form

$$\hat{H}_R^K = \begin{pmatrix} 0 & 0 & 0 & -\frac{3\lambda_R a}{2}\left(k_x + ik_y\right) \\ 0 & 0 & 3i\lambda_R & 0 \\ 0 & -3i\lambda_R & 0 & 0 \\ -\frac{3\lambda_R a}{2}\left(k_x - ik_y\right) & 0 & 0 & 0 \end{pmatrix}. \tag{3.28}$$

Only taking the zeroth-order of Eq. 3.28 into account leads to the effective term in Eq. 2.27 [41, 82, 150].

3.4.1. The Trigonal Warping of Rashba-type Spin-orbit Coupling

The spinless single-orbital model for the honeycomb lattice exhibits two non-equivalent Dirac cones in the reciprocal space. Since the two Dirac cones are related by time-reversal symmetry, they exhibit opposite winding numbers, as a consequence of their different chirality [192], which affects the alignment of momentum and sublattice spin in their vicinity. In this section the effect of the trigonal warping due to the Rashba-type spin-orbit coupling will be discussed in context of their winding numbers, in which this alignment is encoded. Together with the Hamiltonian for pristine graphene at the K-point, the Hamiltonian in Eq. 3.28 results in a trigonal warping of the Dirac cones, and Rashba-type spin-orbit coupling splits each cone into four distinct ones. An example is depicted in Fig. 3.6, where the two bands (upper valence and lower conduction band) around the Fermi level are shown for the K and K' point. At the original location of each Dirac cone, a point remains, where the bands touch. The other three additional cones extend in an angle of $\frac{2\pi}{3}$ around it. For the description of the splitting of a single Dirac point, the origin is fixed at the position of the original Dirac
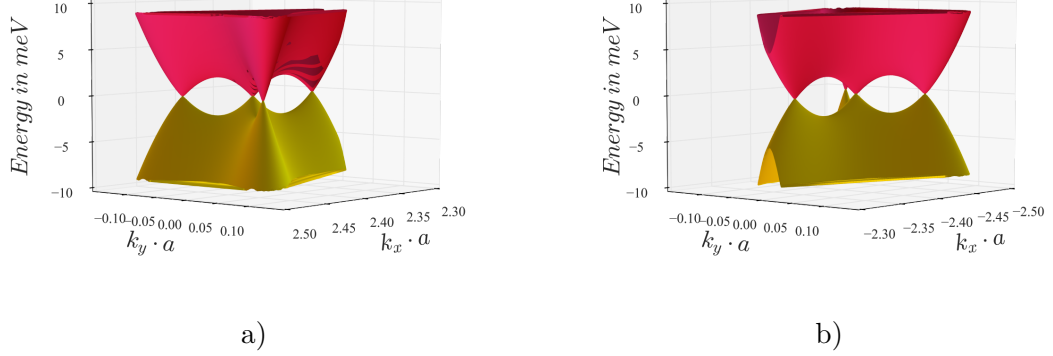
FIGURE 3.6.: The trigonal splitting at *a)* the K point and *b)* at the K' point. Here $\lambda_R = 0.067\,\text{eV}$, as in Eq. 3.28.

cones $\pm\frac{4\pi}{3\sqrt{3}a}$. The three minima of the energy bands appear located at a distance $3v_\lambda\lambda_R/v_F^2$ from the central cone, where $v_\lambda = \frac{3\lambda_R a}{2\hbar} \ll \lambda_R$ and $v_F = 3ta/(2\hbar)$ as occurring in Eq. 3.28. There are two parabolic bands located further away from the Fermi edge which are not shown in Fig. 3.6. They are the upper conduction and lower valence band. The eigenstates of the Hamiltonian are obtained at points in k-space forming a circular path around each Dirac cone and the sublattice spin expectation value is computed with them. The components of the vector $(\langle\hat{\sigma}_x\rangle, \langle\hat{\sigma}_y\rangle)$ are then used to discuss the alignment of the sublattice spin for these states. In Fig. 3.7 the sublattice spin expectation values around all of the four Dirac cones at both K and K' points are depicted. One can see that at the K-point (a and b) the winding number is 1, while at the K'-point it is -1.

The Winding Numbers of the Trigonal Splitting

For the winding numbers, integration paths in reciprocal space with a very small radius around the Dirac points are used. The components of the sublattice spin expectation values are computed using, $\vec{k}(t) = k\left(\cos t, \sin t\right)$, as

$$\langle\hat{\vec{\sigma}}(t)\rangle = \left(\langle\hat{\sigma}_x(t)\rangle, \langle\hat{\sigma}_y(t)\rangle, \langle\hat{\sigma}_z(t)\rangle\right), \tag{3.29}$$

where each of the $\langle\hat{\sigma}_i(t)\rangle$ is to be understood as the expectation value of the corresponding sublattice spin operator at the momentum $k(t)$. With this vector, after it is normalized for numerical stability, the winding number ν is obtained via [34]

$$\nu = \frac{1}{2\pi}\int_{-\pi}^{\pi}\langle\hat{\vec{\sigma}}(t)\rangle \times \left(\frac{\mathrm{d}}{\mathrm{d}t}\langle\hat{\vec{\sigma}}(t)\rangle\right)\mathrm{d}t, \tag{3.30}$$
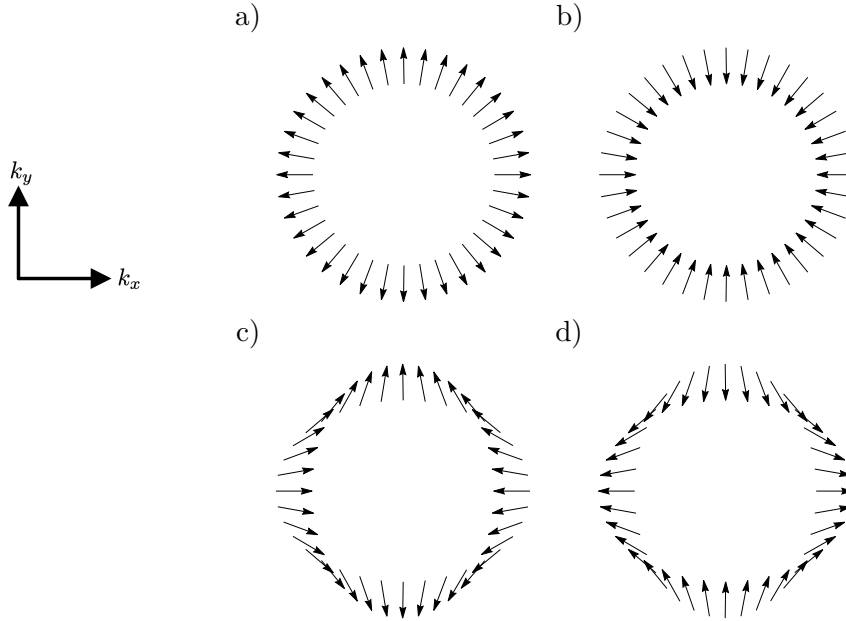
FIGURE 3.7.: The sublattice spin expectation value for graphene taken on a path around all four Rashba-split Dirac cones. At the K-point: a) lower conduction band and b) valence band, at the K'-point: c) conduction band and d) valence band. Each arrow has the components $\langle \hat{\sigma}_x \rangle$ and $\langle \hat{\sigma}_y \rangle$ is depicted at the point in k-space for which it is computed. The winding numbers are $1, 1, -1, -1$ for a,b,c,d.

for each of the four eigenstates of the Hamiltonian individually. This results in the winding numbers presented in Tab. 3.3. As can be seen, the winding numbers of the four individual Rashba-split Dirac cones add up (in row Σ) to what is obtained when the circle encloses all four cones at once, given in Fig. 3.7. The expression for the winding number, Eq. 3.30, can be viewed as the number of times that the sublattice spin expectation values rotate, while the momentum - at which it is computed - revolves around a Dirac point. Along each of the four circular paths in k-space the sublattice spin changes its orientation, resulting in a winding number of ± 1 [75, 159]. The upper conduction band does only have a non-trivial winding number at the location of the central cone. This central cone of the lower conduction and that of the upper valence band exhibits a winding number of ± 2 and the three outer Dirac cones ∓ 1, see Fig. 3.8. For the lower valence, at the locations of the three off-center cones, there is no cone and thus a non-trivial winding number is only found at the location of the central Dirac point. The analytical computation of the winding numbers is discussed in the next section.

(q_x, q_y)	$V_{\text{low}}^{K'}$	$V_{\text{up}}^{K'}$	$C_{\text{low}}^{K'}$	$C_{\text{up}}^{K'}$	V_{low}^{K}	V_{up}^{K}	C_{low}^{K}	C_{up}^{K}
$(\pm \cos \frac{4\pi}{3}, \pm \sin \frac{4\pi}{3})$	0	-1	-1	0	0	1	1	0
$(\pm \cos \frac{2\pi}{3}, \pm \sin \frac{2\pi}{3})$	0	-1	-1	0	0	1	1	0
$(0,0)$	-1	2	2	-1	1	-2	-2	1
$(\pm 1, 0)$	0	-1	-1	0	0	1	1	0
Σ	-1	-1	-1	-1	1	1	1	1

TABLE 3.3.: Winding numbers of the respective Dirac cone around the trigonally split Dirac cones, due to Rashba spin-orbit coupling in a radius of $3v_\lambda \lambda_R$ around the K (K') point for the up(per) and low(er) valence (V) and conduction band (C). All coordinates are given relative to the respective Dirac cone, ($-$ for K' and $+$ for K) and $(0,0)$ marks the central cone. The sum of all cones is denoted Σ.

An Analytical Model for Computation of the Sublattice Spin Expectation Values

The following analytical results have been obtained in the Bachelor thesis of Kazankin-Berg [193], which was planned and supervised by the author, where more details can be found. Expectation values for the sublattice spin expectation values of the upper valence and lower conduction bands at the K and K' points are shown in Fig. 3.8. The 4×4-dimensional Hamiltonian in Eq. 3.28 can be used to compute the expectation value of $\langle \hat{\sigma}_x \rangle$ and $\langle \hat{\sigma}_y \rangle$ for the lower conduction band of the central cone at the K-point analytically. In order to achieve this, the eigenstates of the system are analytically solved and their expectation values for the sublattice spins computed. This results in long functional relations with polynomials in k_x, k_y, v_λ and λ_R. These can then be approximated in a Taylor-series in lowest order of interaction parameters v_λ and λ_R. Using $k_x + ik_y = |k| \cdot e^{i\phi}$, one obtains $\langle \hat{\sigma}_x \rangle \sim k \cdot \sin 2\phi$ and $\langle \hat{\sigma}_y \rangle \sim k \cdot \cos 2\phi$. This method does not work for the three outer cones, because the resulting expressions exhibit many singularities in the interaction parameters of the Rashba Hamiltonian. Therefore an analytical 2×2-dimensional model is developed, which allows the calculation for the sublattice spin expectation values around the off-center cones. The result for the central cone above is reproduced by this reduced model[1].

As a first step, Löwdin perturbation theory is used and the basis $\{\psi_{A\uparrow}, \psi_{B\uparrow}, \psi_{A\downarrow}, \psi_{B\downarrow}\}$ is reduced to only two relevant states. The Rashba spin-orbit coupling in Eq. 3.28 introduces a coupling of one spin component on one sublattice with the opposite spin-component of the opposite sublattice. The magnitudes of the two matrix elements for these interactions differ, as $\frac{3\lambda_R a}{2\hbar} \ll \lambda_R$, and thus the Hamiltonian can be separated into two weakly coupled sections. The graphene Hamiltonian for the K-point is now considered as the coupling between the two pairs of states $\{\psi_{A\uparrow}, \psi_{B\downarrow}\}$ and $\{\psi_{B\uparrow}, \psi_{A\downarrow}\}$. After reordering, the Hamiltonian can be

---

[1]The discussion is limited to the K-point, because the procedure is similar for the K'-point.

written as

$$\begin{pmatrix} H_{aa} & H_{ab} \\ H_{ba} & H_{bb} \end{pmatrix} \begin{pmatrix} g_a \\ g_b \end{pmatrix} = E \begin{pmatrix} g_a \\ g_b \end{pmatrix}. \tag{3.31}$$

Here one part of the Hilbert space is given by $g_a = \{g_{a\uparrow}, g_{a\downarrow}\} = \{\psi_{A\uparrow}, \psi_{B\downarrow}\}$ and the other part for b analogously. Then for the g_b component, with the identity element on the b-space $\mathbf{1}_b$, the expression

$$g_b = (E \cdot \mathbf{1}_b - H_{bb})^{-1} \cdot H_{ba} \cdot g_a \tag{3.32}$$

is obtained, which is used in the corresponding equation for g_a. This leads to an effective Hamiltonian only on the subspace for g_a, where the energy E is approximated to be negligibly small. The resulting Hamiltonian according to the Löwdin downfolding method is obtained via $H_{\text{eff}} = H_{aa} - H_{ab} \cdot H_{bb}^{-1} \cdot H_{ba}$ and given as

$$H_{\text{eff}}^K = \begin{pmatrix} 0 & -\hbar v_\lambda k - i\frac{\hbar^2 v_F^2 k^{*2}}{3\lambda_R} \\ -\hbar v_\lambda k^* + i\frac{\hbar^2 v_F^2 k^2}{3\lambda_R} & 0 \end{pmatrix} \tag{3.33}$$

in the basis $\{\psi_{A\uparrow}, \psi_{B\downarrow}\}$. A similar result has been obtained for the approximation of twisted bilayer graphene [192].

From Eq. 3.31, the expectation values for the 4×4-model of the sublattice spin are computed via $\langle \hat{\sigma}_i \rangle = (g_a^*, g_b^*)\hat{\sigma}_i(g_a, g_b)^T$ and can be expressed as

$$\langle \hat{\sigma}_x \rangle = 2 \cdot \text{Re}\left(g_{a\uparrow}g_{b\uparrow}^*\right) + 2 \cdot \text{Re}\left(g_{a\downarrow}g_{b\downarrow}^*\right) \tag{3.34}$$

$$\langle \hat{\sigma}_y \rangle = -2 \cdot \text{Im}\left(g_{a\uparrow}g_{b\uparrow}^*\right) + 2 \cdot \text{Im}\left(g_{a\downarrow}g_{b\downarrow}^*\right). \tag{3.35}$$

In order to obtain an analytical expression for the expectation values Eqs. 3.34 and 3.35, the operator in the expression for g_b, Eq. 3.32, is Taylor-expanded in lowest order in $\vec{q}$ around any of the four Rashba-split Dirac cones by replacing $\vec{k}$ from the complex expression with

$$\vec{q} + \vec{K^j} \to (q_x + K_x^j) + i \cdot (q_y + K_y^j) \approx |K^j|e^{i\delta_j} \tag{3.36}$$

for the momentum $\vec{q}$ around the j-th non-central Rashba-split cone K^j. The coordinates of these three cones are defined relative to the central Dirac point and therefore the phase $\delta_j = \arctan K_x^j/K_y^j$ is specific to each of the cones. For the central cone, the resulting expression is in lowest order $\sim |q|$, because there $\vec{q} \to |q|e^{i\phi}$, while a constant term is derived for the non-central cones in lowest order, independent of $|q|$, because $|q| \ll |K^j|$.

By using these expressions, the sublattice spin expectation values in Eqs. 3.34 and 3.35 are simplified. Because the terms $|K^j|e^{i\delta_j}$ for the off-center cones do not depend on $|q|$, $g_{a\uparrow}g_{b\downarrow}^*$ can be expressed in terms of only the g_a or only the g_b coefficients.
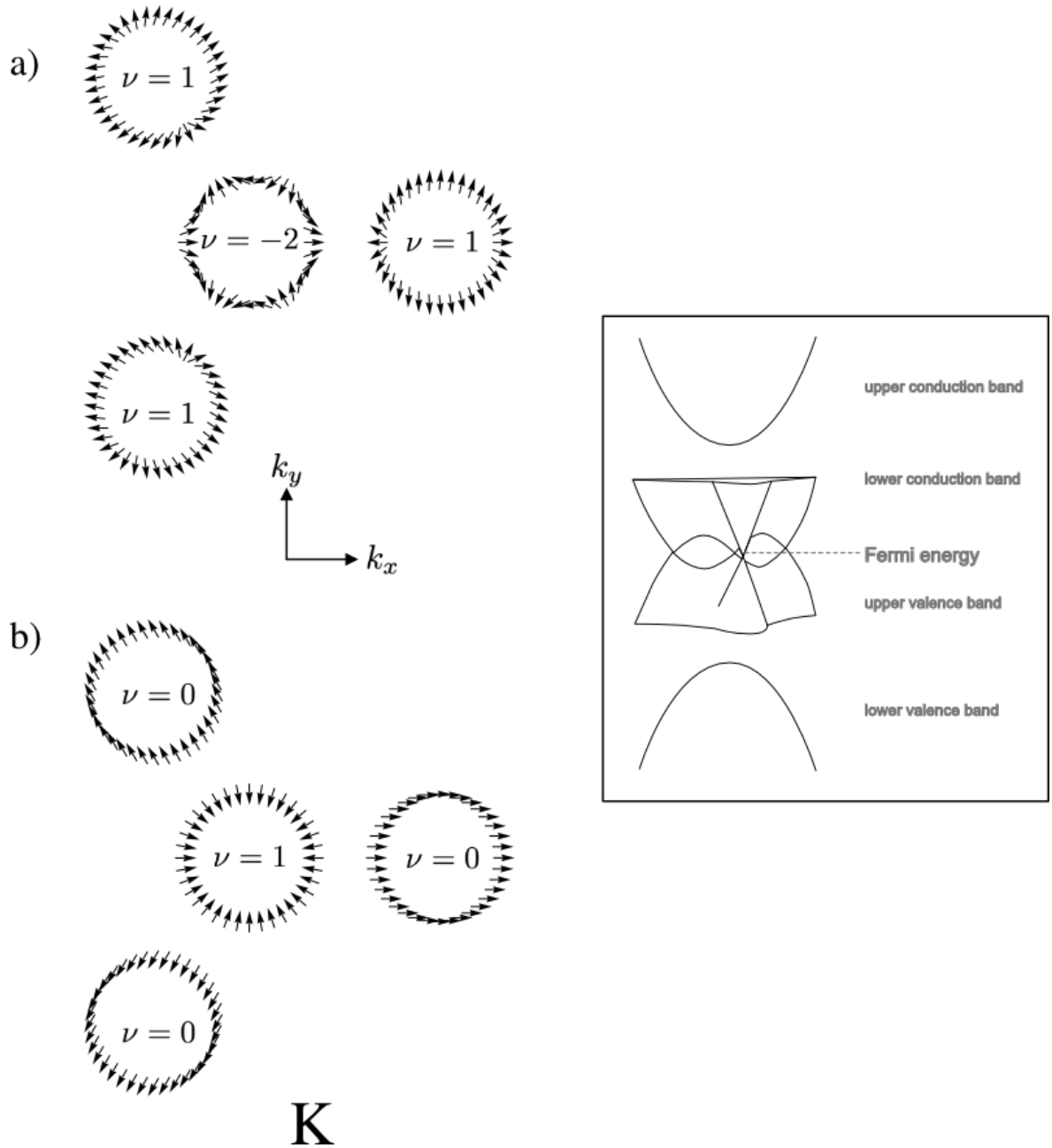
FIGURE 3.8.: Four examples of the sublattice spin expectation values around at the location in k-space of the four Dirac cones. Each arrow shows the sublattice spin direction with the components $\langle \sigma_x \rangle$ and $\langle \sigma_y \rangle$ at the respective point in k-space. For each cone, the winding numbers ν are indicated. The inset shows the location of the bands around the Fermi energy. left: a) Expectation values for the lower conduction band at the K-point. b) Lower valence band at the K-point, which is more remote from the Fermi edge than the upper valence band. right: c) Lower conduction band and d) lower valence band at the K'-point.

c)

$\nu = -1$

$\nu = -1$

$\nu = 2$

$\nu = -1$

d)

$\nu = 0$

$\nu = 0$

$\nu = -1$

$\nu = 0$
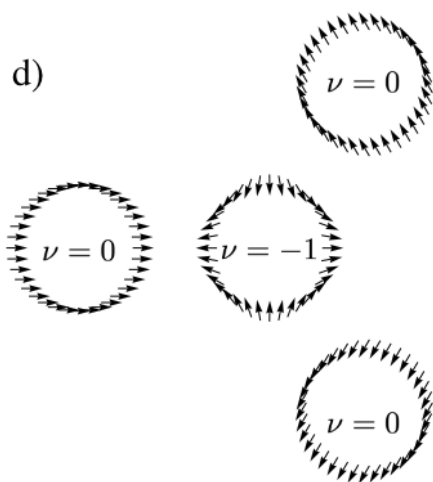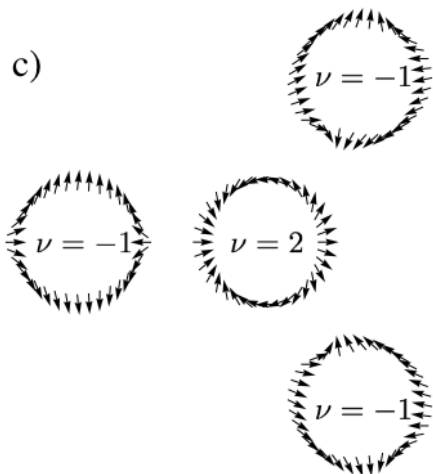
K′

This effectively decouples both pairs of states. As a consequence, the expectation values of the sublattice spin in $\langle \hat{\sigma}_{x/y,\text{eff}} \rangle$ for the j-th off-center cones are computable via the effective 2×2-Hamiltonian in Eq. 3.33 by

$$\langle \hat{\sigma}_{x,\text{eff}} \rangle = 2\text{Re}(g_{a\uparrow} g_{a\downarrow}^*) \tag{3.37}$$

$$\langle \hat{\sigma}_{y,\text{eff}} \rangle = -2\text{Im}(g_{a\uparrow} g_{a\downarrow}^*). \tag{3.38}$$

This leads to the expectation values of the 4×4-Hamiltonian via

$$\langle \hat{\sigma}_x \rangle = -2\frac{v_\lambda}{v_F} \cdot [\langle \hat{\sigma}_{x,\text{eff}}^j \rangle \cdot \sin \delta_j - \langle \hat{\sigma}_{y,\text{eff}}^j \rangle \cos \delta_j] \tag{3.39}$$

$$\langle \hat{\sigma}_y \rangle = -2\frac{v_\lambda}{v_F} \cdot [\langle \hat{\sigma}_{x,\text{eff}}^j \rangle \cdot \cos \delta_j + \langle \hat{\sigma}_{y,\text{eff}}^j \rangle \sin \delta_j], \tag{3.40}$$

with constant $v_\lambda = \frac{3\lambda_R a}{2\hbar} \ll \lambda_R$ for the off-center cones. The expressions for the $\langle \hat{\sigma}_{x/y,\text{eff}} \rangle$ are derived as e.g. $\langle \hat{\sigma}_{x,\text{eff}} \rangle \sim \frac{6\cos\phi}{\sqrt{5+4\cos 2\phi}}$, which resembles a cosine-like functional relation, that closely matches the numerical results in Fig. 3.8. The terms $\sim \sin \delta_j$ in Eqs. 3.39 and 3.40 are important, because they correspond to the correct relative phase of the x- and y-components of the sublattice spin expectation values. As can be seen in Fig. 3.8, the sublattice expectation values around all three outer Dirac cones for each of the bands are almost identical, apart from a rotation. This rotation is encoded in the δ_j.

In the case of the central cone, the lowest order expansion of Eq. 3.33 is linear in $\vec{q}$, such that the simplified expressions for the expectation values become

$$\langle \hat{\sigma}_x \rangle = -4\frac{\hbar v_F}{3\lambda_R}|q| \cdot [\langle \hat{\sigma}_{x,\text{eff}}^{\text{center}} \rangle \cdot \sin \phi - \langle \hat{\sigma}_{y,\text{eff}}^{\text{center}} \rangle \cos \phi] \tag{3.41}$$

$$\langle \hat{\sigma}_y \rangle = -4\frac{\hbar v_F}{3\lambda_R}|q| \cdot [\langle \hat{\sigma}_{x,\text{eff}}^{\text{center}} \rangle \cdot \cos \phi + \langle \hat{\sigma}_{y,\text{eff}}^{\text{center}} \rangle \sin \phi]. \tag{3.42}$$

In this case, the phase $\phi = \arctan q_x/q_y$ is introduced, which depends on the coordinates of the momentum $\vec{q}$. This way, the sublattice expectation values for the central cone at the K-Dirac point are verified to be $\langle \hat{\sigma}_x \rangle \sim |q| \cdot \sin 2\phi$ and $\langle \hat{\sigma}_y \rangle \sim |q| \cdot \cos 2\phi$, confirming the result obtained from the 4×4-model.

A full list of the expressions for $\langle \hat{\sigma}_{x,\text{eff}}^{\text{center}} \rangle$, $\langle \hat{\sigma}_{y,\text{eff}}^{\text{center}} \rangle$, $\langle \hat{\sigma}_{x,\text{eff}}^{j} \rangle$ and $\langle \hat{\sigma}_{y,\text{eff}}^{j} \rangle$ can be found in [193].

3.5. Magnetic Field and Staggered Sublattice Potential

A central feature of the effect of strong magnetic fields on an electron is the splitting of the electronic energies into Landau levels [71, 194]. In a two-dimensional solid, subject to a perpendicular magnetic field, the electrons move around the plane in cyclotron orbits. The area enclosed by these orbits is proportional to the magnetic flux and the energy and degeneracy of these orbits depend on the strength of the field as well. A central concept by Aharanov and Bohm in 1959 [195] was that electrons in magnetic fields are not affected by the magnetic field directly, but rather by the underlying vector potential. This is encoded in the electronic motion as so-called Peierls phase in two dimensions.

3.5.1. The Peierls Substitution

The Peierls substitution [196, 197] is a geometrical phase that an electron picks up, when it moves in an external magnetic field $\vec{B} = \vec{\nabla} \times \vec{A}$, described by the vector potential $\vec{A}$. The tight-binding description of the electronic band structure takes into account the structure of the vector potential, which modifies the canonical momentum of the charged particle and thus the hopping amplitude is not real anymore, but acquires a spatially-varying phase [198]. In the Landau gauge, the vector potential for a constant magnetic field in z-direction $\vec{B} = (0, 0, B)$ is $\vec{A} = (-By, 0, 0)$ [199]. This relates the canonical momentum $\vec{p}$ to the mechanical momentum $\vec{\Pi} = \vec{p} - e\vec{A}$ [148], where the individual components do not commute anymore, due to the vector potential [194]

$$[\Pi_x, \Pi_y] = ie\hbar B_z. \tag{3.43}$$

This results in the *Peierls phase*, which associates these commutation relations with the hopping terms of the tight-binding model. As a consequence, electronic motion along a closed circuit acquires a phase directly proportional to the number of enclosed magnetic flux quanta. In the honeycomb lattice, the smallest closed circuit a particle can take is around one hexagon of the lattice and the smallest number of flux quanta possibly enclosed is $\phi_0 = \frac{h}{e}$, a singular magnetic flux quantum. This is illustrated in Fig. 3.9 a). The phase acquired for each hopping is $\Phi_{i,i+1}$. The phase Φ_{tot} around one hexagon is equal to

$$\Phi_{\text{tot}} = \sum_{i=1}^{6} \Phi_{i,i+1} = -\frac{e}{\hbar} \int_{\text{hex}} \vec{A} \cdot d\vec{r} = \frac{2\pi}{\phi_0} B \cdot F_{\text{hex}}, \tag{3.44}$$

where $F_{\text{hex}} = \frac{a^2 3\sqrt{3}}{2}$ is the surface of the hexagon, a is the lattice constant - one edge length of the hexagon - and $B \cdot F_{\text{hex}}$ is the flux. By parametrization of one hopping along one of the vectors $\boldsymbol{\delta}_i$, connecting neighboring lattices sites, the integral leading to the phase can be formulated as $\Phi_{i,j} = -\frac{e}{\hbar} \int_{\vec{r}_i}^{\vec{r}_j} \vec{A} d\vec{r} = -\frac{e}{\hbar} \int_0^1 \vec{A}(\vec{r}(t)) \dot{\vec{r}}(t) dt$, where $\vec{r}(t) = \vec{r}_i + (\vec{r}_j - \vec{r}_i)t + \vec{r}_i$ and
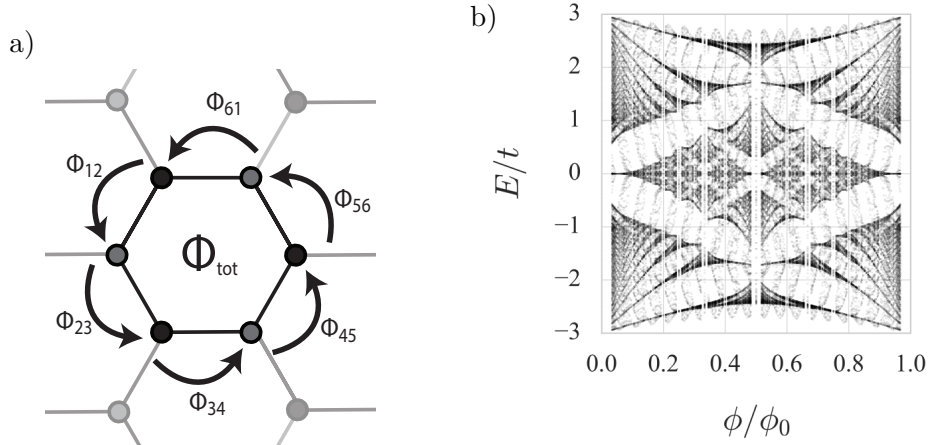
FIGURE 3.9.: a) The total phase and individual phases acquired for the hopping along a close path around one primitive cell of graphene. b) Hofstadter butterfly for the honeycomb lattice as computed from the tight binding model for graphene discussed in this thesis. The lattice is finite with 40×40 sites and contains only p_z-orbitals. All data points within the *wings* of the butterfly are due to finite size effects.

$\dot{\vec{r}}(t) = \vec{r}_j - \vec{r}_i$, connecting two sites i and j located at $\vec{r}_i$ and $\vec{r}_j$, respectively. The result is

$$\Phi_{i,j} = \frac{2\pi}{\phi_0} B (r_i^y + \frac{1}{2}(r_j^y - r_i^y)) \cdot (r_j^x - r_i^x), \tag{3.45}$$

where the x- or y-components of the three displacement vectors $\boldsymbol{\delta}_1$, $\boldsymbol{\delta}_2$ and $\boldsymbol{\delta}_3$ replace $\vec{r}_j - \vec{r}_i$, as indicated in Fig. 3.9 a). There the hopping amplitudes from atom i to atom j acquire the factor $e^{i\Phi_{ij}}$. Apart from one absolute position of the i-th atom, denoted r_i^y, the phase only depends on the relative displacement of the two neighbors. It is also only finite, if the x-components of these displacements differ. The total flux is then proportional to the area of the hexagon F_{hex} [187]. One can show, that the Peierls phase in graphene leads to the Harper equation for the honeycomb lattice [200–202], which describes a fractal structure known as the Hofstadter butterfly [203]. This fractalization of the band structure is determined by the number of flux quanta passing through the unit cell of the graphene sample [204]. If the number of flux quanta is related to the number of primitive unit cells by a rational number, a magnetic unit cell does not fall together with a primitive cell across the lattice anymore. Therefore the boundaries of the magnetic unit cells are not those of the Brillouin zone any longer, such that band gaps open. The shape of the band structure is specific to the lattice geometry and the way of splitting depends on the ratio of the magnetic flux through the magnetic unit cell and the flux through a primitive unit cell. The resulting shape is the Hofstadter butterfly, as depicted in Fig. 3.9 b) for the hexagonal lattice. Here 40×40 atoms forming a finite size honeycomb lattice are subjected to a magnetic field with varying fluxes, where the ratio of both the flux quanta in the whole lattice and the number of magnetic unit

cells is a rational number. The figure is computed from the tight binding model described in this chapter, but without the inclusion of *d*-orbitals or spin-orbit coupling. Without any closed periodic boundary conditions, the sample has a finite number of lattice sites and four edges. This limits the number of possible fractions in which way the magnetic unit cells can form within the honeycomb lattice. Therefore at some energies the splittings deviate slightly from those for the Hofstadter butterfly for the infinite lattice, as can be seen in the wings of the butterfly in Fig. 3.9 b), where the butterfly for the periodic system does not exhibit any energy levels.

3.5.2. The Zeeman Term

A magnetic field is not only changing the momentum of an electron, as discussed in the last section, but the magnetic moment of its motion couples to the magnetic field vector, such that its energy changes as well. The magnetic interaction energy of a charged particle in a magnetic field is [205]

$$H_{\text{mag}} = -g\mu_B \hat{\vec{J}}\vec{B},\tag{3.46}$$

with the total angular momentum $\hat{\vec{J}}$ and the magnetic field $\vec{B}$. Here g is the Landè factor and μ_B the Bohr magneton. For orbital- and spin-magnetic moments g is either 1 or 2 respectively. In the basis of sites, orbitals and projections on the quantization axis along the z-direction - as discussed in this chapter - the matrix elements of H_{mag} for orbital o at site i can be written as [97, 206]

$$\langle -\vec{\mu}_s \cdot \vec{B}\rangle_{o,i} = m_s g_s \mu_B B,\tag{3.47}$$

the the Landè-factor $g_s = 2$ for the spin and $m_s = \pm 1/2$ for either of the two spin components. This essentially shifts the spin up components up in energy by $1/2\mu_B B$ and the spin down components by $-1/2\mu_B B$. Since the *d*-orbitals are only sparsely populated, only the $m_l^d = 0$ and $m_l^p = 0$ components of the angular momentum multiplet for both *p*- and *d*-orbitals are considered and interactions thereof.

3.5.3. The Staggered Sublattice Potential

The staggered sublattice potential is another effect that mediates energy shifts on specific states in the tight-binding model by acting on the different spin species [207]. Graphene and similar compounds with bipartite lattices, such as transition-metal dichalcogenides, exhibit an SU(2) quantum number, which relates to the relative occupations of the sublattices and leads to the sublattice spin. The interaction H_{stag} of the staggered sublattice potential can be understood as a Zeeman effect acting on the sublattice spin and thus on the different constituents of the two-atomic basis. Let $\vec{\sigma}$ be the sublattice spin, then the matrix elements

are independent of orbital or real spin and only depend on the type of basis atom and thus its sublattice spin

$$H_{\text{stag}} = \delta \hat{\sigma}_z, \tag{3.48}$$

where δ is the interaction strength. Such a situation can arise, if e.g. a planar material with two-atomic basis is brought in contact with a substrate with two-atomic basis of different lattice constant. An example for this is graphene on *hexagonal Boron nitride* [208]. There the lattice mismatch causes each of the two basis atoms to be subject to a different potential, resulting in a gauge field. This can be described as an energy shift proportional to the sublattice spins of the atoms. In the context of topological insulators, a system may be rendered topologically trivial by the application of such potential [26, 41].

4. Graphene as a Topological Insulator

4.1. Introduction

The conducting edge or surface states, which are central to the peculiar properties of topological insulators, are a direct result of the transition at the contact surface of two materials with different topological orders [209]. At a boundary for example, which connects areas with different topological states, electrons can propagate reflectionless in the direction parallel to the interface, because of the broken time-reversal symmetry of the system [210].

Apart from the quantum Hall effect, where this novel state of matter was first discovered, a number of related effects of similar nature were soon found [33, 41, 44, 211–213]. In general, states of matter capable of exhibiting such effects are collectively classified as *topological insulators* [23, 42].

The classification of such systems makes use of the conservation of various symmetries and hence Hamiltonians are commonly described by their invariance under specific transformations. It ultimately led to the *10-fold way*, which has its roots in random-matrix theory [214–216]. It describes which symmetries in which spatial dimensions result in what kind of topological insulator - if it is possible to exist at all.

Experimental evidence for this novel state of matter has been rich and it could be observed in different materials, such as HgTe and CdTe semiconductor quantum wells [42, 211]. In graphene, the chirality of the edge states could be verified [217] as a first step to prove its topological characteristics. For bilayer bismuth the truly one-dimensional character of the edge states has been observed and their topological properties verified, such as coherent propagation without backscattering [218]. If edge states are helical, their momentum is tied with their spin [79, 213] and the edge states feature pairs of counter-propagating states. In case of the Chern insulator, each edge is chiral, the edge states on each edge propagate in only one direction and because time-reversal symmetry is broken, they do not have a counter propagating partner at the same edge [79]. In graphene, the sublattice structure is responsible for the fact that electrons and holes have opposing chiralities. This peculiar sublattice structure is originating from the existence of two Dirac cones in the graphene reciprocal lattice [219–222].

In the following, the Kane-Mele model of a topological insulator is introduced by highlighting the bulk-boundary correspondence, which leads to the edge states. After that the behavior of these edge states is analyzed by numerical computation using the tight-binding model presented in the previous chapter.

4.2. Bulk-boundary correspondence in Graphene

The bulk-boundary correspondence is a theorem that states that the bulk characteristics and the edge characteristics should both reflect the topological character of the system equally well and in agreement.

When two bulk materials meet at an interface, one with trivial and the other with non-trivial Chern number, the energy gap must close at the contact point. This is significant, because a material with non-trivial Chern number cannot pass to a trivial insulator without also changing its bulk topological invariant. It also causes the existence of zero energy states exactly at the fringe, where tightly localized states can exist, in order to facilitate the transition between the two topologically different materials [23]. The chirality of the interface states can be seen if the solution of a real space Hamiltonian at such an interface is analyzed, which shows the localization of the states and their linear group velocity, such that the gap between the conduction and valence band is bridged [209]. This relation is called *bulk-boundary correspondence* and the pure existence of gapless edge states is enough to qualify for the aforementioned transition from one Chern number to another [34]. In the case of a Chern insulator, the difference of the number of left moving and right moving states per edge is the edge topological invariant [23, 25, 209].

4.2.1. Bulk Topological Invariant

For the derivation of the bulk-topological invariant the spinless Hamiltonian in Eq. 3.9 is used and in the sublattice spin basis (σ_i denote the Pauli matrices for $i \in \{x, y, z\}$), such a Hamiltonian can be expressed as [34]

$$H = \boldsymbol{d}\left(\mathbf{k}\right) \cdot \boldsymbol{\sigma}, \tag{4.1}$$

where $\boldsymbol{d}\left(\mathbf{k}\right)$ is a vector mapping the two dimensional space of momenta onto a three-dimensional space of 2×2-dimensional Hamiltonians. By solving the eigenvalue problem of the Hamiltonian in Eq. 4.1, the components of $\boldsymbol{d}\left(\mathbf{k}\right)$ can be identified with the expectation values of the sublattice spin $\langle \boldsymbol{\sigma} \rangle$. Then a function is defined, $\mathbf{k} : \{0, 2\pi\} \rightarrow \mathbb{R}^2$, $t \mapsto \mathbf{k}(t) = (k_x(t), k_y(t))$, such that its two components describe a circle in k-space. With this, the Chern number can be computed as [34]

$$\nu = \frac{1}{2\pi} \int_0^{2\pi} \left(\frac{\boldsymbol{d}\left(\mathbf{k}(t)\right)}{\left|\boldsymbol{d}\left(\mathbf{k}(t)\right)\right|} \times \frac{d}{dt} \left(\frac{\boldsymbol{d}\left(\mathbf{k}(t)\right)}{\left|\boldsymbol{d}\left(\mathbf{k}(t)\right)\right|} \right) \right)_z \mathrm{d}t. \tag{4.2}$$

This definition is only valid for a Chern insulator. Graphene without a time-reversal symmetry-breaking magnetic field does not belong to this class of materials. Nonetheless the bulk topological invariant of the spinless case of a two-band model for graphene can be computed, which results in the windings shown in Fig. 3.7 and winding numbers in Tab. 3.3. The windings around the Dirac cones for the simple two-band model can be verified by inserting

a path in k-space, as explained above, in the low-energy form of the graphene Hamiltonian Eq. 3.10 and the winding numbers can be computed. The latter is a conserved quantity, such that the sum of the winding numbers of the trigonal warping due to the Rashba-type spin-orbit coupling resembles the winding number around all four cones [187, 193].

4.2.2. The Existence of Edge States

This section is based on [223]. For graphene, terminated by edges in one dimension, Eq. 4.1 can be used to show that there must exist zero energy states. In the sublattice representation, without real spin, $\boldsymbol{d}(\mathbf{k}) = t\left(1 + \cos\mathbf{k}\,\mathbf{a}_1 + \cos\mathbf{k}(\mathbf{a}_2 - \mathbf{a}_1), -\sin\mathbf{k}\,\mathbf{a}_1 - \sin\mathbf{k}(\mathbf{a}_2 - \mathbf{a}_1), 0\right)$. The vectors $\boldsymbol{a}_1$ and $\boldsymbol{a}_2$ are the lattice vectors defined in Eq. 3.1. In the low-energy approximation around one of the Dirac points, together with Eq. 4.1, this leads to Eq. 3.10. The zigzag edge is parallel to the x-direction and to account for this fact, $\boldsymbol{d}$ is first rewritten in k_x and k_y coordinates. Then one obtains a part that is depending on the now pseudomomentum k_y, separated in the component $d_\parallel$ in the xy-plane and on $d_\perp$ perpendicular to it,

$$d_\parallel = 2t\cos\frac{\sqrt{3}a}{2}k_x(\cos\frac{3a}{2}k_y, -\sin\frac{3a}{2}k_y, 0) \tag{4.3}$$

$$d_\perp = (0,0,0) \tag{4.4}$$

and another in-plane component that is independent of k_y and defines the offset from the origin, namely

$$d^0 = (t,0,0). \tag{4.5}$$

The theorem 1a presented in [223] now states that if $d_\parallel$ encloses the origin, which is the case when the radius of $d_\parallel$ is larger then the displacement d^0, the energy of the zero modes is given by $|d_\perp|$, which in this case is zero. For fixed momentum k_y, this defines a condition for k_x, where the edge states have zero energy, namely

$$1 < 2\cos\frac{\sqrt{3}a}{2}k_x. \tag{4.6}$$

It leads to the interval $-\frac{2\pi}{3\sqrt{3}a} < k_x < \frac{2\pi}{3\sqrt{3}a}$, where the zero energy modes exist. The verification of this will be shown in Sec. 4.4, when the dispersion relation of the graphene tight-binding model with edges is discussed.

4.3. The Kane-Mele model

The Kane-Mele model [26, 41] is an extension of the model proposed by Haldane [31]. Haldane's original model exhibits the integer quantum Hall effect, due to the inclusion of a time-reversal breaking field, which respects all symmetries of the lattice and does not lead to a net flux through the unit cell. Due to this field, the Hamiltonian acquires chirality. Furthermore, the time-reversal breaking leads to closing and reopening of the band gap at only one of the Dirac points of the graphene lattice. This gap is then of the opposite sign compared to the other, which sets the Hamiltonian into a topological state [31, 41]. In the Kane-Mele model the time-reversal symmetry is restored, where two copies of the Haldane model are linked by intrinsic spin-orbit coupling, such that each state has a time-reversal symmetric partner. This way, the net magnetic flux is still zero and each model individually exhibits the integer quantum Hall effect. Kane and Mele argue, that another effect of similar nature as the quantum Hall effect exists nonetheless, which features spin transport at the edges of a topological insulator, instead of charge transport. The Kane-Mele model is described by a tight-binding Hamiltonian for the π-bands of a honeycomb lattice, such as graphene, with hopping parameter t. This hopping is given in the first term in

$$H = t \sum_{\langle ij \rangle} \hat{c}_i^\dagger \hat{c}_j + i\lambda_{\mathrm{SO}} \sum_{\langle\langle ij \rangle\rangle} \nu_{ij} \hat{c}_i^\dagger \hat{s}^z \hat{c}_j + i\lambda_{\mathrm{R}} \sum_{\langle ij \rangle} \hat{c}_i^\dagger (\hat{\boldsymbol{s}} \times \boldsymbol{d}_{ij})_z \hat{c}_j + \lambda_\nu \sum_i \xi_i \hat{c}_i^\dagger \hat{c}_i, \qquad (4.7)$$

with the creation and annihilation operators $\hat{c}_i^\dagger$ and $\hat{c}_i$ for an electron at site i. The second term describes the intrinsic spin-orbit coupling via next-nearest-neighbor hopping and an interaction parameter λ_{SO}. It is a mapping from the higher d-orbitals in the space of the π-band [26, 80]. The matrix element ν_{ij} is $+1$ if the hopping along two neighboring sites is clockwise and it is -1 if the hopping follows a counter-clockwise path. This term is what links the two spin species together. Within one spin type the low-energy form of the intrinsic spin-orbit coupling assumes the form of a magnetic field. But the sign of this field is opposite for each spin species and thus it conserves time-reversal symmetry when both spins are considered as a whole. The third term breaks the mirror-symmetry along the direction perpendicular to the graphene plane and describes the Rashba-type spin-orbit coupling within the π-band. The vector $\boldsymbol{d}_{ij}$ is the displacement vector between the two neighbors i and j and the vector $\hat{\boldsymbol{s}}$ is the vector containing the Pauli matrices, which are defined on the real spin space. The fourth and last term is a staggered sublattice potential. For one of the sublattices $\xi_i = 1$ and for the other $\xi_i = -1$, which causes a transition from the quantum spin Hall topological phase to that of the trivial insulator at $3\sqrt{3}\lambda_{\mathrm{SO}} < \lambda_\nu$ [26]. Even though the Rashba-type spin-orbit coupling and the staggered sublattice potential perturb the $\hat{s}^z$ conservation and the two-fold rotational symmetry of the system, still a finite region around the unperturbed point in parameter space exhibits the quantum spin Hall effect [26]. If the staggered sublattice potential becomes too strong, such that $\lambda_\nu > 3\sqrt{3}\lambda_{\mathrm{SO}}$, the system leaves the topological state and becomes insulating. The same holds true for the Rashba-type spin-orbit coupling, which does not destroy the quantum topological state as long as $\lambda_{\mathrm{R}} < 2\sqrt{3}\lambda_{\mathrm{SO}}$.
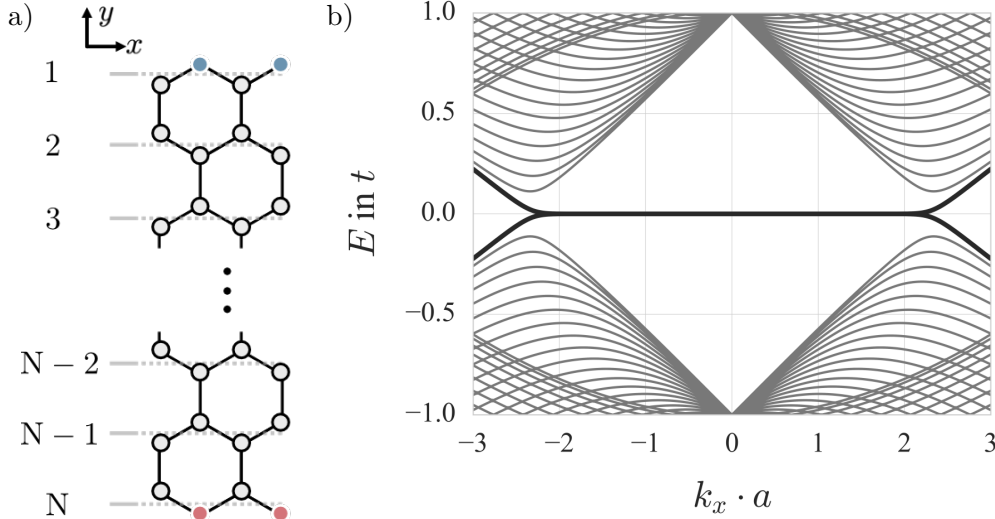
4.4. Helical Edge States

FIGURE 4.1.: a) The population of two edge states of graphene as a solution to the tight-binding model at the Γ-point. The population of one state is indicated by blue and that of the other by red color. At finite momenta, the edge states acquire exponentially small bulk population. b) Dispersion relation of a $N = 30$ nanoribbon with only p_z-orbitals. The energy bands of the edge states are shown in black and those of the bulk states in gray.

For the computation of the quantum spin Hall effect, the tight-binding model with edges as given by Eq. B.3 is used. The periodic boundary conditions are kept along the x-direction, but opened along the y-direction and terminated by a zigzag edge at each end. A spatial occupation of the solution of the one-dimensionally periodic graphene sample is depicted in Fig. 4.1 a), where the periodic axis is also taken parallel to the x-direction. In this plot the occupation per site of two of the eigenstates for $k_x = 0$ is indicated by coloring - blue coloring resembles one edge state and the red color another. The edge states are confined to one edge each and exclusively located at either sublattice. A band structure featuring edge states is shown in Fig. 4.1 b). For a semi-infinite sample, the edge states would loose their edge character only for $\frac{2\pi}{3\sqrt{3}} < |k_x \cdot a|$, where no midgap states are expected to exist anymore [224]. Notice, that in the tight-binding model described here, the unit cell is twice as wide as in the literature [210, 224] and in order to reflect the smaller Brillouin zone, all translations leading to the condition for the edge states Eq. 4.6 must obtain a factor of $1/2$. Then the condition for the edge states becomes $-\frac{4\pi}{3\sqrt{3}} < k_x \cdot a < -\frac{4\pi}{3\sqrt{3}}$, which is observable in the band structure in Fig. 4.1 b).

Finite size effects open up a small gap already in the close vicinity of the Dirac points. The gap for finite systems exactly at the point $k_x = \frac{4\pi}{3\sqrt{3}a}$ is dependent on the nanoribbon

size. With N as the number of rows of the nanoribbon, the gap is proportional to $\frac{3\pi}{2} \frac{1}{W+1}$ with $W = \frac{3N}{2} - 1$ being the ribbon width of the nanoribbon in units of lattice constant a [50]. As a result the gap closes, as N grows. Nonetheless, the edge-like states cross the gap, such that the nanoribbon is insulating in the bulk, but conducting at the edges. In fact all zigzag nanoribbons are considered metallic [49], while the bulk of graphene is a semimetal. The helicity of the edge states is only given when intrinsic spin-orbit coupling is present - either by the second nearest-neighbor hopping as in Eq. 4.7 or via the actual matrix elements Eq. 3.24 and an extended Hilbert space with d-orbitals. The intrinsic spin-orbit coupling opens up a gap at the Dirac points, such that the edge bands obtain a slope. This gap is on the order of $26\,\mu$eV [80], corresponding to 0.3 K.

The nature of this type of gap, which shifts the energy of one real-spin type at one Dirac point in one direction and in the opposite direction at the other Dirac point, causes the states to obtain this helicity. Consequently, the group velocity of the edge states connects the valence band at one Dirac cone with the conduction band at the other continuously. Without the intrinsic spin-orbit coupling, the gap at the Dirac points would not open and thus the states with different helicities, but located at identical edges, would be degenerate everywhere between the two Dirac points. This is also why no spin currents could flow and thus the quantum spin Hall effect could not be observed, as the direction of propagation had no way of knowing which spin component at each edge had which helicity [79]. If only one type of spin species would be considered in the model, states on opposite edges would travel in opposite directions [207, 225] and chirality, the locking of sublattice spin and propagation direction, could be defined [75]. In a time-reversal symmetric topological insulator, the chirality is lifted, because each edge obtains another state of opposite spin and opposite propagation direction due to Kramers degeneracy and therefore the system is said to exhibit *counter-propagating spin-filtered* edge states [26, 41] instead of chiral edge states. The edge states are propagating without backscattering at nonmagnetic impurities. In the quantum Hall effect, the dissipationless transport is facilitated, because at each edge no channel for possible backscattering is available, while in the quantum spin Hall effect the destructive interference of the two counter-propagating states at each edge suppresses backscattering [39]. The analysis of helicity becomes more complicated, when additional effects on the band structure from the d-orbitals are taken into account, which change the dispersion relation of the edge states locally, even without intrinsic spin-orbit coupling. Such a situation is depicted in Fig. 4.2. There, two band structures are depicted, one with only p_z-orbitals (left) and one with also d_{xz}- and d_{yz}-orbitals (right), and with intrinsic spin-orbit coupling. The nanoribbons have both $N = 30$ rows and 4 columns. Including intrinsic spin-orbit coupling of magnitude $\xi_d = 0.8$ meV does not change the dispersion relation on the right of Fig. 4.2 at this energy scale, compared to the one without intrinsic spin-orbit coupling. A finite slope of the edge states is observable for all $k_x \neq 0$ in the case of included d-orbitals. For the case with only p_z-orbitals, the slope remains zero, but the edge states are still confined to the edges, fulfilling Eq. 4.6. Due to the similar transformation behavior, see appendix
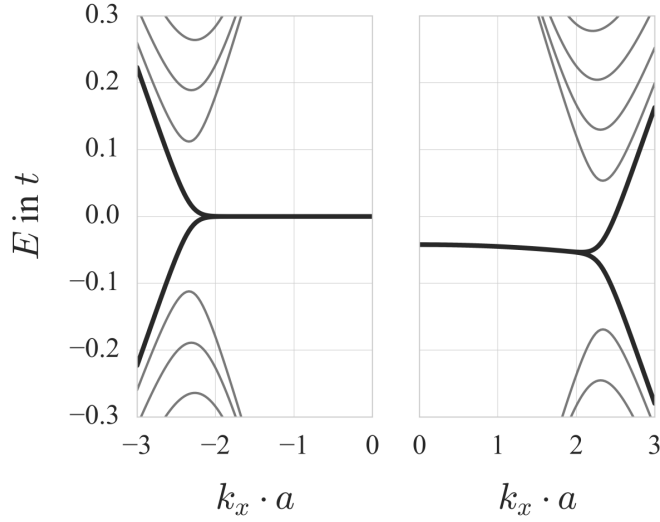
FIGURE 4.2.: Half of a dispersion relation of a nanoribbon of size $N = 30$ with only p_z-orbitals (left) and additionally d_{xz}- and d_{yz}-orbitals with intrinsic spin-orbit coupling $\xi_d = 0.8\,\text{meV}$ (right). The slope of the edge state energy due to the inclusion of the d-orbitals is visible, as well as an energy shift at $k_x = 0$.

A.1, the momentum and sublattice spin can be interchanged, such that in analogy to the alignment of momentum and spin, leading to helicity $\frac{\boldsymbol{k}\hat{\boldsymbol{s}}}{|\boldsymbol{k}|}$, the *edge helicity* [151] becomes the alignment of real spin and sublattice spin $\langle \hat{\sigma}_z \cdot \hat{s}_z \rangle$, which is a good quantum number.

The presence of two states with opposing real spin at each edge is not changed by the addition of the d-orbitals. Since the deformation of the edge bands is not originating from a gap opening at the two Dirac points, all four energy bands of the edge states obtain the same slope. Hence the finite slope is not leading to helicity, similar to the intrinsic spin-orbit coupling, because the real spin is not locked to the propagation direction.

4.5. Edge States with Rashba-type Spin-orbit Coupling and Magnetic Field
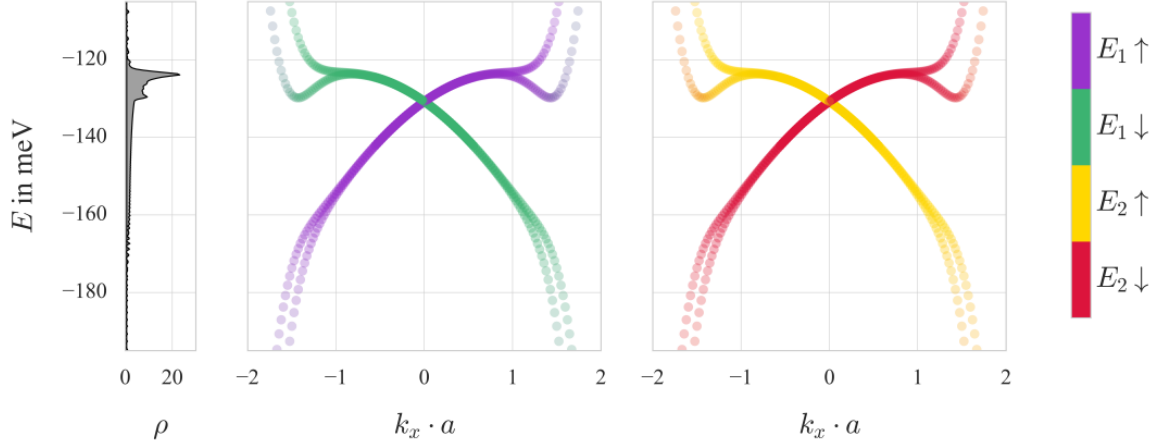
FIGURE 4.3.: The four edge states in a nanoribbon with 10 rows of atoms. The density of states is depicted on the left, where the parts of the bands with low dispersion result in peaks. The bands are colored by edge and real spin, showing a degeneracy of bands with positive edge helicity and of bands with negative helicity. It is $\xi_d = 2.1\,\text{eV}$ and $\lambda_R = 0.06\,\text{eV}$.

The topological characteristics of the graphene nanoribbon can be understood when the occupation of lattice sites and spin polarization of the edge states is considered at the same time, revealing information about their helicity. In a model with 10 rows of atoms, p_z-, d_{xz}- and d_{yz}-orbitals and with Rashba spin orbit coupling of strength $\lambda_R = 0.06\,\text{eV}$, the bands remain fourfold degenerate only at $k_x \cdot a = 0$. Here, the intrinsic spin-orbit coupling is overemphasized with $\xi_d = 2.1\,\text{eV}$ for a stronger effect on the band structure, but leads to qualitatively similar results at smaller values of ξ_d, because the Rashba-type spin-orbit coupling is very small. In Fig. 4.3 the edge states are depicted, where the energy bands are colored by the edge and real spin expectation values of the edge states. Since both edges belong to different sublattices, this labeling is equivalent to the sublattice spin.

The edge states dispersing with positive group velocity have parallel alignment of real- and sublattice spin, since the purple and red curves have positive edge helicity $\langle \hat{s}_z \cdot \hat{\sigma}_z \rangle$. The other two curves are their time-reversal partners, which have negative edge helicity. A trigonal warping in the lower conduction and upper valence band is visible in the vicinity of the Dirac cones. At around $k_x \cdot a = \pm 1$, the bands start to split and the $\hat{s}_z$ degeneracy is lifted, which occurs due to the influence of the Rashba spin-orbit coupling. At around $k_x \cdot a = \pm 1.5$ both pairs of bands exhibit largest splitting. Both states $|\text{E}_1 \uparrow\rangle$ and $|\text{E}_2 \downarrow\rangle$ are mixed, such that $\hat{s}_z$ is no longer conserved. The same happens with the other two states with negative helicity, $|\text{E}_1 \downarrow\rangle$ and $|\text{E}_2 \uparrow\rangle$.
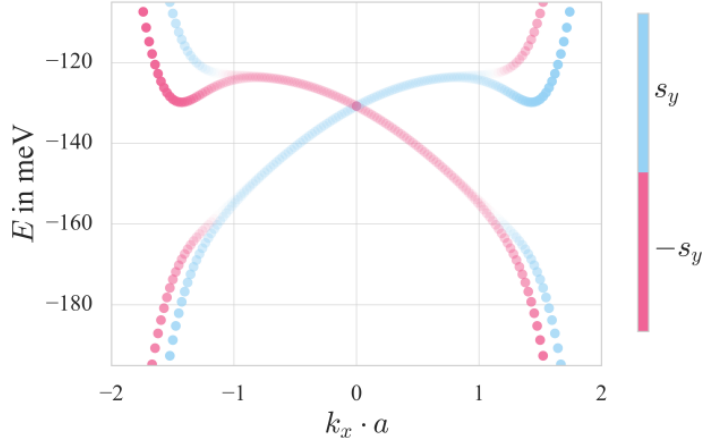
FIGURE 4.4.: Result of the calculation as in Fig. 4.3 with $\xi_d = 2.1\,\text{eV}$ and $\lambda_R = 0.06\,\text{eV}$, colored by the $\hat{s}_y$ component of the real spin. The Rashba spin-orbit coupling acts on the bands at the Dirac points and couples states of opposite spins, such that a gap of $\hat{s}_y$ polarized states arises at $k_x \cdot a = \pm 1.0$.

The density of states for the crossing is shown in the left of Fig. 4.3 and the gapless crossing of the edge states is indicated by the gapless density of states everywhere around the Fermi edge at $-131\,\text{meV}$. An asymmetry of the dispersion - mainly due to the shift of $V_{pd\pi}$ - is caused by the interaction among the d-orbitals with $V_{dd\delta}$. The change of the slopes of the bands introduced by the Rashba-type spin-orbit coupling at $k_x \cdot a = \pm 1.5$ is indicated by a peak in the density of states. The low-energy expression for the Rashba spin-orbit coupling around the Dirac points, Eq. 2.27, shows a dependence of the y-component of the real spin on the momentum k_x and thus on the alignment with the sublattice spin $\hat{\sigma}_x$. At some point this Rashba spin-orbit coupling, which is a bulk property, starts to affect the dispersion of the edge states, the closer they are to either of the Dirac cones. As a consequence, both a splitting at $k_x \cdot a = \pm 1.5$ and a polarization of the $\hat{s}_y$-component take place. This can be seen if the states in Fig. 4.3 were colored by their $\hat{s}_y$-expectation value, which is shown in Fig. 4.4. While a four-fold degeneracy of the energy is observed in the vicinity of the Brillouin zone center, the splitting of the bands around the Dirac points happens due to the $\hat{s}_y$-polarization along the direction of momentum k_x, leading to a remaining two-fold degeneracy.

Next, the edge states with intrinsic spin-orbit coupling are subjected to a magnetic field of strength $B = 25\,\text{T}$, but no Rashba spin-orbit coupling. Then the $\hat{s}_z$-polarization is maintained, but the degeneracy of the edge states at $k_x \cdot a = 0$ is lifted. This is shown in Fig. 4.5, where the edge states again cross the energy gap. The magnetic field lifts the spin degeneracy and destroys time-reversal symmetry. As depicted, the red and purple curve with positive helicity (parallel real and sublattice spins) still disperse with positive group velocity, but are non-degenerate in energy for every $k_x \cdot a$. The same is true for the other two states
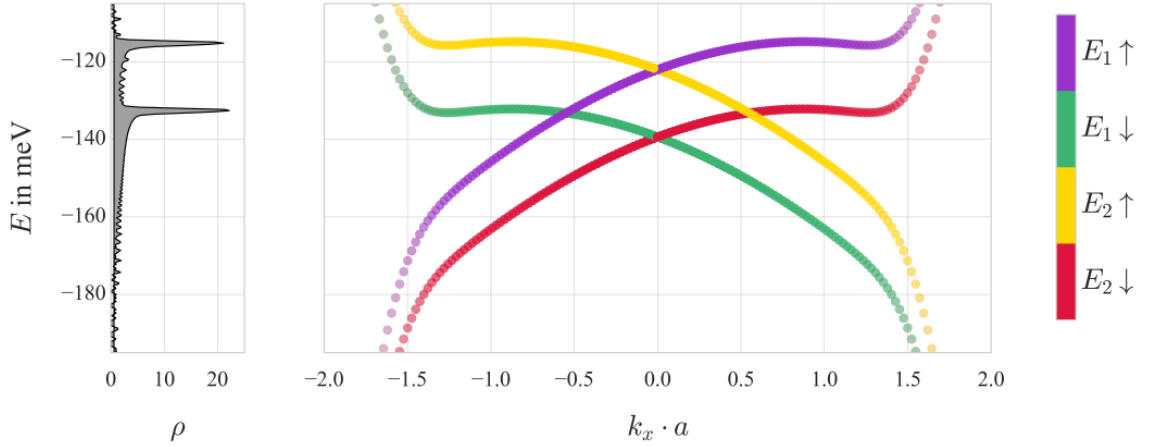
FIGURE 4.5.: Dispersion relation of the four edge states in a nanoribbon with 10 rows and $\xi_d = 2.1\,\text{eV}$, without Rashba-type spin-orbit coupling, but under the influence of a magnetic field of strength $B = 25\,\text{T}$. The states are colored by edge and real spin component.

with opposite edge helicity. Those two states with real spin $\uparrow$ are higher in energy than the two $\downarrow$-states, because of the Zeeman splitting by the magnetic field. Hence two peaks are shown in the density of states, one for each real-spin species. The resulting material is a Weyl semimetal, because it has edge band crossings, which are singly degenerate [226, 227] and can thus be regarded as a time-reversal broken topological insulator. If additionally Rashba spin-orbit coupling of again $\lambda_R = 0.06\,\text{eV}$ is introduced, as shown in Fig. 4.6, the coupling of different $\hat{s}_z$ values at identical edges changes the material to a trivial insulator. However, the density of states remains finite everywhere, because the dispersion of the bands obscures the band gap. The only indication of the avoided crossing is the additional peak in the density of states in Fig. 4.6 at $-135\,\text{meV}$, which expresses the second saddle point in the dispersion relation. The other two peaks at at $-118\,\text{meV}$ and at at $-133\,\text{meV}$ are identical to the previous case in Fig. 4.5. In this situation the density of states cannot be used to classify the topological state of the system. As in the previous case without a magnetic field, the polarization of the $\hat{s}_y$-component is responsible for the splitting away from $k_x \cdot a = 0$, c.f. Fig. 4.7. At the Brillouin zone center the Rashba-type spin-orbit coupling is zero. At $k_x \cdot a = \pm 0.5$, however, the two $\hat{s}_z$-components for each edge couple and a gap opens, making the material truly insulating and thus topologically trivial.
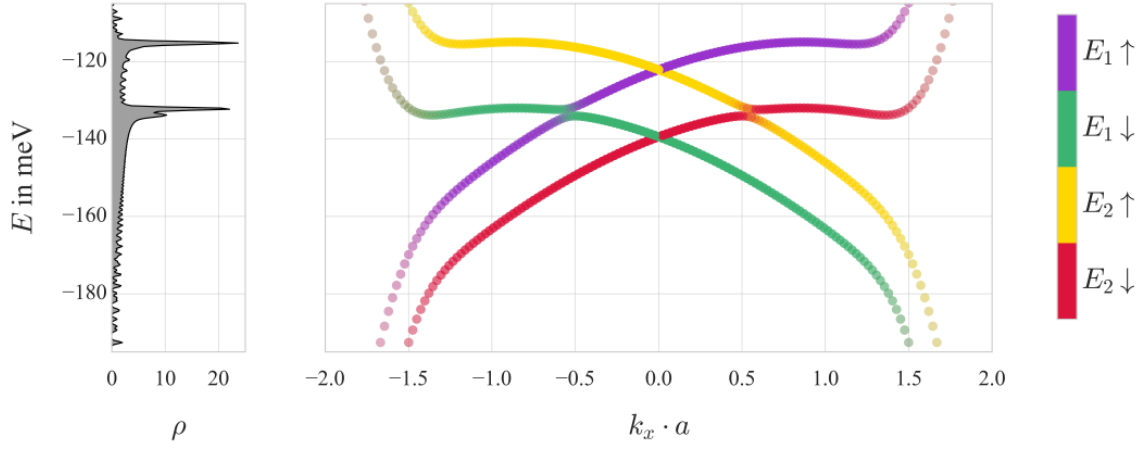
FIGURE 4.6.: Additionally to the parameters $\xi_d = 2.1\,\text{eV}$ and $B = 25\,\text{T}$ of Fig. 4.5, the Rashba spin-orbit coupling strength is set to $\lambda_R = 0.06\,\text{eV}$. The dispersion relation then shows avoided crossings at $k_x \cdot a = \pm 0.5$.
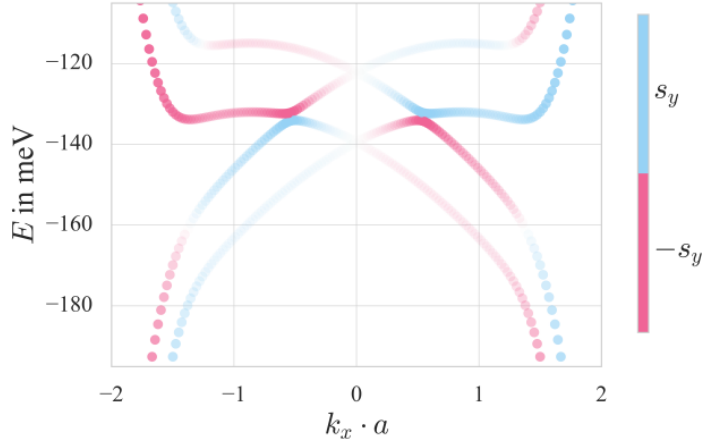
FIGURE 4.7.: Dispersion relation depicted in Fig. 4.6 for the four edge states in a nanoribbon with 10 rows and $\xi_d = 2.1\,\text{eV}$, $\lambda_R = 0.06\,\text{eV}$ and a magnetic field $B = 25\,\text{T}$, colored by $\hat{s}_y$ component. The influence of the Rashba spin-orbit coupling is shown, where the polarization of the $\hat{s}_y$ components introduces an avoided crossing at $k_x \cdot a = \pm 0.5$. At $k_x \cdot a = 0$ the faded area corresponds to areas of the Brillouin zone of small $\hat{s}_y$-polarization.

5. Electronic Interaction in a Multi-Orbital Hubbard Model

Up until now the independent-electron picture has been considered. Including interactions may drastically change the electronic properties of the edge states in graphene nanoribbons, because different magnetic phases have different electronic and magnetic characteristics. This may determine whether the ground state of these ribbons is a topologically insulating phase or not. In reality, magnetic edge states are not very likely to be observed. Passivation with hydrogen atoms may help meeting the requirements. Overpassivation of edge atoms, however, can cause the Fermi edge to be far away from the magnetic instability, such that experimentally available samples are non-magnetic by default [177]. So far many experimental efforts have been undertaken to find magnetic edge states, employing methods such as scanning tunneling microscopy (STM) and scanning tunneling spectroscopy (STS) [228]. These methods probe and confirm the local density of electronic states at the zigzag edges of graphene nanoribbons. More recent experiments have found a gap opening in the local density of states which depends on the ribbon size, confirming magnetic ordering of the edges phases [47, 229], even at room temperature [230]. Other efforts include near-edge x-ray absorption (NEXAFS) or electron-spin resonance (ESR) on samples of graphene [231]. Many of these experiments have claimed to prove the existence of magnetic edge states, but the accuracy of these findings allow for explanations other than the occurrence of magnetic edge states [232]. Furthermore, experiments usually probe only either the edge character of electronic states in graphene or the alignment of the spin degree of freedom - but not both simultaneously, such that a combination of NEXAFS and ESR should be used to investigate these two features at the same time.

It is hard to produce a large enough amount of samples with sufficiently clean and precise zigzag edges to be able to collect conclusive results [233]. A model for the description of electronic interactions, which may be capable helping the understanding of magnetism in the edges of graphene nanoribbons, is the Hubbard model [234–236]. It allows for inclusion of the electronic interaction in the tight-binding approach by an on-site interaction term and it is the simplest model for discussing the mutual influence of the interaction and kinetic energy [237]. Variations of this model are also possible, such as a range of *extended Hubbard models*, which may include interactions also from neighboring atoms. In the model presented in this work, instead of a spatially extended Hubbard model, a multi-orbital Hubbard model in the mean-field approximation is used, where a single site is subject to on-site interaction terms from different orbitals [238]. In many cases edge states in graphene nanoribbons

are discussed by using density-functional theory (DFT) [91, 239], where the ground state energy is described by using a functional, which is called the *exchange-correlation potential*. This potential may be used to solve the Schrödinger equation effectively in a single-particle picture, by using formulae to express an effective exchange-correlation potential. One of the common approximations in the literature is the so-called *local-spin-density approximation* (LSDA) [93, 240]. Others might be the *local density approximation* or the *generalized gradient approximation*.

However, for the goal of computing the magnetic edge states in a spatially extended graphene sample, a mean-field method may suffice, because the number of states and atoms limits the efficiency of DFT calculations and the loss of accuracy may be negligible. Such an approach leads to the *Hartree-Fock Equations*. Because of their non-linear character, these equations must be solved iteratively, such that a self-consistent solution for the electronic wave functions can be found. In the following, the onset of magnetism is covered. Then the formulation of electronic interactions in a multi-orbital Hubbard model is discussed. In a next step, the model is approximated with a mean-field, before the principle of self-consistently solving such a mean-field approach is described.

5.1. Onset of Magnetism in Graphene Nanoribbons

In order to explain the onset of spontaneous ferromagnetism, a model derived by Stoner [237] can be used to quantify the competition between kinetic energy and repulsion due to the Coulomb interaction. In Stoner's model it is shown that the susceptibility for a critical Coulomb interaction strength U_{crit} causes parallel alignment of spins, which depends on the density of states at the Fermi energy $\rho(E_F)$. The critical Coulomb interaction according to the Stoner model is

$$1 \leq U_{\mathrm{crit}} \cdot \rho(E_F). \tag{5.1}$$

If the density of states at the Fermi energy becomes very large, even small electronic interaction strengths are enough to compete with the kinetic energy of the states, resulting in a preferred parallel spin alignment.

Two-dimensional graphene is a zero-gap semiconductor, and without edge states, it has zero density of states at the Fermi energy [241]. As a consequence, bulk graphene is non-magnetic in the ground state. In the case of edge states of graphene nanoribbons, the dispersion of the bands at the Fermi energy is rather flat, due to the localization of the corresponding states at the edges. The very small bandwidth, due to the small kinetic energy of the edge states, leads to a peak in the density of states at the Fermi energy and causes a tendency for edge magnetism.

Graphene has a bipartite lattice and in this case, the Hubbard model at half-filling can be mapped onto an effective antiferromagnetic Heisenberg model [241]. Due to the two sublattices of the system, each sublattice on its own exhibits ferromagnetic ordering, but as the neighbors of each site belong to different sublattices, neighboring states are polarized in opposite directions. In the case of nanoribbons with zigzag edges, the edge states populate the outermost sites of the ribbon and each edge belongs to a different sublattice exclusively. Consequently, the spins along each edge align in parallel and a local ferrimagnetic ordering of the spins is found. For sites further away from the edges the strength of this spin polarization is weaker as a result of the localization of the edge states. Both edges may exhibit a very large spin polarization, while the whole lattice may still feature a zero total spin magnetic moment, in agreement with Lieb's theorem [242]. This theorem states that the ground state of a bipartite lattice at half-filling with equal number of sites of each sublattice, exhibits a zero spin magnetic moment.

Due to the localized nature of the edge states, the system can be regarded as a Heisenberg model with two step ladder geometry, which exhibits ferromagnetic intra-edge exchange and antiferromagnetic inter-edge exchange [241]. The magnitude of the parameters obtained by numerical fitting reveals, that the inter-edge exchange is two orders of magnitude smaller than the intra-edge exchange, suggesting that the alignment of the the edges magnetic moments for $U = 0.1t$ is nearly independent. While the intra-edge exchange is barely affected by the distance between the edges, the inter-edge exchange decreases rapidly, if the edges are further apart. A more detailed analysis shows, that the inter-edge exchange (also called

superexchange) arises due to three contributions, the band energy, the exchange energy and spin polarization [243], all favoring an alignment of the magnetic moments at each edge opposite to each other. This will be discussed in more depth, when the properties of each edge magnetic phase are analyzed in the next chapter.

The influence of the *d*-orbitals, which affect the dispersion relation of the π-like edge states, is expected to play a role in the magnetic properties of the ground state, because the occurrence of magnetization depends on the density of states at the Fermi energy.

Other than that, the amount of doping of such a system shifts the Fermi energy away from the magnetic instability. As a result, the onset of magnetization and the phase of the ground state may be determined by breaking electron-hole symmetry or observing the system away from half-filling [49].

5.2. Electronic Interaction in the Single-orbital Hubbard Model

The Hamilton operator for interacting electrons in a solid in spatial representation is [93]

$$H = \sum_{i=1}^{N} \frac{\mathbf{p}_i^2}{2m_e} + \sum_{i=1}^{N} V(\mathbf{r}_i) + \frac{1}{2} \sum_{i \neq j} \frac{e^2}{|\mathbf{r}_i - \mathbf{r}_j|}, \tag{5.2}$$

where $V(\mathbf{r})$ is the potential of the periodic lattice and N is the number of electrons in the system with the mass m_e. The representation is suited to describe the electronic interaction, but the first two terms of the Hamiltonian Eq. 5.2 are diagonal in the Bloch basis [237], while the latter is diagonal in that of the real space basis, instead. Therefore a conversion to Fock space via the field operators $\hat{\phi}(\mathbf{r})$ is performed, where $\hat{\phi}(\mathbf{r}) = \sum_i \phi_i(\mathbf{r})\hat{c}_{k_i}$ and $\hat{\phi}^\dagger(\mathbf{r}) = \sum_i \phi_i^*(\mathbf{r})\hat{c}_{k_i}^\dagger$ annihilate and create a particle at position $\mathbf{r}$. Here the wave functions $\phi_i^*(\mathbf{r})$ and $\phi_i(\mathbf{r})$ can be any single-particle basis set for the Hilbert space, like a real space representation, such as the localized Wannier functions, or the Bloch basis set, defined by the band index n, the momentum vector $\mathbf{k}$ and the spin σ [93]. By using these field operators the interaction part of the Hamiltonian Eq. 5.2 can be expressed in the second quantization representation as [237]

$$H_1 = \frac{1}{2} \int d^3\mathbf{r}_1 \int d^3\mathbf{r}_2 \, \hat{\phi}^\dagger(\mathbf{r}_1)\hat{\phi}^\dagger(\mathbf{r}_2) \frac{e^2}{|\mathbf{r}_1 - \mathbf{r}_2|} \hat{\phi}(\mathbf{r}_2)\hat{\phi}(\mathbf{r}_1). \tag{5.3}$$

The non-interacting part H_0 of the Hamiltonian has been largely dealt with in Chapter 3 and is thus not discussed here again. As described there, a real-space representation of a system can be found by using a set of localized Wannier functions at the individual atomic sites, but an approximation to them via the atomic orbital basis is used, in order to exploit their symmetries. By formulating the non-interacting part of the Hamiltonian Eq. 5.2 as tight-binding model, where the electrons are confined to a site and hopping among different sites i and j is enabled by a hopping matrix element t_{ij}, the interacting part in Eq. 5.3 can be included, by using the atomic orbitals in Eq. 5.2 with site index i, such that the total Hamiltonian in second quantization reads [244]

$$H = \sum_{i,j,\sigma,\sigma'} t_{i,j}\hat{c}_{i,\sigma}^\dagger\hat{c}_{j,\sigma'} + \frac{1}{2} \sum_{\sigma,\sigma'} \sum_{i,j,k,l} u_{i,j,k,l}\hat{c}_{i,\sigma}^\dagger\hat{c}_{j,\sigma'}^\dagger\hat{c}_{k,\sigma'}\hat{c}_{l,\sigma}. \tag{5.4}$$

Band indices n and n' at each creation and annihilation operator are suppressed here. The matrix elements are given as [93]

$$t_{i,j} = \int d^3\mathbf{r} \, \phi^*(\mathbf{r} - \mathbf{R}_i) \left(\frac{\mathbf{p}^2}{2m} + V(\mathbf{r}) \right) \phi(\mathbf{r} - \mathbf{R}_j) \tag{5.5}$$

and

$$u_{i,j,k,l} = \int d^3\mathbf{r}_1 \int d^3\mathbf{r}_2 \, \phi^*(\mathbf{r}_1 - \mathbf{R}_i)\phi^*(\mathbf{r}_2 - \mathbf{R}_j) \frac{e^2}{|\mathbf{r}_1 - \mathbf{r}_2|} \phi(\mathbf{r}_2 - \mathbf{R}_k)\phi(\mathbf{r}_1 - \mathbf{R}_l). \tag{5.6}$$

In this context, Hubbard [234–236, 245] introduced a single-band model for the Coulomb interaction of electrons, which is called the *Hubbard model*,

$$H = -t \sum_{\langle i,j \rangle} \sum_{\sigma \in \{\uparrow,\downarrow\}} \hat{c}_{i,\sigma}^{\dagger} \hat{c}_{j,\sigma} + U \sum_{i} \hat{n}_{i,\uparrow} \hat{n}_{i,\downarrow}. \tag{5.7}$$

This model is comprised of one band with two types of spin and the Coulomb interactions are limited to short-range on-site interactions with strength U. Thus, all of the field operators in the sum in the second term of Eq. 5.4 are taken at the same site and do not have a band index. The hopping matrix element is confined to nearest neighbors only and independent of the site indices. The model includes the spin, reflected in the last term of Eq. 5.7, where the repulsion between states of opposite spins at the same sites is incorporated via the density operators $\hat{n}_{i,\sigma}$ for site i and spin σ. It serves as a basic model for the description of electronic interaction. Extensions to the original Hubbard model have been made and resulted in different kinds of *extended Hubbard models* [246–248], which may include long-range interactions or multi-band tight-binding models, such as discussed in the next section of this chapter. These models require an extension of the single-orbital Hubbard model to more than one orbital, such that band indices will be included in the following. In this case, an exchange term may also be introduced into the multi-orbital Hubbard model which couples on-site wave functions of different orbitals. Screening and long-range correlation are neglected [249]. For the description of metals where the Fermi energy lies within the conduction band of the system, using only a single-orbital Hubbard model may be justified. However in the case presented here, the influence of the higher energy d-orbitals on the total energy of the model is of interest and therefore more than one orbital is regarded.

5.3. Definition of a Multi-orbital Hubbard Model

From the general formulation of the interaction operator in Eq. 5.4, only terms coupling states located at the same site will be included and therefore no explicit site index is written. The orbital indices i, j, k, l will be labeled either by p, when p_z-orbital are regarded or n, when any of the five d-orbitals are considered. The interaction matrix elements $u_{i,j,k,l}$ will be denoted

$$\langle ij|\hat{V}|kl\rangle := \int \mathrm{d}^3\mathbf{r}_1 \int \mathrm{d}^3\mathbf{r}_2 \, \phi_{i,\sigma}^*(\mathbf{r}_1) \, \phi_{j,\sigma'}^*(\mathbf{r}_2) \frac{V}{|\mathbf{r}_1 - \mathbf{r}_2|} \phi_{k,\sigma'}(\mathbf{r}_1) \, \phi_{l,\sigma}(\mathbf{r}_2). \qquad (5.8)$$

Adding an orbital index to the wave functions in Eq. 5.6, leads to the term describing the interaction among p_z-orbitals

$$H_{pp} = \langle pp|\hat{V}|pp\rangle \, \hat{c}_{p\uparrow}^\dagger \hat{c}_{p\downarrow}^\dagger \hat{c}_{p\downarrow} \hat{c}_{p\uparrow}. \qquad (5.9)$$

The interaction matrix element U_p among p_z-orbitals is computed via $U_p := \langle pp|\hat{V}|pp\rangle$. This is the Coulomb repulsion of two electrons of opposite spins in the p_z-orbital at a single site. By including d-orbitals in the tight-binding model, various combinations for electronic interactions in Eq. 5.4 are possible. The first is

$$H_{pd}^1 = \sum_{n,\sigma,\sigma'} \langle pn|\hat{V}|pn\rangle \hat{c}_{p\sigma}^\dagger \hat{c}_{n\sigma'}^\dagger \hat{c}_{n\sigma'} \hat{c}_{p\sigma}. \qquad (5.10)$$

Here the Coulomb repulsion among electrons in p_z-orbitals with any of the d-orbitals is described. In practice the d-orbitals are located far away from the Fermi energy, while the band structure is dominantly described by the p_z-orbitals already. As a consequence, the Coulomb repulsion among different d-orbitals in Eq. 5.8 is neglected in this work. Therefore Eq. 5.10 contains only terms, where $i = k = p$ labels a state in a p_z-orbital and $j = l = n \in \{d_{xz}, d_{yz}, \dots\}$ one of the five d-orbitals and vice versa. Since more than one orbital is included in the extended Hubbard model, another interaction term may arise, namely

$$H_{pd}^2 = \sum_{n,\sigma,\sigma'} \langle pn|\hat{V}|np\rangle \hat{c}_{p\sigma}^\dagger \hat{c}_{n\sigma'}^\dagger \hat{c}_{p\sigma'} \hat{c}_{n\sigma}. \qquad (5.11)$$

As before, one of the indices describes a p_z-orbital, while the other refers to any of the 5 d-orbitals and no other interaction matrix elements are considered. By defining the real matrix elements $V_n := \langle pn|\hat{V}|pn\rangle$ for the Coulomb repulsion depending on a p_z-orbital and the n-th d-orbital and $J_n := \langle pn|\hat{V}|np\rangle$ for the Coulomb exchange interaction matrix elements, the relevant parts of the electronic interaction Hamiltonian in the multi-orbital Hubbard model

can be summarized as

$$H_{pd} = H_{pp} + H_{pd}^1 + H_{pd}^2 \tag{5.12}$$

$$= U_p \hat{c}_{p\uparrow}^\dagger \hat{c}_{p\downarrow}^\dagger \hat{c}_{p\downarrow} \hat{c}_{p\uparrow}$$

$$+ \sum_n \left(V_n \left(\hat{c}_{p\uparrow}^\dagger \hat{c}_{n\downarrow}^\dagger \hat{c}_{n\downarrow} \hat{c}_{p\uparrow} + \hat{c}_{p\downarrow}^\dagger \hat{c}_{n\uparrow}^\dagger \hat{c}_{n\uparrow} \hat{c}_{p\downarrow} + \hat{c}_{p\uparrow}^\dagger \hat{c}_{n\uparrow}^\dagger \hat{c}_{n\uparrow} \hat{c}_{p\uparrow} + \hat{c}_{p\downarrow}^\dagger \hat{c}_{n\downarrow}^\dagger \hat{c}_{n\downarrow} \hat{c}_{p\downarrow} \right) \right.$$

$$\left. + J_n \left(\hat{c}_{p\uparrow}^\dagger \hat{c}_{n\downarrow}^\dagger \hat{c}_{p\downarrow} \hat{c}_{n\uparrow} + \hat{c}_{p\downarrow}^\dagger \hat{c}_{n\uparrow}^\dagger \hat{c}_{p\uparrow} \hat{c}_{n\downarrow} + \hat{c}_{p\uparrow}^\dagger \hat{c}_{n\uparrow}^\dagger \hat{c}_{p\uparrow} \hat{c}_{n\uparrow} + \hat{c}_{p\downarrow}^\dagger \hat{c}_{n\downarrow}^\dagger \hat{c}_{p\downarrow} \hat{c}_{n\downarrow} \right) \right). \tag{5.13}$$

By comparing the terms in this interaction Hamiltonian, it becomes clear that the terms in the last two lines, where all four operators share the same spin, are identical apart from one permutation. This results in a relative sign, whereas they have different prefactors V_n and J_n and therefore the terms can be rearranged to

$$H_{pd}^{ee} = U_p \hat{n}_{p\uparrow} \hat{n}_{p\downarrow} + \sum_n \left(V_n \left(\hat{n}_{p\uparrow} \hat{n}_{n\downarrow} + \hat{n}_{p\downarrow} \hat{n}_{n\uparrow} \right) + J_n \left(\hat{c}_{p\uparrow}^\dagger \hat{c}_{n\downarrow}^\dagger \hat{c}_{p\downarrow} \hat{c}_{n\uparrow} + \hat{c}_{p\downarrow}^\dagger \hat{c}_{n\uparrow}^\dagger \hat{c}_{p\uparrow} \hat{c}_{n\downarrow} \right) \right.$$

$$\left. + \left(V_n - J_n \right) \left(\hat{n}_{p\uparrow} \hat{n}_{n\uparrow} + \hat{n}_{p\downarrow} \hat{n}_{n\downarrow} \right) \right), \tag{5.14}$$

where the particle number operators $\hat{n}_{i\sigma} := \hat{c}_{i\sigma}^\dagger \hat{c}_{i\sigma}$ have been inserted. The Coulomb repulsion of electrons with different spins in the p_z-orbital at a single site is given by the first term in Eq. 5.14 and by the second term, when one of the electrons occupies a d-orbital instead. In the third term the non-classical exchange is shown, which represents the energy of exchanging the spin of electrons in different orbitals. The last term describes the Coulomb repulsion of electrons in different orbitals, but with identical spin. There are similar forms of the above electronic interaction Hamiltonian in the literature [237, 250–252]. The magnitude of the parameters derived here is discussed in a later section.

5.4. Decomposition of the Electronic Interaction Operator into the Mean-field Approximation

In this section the terms in the many-body Hamiltonian Eq. 5.14 are rewritten, such that they can be solved iteratively with the mean-field method. Spin-rotational invariance may be of importance, if the spin conservation along the z-axis is perturbed, i.e. by Rashba-type spin-orbit coupling. Therefore in the following derivation, additional terms for maintaining spin-rotational invariance are introduced in the mean-field approximation. These terms will be zero in the numerical computations performed in this work, but are stated for completeness, because the Hubbard model is also spin-rotational invariant.

5.4.1. Interaction among p_z-orbitals

The density operators in Eq. 5.9, e.g. $\hat{n}_\uparrow$, are expressed as a fluctuation $\Delta\hat{n}_\uparrow$ around their mean-value $\langle\hat{n}_\uparrow\rangle$. Then the terms quadratic in the fluctuation are neglected. It follows for the electronic densities [237]

$$\hat{n}_\uparrow\hat{n}_\downarrow = (\langle\hat{n}_\uparrow\rangle + \Delta\hat{n}_\uparrow)(\langle\hat{n}_\downarrow\rangle + \Delta\hat{n}_\downarrow) \approx -\langle\hat{n}_\uparrow\rangle\langle\hat{n}_\downarrow\rangle + \hat{n}_\uparrow\langle\hat{n}_\downarrow\rangle + \hat{n}_\downarrow\langle\hat{n}_\uparrow\rangle. \tag{5.15}$$

While approximating the two-body operator as an effective potential, this reformulation does not conserve spin rotational invariance [245] and is only valid for systems, where the spin $\hat{s}_z$-component is conserved. For the formulation of a spin-rotational invariant mean-field approximation, additional terms may be formed from the two density operators, because these are comprised of two field operators, each. Rearrangement of the field operators leads to

$$\hat{n}_\uparrow\hat{n}_\downarrow = \hat{c}_\uparrow^\dagger\hat{c}_\uparrow\hat{c}_\downarrow^\dagger\hat{c}_\downarrow = -\hat{c}_\uparrow^\dagger\hat{c}_\downarrow\hat{c}_\downarrow^\dagger\hat{c}_\uparrow. \tag{5.16}$$

The decomposition of the Eq. 5.16 into the mean-field picture is

$$-\hat{c}_\uparrow^\dagger\hat{c}_\downarrow\hat{c}_\downarrow^\dagger\hat{c}_\uparrow \approx -\left(-\langle\hat{c}_\uparrow^\dagger\hat{c}_\downarrow\rangle\langle\hat{c}_\downarrow^\dagger\hat{c}_\uparrow\rangle + \hat{c}_\uparrow^\dagger\hat{c}_\downarrow\langle\hat{c}_\downarrow^\dagger\hat{c}_\uparrow\rangle + \hat{c}_\downarrow^\dagger\hat{c}_\uparrow\langle\hat{c}_\uparrow^\dagger\hat{c}_\downarrow\rangle\right), \tag{5.17}$$

where again terms quadratic in the fluctuations are neglected. These expectation values will be zero when the system does not contain $\hat{s}_z$-non-conserving terms. The pairs of operators in this decomposition can be identified with the spin raising $\hat{S}^\dagger = \hat{c}_\uparrow^\dagger\hat{c}_\downarrow$ and lowering operator $\hat{S}^- = \hat{c}_\downarrow^\dagger\hat{c}_\uparrow$, which will form the x- and y-components of the spin $\hat{S}^x = \frac{1}{2}\left(\hat{S}^\dagger + \hat{S}^-\right)$ and $\hat{S}^y = \frac{1}{2i}\left(\hat{S}^\dagger - \hat{S}^-\right)$. By identifying $\langle\hat{S}^z\rangle = \frac{1}{2}(\langle\hat{n}_\uparrow\rangle - \langle\hat{n}_\downarrow\rangle)$ and $\langle\hat{n}\rangle = \langle\hat{n}_\uparrow\rangle + \langle\hat{n}_\downarrow\rangle$, the following relations can be established

$$\langle\hat{n}_\uparrow\rangle\langle\hat{n}_\downarrow\rangle = \frac{1}{4}\left(\langle\hat{n}\rangle^2 - 4\langle\hat{S}^z\rangle^2\right) \tag{5.18}$$

$$\hat{n}_\uparrow\langle\hat{n}_\downarrow\rangle + \hat{n}_\downarrow\langle\hat{n}_\uparrow\rangle = \frac{1}{2}\left(\hat{n}\langle\hat{n}\rangle - 4\hat{S}^z\langle\hat{S}^z\rangle\right). \tag{5.19}$$

Together, they lead to the relations $\hat{S}^-\langle\hat{S}^\dagger\rangle + \hat{S}^\dagger\langle\hat{S}^-\rangle = 2\hat{S}^x\langle\hat{S}^x\rangle + 2\hat{S}^y\langle\hat{S}^y\rangle$ and $\langle\hat{S}^\dagger\rangle\langle\hat{S}^-\rangle = \langle\hat{S}^x\rangle^2 + \langle\hat{S}^y\rangle^2$. The mean-field electron-electron interaction of the Hubbard model for the p_z-orbitals can then be written as the sum of the two decompositions

$$\hat{n}_\uparrow\hat{n}_\downarrow \approx \frac{\hat{n}\langle\hat{n}\rangle}{2} - 2\vec{S}\langle\vec{S}\rangle - \frac{\langle\hat{n}\rangle^2}{4} + \langle\vec{S}\rangle\langle\vec{S}\rangle. \tag{5.20}$$

This operator conserves spin-rotational invariance, because all spin components are treated on equal footing.

5.4.2. Interaction among p_z- and d-orbitals

In this section, one of the terms in Eq. 5.14, $\hat{c}_{p\uparrow}^\dagger\hat{c}_{n\downarrow}^\dagger\hat{c}_{p\downarrow}\hat{c}_{n\uparrow}$, will be decomposed the same way as in the previous section. The spin-rotational invariance-conserving parts will obtain a sign relative to the other non-conserving parts, due to the commutation relations of the field operators. It follows

$$\begin{aligned}
\hat{c}_{p\uparrow}^\dagger\hat{c}_{n\downarrow}^\dagger\hat{c}_{p\downarrow}\hat{c}_{n\uparrow} \approx &- \langle\hat{S}_p^\dagger\rangle\hat{S}_n^- - \langle\hat{S}_n^-\rangle\hat{S}_p^\dagger + \langle\hat{c}_{n\downarrow}^\dagger\hat{c}_{p\downarrow}\rangle\hat{c}_{p\uparrow}^\dagger\hat{c}_{n\uparrow} \\
&+ \langle\hat{c}_{p\uparrow}^\dagger\hat{c}_{n\uparrow}\rangle\hat{c}_{n\downarrow}^\dagger\hat{c}_{p\downarrow} - \langle\hat{c}_{p\uparrow}^\dagger\hat{c}_{n\uparrow}\rangle\langle\hat{c}_{n\downarrow}^\dagger\hat{c}_{p\downarrow}\rangle + \langle\hat{S}_p^\dagger\rangle\langle\hat{S}_n^-\rangle.
\end{aligned} \tag{5.21}$$

Here the spin-rotational invariance is ensured through the spin raising and lowering operators for each of the orbitals. If all of the two-body operators are decomposed into mean-field operators, the result is

$$\begin{aligned}
H_{pd} \approx &\frac{U_p}{2}\left(\hat{n}\langle\hat{n}\rangle - 4\hat{S}^z\langle\hat{S}^z\rangle - \left(\frac{\langle\hat{n}\rangle^2}{2} - 2\langle\hat{S}^z\rangle^2\right)\right) \\
&+ \sum_n\Bigg[V_n\Big(\langle\hat{n}_{p\uparrow}\rangle\hat{n}_{n\downarrow} + \langle\hat{n}_{n\downarrow}\rangle\hat{n}_{p\uparrow} + \langle\hat{n}_{p\downarrow}\rangle\hat{n}_{n\uparrow} + \langle\hat{n}_{n\uparrow}\rangle\hat{n}_{p\downarrow} - \langle\hat{n}_{p\uparrow}\rangle\langle\hat{n}_{n\downarrow}\rangle - \langle\hat{n}_{p\downarrow}\rangle\langle\hat{n}_{n\uparrow}\rangle\Big) \\
&+ J_n\Big(\langle\hat{c}_{n\downarrow}^\dagger\hat{c}_{p\downarrow}\rangle\hat{c}_{p\uparrow}^\dagger\hat{c}_{n\uparrow} + \langle\hat{c}_{p\uparrow}^\dagger\hat{c}_{n\uparrow}\rangle\hat{c}_{n\downarrow}^\dagger\hat{c}_{p\downarrow} - \langle\hat{c}_{p\uparrow}^\dagger\hat{c}_{n\uparrow}\rangle\langle\hat{c}_{n\downarrow}^\dagger\hat{c}_{p\downarrow}\rangle + \langle\hat{c}_{p\downarrow}^\dagger\hat{c}_{n\downarrow}\rangle\hat{c}_{n\uparrow}^\dagger\hat{c}_{p\uparrow} \\
&+ \langle\hat{c}_{n\uparrow}^\dagger\hat{c}_{p\uparrow}\rangle\hat{c}_{p\downarrow}^\dagger\hat{c}_{n\downarrow} - \langle\hat{c}_{n\uparrow}^\dagger\hat{c}_{p\uparrow}\rangle\langle\hat{c}_{p\downarrow}^\dagger\hat{c}_{n\downarrow}\rangle\Big) \\
&+ (V_n - J_n)\Big(\langle\hat{n}_{p\uparrow}\rangle\hat{n}_{n\uparrow} + \langle\hat{n}_{n\uparrow}\rangle\hat{n}_{p\uparrow} - \langle\hat{n}_{n\uparrow}\rangle\langle\hat{n}_{p\uparrow}\rangle - \langle\hat{c}_{p\uparrow}^\dagger\hat{c}_{n\uparrow}\rangle\hat{c}_{n\uparrow}^\dagger\hat{c}_{p\uparrow} - \langle\hat{c}_{n\uparrow}^\dagger\hat{c}_{p\uparrow}\rangle\hat{c}_{p\uparrow}^\dagger\hat{c}_{n\uparrow} \\
&+ \langle\hat{c}_{n\uparrow}^\dagger\hat{c}_{p\uparrow}\rangle\langle\hat{c}_{p\uparrow}^\dagger\hat{c}_{n\uparrow}\rangle + \langle\hat{n}_{p\downarrow}\rangle\hat{n}_{n\downarrow} + \langle\hat{n}_{n\downarrow}\rangle\hat{n}_{p\downarrow} - \langle\hat{n}_{n\downarrow}\rangle\langle\hat{n}_{p\downarrow}\rangle - \langle\hat{c}_{p\downarrow}^\dagger\hat{c}_{n\downarrow}\rangle\hat{c}_{n\downarrow}^\dagger\hat{c}_{p\downarrow} \\
&- \langle\hat{c}_{n\downarrow}^\dagger\hat{c}_{p\downarrow}\rangle\hat{c}_{p\downarrow}^\dagger\hat{c}_{n\downarrow} + \langle\hat{c}_{n\downarrow}^\dagger\hat{c}_{p\downarrow}\rangle\langle\hat{c}_{p\downarrow}^\dagger\hat{c}_{n\downarrow}\rangle\Big)\Bigg],
\end{aligned} \tag{5.22}$$

where terms for conserving spin-rotational invariance are not included, for the reasons mentioned above. In this Hamiltonian the site index is suppressed, but all of these expectation values are site-dependent. For the full result with all terms ensuring spin-rotational invariance, see the appendix Eq. C.1.

5.5. Parameters of the Electronic Interaction and Limits of the Model

Experimentally obtained data for graphene cannot be used to formulate precise parameters for the Coulomb interaction in graphene, unfortunately [49]. Therefore a discussion on the expected magnitude of these parameters is given here. As Hubbard prognosed in his work [234–236], a hierarchy of interactions for the electron-electron interaction can be established. They assumed parameters for the repulsion on the order of $U \sim 10\,\mathrm{eV}$, for coupling p_z- and d-orbitals of $V_n \sim 2\,\mathrm{eV}$ and $J_n \sim 0.5\,\mathrm{eV}$ for the exchange [237]. Hence the matrix elements of the Coulomb repulsion play a dominant role, compared to those of the exchange. Using *PySCF*, a Python package for self-consistent-field calculations [253], an estimate for the parameters is calculated directly for the *ccpvdz* basis set of an isolated carbon atom. It is a rough approximation, because no screening is considered. Screening due to electrons from the other carbon atoms in a graphene lattice should not be neglected, because of the delocalized nature of the half-filled p_z-orbitals [254, 255]. The Coulomb interaction parameters, computed by using *PySCF*, are on the order of $U \sim 13\,\mathrm{eV}$, $V_n \sim 9\,\mathrm{eV}$ and $J_n \sim 2\,\mathrm{eV}$ for the d_{xz}- and d_{yz}-orbitals. Only these two orbitals will be considered additionally to the p_z-orbitals from now on, because the other d-orbitals do not couple to the p_z-orbitals due to their symmetry, justifying such an approximation. In any case, it is found for the other three d-orbitals that the Coulomb repulsion is also of the same magnitude $V_n \sim 9\,\mathrm{eV}$, but the exchange is smaller for the d_{z^2} and $d_{x^2-y^2}$-orbitals, giving $J_n \sim 0.5\,\mathrm{eV}$. In the literature the order of magnitude of these parameters is different from what was computed via *PySCF*.

In the case of graphene nanoribbons with zigzag edges, local effects due to the edge states have been found to introduce correlations into these systems, affecting the onset of magnetism [254]. Rigorous quantum chemical computations find values for the intra-atomic Coulomb repulsion on the order of about $20\,\mathrm{eV}$, which are then reduced to around $3\,\mathrm{eV}$ due to screening by the 4s electrons [240]. Remarkably, the single-orbital model can adequately describe many-electron effects in graphene [49].

In order to obtain parameters from experimental data and ab-initio calculations, the single-orbital Hubbard model is compared to DFT calculations. It has been found to agree best with the first principle results when $U/t \sim 1.1 - 1.3$ in the case of generalized-gradient approximation to the exchange-correlation functional, where the range of $U = 3.0\,\mathrm{eV} - 3.5\,\mathrm{eV}$ is assumed, which is also found in experiments [49]. However, fitting the single-orbital Hubbard model to local spin-density approximation yield $U/t = 0.9$ [49, 256] and by employing magnetic resonance studies, U is suggested to be at least of the order of $3\,\mathrm{eV}$ [49, 257]. Using quantum Monte Carlo computations with $t \sim 3\,\mathrm{eV}$ the interaction strength $U \sim 7\,\mathrm{eV}$ is found to be the maximum value for that a single-orbital Hubbard model is sufficiently accurate. Increasing U any further, leads to passing a Mott-Hubbard transition, where an antiferromagnetically ordered insulating state is reached [49].

Given the uncertainty of the actual value of the parameters and the accuracy of the model,

the parameters used in this work are varied between $U \sim 0\,\text{eV}$ and $U \sim 2.3t \approx 7\,\text{eV}$, in order to account for the possible parameter ranges, while J_n and V_n are also considered in comparable magnitudes. While the general magnetic properties of the full DFT calculation can adequately be described by a single-orbital Hubbard Hamiltonian, the multi-orbital model will be required for considering the influence of the d-orbitals on the properties of the edge states in the ground state of graphene. Due to the small occupation of orbitals other than p_z, correlations of the electrons in graphene do not play a dominant role [258]. Thus, employing mean-field methods is a good approximation in the parameter ranges discussed here, as suggested by [179]. Other than that, a spatially extended Hubbard model is not used in this work, because the contributions to the electronic interaction due to neighboring atoms are weak compared to those in a single site.

5.6. Computing the Self-consistent Field

In problems where a self-consistent solution is required, some sort of convergence criterion is formulated. The solution is considered self-consistent, if after a number of iterations, it fulfills this requirement. In order to start solving the mean-field problem, values for the matrix elements in the Hamiltonian in Eq. 5.22 must be fixed before the first iteration. The characteristics of the initial set of matrix elements will strongly affect the efficiency of reaching a solution, such that a good guess helps to lower computation time. In quantum chemical applications, usually a density-matrix is computed [259] and the convergence of its entries is considered an appropriate measure. The occupation of electrons in p_z- and d-orbitals is compared against the previous step as

$$\Delta_\rho = \sum_{k,\sigma} \left(\rho_i^{k,\sigma} - \rho_{i-1}^{k,\sigma} \right).$$ (5.23)

The populations for the i-th iteration of the k-th state of spin σ are given by the respective diagonal element of the density matrix $\rho_i^{k,\sigma} = \langle \psi | \rho_{i,k,k}^{\sigma,\sigma} | k, \sigma \rangle \langle k, \sigma | \psi \rangle = \langle n_{k,\sigma}^i \rangle$. Practically, a convergence on the order of $\Delta_\rho \sim 10^{-10}$ between iterations is reached after only a few steps, if only p_z-orbitals are considered. Inclusion of the two d-orbitals usually converges towards $\sim 10^{-12}$ within 12-15 iterations and $\sim 10^{-20}$ within 40 iterations, depending on the initial guess. When such a high number of iterations is used, the energy of the resulting system converges with an accuracy of 1×10^{-9} eV to 1×10^{-7} eV for single- and multi-orbital computations. Due to the finite sampling of the reciprocal space in the computation, the numerical error may be on the order of 1×10^{-1} meV. The python code written for this project uses 20 nodes of the local PHYSnet cluster to perform direct diagonalization of the Hamilton operator at a sampling of 801 points across the Brillouin zone in parallel during each iteration. With this method 35 iterations of a multi-orbital Hubbard model with two d-orbitals and $N = 8$ rows take about 75 hours and for $N = 12$ about 150 hours. The general procedure on how to compute the occupation of states in a solid, as well as the chemical potential is common in theoretical solid state physics or quantum chemistry [93, 245, 259] and a good overview is given in [184], which is adapted here. A solution is computed from a Hamiltonian in the mean-field approximation. From the band structure of the system the density of states is computed, see Sec. 3.2.4, and from the density of states, the occupation of states is obtained, according to the Fermi-Dirac distribution [148]. The number of particles for half-filling corresponds to the number of sites of the system. By imposing the result of the integral to be equal to the particle number of a half-filled system, this method allows for computation of the chemical potential μ. The number of occupied states is

$$n = \int_{-\infty}^{\infty} \rho(E) \frac{1}{e^{(E-\mu)/k_B T} + 1} \mathrm{d}E.$$ (5.24)

The computation is started, where in the Fermi-Dirac distribution $k_B T = 3.45 \times 10^{-4}$ eV. This is done for convergence purposes, because of the strong slope at the chemical potential

for zero temperature. The above values correspond to $T = 4\,\mathrm{K}$, but the computation is considered to lead to similar results at $T = 0$. In practice the chemical potential is obtained, by varying μ in the integral in Eq. 5.24 and numerically solving it, until both sides of the equation match up, while n is fixed. For a solution with a broken particle-hole symmetry it is required to fix n with a small offset from half-filling. This way the computation may converge to a system with electron or hole doping. The expectation values of the number operators at each point $\boldsymbol{k}$ in the Brillouin zone for the orbitals o and spins σ at site i are then given by

$$\langle \hat{n}_{\sigma,o}^i(\boldsymbol{k})\rangle = \sum_{j,\sigma',o'} \frac{1}{e^{(E_{j,o'}^{\sigma'}(\boldsymbol{k})-\mu)/k_B T} + 1}\langle \chi_{\sigma',o'}^j(\boldsymbol{k})|\hat{n}_{\sigma,o}^i|\chi_{\sigma',o'}^j(\boldsymbol{k})\rangle. \tag{5.25}$$

It is to be noted here, that the expectation values in the matrix elements of the Hamiltonian 5.22 depend on the point $\boldsymbol{k}$ in reciprocal space as well. Other expectation values necessary for the mean-field computation are derived in analogy to Eq. 5.25. The internal energy of the system is obtained by considering the number of occupied states of each energy, leading to

$$E_{\mathrm{int}} = \int_{-\infty}^{\infty} \rho(E) \frac{E}{e^{(E-\mu)/k_B T} + 1}\mathrm{d}E. \tag{5.26}$$

With the internal energy, the phase diagram in later sections will be characterized, because the temperature is only included for convergence purposes. The free energy is given by $F = E_{\mathrm{int}} - TS$, which would be required for finite temperatures. The entropy S is computed via

$$S = -k_B \int_{-\infty}^{\infty} \mathrm{d}E\,\mathfrak{F}(E)\ln\mathfrak{F}(E) + (1-\mathfrak{F}(E))\ln(1-\mathfrak{F}(E)), \tag{5.27}$$

where $\mathfrak{F}(E) = \frac{1}{e^{(E-\mu)/k_B T}+1}$ is the Fermi-Dirac distribution.

6. Magnetic Phases of Edge States in Graphene Nanoribbons

6.1. Description of the Phases

In graphene nanoribbons with interactions different types of edge magnetism can occur [213, 241]. All have in common that the properties of the edges are somewhat extraordinary, compared to those of the bulk. For the magnetic states at half-filling, the spins always polarize in parallel along a single edge. Sites in close vicinity to the edges, belonging to the same sublattice, show a finite spin polarization in the same direction and those sites belonging to the other sublattice polarize in the opposite direction. This *local ferrimagnetic* spin-alignment is strongest near each edge, but it decays into the bulk, such that the ribbons only show a very weak spin polarization in their centers.

The magnetic phase where the spin polarization of the two edges is opposite has a band structure with a gap at the Fermi level. This gapped phase will be called antiferromagnetic edge phase (AFM), because of the antiparallel spin polarization of the two edges relative to each other. In this case, each sublattice has the same direction of spin polarization everywhere in the sample. Since both edges belong to different sublattices, they assume an opposing spin polarization.

The other type of magnetic solution at half-filling is the ferromagnetic edge phase (FM), which does not show a band gap. Since here both edges have parallel spin alignment, the direction of spin polarization for each sublattice must switch its sign at the center of the ribbon, which leads to a domain wall. A variety of other states with varying degree of edge magnetism can be found, once weak doping is considered [260], but with considerable amount of doping, a non-magnetic phase is obtained. Doping may be used to control the edge magnetization, because the Fermi energy is shifted from the instability of the density of states, which is required for the onset of magnetism. Therefore, the interactions of the edges at opposing ends of the sample can be influenced by the charge carrier concentration and consequently, doping provides a method for controlling the magnetic properties of the ground state [49]. The remaining phases can be considered intermediate phases, occurring at finite, but much smaller doping than the non-magnetic phase. It has been shown via non-collinear density functional theory that doping can cause the magnetic edges to attain non-parallel spin [261]. Furthermore, the band structures of these phases may show similarities to both magnetic phases at half-filling, but have their spins align partly in the graphene plane.

In this thesis, the focus is laid on only three different solutions to the mean-field problem,

the two magnetic phases obtained for a half-filled system and the non-magnetic phase for larger doping. There is no spin polarization in the non-magnetic phase, but a charge in-homogeneity with increased occupation of the edge sites. The topological properties of the three phases are discussed by analyzing their symmetries. In a next step the influence of the d-orbitals of graphene on the properties of the phases is discussed by considering the electronic interactions therein. The effect of different interaction strengths is examined, as well as the energetic separation of the p_z- and d-orbitals. For the non-magnetic phase, the amount of doping and its effect on the internal energy and Fermi energy is explored.

In order to obtain the energy of these phases, the spin-rotational invariance-conserving terms in the mean-field interaction are not required, because the conservation of $\hat{s}_z$ will not be violated. While the Hartree-Fock approximation can overestimate magnetic order, it is found to be sufficiently accurate for describing the weak magnetic correlation of the edge states in graphene [241]. Considering strong correlation effects is not expected to change the magnetic ground state of zigzag nanoribbons, which justifies the mean-field approximation further [50].

6.1.1. Breaking Symmetries

The mean-field Hamiltonian in the form of Eq. 5.22 satisfies several symmetries, whereas the symmetry of the initial guess for the matrix elements affects the symmetry of the self-consistent solution. For obtaining a specific solution, it is relevant whether the initial guess breaks a specific symmetry, such as particle-hole symmetry (PHS) or time-reversal (TR) symmetry. For the AFM solution, spin-spatial symmetry needs to be broken such that one side of the sample exhibits one spin alignment and the other side of the sample an opposite alignment. For the FM edge phase on the other hand, TR symmetry must be broken. This can be realized if the state used for initial guess of matrix elements exhibits a spin-magnetic moment, e.g. an equally distributed spin-imbalance across the sample or a spin polarization, where the spins at both edges are aligned in parallel and the bulk is not polarized at all. Finally, for the non-magnetic case, PHS must be broken, which is achieved by doping.

6.1.2. Non-magnetic Edge Phase

The non-magnetic phase may arise from doping of the graphene sample while maintaining time-reversal invariance. It is topologically very similar to the situation where no electron-electron interactions are considered. All four edge states cross the band gap, similar to the non-interacting system.

In Fig. 6.1 a) the four edge bands are plotted and colored by their *bulk chirality*-expectation value $\langle \frac{\hat{\sigma}_x \cdot k_x}{|k_x|} \rangle$, which is well defined around the Dirac points. The energy is fourfold degenerate at $k_x = 0$. In Fig. 6.1 b) the real spin and sublattice spin expectation values are shown for the four bands, and each band is colored by its respective expectation value. The sublattice spin of edge 1 corresponds to the up component, which denotes sublattice A, while edge 2
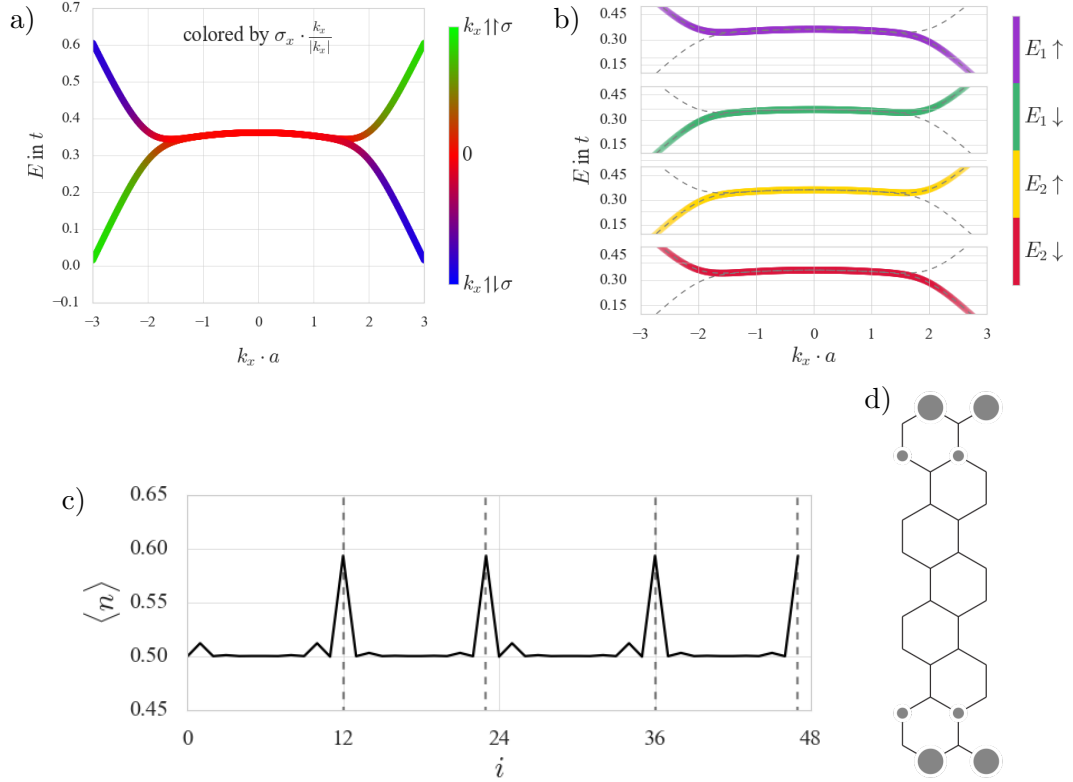
FIGURE 6.1.: a) The dispersion relation of the four edge states for $N = 12$ in the non-magnetic phase colored by the bulk chirality for $U = 0.6t$. The system is doped with $\Delta N = 1.92$ electrons above half-filling. b) The states are colored by sublattice A on edge 1 and B on edge 2, which are labeled by E_1 or E_2, together with the real spin expectation value. The dashed lines indicate the other states. c) The density expectation value for the non-magnetic phase. The surplus of population is located at the sample edges without spin polarization. d) A schematic overview of a the occupation additional to half-filling at each site.

corresponds to sublattice B and the down component. The labels E_1 and E_2, denoting the different edges, are used for that purpose. The bands cross according to the *edge helicity* $\langle \hat{\sigma}_z \cdot \hat{s}_z \rangle$ [151], which is a good quantum number in the vicinity of the Γ-point. For larger nanoribbons, the area of sublattice and real spin polarization in the Brillouin zone center increases. Since it is computationally more involved, much larger nanoribbons do not find consideration in this thesis. The dispersion relation of the non-magnetic phase resembles the non-interacting single-orbital system with an effective next-nearest-neighbor hopping $t' > 0$ and an overall energy shift, similar to the right of Fig. 4.2. In Fig. 6.1 c) density expectation

for the non-magnetic phase is shown per site[1] i. The density expectation value per spin is

$$\langle n_i \rangle = \frac{1}{2} \left(\langle n_{\uparrow,i} \rangle + \langle n_{\downarrow,i} \rangle \right). \tag{6.1}$$

The sites located at the outer zigzag edge are indicated by dashed lines. The unpolarized occupation of the edges compared to the bulk is increased, with both spin polarizations in equal amounts. If the system were to be doped with holes, the population there would be slightly diminished. A schematic overview of the spatial distribution of the phase is given in Fig. 6.1 d), where the sites with an occupation other than half-filling are indicated grey, while the size is proportional to the amount. At each edge only sites belonging to the same sublattice are occupied.

In the two spin-polarized magnetic phases, the Stoner criterion provides an explanation, why the pronounced peak of the density of states at the Fermi edge leads to the onset of magnetism, which is seen in the dispersion relation in Fig. 6.1 a). Doping the sample with electrons or holes moves the Fermi energy away from this instability region and the resulting solution does not exhibit a magnetic moment anymore [49, 177, 260]. In the case of $U = 0.6t$ at half-filling, the Fermi energy is shifted to $E_F = 0.3t$, but the energy of the non-magnetic phase exhibits a larger shift. This will be discussed in-depth in Sec. 6.3.

6.1.3. Ferromagnetic Edge Phase

It is a result from the Hartree-Fock approximation of the Hubbard model, that the Hubbard interaction causes electronic states of spin-up and -down to split [240].

In the FM phase both edges of the system show parallel spin polarization with respect to each other, resulting in a finite spin-magnetic moment of the sample. Consequently, the states in Fig. 6.2 a) are not four-fold degenerate. The energies are shown for a nanoribbon with $N = 12$ rows and 4 columns at $U = 0.6t$. The edge chirality $\langle \hat{\sigma}_z \cdot \hat{s}_z \rangle$ is a good quantum number for the edge states and they polarize accordingly, as can be seen in Fig. 6.2 b), where the crossing of the four states is shown individually. The states are colored by the edge they are located at and which spin polarization $\langle \hat{s}_z \rangle$ they have. The remaining edge states are indicated by dashed lines and it can be seen that the two spin-down states are higher in energy than the two spin-up states, while each edge hosts one type of spin. Whether the two spin-up or spin-down states are higher in energy, depends on the initial state. This result here is energetically degenerate with the solution obtained from a time-reversed initial state.

Closer to the Dirac cones, the kinetic exchange lowers the energy for antisymmetric spatial wave functions. Two states with mostly opposite spin cross the band gap in the vicinity of each Dirac point. The mechanism of the coupling of states localized at two opposing edges can be described in analogy to the superexchange mechanism [177, 243]. Here an exchange in spatially distant electronic wave functions is mediated through the bulk. The spin gap at

---

[1] The sites are labeled column-wise in ascending order starting with 0 on the top of the leftmost column and ending with site 47 on the bottom right.
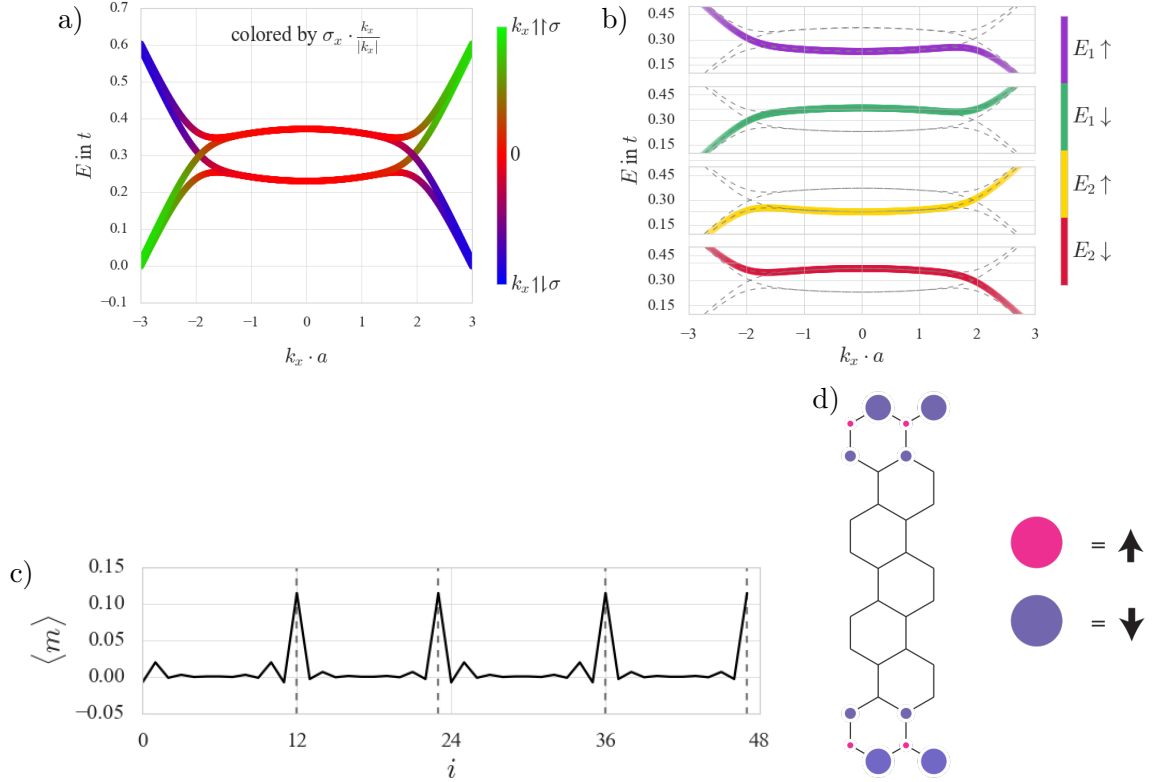
FIGURE 6.2.: a) The dispersion relation of a graphene nanorribon with $N = 12$ rows with $U = 0.6t$ in the ferromagnetic edge phase. The bands are colored according to their bulk chirality. b) The edge chirality $\hat{\sigma}_z \cdot \hat{s}_z$, of the edge states from a). The bands are separated for better visibility and the other states are drawn with dashed lines for comparison. c) The expectation value of the magnetization resolved per lattice site. The four edge atoms are marked with dashed vertical lines. d) A schematic overview of which atoms are polarized by which spin.

the Brillouin zone center follows from a ferromagnetic spin exchange. This will be discussed in the next section in detail.

From a topological standpoint, chiral symmetry is the reason for the occurrence of gap-crossing states [34]. The FM phase exhibits chiral symmetry, because the state of the system with parallel relative spin alignment of the edges remains symmetric when interchanging both sublattices. As a consequence, C_2-rotational symmetry is preserved, which is reflected in the dispersion relation. This can be seen in Fig. 6.2 b), where the dispersion of lower-energy spin-up states at the two edges remains symmetric with reversing the sign of the momentum k_x [262]. The same is true for the other two bands. As the system has explicitly broken time-reversal symmetry, the spin states are not degenerate anymore [49]. The local magnetization

is

$$\langle m_i \rangle = \frac{1}{2} \left(\langle n_{\uparrow,i} \rangle - \langle n_{\downarrow,i} \rangle \right), \tag{6.2}$$

see Fig. 6.2 c). A parallel spin polarization of the two edges is visible, while most of the bulk remains unpolarized. The sites in close vicinity to the edges exhibit a very small spin polarization in the opposite direction, showing the aforementioned locally ferrimagnetic structure. A schematic view of this is depicted in Fig. 6.2 d). The electronic density on the other hand is distributed equally across the sample. Current experimental efforts have not succeeded in verifying magnetic edge states as of yet [262].

6.1.4. Antiferromagnetic Edge Phase

In the AFM phase, both edges exhibit opposing spin polarization with respect to each other, while a locally ferrimagnetic ordering among the sublattices at sites close to each edge is present. Again the spins along each edge are aligned in parallel, but in this phase the total spin magnetic moment is zero. The band structure shows a clear gap. Spin-spatial broken symmetry is required to obtain the AFM solution [49, 263]. As can be seen in Fig. 6.3 a), the dispersion relation of a nanoribbon with $N = 12$ rows and 4 columns at $U = 0.6t$ exhibits a band gap, indicating that the AFM phase is insulating [110]. Similar to the previous two phases, the bulk chirality $\hat{\sigma}_x \cdot \frac{k_x}{|k_x|}$ remains only a good quantum number in the vicinity of the Dirac cones. The band gap near the Dirac points is influenced by the width of the nanoribbon, which will be discussed in Sec. 6.2.1. In one-dimensional systems, no finite-momentum long-range spin-order is expected, when the system exhibits full spin-rotational symmetry [50, 264]. Therefore the AFM phase is not caused by long-range order.

In Fig. 6.3 b) the product of sublattice and real spin expectation values is again used to color each of the states. One can see that the two states where $\langle \hat{\sigma}_z \cdot \hat{s}_z \rangle = -1$ are lower in energy than both with parallel relative sublattice and real spin alignment, $\langle \hat{\sigma}_z \cdot \hat{s}_z \rangle = 1$. Thus, for the two occupied states, the real and sublattice spin are antiparallel. Topologically, the antiferromagnetic exchange interaction acts as a staggered sublattice potential, which introduces a spin-dependent gap with opposite sign for states localized at different edges and thus destroys the topologically insulating phase [26, 265]. The origin of the gap is the broken chiral symmetry [266] originating from the spin polarization of the edges in opposing directions.

In Fig. 6.3 c) the magnetic expectation value of the AFM phase is shown, resolved per nanoribbon site. Similar to the case of the FM phase, the electronic density is equally distributed across the whole sample. A schematic of the distribution of the spin is given in Fig. 6.3 d).
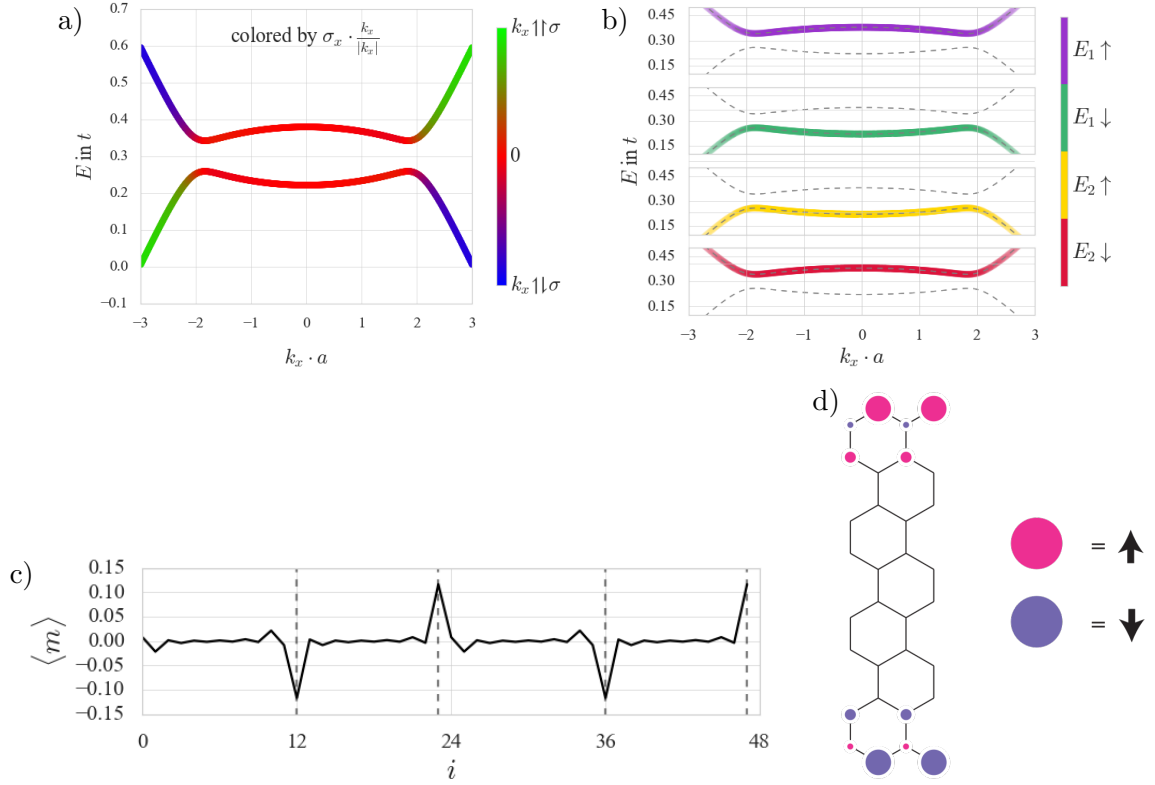
FIGURE 6.3.: a) The dispersion of the four edge states in a graphene nanoribbon with $N = 12$ rows, 4 columns and at $U = 0.6t$ in the antiferromagnetic phase. b) The states are colored by their sublattice spin and real spin quantum numbers. The gap is separating states with opposite edge chirality $\hat{s}_z \cdot \hat{\sigma}_z$. c) The expectation value of the magnetization and density resolved per site. The four edge atoms are marked with vertical dashed lines. d) A schematic overview of which atoms are polarized by which spin.

6.2. Comparison of the two Magnetic Phases

In this section, the two magnetic solutions are compared with each other. The energetic competition of these two phases can be explained by a mechanism called *inter-edge superexchange*, which will be discussed first. Then the magnetization of the edge atoms and the bulk is treated and how it is affected by the interaction strength.

6.2.1. Inter-edge Superexchange

The theoretical model which can be used to describe the theory of superexchange among states localized at different edges of graphene nanoribbons has been discussed in the literature [243, 267] and is reproduced here to analyze the band structures of the two magnetic phases. The Hamilton operator in the mean-field picture for a one-dimensional periodic ribbon with edges takes the form

$$H = \sum_{\langle x,x' \rangle} \sum_{\langle i,j \rangle, \sigma} t_{ij} \hat{c}_{x,i,\sigma}^\dagger \hat{c}_{x',j,\sigma} + U \sum_{x,i,\sigma} \hat{n}_{x,i,\sigma} \langle \hat{n}_{x,i,\bar{\sigma}} \rangle. \tag{6.3}$$

Here the indices i and j are intra-unit cell indices, whereas the indices x and x' label different unit cells along the periodic direction, parallel to the zigzag edges. Without the interactions, a similar Hamiltonian has been examined in-depth in Sec. 3.2.2, but including a periodic and a non-periodic direction is important here for discussing the valence and conduction bands which describe the edge states.

In Eq. 6.3 the annihilation (and creation) operators $\hat{c}_{x,i,\sigma}^{(\dagger)}$ destroy or create a particle at site i in unit cell x with spin σ. For computing the energy of the magnetic phases self-consistently, it is enough to only consider the valence and conduction bands, which is a very good approximation [267]. This can be done by performing the Fourier transformation, where bands other than the valence and conduction bands are projected out via [267]

$$\hat{c}_{x,i,\sigma}^\dagger = \frac{1}{\sqrt{L}} \sum_k e^{-ikx} (\psi_{k,+}^*(i) \hat{c}_{k,\sigma,+}^\dagger + \psi_{k,-}^*(i) \hat{c}_{k,\sigma,-}^\dagger) \tag{6.4}$$

at the same time. The operator $\hat{c}_{k,\sigma,\pm}^{(\dagger)}$ annihilates (creates) a particle in the conduction band $(+)$ or valence band $(-)$ with momentum k and spin σ. The spin-degenerate valence and conduction bands of the non-interacting system have wave functions $\psi_{k,\pm}$. They have the energies defined by $H_k^{U=0} \psi_{k,\pm} = \pm T(k) \psi_{k,\pm}$, where $H = \sum_k H_k$, which leads to the common single-particle dispersion for the edge states shown in the left of Fig. 4.2. The Fourier transformation of the Hubbard interaction term in Eq. 6.3 in a basis similar to Eq. B.1 is diagonal in k.

The valence and conduction bands, which are given by the edge states, can be separated into states localized on the left (L) and right (R) side of the sample. For this purpose the

operators

$$\hat{c}^{(\dagger)}_{k,\sigma,\mathrm{L}} := \frac{1}{2}\left(\hat{c}^{(\dagger)}_{k,\sigma,+} + \hat{c}^{(\dagger)}_{k,\sigma,-}\right) \tag{6.5}$$

$$\hat{c}^{(\dagger)}_{k,\sigma,\mathrm{R}} := \frac{1}{2}\left(\hat{c}^{(\dagger)}_{k,\sigma,+} - \hat{c}^{(\dagger)}_{k,\sigma,-}\right) \tag{6.6}$$

are defined. The wave functions for the states mostly localized on the left or right side of the ribbon are given by $\psi_{k,L} := \frac{1}{\sqrt{2}}\left(\psi_{k,-} + \psi_{k,+}\right)$ and $\psi_{k,R} := \frac{1}{\sqrt{2}}\left(\psi_{k,+} - \psi_{k,-}\right)$ [243], in analogy to the operators in Eqs. 6.5 and 6.6. Then it follows that the two L/R states both have the same energy $T(k)$.

The expectation values of the density operators at each site i of the unit cell are taken as $\langle \hat{n}_{i,\sigma}\rangle = \frac{1}{2} + m^P(i)\bar{\sigma}$, where $m^P(i)$ is the magnetization at each site for phase $P \in$ {FM, AFM}, which is defined below, and $\sigma = \pm 1$ [267]. From the strict localization of the two edge states on different sublattices, it follows that $\psi_{k,L}(i)\cdot\psi_{k,R}(i) = 0$ at every intra-unit cell site i and at each k individually [243]. This leads to the 2×2-Hamiltonian per spin for the FM phase

$$H = \sum_{k,\sigma}(\hat{c}^{\dagger}_{k,\sigma,\mathrm{R}}, \hat{c}^{\dagger}_{k,\sigma,\mathrm{L}})\begin{pmatrix} \frac{U}{2} - \sigma\Delta^{FM}(k) & T(k) \\ T(k) & \frac{U}{2} - \sigma\Delta^{FM}(k) \end{pmatrix}\begin{pmatrix} \hat{c}_{k,\sigma,\mathrm{R}} \\ \hat{c}_{k,\sigma,\mathrm{L}} \end{pmatrix}, \tag{6.7}$$

and for the AFM phase

$$H = \sum_{k,\sigma}(\hat{c}^{\dagger}_{k,\sigma,\mathrm{R}}, \hat{c}^{\dagger}_{k,\sigma,\mathrm{L}})\begin{pmatrix} \frac{U}{2} - \sigma\Delta^{AFM}(k) & T(k) \\ T(k) & \frac{U}{2} + \sigma\Delta^{AFM}(k) \end{pmatrix}\begin{pmatrix} \hat{c}_{k,\sigma,\mathrm{R}} \\ \hat{c}_{k,\sigma,\mathrm{L}} \end{pmatrix} \tag{6.8}$$

in the L/R-basis [243]. The spin splitting at the Brillouin zone center for phase P is defined as

$$\Delta^P(k) := U\sum_i |\psi_{k,L}(i)|^2 m^P(i) \tag{6.9}$$

and the magnetization for each of the phases is given by [243]

$$m^{AFM}(i) := \int_{-\frac{\pi}{a}}^{\frac{\pi}{a}} dk\left(|\psi_{k,L}(i)|^2 - |\psi_{k,R}(i)|^2\right)\mathrm{Pol}(k) \tag{6.10}$$

$$m^{FM}(i) := \int_{-k_0}^{k_0} dk\left(|\psi_{k,L}(i)|^2 + |\psi_{k,R}(i)|^2\right). \tag{6.11}$$

The left-right polarization is given by $\mathrm{Pol}(k)$, which ranges between 0 and 1, and is determined by the self-consistent solution of the mean-field equations for the AFM phase.
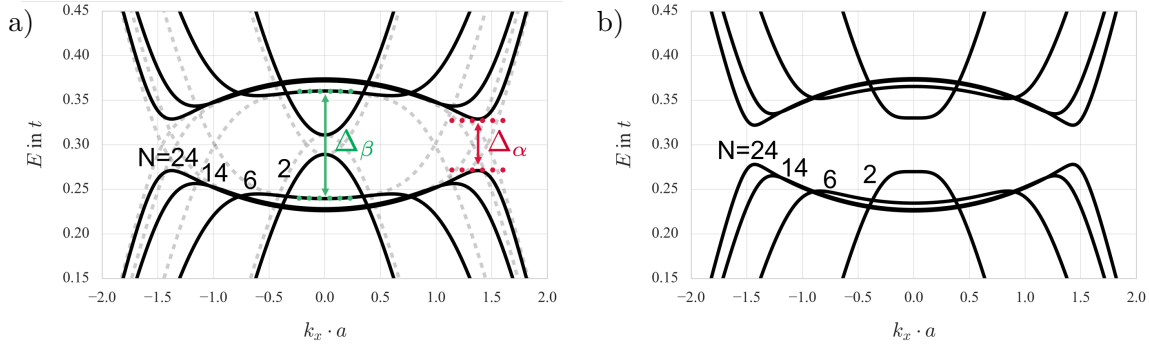
FIGURE 6.4.: Multiple band structures of the edge states for nanoribbons with N rows and $U = 0.6t$. a) The FM phase and b) the AFM phase. The energy of the states crossing the Fermi level are shown in dashed gray lines for better visibility. The two types of gaps Δ_α and Δ_β are shown.

In this model, the off-diagonal entries in Eqs. 6.7 and 6.8, obtained from the non-interacting Hamiltonian, have the effect of an *inter-edge hopping*. This hopping increases for momenta away from the Brillouin zone center and causes a larger mixing of the edge states with identical spins localized on opposite ends of the sample. This is what causes a symmetric-antisymmetric polarization [243], which competes with the left-right polarization at each k. The diagonal entries in Eqs. 6.7 and 6.8 describe the energy splitting due to the different spin polarizations of the self-consistent solutions. If both spin species are included, the Hamiltonian for the AFM phase has the two-fold degenerate eigenenergies $E(k) = \pm\sqrt{\Delta^{AFM}(k)^2 + T(k)^2}$, which are separated by an energy gap. For $|k| < |k_0|$ it is $T(k) \approx 0$, such that $\Delta^{AFM}(k)$ controls the linear combination of valence and conduction bands which forms the occupied states. At the Brillouin zone border, the valence and conduction bands minimize their energy by forming an antisymmetric linear combination due to increased inter-edge hopping as a result of the energy $T(k)$, because for $|k_0| < |k|$ it is $\Delta^{AFM}(k) \approx 0$. The momentum k_0 is used to denote the point where the influence of the two polarizations interchanges [243] and it is important to note, that the AFM phase can minimize its energy at both the Brillouin zone center and border, without crossing the band gap, with the same two occupied states. The gap Δ_α, which will be examined below, is defined at k_0, see Fig. 6.4.

For the FM states, the spin polarization of the states at the Brillouin zone center is governed by $\Delta^{FM}(k)$, leading to the occupation of left-right polarized states with identical spins at each edge. Precisely at k_0 the influence of $T(k)$ becomes larger than that of $\Delta^{FM}(k)$, such that it is again energetically favorable for the occupied states to form antisymmetric states with respect to the inter-edge hopping, but as a result two states must cross the band gap. The occupied bands for $|k| < |k_0|$ do not contribute to $m^{FM}(i)$ because of a lack of spin-polarization. This leads to the four energies $E(k) = \pm\Delta^{FM}(k) \pm |T(k)|$ [243].

The energetic difference of the AFM and FM phase is almost exclusively given by the higher
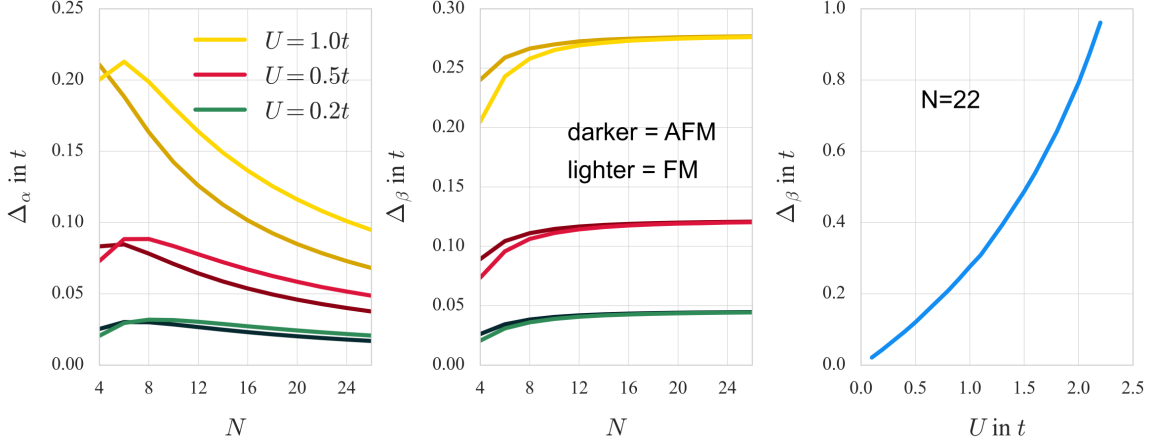
FIGURE 6.5.: left and center: The two gaps Δ_α in the vicinity of the Dirac points and Δ_β at the Brillouin zone center for the two phases AFM (darker shade) and FM (lighter shade) for three different Coulomb interaction strengths $U = 0.2t$, $U = 0.5t$ and $U = t$. The number N of rows is varied. right: The gap Δ_β for $N = 22$ as a function of U.

energy of the two gap crossing states in the vicinity of k_0 [243]. These considerations allow for an analysis of the gaps in the dispersion relations of graphene nanoribbons of different size and interaction strengths. For this, two gaps are defined,

$$\Delta_\alpha := \sqrt{\Delta^P(k_0)^2 + 4|T(k_0)|^2} \tag{6.12}$$

$$\Delta_\beta := 2\Delta^P(0), \tag{6.13}$$

which are depicted in Fig. 6.4 a). Here the band structures for the FM phase (shown in a) and the AFM phase (b) are depicted for $U = 0.6t$ and the number of rows of the nanoribbon is indicated. Since the eigenvalues of the AFM phase are doubly degenerate, which is not the case for the FM phase, where this degeneracy is only occurring at the Brillouin zone center, the appropriate states for comparing the gaps must be chosen. Therefore the choice of the gap crossing bands of the FM phase used for this analysis are marked bold, while the others are depicted via dashed lines. The gap close to the Dirac point Δ_α is defined at the point k_0 in the Brillouin zone where the two bands of the AFM phase exhibit smallest gap, whereas in the case of the FM phase, two edge states (the dashed lines) cross the gap.

Δ_β is defined as the splitting between the pairs of bands at the Brillouin zone center. The gap sizes for Δ_α and Δ_β are shown in Fig. 6.5 (left and center), as a function of the number of rows of the nanoribbon N. Δ_α becomes smaller when N increases because of the size dependence of the inter-edge hopping [243], which has a similar origin as the localization of the edge states in finite size nanoribbons, discussed in Chapter 4. For larger U, Δ_α becomes larger, because of the larger band separation in the Brillouin zone center.
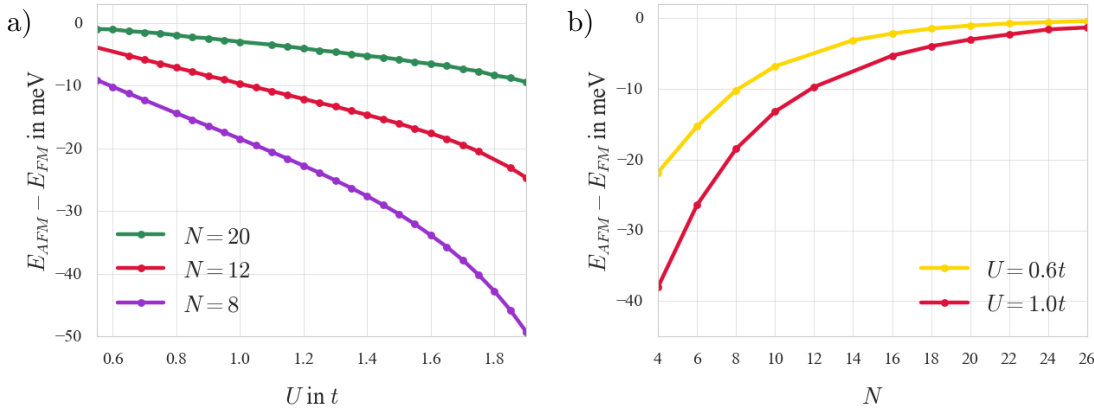
FIGURE 6.6.: a) The energy differences for the magnetic phases AFM and FM as a function of U for three different ribbon sizes N. b) The energy difference of the two magnetic phases as a function of N.

The gap Δ_β is mainly influenced by the magnetization of the lattice. Due to the exponentially small overlap of the edge states in very wide ribbons, it converges to approximately $U m^P$ [237]. The total magnetization of the lattices m^P is slightly different for the two phases, because in the FM phase the magnetization of sites belonging to a single sublattice switches sign at the ribbon center. This is not the case for the AFM phase as was was explained in Secs. 6.1.3 and 6.1.4. As a consequence the magnetization in the FM phase exhibits a domain wall, which causes an overall smaller magnetization, resulting in a smaller gap Δ_β. Therefore this gap is size-dependent - especially in narrow nanoribbons - and becomes nearly identical for both phases in longer ribbons. The increasing size of Δ_β for larger interaction strengths is shown in Fig. 6.5 (right), where Δ_β for nanoribbons of $N = 22$ rows for different U is depicted. The result is numerically identical for AFM and FM phases at the scale of this figure, and the gap in both phases is proportional to U.

6.2.2. Energy of the Magnetic Edge Phases

In this section, the energies of the two magnetic phases are compared. The theorem by Lieb for the ground state of the bipartite lattice in the case of repulsive electronic interactions was already mentioned. More precisely, it states that the ground state at half-filling has a total spin of $|S| = \frac{|B|-|A|}{2}$ [242], where $|A|$ and $|B|$ correspond to the number of sites belonging to the two sublattices A and B. It follows from this, that the ground state at half-filling should always be the AFM edge phase, regardless of ribbon size and for every $U > 0$. In order to verify the magnetic ground state of the system, the energy differences of the two phases are computed for different interaction strengths and ribbon lengths. The energy differences are shown in Fig. 6.6 a) for three different ribbon sizes as U is varied. As can be seen the
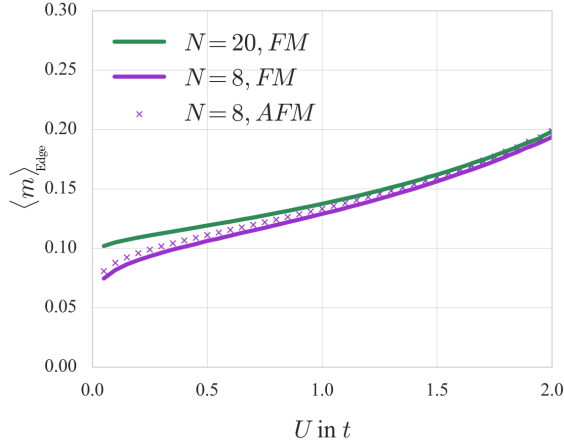
FIGURE 6.7.: The expectation value of $\langle m \rangle_{\text{Edge}}$ for an edge atom in the FM and AFM phase.

energy difference is up to $50\,\text{meV}$ at $U = 1.9t$ for $N = 8$. The AFM phase is always the phase with lower energy, in agreement with Liebs theorem. The smaller edge separation in smaller ribbons, such as $N = 8$, results in a larger energy benefit for the AFM phase, due to the inter-edge superexchange mechanism. The larger N, as can be seen in Fig. 6.6 b), the smaller this energy gain, regardless of U. In the continuum limit both phases become degenerate. This result can also be related to Lieb's theorem, because the ground state at half-filling would still have a vanishing total spin polarization, similar to the AFM phase.

6.2.3. Magnetization at the Edges

In Fig. 6.7 the magnetization $\langle m \rangle_{\text{Edge}} = \frac{1}{2}\left(\langle n_{\uparrow,\text{Edge}} \rangle - \langle n_{\downarrow,\text{Edge}} \rangle\right)$ of an edge site in a nanoribbon for $N = 8$ and $N = 20$ as function of U is depicted for the two magnetic phases. The magnetization becomes larger as U increases, converging to $\langle m \rangle_{\text{Edge}} \simeq 0.2$ for $U \simeq 2.0t$. Since along one edge all sites belong to the same sublattice and exhibit ferromagnetic spin alignment, the staggered magnetization of the AFM and FM phase become comparable. For larger ribbons it is nearly identical for both phases, as explained in a previous section. At $N = 20$, $\langle m \rangle_{\text{Edge}}$ is identical for both phases on the scale of Fig. 6.7, and for $N = 8$ it is only slightly different $(\langle m_{AFM} \rangle - \langle m_{FM} \rangle)/\langle m_{AFM} \rangle = 2.6 \times 10^{-2}$, as previously reported in [50].

6.3. The Non-magnetic Solution at Different Filling Factors

In this section, the energy of the non-magnetic phase is discussed. The computations performed in this work consider the same doping per spin, such that doped solutions with a finite spin magnetic moment are avoided. A half-filled system has a number of particles equal to the number of sites $N' = 4N = 48$. The total doping ΔN of the sample is defined as the occupation difference of the system above or below the half-filled lattice. On the left of Fig. 6.8 a) the dispersion relation of a hole-doped nanoribbon in the nonmagnetic phase is depicted. The doping is $\Delta N = -3.8$ and, for such hole doped system, the edge state dispersion at the Brillouin zone center is bent downwards. On the right of the same figure, the case for electron doping with $\Delta N = 1.74$ indicates an upward bent dispersion. If the doping is increased to $\Delta N = 3.8$, all bands are similar in appearance, but are shifted upwards in comparison. In b) of Fig. 6.8 the electronic densities are depicted for each site of the lattice. For hole doping, the electronic densities of all lattice sites are reduced from half-filling and the edge sites exhibit prominent gaps in the electronic densities, while for electron doping the electronic density is slightly elevated in the bulk and the edge sites show clear peaks. On the right of the figure, the electronic density per spin of a bulk site ($i = 8$) is shown at $U = 1.0t$ for different electron doping. A strong proportionality on ΔN is observed.

6.3.1. Energy of the Non-magnetic Phase

Next, the influence of doping on the internal energy of the non-magnetic phase is examined. For this, the Hubbard model Hamiltonian, Eq. 5.9 is considered before the mean-field approximation. The single-orbital model at filling of $\frac{1}{2}$ per site can be rewritten as [268]

$$
\begin{aligned}
H_{pp}^{ee} &= U \sum_i \left(\hat{n}_{i\sigma} - \frac{1}{2} \right) \left(\hat{n}_{i\bar{\sigma}} - \frac{1}{2} \right) \\
&= U \sum_i \hat{n}_{i\sigma} \hat{n}_{i\bar{\sigma}} - \frac{U}{2} \sum_i (\hat{n}_{i\sigma} + \hat{n}_{i\bar{\sigma}}) + \frac{UN'}{4}.
\end{aligned}
\tag{6.14}
$$

Here i is the site index. While the chemical potential is set to zero, a shift of the Fermi energy E_F by $\frac{U}{2}$, due to the half-filling condition, is evident in this form of the Hamiltonian. Furthermore, an energy shift of $\frac{UN'}{4}$ is obtained. The energy shift for a doped compared to a half-filled system can be derived with a filling per spin of $\frac{1}{2} + \frac{\Delta N}{2N'}$. Here the total doping per lattice ΔN is divided in equal amounts on each site and spin. Then the energy shift of the doped system is not $\frac{UN'}{4}$ anymore, but a polynomial quadratic in ΔN, given by

$$
E(U, \Delta N) = \frac{UN'}{4} + \frac{U\Delta N}{2} + \frac{U\Delta N^2}{4N'}.
\tag{6.15}
$$

The energy of a doped nanoribbon with $N = 8$ and $U = 0.6t$ is shown in Fig. 6.9 a). Around $\Delta N = 0$ there is a region, where the energy is nearly linearly depending on ΔN.
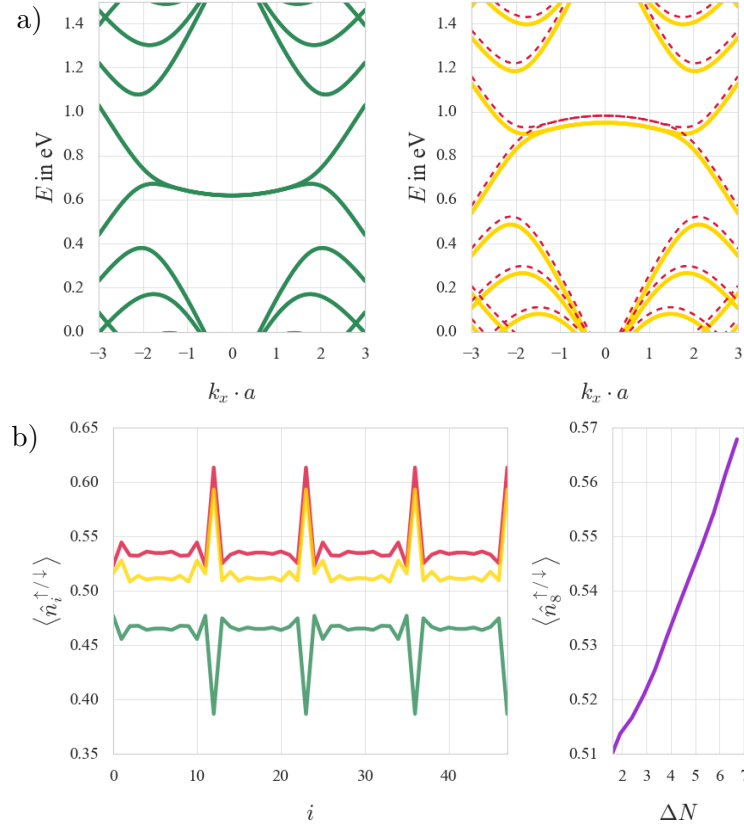
FIGURE 6.8.: a) left: The dispersion relation of a nanoribbon with $N = 12$ with p_z-orbitals where $U = 1.6t$ and $\Delta N = -3.8$. right: The same system with $\Delta N = 1.74$ (yellow) and $\Delta N = 3.8$ (red). b) left: Density expectation values with $N = 12$, with $U = 1.6t$ and $\Delta N = -3.8$ (green), $\Delta N = 1.74$ (yellow) and $\Delta N = 3.8$ (red). right: Density of expectation value of a bulk site $i = 8$ for $U = 1.0t$ shows a quadratic dependency on ΔN.

At approximately $|\Delta N| > 1.3$, however, a stronger quadratic dependency on the doping is observable. This separates the effect of doping into two different regimes. As a consequence, there is a preferred amount of doping, which is energetically favorable and given at the transition point $\Delta N \approx -1.3$ from one regime into the other. In Fig. 6.9 b) different dispersion relations are depicted to illustrate the two different regimes.

The energy in each case is shifted to coincide with the Fermi energy, such that $E - E_F = 0$ in each case. Increasing the filling of the lattice in equal amounts, shifts the Fermi energy in nearly equal steps for up to a doping of $\Delta N = 0.96$. Due to finite size effects at a finite doping of around $\Delta N = 1.28$ the Fermi energy is shifted by a much larger amount than for the weaker cases. The results can be compared to those for even larger doping in Fig. 6.8 a), where larger energy shifts are also observable. The reason for the finite size effects is, that enough
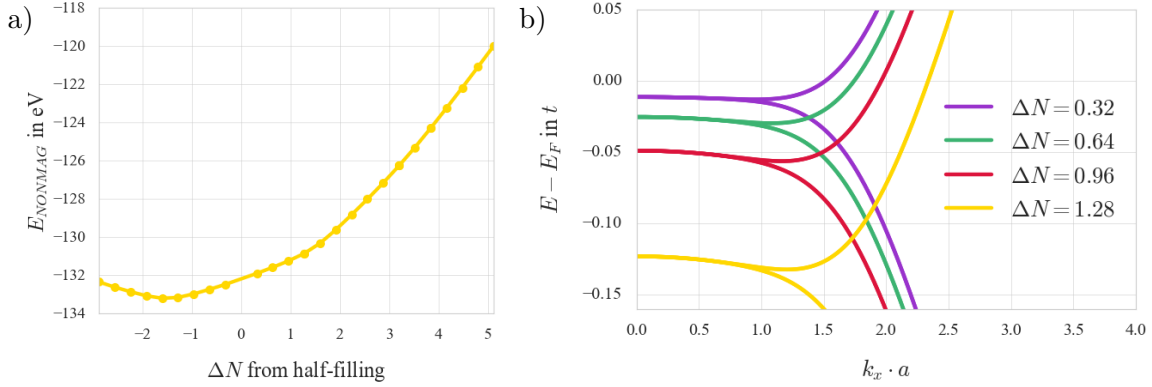
FIGURE 6.9.: a) The energy of the non-magnetic phase for different amounts of doping for $N = 8$ and $U = 0.6t$. b) Dispersion relations for different amounts of doping for the same system. The Fermi energy of all phases is shifted to coincide with $E = 0$ in the plots.

doping is introduced, such that the bulk bands at the Dirac cones also become filled, which changes the energy dependency of the doped nanoribbons from weakly quadratic to strongly quadratic, as shown in Fig. 6.9 a). This is more evident, when a quadratic polynomial of the form

$$E(U, \Delta N) = a_1(U)\Delta N^2 + a_2(U)\Delta N + a_3(U). \tag{6.16}$$

is fitted against this data. Linear functions can be used for the three functions $a_1(U)$, $a_2(U)$ and $a_3(U)$, such that

$$a_j(U) = a_{j1} \cdot U + a_{j2} \tag{6.17}$$

for $j \in \{1, 2, 3\}$. Apart from finite size effects, such as the k-space resolution of the computations, which translate to numeric errors in the fitting parameters, the predictions of Eq. 6.15 are met quite well. The term a_{32} in Eq. 6.16 is given by the system without interaction and is very close to the energy of the two magnetic phases. The term a_{31} is fitted to be equal to $\frac{N'}{4}$. The terms $a_{21} = \frac{1}{2}$ and $a_{22} = 0$, are achieved by the fitting very well. The term $a_{11} = \frac{1}{4N'}$ is also reproduced.

The term a_{12} on the other hand is not present in the energy shift in Eq. 6.15, but obtained as result of the fit. It is independent of the interaction strength and only denotes the energy shift due to increased doping. It is $\sim N'^{-1}$, similar to a_{11}, but originates from the filled bulk bands in the band dispersion of the nonmagnetic phase as a consequence of the doping.

In Fig. 6.10 the energy dependency of the doped solution for a constant doping per site of $\frac{\Delta N}{N'} = 0.041$ is shown. For all U the energy shows a linear relation to N', because the first term of the energy shift in Eq. 6.15 is linear in N' and the most dominant. The second term is constant for constant U and ΔN, and the last term ΔN^2 is $\sim N'^{-1}$, such that it becomes less relevant for the energy of larger ribbons.
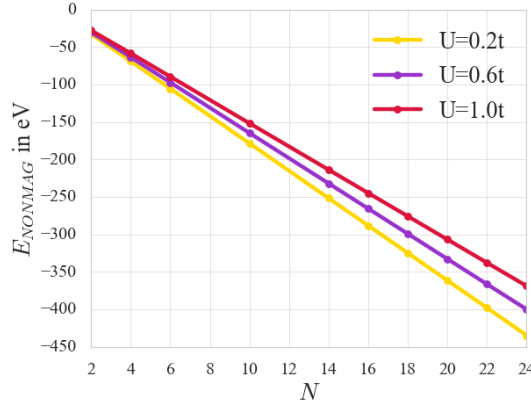
FIGURE 6.10.: The energy of the non-magnetic phase for constant doping per site $\frac{\Delta N}{N'} = 0.041$ for varying length and different interaction strengths $U = 0.2t$, $0.6t$ and t.

6.3.2. The Fermi Energy

The two regimes of doping discussed in the last section, also show in the Fermi energy. For strong doping of $|\Delta N| > 2$ and for different U the Fermi energy is shown in Fig. 6.11 a). A function $\arctan(\Delta N)$ fits very well to the data, which is indicated in the figure. For zero doping, the Fermi energy would correspond to that of the magnetic phases, shown by a horizontal bar in the figure. For smaller doping, however, the Fermi energy exhibits a different dependency, namely $\tan(\Delta N)$, given in Fig. 6.11 b). Here the dashed lines show the dependency of the larger doping, where the transition point of the two regimes is at approximately $|\Delta N| > 1.3$.

The different behavior of the Fermi energy in the two doping regimes can be understood in the light of the density of states, which was discussed at the hands of Fig. 3.4 for ribbons without electronic interactions. The small doping regime corresponds to the peak around $E/t = 0$, which is also occurring in the non-magnetic phase of graphene. Once larger doping is considered, the Fermi energy is moved away from the central peak, such that the Dirac cones start to become filled. In two-dimensional graphene, this behavior would follow $E_F(\Delta N) = v_F \hbar \sqrt{\pi \Delta N}$ [269]. Due to the very small system considered here, the Dirac cones consist of only a few bands, such that $\arctan(\Delta N)$ fits better to the data for the larger doping regime. For the smaller doping regime, the $\tan(\Delta N)$ behavior is similar in appearance to that of the zeroth Landau level in graphene samples with a magnetic field [269].

In very large, but finite size nanoribbons, the amount of doping at which the bulk states at the Dirac points become filled, becomes very small, due to the small separation of the bulk energy bands, which reduces the small-doping regime to only a very narrow interval of doping.
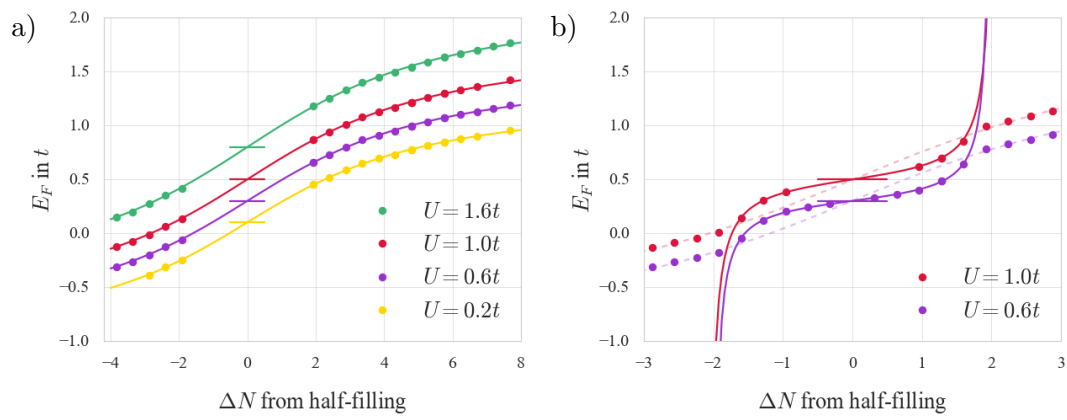
FIGURE 6.11.: a) The Fermi energy for $N = 8$, different U and larger doping can be fitted to $\arctan(\Delta N)$. b) For smaller doping the Fermi energy can be fitted via $\tan(\Delta N)$. The dashed lines correspond to the larger doping fit. The horizontal bars indicate the Fermi energy of the two magnetic phases at half-filling, respectively.

6.4. The Two Magnetic Phases in the Multi-orbital Tight-binding Model
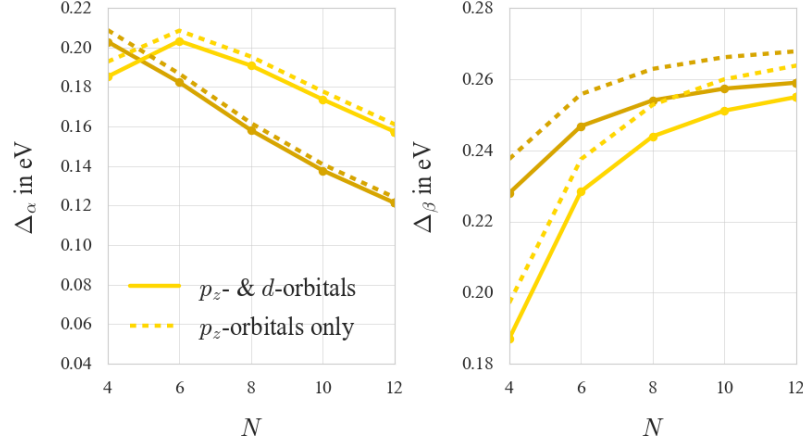
FIGURE 6.12.: The two different band splittings indicated in Fig. 6.5 for the FM (lighter) and AFM (darker) phases in a multi-orbital model at $U = t$ and $V = J = 0$ for nanoribbons of different sizes. The results from the single orbital case (dashed) are also shown.

In this section, the multi-orbital results including the d_{xz}- and d_{xy}-orbitals and intrinsic spin-orbit coupling with $\xi_d = 0.8\,\text{meV}$ are presented. For this, nanoribbons of $N = 8$ are used, because qualitatively no different behavior is expected for larger ribbons. First, the change of the dispersion relation of the two magnetic phases is compared with the single-orbital model. Then the d-orbital occupation of the two magnetic phases is examined and lastly the magnetic ground state in the multi-orbital model is discussed.

6.4.1. Δ_α and Δ_β

The energy splittings Δ_α and Δ_β in the dispersion relation of the single-orbital model have been defined in Fig. 6.4 a) and are reexamined here again in light of the new model. As a consequence of the presence of the d-orbitals in the system, Δ_α and Δ_β for the multi-orbital model become reduced, which is shown in Fig. 6.12. Electrons partly occupying the d-orbitals, rather than the p_z-orbitals, are not only subject to the electronic interaction of strength $U = t$, but also of the d-orbital repulsion and exchange parameters, which are given by $V = 0$ and $J = 0$ in this case. As a consequence of the finite d-orbital occupation, the effective U of the electrons occupying mostly the p_z-orbitals is a little smaller than in the single-orbital model, resulting in a reduced separation of the energy bands, on the order of $10\,\text{meV}$. This will be shown in the next section by examining the multi-orbital Hamiltonian.

The strength of the intrinsic spin-orbit coupling for varying values up to $\xi_d = 16\,\text{meV}$
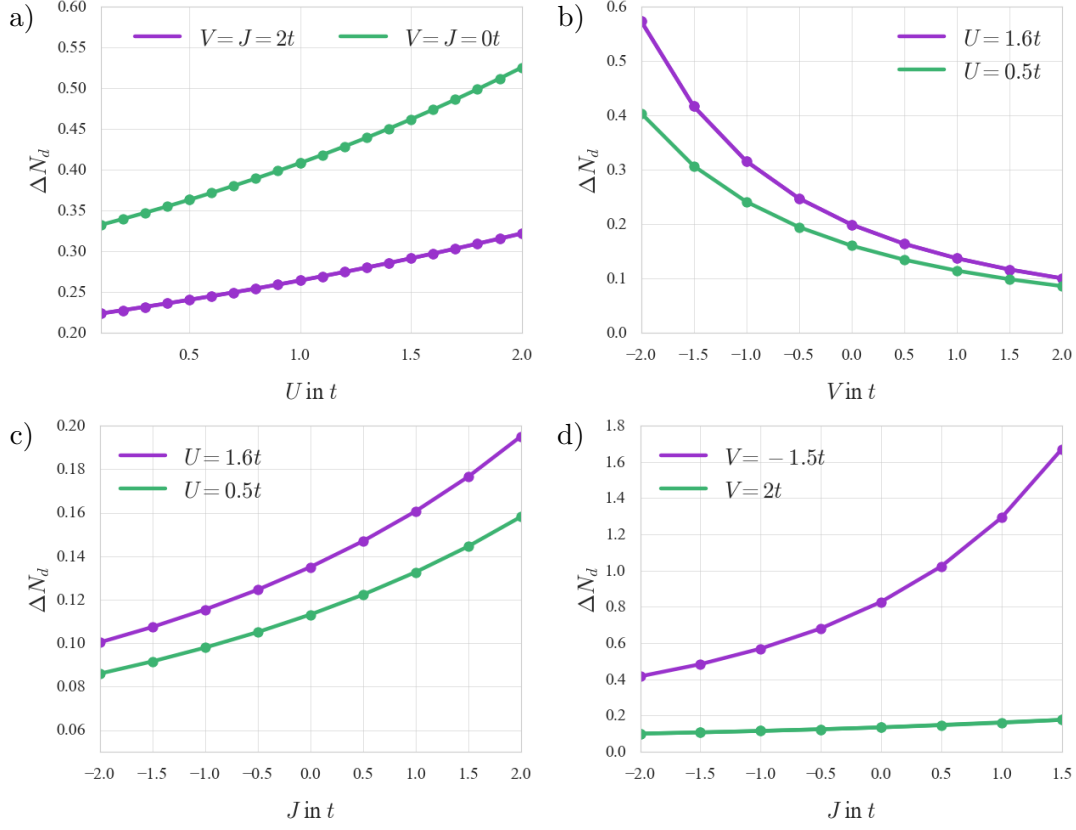
FIGURE 6.13.: Total d-state occupation of a ribbon with $N = 8$ plotted for different interaction strengths. Both FM and AFM phase have identical occupation in each case.

is found to not lead to any numerical differences compared to the results obtained here. This can be understood in light of the effect of the electronic interactions, which are on the 100 meV-scale. The interactions overshadow any effect on the sub-meV scale, which is the expected energy scale of the gap opening from the intrinsic spin-orbit coupling. Therefore, the parameter ξ_d is kept fixed at 0.8 meV in the following computations.

6.4.2. d-state Occupation

The finite d-state occupation depends in the electronic interaction, which is discussed in the following. In order to derive how the occupation of the d-orbital depends on the electronic interactions, the procedure in Eq. 6.14 must be applied to the d-orbital Hubbard Hamiltonian Eq. 5.14. For this the Hamiltonian is again considered before the mean-field approximation. At half-filling the p_z-orbitals have an occupation per site and spin of $\frac{\Delta N_p}{2N'} = \frac{1}{2} - \epsilon$ and the d-orbitals of $\frac{\Delta N_d}{2N'} = \epsilon$ for some small $\epsilon > 0$. This leads to a shift of the d-orbital energy,

proportional to $2V - J$ from E_d, because for the electronic interactions per site in the d-orbitals follows that

$$H_d^{ee} = \sum_{n,\sigma} \left[V \left(\hat{n}_{p\sigma} - \frac{\Delta N_p}{2N'} \right) \left(\hat{n}_{n\bar{\sigma}} - \frac{\Delta N_d}{2N'} \right) + J\hat{c}_{p\sigma}^\dagger \hat{c}_{n\bar{\sigma}}^\dagger \hat{c}_{p\bar{\sigma}} \hat{c}_{n\sigma} \right.$$

$$\left. + (V - J) \left(\hat{n}_{p\sigma} - \frac{\Delta N_p}{2N'} \right) \left(\hat{n}_{n\sigma} - \frac{\Delta N_d}{2N'} \right) \right] - E_d \sum_{n,\sigma} \hat{n}_{n\sigma} \tag{6.18}$$

$$= \sum_{n,\sigma} \left[V\hat{n}_{p\sigma}\hat{n}_{n\bar{\sigma}} + J\hat{c}_{p\sigma}^\dagger \hat{c}_{n\bar{\sigma}}^\dagger \hat{c}_{p\bar{\sigma}} \hat{c}_{n\sigma} + (V - J)\hat{n}_{p\sigma}\hat{n}_{n\sigma} \right] - \sum_{n\sigma} \left(E_d + \frac{\Delta N_p}{2N'} \left(2V - J \right) \right) \hat{n}_{n\sigma}$$

$$- \sum_{n\sigma} \frac{\Delta N_d}{2N'} \left(2V - J \right) \hat{n}_{p\sigma} + \sum_{n\sigma} \left(2V - J \right) \frac{\Delta N_p}{2N'} \frac{\Delta N_d}{2N'}. \tag{6.19}$$

The index n labels the different d-orbitals. An additional site index i is omitted here, similar to previous discussions, but by including a sum over this index the multi-orbital equivalent of Eq. 6.14 is obtained. The three terms inside the first sum in Eq. 6.19 are given by the Hubbard Hamiltonian for the d-orbitals. The last term in the first line is the shifted d-orbital energy. The first term of the second line is a shift of the Fermi energy, affecting mostly the energy of the p_z-orbitals. The last term is a total energy shift, due to the finite occupation of both p- and d-orbitals.

The influence of the parameters V and J on the numerical results are discussed next. When V and J are kept constant, an increasing U leads to an increased occupation of the d-orbitals, shown in Fig. 6.13 a). The occupations for both AFM and FM phases are identical. When the electronic interactions V and J are reduced, the occupation of the d-orbitals becomes larger, because the electrons have lower interaction energy in this case. If the interaction is increased to $V = 2t$ and $J = 2t$, this occupation becomes much smaller. In b) of the figure, it is shown that regardless of U the d-state occupation is reduced with increasing V. Furthermore, the occupation becomes nearly identical for both U, when $V = 2t$. This effect is reversed when changing J, due to the opposite sign in the Hamiltonian in Eq. 6.19. Furthermore, its influence on the occupation is smaller than that of V, as can be seen in c). Since the effect of V on the d-state occupation is dominant, as shown in d), the effect of J depends on it. For negative V, the d-state occupation is large, such that changing J has a large influence. If V is large and positive, the d-state occupation is very small and changing J has nearly no influence.

The d-orbital occupation affects the magnetism of the different sites in the ribbon only slightly, as is shown in Fig. 6.14 for the AFM phase in an $N = 12$ ribbon. Here the occupation of p-orbitals and d-orbitals is computed per site and spin, as well as the magnetization per site and spin for two cases $V = 2t$ and $V = -2t$. The overall qualitative picture of the single-orbital results for the AFM phase is not changed, but the finite occupation of d-orbitals, leads to a nearly constant occupation of the bulk, which is reduced at the edge sites. The density variation in $\langle n_d \rangle$ is only visible, when the d-orbital occupation is enhanced by $V = -2t$ (red),
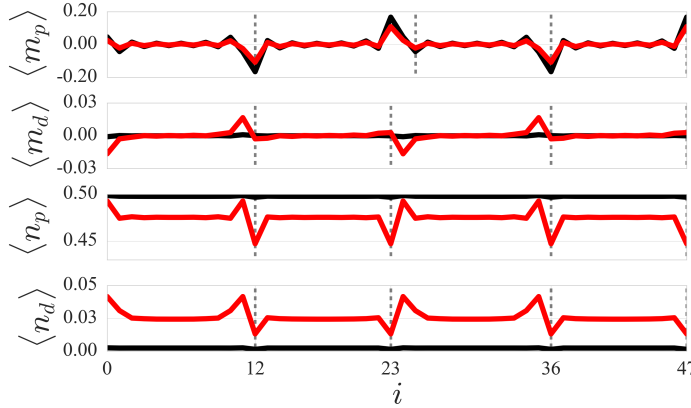
FIGURE 6.14.: The expectation value of magnetization per site and occupation per site and spin for $N = 12$, $U = 1.6t$ and $J = 0.5t$ for $V = -2t$ (red) and $V = 2t$ (black).

otherwise the single-orbital result is reproduced, where no density variation is observed in the sample.

6.4.3. Magnetic Ground State

Next, the energy difference of the two magnetic phases is computed and compared to the single-orbital results. The d-orbitals affect the two magnetic phases in the same way. One indicator for this is that both phases have an identical d-orbital occupation for any combination of p_z-orbital repulsion U, d-orbital repulsion V and exchange J, as was discussed in the previous section.

Therefore, the energy shift of the magnetic solutions due to the d-orbital occupation in the last term in Eq. 6.19 is the same for both phases. The direct consequence is that no combination of $U > 0$, $V > 0$ and $J > 0$ is expected to lead to an FM ground state which would oppose the single-orbital result for Lieb's theorem. The only possibility for $U > 0$ to reach a magnetic ground state with finite spin magnetic moment would be having $V < 0$, such that an increased d-orbital occupation and interaction strengths thereof could dominate the p-orbital interaction. Then Liebs theorem for attractive interactions could lead to a ground state with finite spin magnetic moment, even though $U > 0$.

In Fig. 6.15 a) the energy difference of the AFM and FM phase for $N = 8$ for varying U is shown, alongside the single-orbital result (dashed line). Here $V = J = 0$, such that the system differs from the single-orbital model only by the presence of the d-orbitals, which is shown to have a negligible influence for $U \leq 1.5t$. For higher interaction strengths the energy of the p_z-orbitals is shifted up, such that the energy difference is influenced on the order of meV, due to the reduced occupation of the p-orbitals and the resulting smaller spin splitting at the Brillouin zone center. In b) the length N of the ribbon is varied for $U = t$,
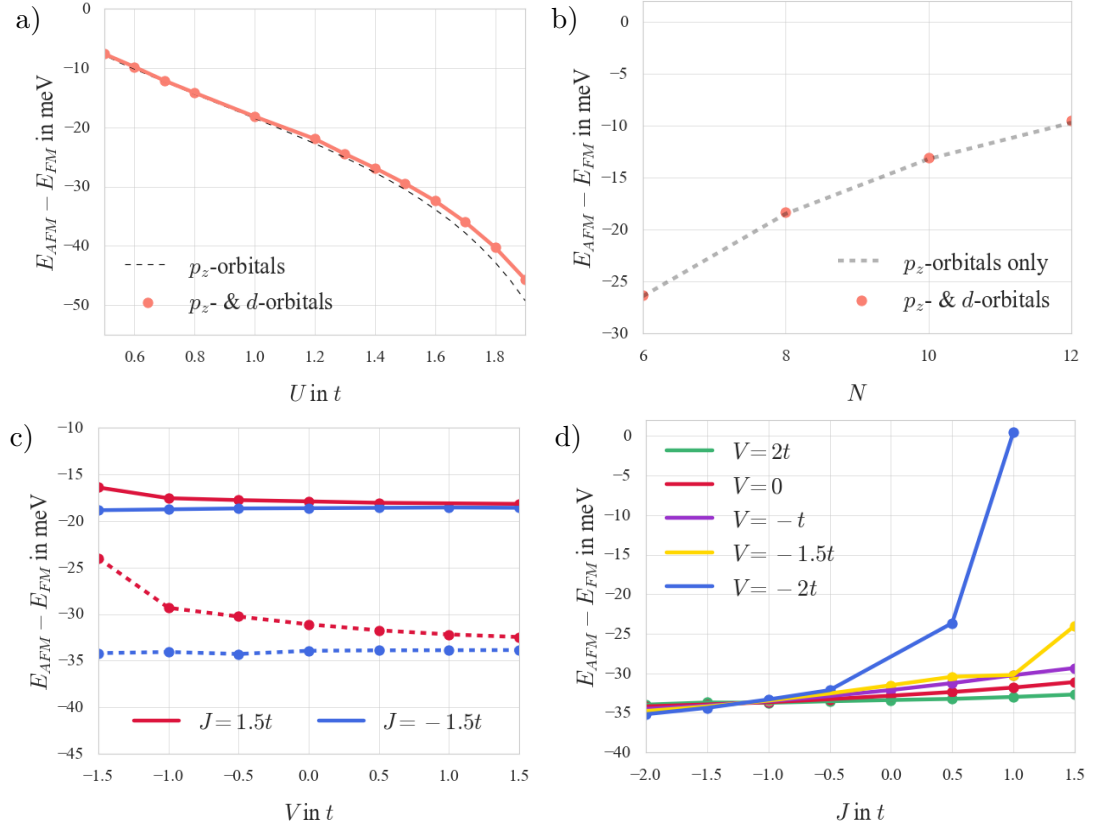
FIGURE 6.15.: The energy difference of AFM and FM phase. The single-orbital results are given by the dashed lines as comparison. For $N = 8$ and a) different U, where $V = 2t$ and $J = 2t$. b) For $U = t$ and $J = V = 0$. c) $U = 1.6t$ (dashed) and $U = t$ (solid), $J = \pm 1.5t$ and for different V. d) $U = 1.6t$, for different V as a function of J.

again where $V = J = 0$, showing no effect at these interaction strengths whatsoever. In c) the energy difference for $U = 1.6t$ (dashed) and $U = t$ (solid) with varying V shows that an increased U leads to the aforementioned increased effect of the d-orbitals, which is strongest for negative V and positive J. This constellation leads to a diminished energy difference of the AFM and the FM phases, but is not enough to lead to an FM ground state. In d), the influence of the d-orbitals is increased, by setting $V = -2t$, such that in combination with $J = t$, the two phases become identical in energy. Again the similar roles of J and V are observed, but with differences in their impact. For larger $J > t$, no solution of the mean-field computations could be obtained, because bulk states become energetically close to the edge states at these interaction strengths.

In conclusion, Lieb's theorem is fundamentally protected by the band structure differences between AFM and FM phases. The only way to make the FM phase energetically favorable
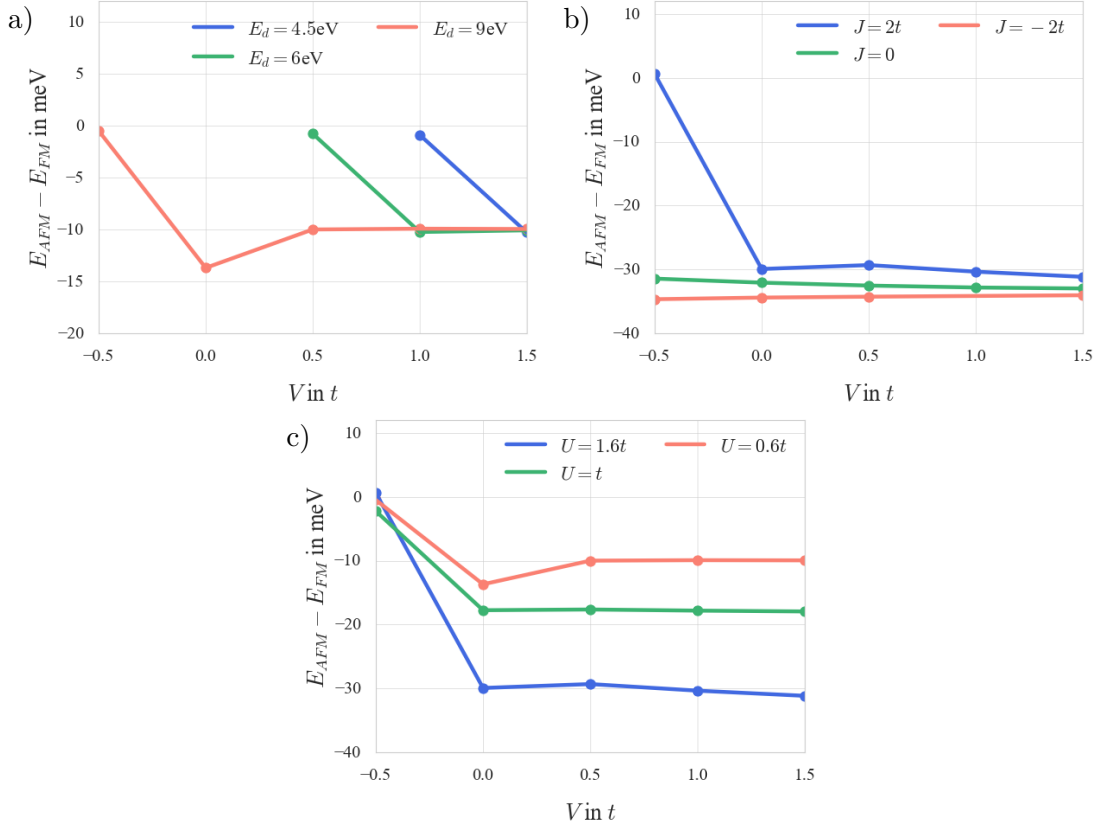
FIGURE 6.16.: Energy differences between FM and AFM phases for $N = 8$, when the d-orbital separation E_d from the p_z-orbitals is varied. a) $J = 2t$ and $U = 0.6t$ b) $E_d = 9\,\text{eV}$ and $U = 1.6t$ c) $E_d = 9\,\text{eV}$ and $J = 2t$.

is to have $V < 0$, such that enough bulk states are created in the band gap, which leads to an entirely different system with different states, where the AFM phase with the same properties as described in the beginning of this chapter is likely not to occur. This case is out of the scope of this thesis, however.

6.4.4. The d-orbital energy separation E_d

A way to increase the d-orbital occupation, other than changing the electronic interaction strengths, is to have a lower d-orbital energy separation E_d from the p_z-orbitals. This would not correspond to graphene anymore, where $E_d = 12\,\text{eV}$. Then the FM and AFM phases would become energetically close already for smaller $V < 2t$. This is shown in Fig. 6.16 a), where E_d is decreased and V varied for constant U and J. One can clearly observe, how a smaller $E_d = 9\,\text{eV}$ requires only $V = -0.5t$ for the two phases to have identical energy, and

a much smaller $E_d = 4.5\,\text{eV}$ allows this even for positive V. For $E_d = 9\,\text{eV}$ a positive J has a larger influence, than for $E_d = 12\,\text{eV}$, which can be seen when Fig. 6.16 b) is compared to the results in Fig. 6.15 d). While a larger U generally leads to a larger energetic difference between the two phases in favor for the AFM phase, a critical value of $V = -0.5t$ has the same influence on the energy difference in all cases. This is shown in Fig. 6.16 c) for $J = 2t$. No self-consistent solution could be obtained where $E_{FM} < E_{AFM}$, such that the data points in Figs. 6.16 a) are only given in a limited range of V.

These findings indicate, that the d-orbital energy shift in the second term of Eq. 6.19 is directly impacting the d-orbital energy separation E_d, as predicted. The lowering of the d-orbital energy closer to the Fermi level changes the valence and conduction bands, because the hybdridization with the π-bands changes their dispersion, such that the relative energy of the two magnetic phases is affected.

6.5. The Non-magnetic Phase in the Multi-orbital Tight-binding Model

6.5.1. d-state Occupation and Energy of the Non-magnetic Phase

In this section, the energetic dependency of the non-magnetic phase is analyzed, similar to the single-orbital case, but with the added complexity of different occupation of different orbitals. In Fig. 6.17 a) the energy of the non-magnetic phase for $N = 8$ is depicted for different doping levels. Here U and J are kept constant. A positive V raises the energy and negative V lowers it. In Fig. 6.17 b) the effect of variation of J shows the opposite behavior and a much weaker influence. A quadratic dependency is given in both cases, which fits the data very well. The energy minimum is not at zero doping, but between $\Delta N = -2$ and $\Delta N = -1$, corresponding to significant hole doping.

In order to analyze the energetic dependency of the nonmagnetic phase, the d-orbital occupation ΔN_d for some doping ΔN is discussed. The result is shown in Fig. 6.18 a), where a negative V again leads to significant occupation of d-orbitals, because of the lower energy separation from the p_z-orbitals in this case. In Fig. 6.18 b) and c) the energy of the non-magnetic phase from Fig. 6.17 is plotted against the occupation ΔN_d, showing a quadratic dependency of the energy in both cases. The overall energy is only slightly influenced by the different interaction strengths V and J and behaves very similar, while only the d-orbital occupation differs. Next, the d-orbital occupation is expressed as a quadratic polynomial in V and in the total doping ΔN, which leads to

$$\Delta N_d(V, \Delta N) = \Delta N^2 \left(\sum_{\alpha=0}^{2} a_{2,\alpha} V^\alpha \right) + \Delta N \left(\sum_{\alpha=0}^{2} a_{1,\alpha} V^\alpha \right) + \sum_{\alpha=0}^{2} a_{0,\alpha} V^\alpha. \tag{6.20}$$

The constants $a_{i,j}$ for $i, j \in \{0, 1, 2\}$ are given by fitting the polynomial to the data in Fig. 6.18 a).

For an understanding of the energy shift due to the electronic interactions, the last term in Eq. 6.19 is considered away from half-filling, which is then added to the energy shift of the p_z-orbitals in Eq. 6.15, where the d-orbital and p-orbital occupations are expressed by the doping ΔN. Thus, the p_z-orbital occupation per site and spin $\frac{\Delta N_p}{2N'}$ is replaced by $\frac{1}{2} + \frac{\tilde{\Delta} N_p}{2N'}$, where the latter term denotes the amount of doping $\frac{\Delta N - \Delta N_d}{2N'}$ in the p_z-orbital. Then the total occupation of each site per spin is $\frac{1}{2} + \frac{\Delta N}{2N'} = \frac{1}{2} + \frac{\tilde{\Delta} N_p}{2N'} + \frac{\Delta N_d}{2N'}$. The energy of the non-magnetic phase is obtained by summing over the two d-orbitals n, the two spins σ and over N' sites, resulting in

$$E(\Delta N, U, V, J) = \frac{UN'}{4} + \frac{U(\Delta N - \Delta N_d)}{2} + \frac{U(\Delta N - \Delta N_d)^2}{4N'}$$
$$+ (2V - J) \left(\frac{1}{2} + \frac{\Delta N - \Delta N_d}{N'} \right) \Delta N_d. \tag{6.21}$$
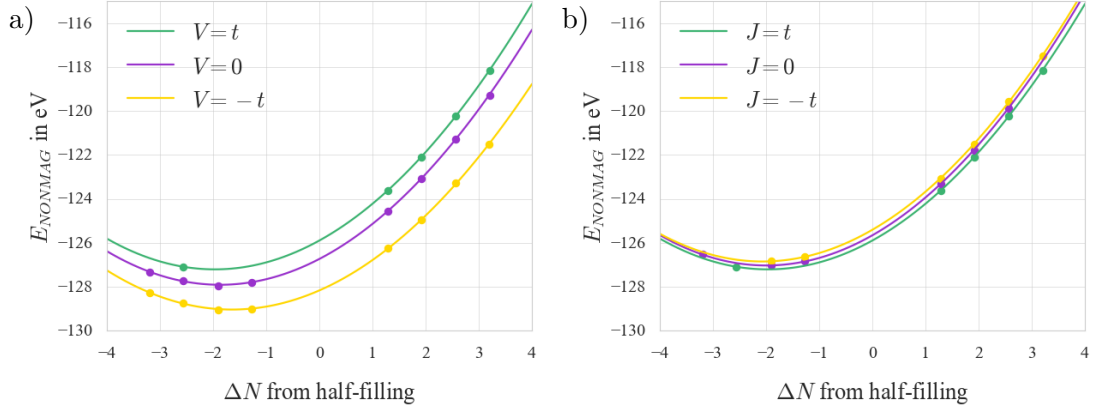
FIGURE 6.17.: The energy of the non-magnetic phase for different doping ΔN of the lattice for $N = 8$. It is $U = t$ and $J = t$ (a) or $V = t$ (b).

It is important to note that this energy does only depend on the total doping ΔN, as ΔN_d is directly related to the total doping via Eq. 6.20. For constant U and J, Eq. 6.21 can be simplified to a function, in appearance very similar to Eq. 6.20, resulting in a polynomial in ΔN and V, where cubic and higher terms can be neglected.

The derived energy shift of the non-magnetic phase in Eq. 6.21 only relies on a fit with the d-orbital occupation, but allows to predict the magnitude of the impact on the energy due to the different electronic interaction strengths very well. Similar to the discussion regarding Eq. 6.16, a term $\sim \Delta N^2$, which is independent of any interaction U, V or J occurs in the fit, but not in the model. As before, this term arises from the strong doping, which is independent of the interaction strength, because bulk states are filled. Thus, neither the presence, nor interaction strength of the d-orbitals lead to a considerable physical consequence for the non-magnetic phase, similar to what was already found for the two magnetic phases at half-filling.

6.5.2. The Fermi Energy

As a consequence of the d-orbitals in the system, electron-hole symmetry is broken, which leads to an asymmetry in the Fermi energy, for different amounts of doping. This can be seen for different V in Fig. 6.19 a) and for different J in b) at around $\Delta N = \pm 1$. The single-orbital result is shown as dashed curve as well. One can see that $V = -t$ has a lower Fermi energy for all doping strengths, compared to $V = 0$ and $V = t$. This is understood with the influence of the d-orbital occupation on the Fermi energy in Eq. 6.19. In the other figure, $J = t$ has a lower Fermi energy than $J = -t$, while all multi-orbital results are lower than the single-orbital results in general. Together with the energy shift from the electronic interactions in the p_z-orbitals in Eq. 6.15, the overall influence of the electronic interactions
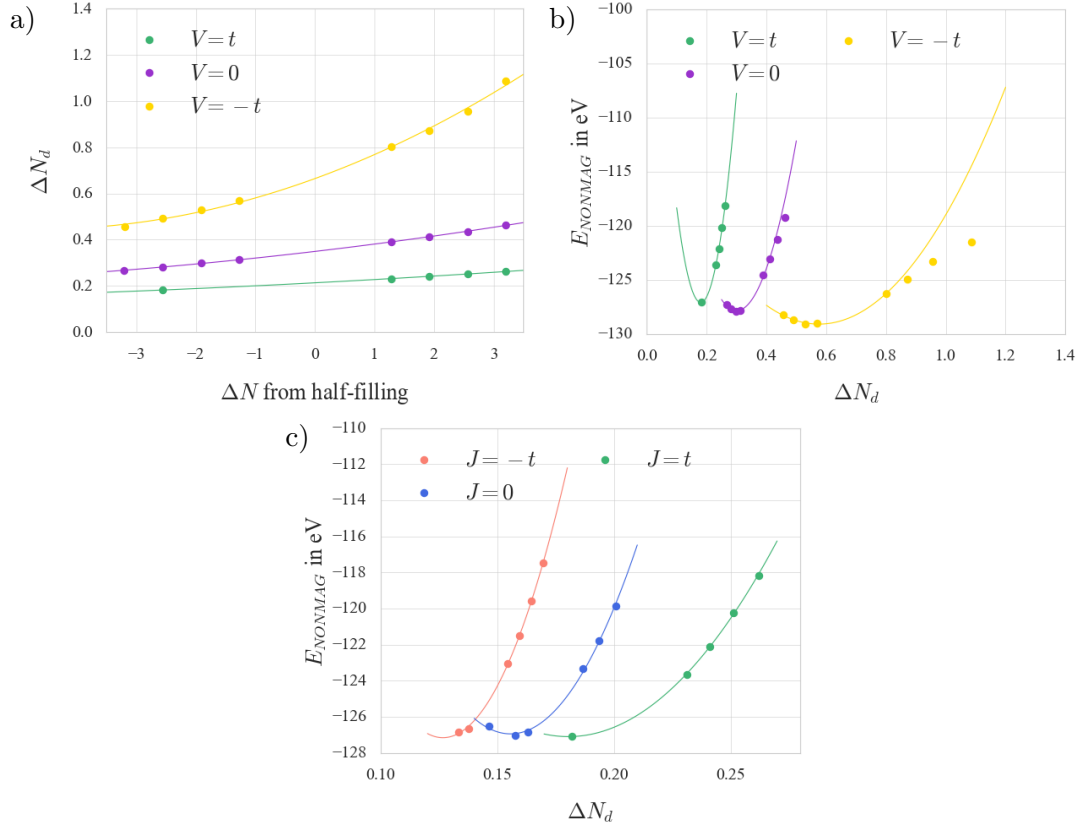
FIGURE 6.18.: a) Total d-state occupation of an $N = 8$ nanoribbon, for $U = t$ and $J = t$ for different V. b) and c) The energy of the non-magnetic phase for the same system plotted against the d-state occupation. Quadratic fits are indicated by the lines in the three figures.

on the Fermi energy is given by

$$E_F = \frac{U \Delta N_p}{2N'} + \sum_n \frac{\Delta N_d}{2N'} \left(2V - J\right). \tag{6.22}$$

Since $\Delta N_p < \Delta N$, the first term of Eq. 6.22 is smaller in the multi-orbital model than in the single-orbital case, resulting in the overall smaller Fermi energy. The second term is much smaller than the first, because $\Delta N_d \ll \Delta N_p$. A negative V and positive J lower the Fermi energy, in agreement with the numerical calculations.
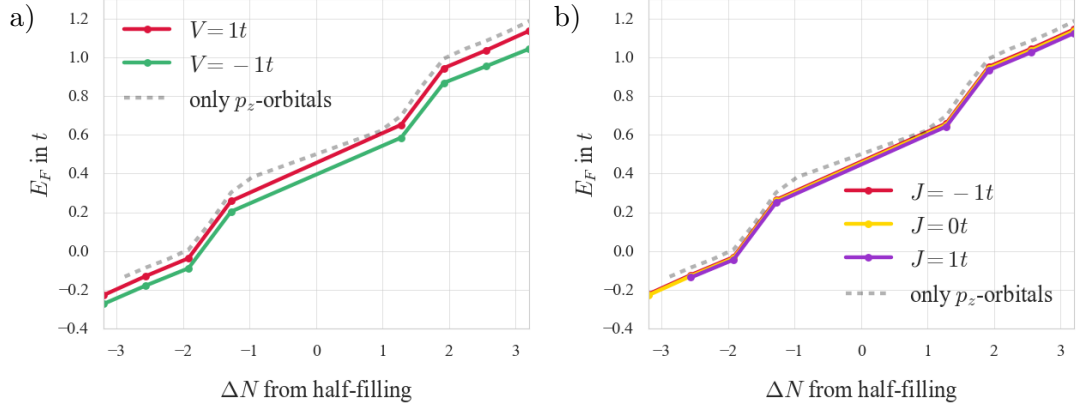
FIGURE 6.19.: Fermi energy for different doping strengths, where $U = t$ and $J = 0$ for different V (left) and for $V = t$ with different J (right).

6.6. Summary of the Tight-binding Model Results

In this chapter the two magnetic phases with FM and AFM configuration have been compared with each other in terms of their physical properties and energy. The energy splitting due to the electronic interactions has been analyzed with respect to the superexchange mechanism. For the single orbital model, the AFM phase is always lower in energy than the FM phase, in agreement with Liebs theorem. Furthermore, the non-magnetic phase has been discussed and a small and a large doping regime have been found, where the energy and Fermi energy exhibit different dependencies on the amount of doping in the system. The non-magnetic phase has an energetic minimum for finite hole doping. This finding is experimentally of high relevance, because of a possible Fermi level shifts of graphene introduced by a substrate. Graphene adsorbed on SiO_2 has been shown to exhibit a hole doping effect [270], which could be used to explain the absence of magnetic edges in experiments. The energy minimum in this work, which was found for very narrow ribbons, is very likely to be encountered in realistic systems, since for very larges ribbon this energy minimum is found already at much smaller doping strengths. Therefore, the Fermi level shift of the substrate could be enough to explain the absence of magnetic edge states in experiments.

In the multi-orbital model, the presence of the d-orbital states was found to change the energy splitting of the two magnetic phases, due to the occupation of these orbitals. This lead to a reduced p_z-orbital occupation, which diminishes the effective electronic interaction strength U for the p-orbitals. A negative d-orbital repulsion V and positive exchange interaction J was found to increase the population of the d-orbitals further and enhance this effect even more. While this changed the relative energy of the FM and AFM phases, no qualitative difference of the physical properties could be found for different $U > 0$, $|V| < 2t$ and $|J| < 2t$ or lengths N of the ribbons. If V is decreased or J is increased up to a certain value, addi-

tional states will become energetically close to the edge states, such that no self-consistent solution could be found. Changing the energetic separation of the d- and p_z-orbitals would reduce the interaction strength where the two magnetic phases become energetically close, but again no FM ground state could be found. Thus, a magnetic ground state with zero spin magnetic moment in agreement with Lieb's theorem has been confirmed for all parameter choices.

Lastly, the non-magnetic phase in the multi-orbital tight-binding model was examined and the d-orbital occupation as result of the doping was discussed. This lead to a modified energetic relation to the doping compared to the single-orbital result. The Fermi energy was also analyzed and how different interaction strengths and levels of doping contribute to it. The main difference compared to the single-orbital model comes from the reduced occupation of the p_z-orbitals which results in a diminished effective p-orbital interaction contribution to the Fermi energy, similar to the two magnetic phases.

7. Deformation of Graphene Nanoribbons

7.1. Introduction: Deformation of Graphene Lattice

In recent years research on the change of the electronic and topological properties of graphene under deformations has lead to the investigation of many interesting new effects. This is true also for materials such as TMDCs [271, 272]. Curvature in carbon nanotubes has shown to increase the weak intrinsic spin-orbit coupling of graphene quite substantially [273]. As was discussed in previous chapters of this work, the horizontal mirror symmetry in flat graphene ensures the conservation of the spin-component perpendicular to the lattice structure, but breaking that symmetry leads to additional spin-orbit coupling effects [125]. In the literature it has been shown, that corrugations in graphene lead to spin-orbit coupling proportional to the curvature of these deformations [274]. In general a deformation of a regular lattice structure may include both bending and strain, but in many studies either feature is examined individually. The change in distances among nearest neighbors may be neglected in a weak bending situation, such that the effect of relative orientation of the atomic orbitals at different lattice sites may be considered dominant. As a consequence, interactions that were previously vanishing due to symmetry become possible and in particular lead to interesting textures of spin orientation of the edge states of graphene [78, 213, 273].

The spin-orbit coupling of the states is affected by the curvature, because σ- and π-bands start to mix [275]. In lowest order this causes a change in the electrochemical potential and breaks particle-hole symmetry, because of the resulting change of the π-band population. Uniaxial strain, which modifies the hopping matrix elements of the system in a given spatial direction, distorts the Brillouin zone of the hexagonal lattice structure and can facilitate the modification of the graphene topology by opening a gap at the Dirac points [194, 276, 277]. Strain and the hybridization of π- and σ-bands in bent systems lead to gauge fields, which may cause effects similar to an external magnetic fields [278]. This can be seen for example, when the Dirac equation is formally considered on curved space [279]. In a more rigorous approach to the bending problem, the curvature effect can be cast into the form of a pseudomagnetic field [280, 281], where the curvature of the deformation gives rise to a formally identical description of the Dirac fermions in curved space as the Landau quantization in a magnetic field.

Combining deformations with actual magnetic fields, triggers a distinction of the two valleys of the Brillouin zone of graphene and mid-gap states at each of these points may arise. Such a description then contains a position- and direction-dependent Fermi velocity [279, 282, 283].

An in-plane deformation of the regular lattice due to strain changes the bond angle and distance of the lattice sites and leads to an enhancement of Rashba-type spin-orbit coupling and even Dresselhaus-type spin-orbit coupling may arise [147]. The comparison of tight-binding calculations with LDA computations have revealed that the change in hopping parameters due to strain is caused by the electronic density redistribution and change in bond length [284].

The Rashba-type spin-orbit coupling originating from the curvature-induced coupling of σ- and π-bands, may result in interesting spin textures [82, 285]. A central part in the discussions presented in this chapter is the qualitative effect of different deformations on the energy and spin alignment of the edge states in graphene nanoribbons. Furthermore, different multi-orbital tight-binding models are used to describe the effect of bending on these low-energy states.

7.2. Description of Bent Graphene Nanoribbons

In the previous chapters of this work, the case of flat graphene was discussed exclusively. If however the geometry of the array of carbon atoms is perturbed by bending, the resulting local curvature and the intrinsic spin-orbit coupling lead to different kinds of spin textures at the edge. Up until now, the literature on this topic was mainly focusing on the effect of the σ- and π-band hybridization, where the effect of higher-energy d-orbitals is completely neglected. It is a central result of this work, that these orbitals may not be neglected in the description of spin-orbit coupling effects in bent graphene nanoribbons. The reason is the dominating effect of the atomic d-orbital spin-orbit coupling over the atomic p-orbital spin-orbit coupling on the π-bands in these ribbons.

Other main results of this chapter include the influence of the intrinsic spin-orbit coupling on the spin alignment of the edge states under different deformations. In order to understand the influence of the bending on the couplings of the orbitals, a range of effective terms is derived from a tight-binding Hamiltonian of bent graphene. For the numerical computation the tight-binding model from Chapter 3.2.4 is extended to include s-, p_x- and p_y-orbitals additionally to the p_z-orbitals. The bending will be introduced by modifying the three-dimensional position of the lattice sites in the tight-binding model. The numerical results are discussed by comparing spin alignment due to deformations perpendicular to and along the zigzag edge.

7.2.1. Derivation of Transition Matrix Elements

As was stated in the discussion of the multi-orbital tight-binding model in Chapter 3, only the d_{xz}- and d_{yz}-orbitals couple to the p_z-orbitals in the case of flat graphene due to symmetry. If however the angle between the local normal vector defining the orbital angular momentum quantization axis and the vector in the direction of the next-nearest neighbor is different than $\pi/2$, the other three d-orbitals become coupled to the p_z-orbitals, as well. The same holds true for the sp^2-hybridized orbitals. In a bent system, the smaller energetic separation of the σ-bands causes a strong coupling to the p_z-bands, while the coupling of the d-orbitals to the p_z-orbitals increases very weakly. The procedure of computing the matrix elements in the Slater-Koster approximation depending on the angles θ between the normals at neighboring sites is outlined in the appendix D. With an azimuthal angle ϕ according to the relative positions of the sites 0 and 1 within the lattice, the angle θ between normals at these sites is computed as illustrated in Fig. 7.1 a) and its value is directly proportional to the curvature of the bending.

For computations in this work a deformation of the graphene sample is only regarded along one of the coordinate axes at a time. Not all of the bonds in the lattice run parallel to these directions, however. Due to the angles of the bonds with respect to the bending direction, the bending angle θ depends not only on the overall deformation of the lattice, but also on the bond within the sample. As shown in Fig. 7.1 b), for bending perpendicular to the zigzag
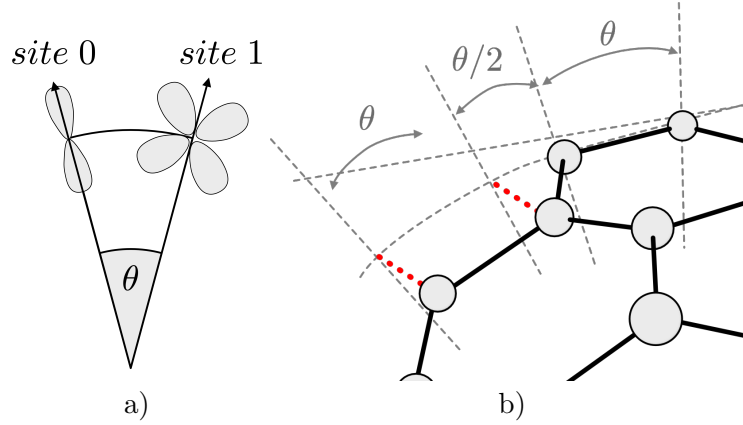
FIGURE 7.1.: a) The coupling between a p_z-orbital at site 0 and a d_{xz}-orbital at site 1 is changed by a bending angle θ. The angle θ is defined as the relative angle between the normals located at two neighboring lattice sites. b) For bending perpendicular to the zigzag edge, the angles of the bonds are θ and $\theta/2$. The projection of the curved graphene and flat graphene including the normals at the four lattice sites in the figure are depicted as guide to the eye.

edge, the polar angle θ varies along the bending direction due to the different directions of the bonds. As stated in [78, 213], the interaction of the p_z-orbitals with the sp^2-hybridized orbitals due to bending results in a term similar to the Rashba-type spin-orbit coupling at the two Dirac points. This is expected for the d-orbitals as well, but the coupling strengths should be different than in the sp^2-hybridized case, because of the different geometrical symmetries of the sp^2- and d-orbitals [285]. Also the effective strength of the p- and d-orbital intrinsic spin-orbit coupling on the edge states is different [80]. Physically, Rashba-type spin-orbit coupling arises in bent samples, because inversion symmetry breaking allows the p_z-orbitals to couple to the p_x- or p_y-orbitals at *neighboring sites*. The intrinsic spin-orbit coupling allows a transition among p-orbitals at *the same site*. This results in an effective hopping in the π-bands with an additional spin-flip, similar to the Rashba-type spin orbit coupling in an external electric field perpendicular to the flat graphene plane, see Eq. 3.27. The resulting matrix elements in the Slater-Koster approximation for the tight-binding model are given in Tabs. 7.1, 7.2, 7.3, and 7.4.

μ_1/ν_0	s	p_x	p_y	p_z
s	$V_{ss\sigma}$	$V_{sp\sigma}\cos\left(\phi\right)\cos\left(\theta\right)$	$V_{sp\sigma}\cos\left(\theta\right)\sin\left(\phi\right)$	$V_{sp\sigma}\sin\left(\theta\right)$
p_x	$-V_{sp\sigma}\cos\left(\phi\right)\cos\left(\theta\right)$	$V_{pp\pi}\sin\left(\phi\right)^2$ $+(V_{pp\sigma}+(V_{pp\pi}-V_{pp\sigma})\sin\left(\theta\right)^2)\cos\left(\phi\right)^2$	$(V_{pp\sigma}-V_{pp\pi})\cos\left(\phi\right)\cos\left(\theta\right)^2\sin\left(\phi\right)$	$(V_{pp\sigma}-V_{pp\pi})\cos\left(\theta\right)\cos\left(\phi\right)\sin\left(\theta\right)$
p_y	$-V_{sp\sigma}\cos\left(\theta\right)\sin\left(\phi\right)$	$(V_{pp\sigma}-V_{pp\pi})\cos\left(\phi\right)\cos\left(\theta\right)^2\sin\left(\phi\right)$	$V_{pp\pi}\cos\left(\phi\right)^2$ $+(V_{pp\sigma}+(V_{pp\pi}-V_{pp\sigma})\sin\left(\theta\right)^2)\sin\left(\phi\right)^2$	$(V_{pp\sigma}-V_{pp\pi})\cos\left(\theta\right)\sin\left(\theta\right)\sin\left(\phi\right)$
p_z	$-V_{sp\sigma}\sin\left(\theta\right)$	$(V_{pp\sigma}-V_{pp\pi})\cos\left(\theta\right)\cos\left(\phi\right)\sin\left(\theta\right)$	$(V_{pp\sigma}-V_{pp\pi})\cos\left(\theta\right)\sin\left(\theta\right)\sin\left(\phi\right)$	$(V_{pp\sigma}-V_{pp\pi})\sin\left(\theta\right)^2+V_{pp\pi}$

TABLE 7.1.: The Slater-Koster matrix elements for the relative angle θ of the normals between orbital μ at site 1 and orbital ν at site 0 for the s- and three p-orbitals. The spatial orientation of the orbitals is mainly given by the angle ϕ. Due to the different parity of the s- and p-orbitals some matrix elements are similar up to a sign.

μ_1/ν_0	p_x
d_{xz}	$\sin\left(\theta\right)((-\sqrt{3}V_{pd\sigma}\cos(\theta)^2+V_{pd\pi}(\cos\left(\theta\right)^2-\sin\left(\theta\right)^2))\cos\left(\phi\right)^2-V_{pd\pi}\sin\left(\phi\right)^2)$
d_{yz}	$(2V_{pd\pi}-\sqrt{3}V_{pd\sigma})\sin\left(\theta\right)\cos\left(\theta\right)^2\sin\left(\phi\right)\cos\left(\phi\right)$
d_{xy}	$\frac{1}{2}\cos\left(\theta\right)(-2V_{pd\pi}(\cos\left(\phi\right)^2-\sin\left(\phi\right)^2)\sin\left(\phi\right)+2\sin\left(\phi\right)\cos\left(\phi\right)^2(\sqrt{3}V_{pd\sigma}\cos\left(\theta\right)^2+2V_{pd\pi}\sin\left(\theta\right)^2)$
d_{z^2}	$\frac{1}{4}\cos\left(\theta\right)\cos\left(\phi\right)(V_{pd\sigma}-3V_{pd\sigma}(\cos\left(\theta\right)^2-\sin\left(\theta\right)^2)-4\sqrt{3}\sin\left(\theta\right)^2)$
$d_{x^2-y^2}$	$\frac{1}{2}\cos\left(\theta\right)\cos\left(\phi\right)(2V_{pd\pi}+(-2V_{pd\pi}+\sqrt{3}V_{pd\sigma})\cos\left(\theta\right)^2(\cos\left(\theta\right)^2-\sin\left(\theta\right)^2))$

TABLE 7.2.: The Slater-Koster matrix elements for the relative angle θ of the normals between orbital μ at site 1 and orbital ν at site 0 for the p_x- and the five d-orbitals.

μ_1/ν_0	p_y
d_{xz}	$(2V_{pd\pi} - \sqrt{3}V_{pd\sigma})\cos(\theta)^2\sin(\theta)\sin(\phi)\cos(\phi)$
d_{yz}	$\sin(\theta)(-V_{pd\pi}\cos(\phi)^2 + (-\sqrt{3}V_{pd\sigma}\cos(\theta)^2 + V_{pd\pi}(\cos(\theta)^2 - \sin(\theta)^2))\sin(\phi)^2)$
d_{xy}	$\frac{1}{2}\cos(\theta)(V_{pd\pi}\cos(\phi) + V_{pd\pi}\cos(3\phi) + (\sqrt{3}V_{pd\sigma}\cos(\theta)^2 + 2V_{pd\pi}\sin(\theta)^2)2\sin(\phi)^2\cos\phi)$
d_{z^2}	$\frac{1}{4}\cos(\theta)(V_{pd\sigma} - 3V_{pd\sigma}(\cos(\theta)^2 - \sin(\theta)^2) - 4\sqrt{3}V_{pd\pi}\sin(\theta)^2)\sin(\phi)$
$d_{x^2-y^2}$	$\frac{1}{2}\cos(\theta)(-4V_{pd\pi}\cos(\phi)^2 + (\cos(\phi)^2 - \sin(\phi)^2)(\sqrt{3}V_{pd\sigma}\cos(\theta)^2 + 2V_{pd\pi}\sin(\theta)^2))\sin(\phi)$

TABLE 7.3.: The Slater-Koster matrix elements for the relative angle θ of the normals between orbital μ at site 1 and orbital ν at site 0 for the p_y- and the five d-orbitals.

μ_1/ν_0	p_z
d_{xz}	$(\sqrt{3}V_{pd\sigma}\sin(\theta)^2 + V_{pd\pi}(\cos(\theta)^2 - \sin(\theta)^2))\cos(\phi)\cos(\theta)$
d_{yz}	$(\sqrt{3}V_{pd\sigma}\sin(\theta)^2 + V_{pd\pi}(\cos(\theta)^2 - \sin(\theta)^2))\sin(\phi)\cos(\theta)$
d_{xy}	$(\sqrt{3}V_{pd\sigma} - 2V_{pd\pi})\cos(\phi)\sin(\theta)\cos(\theta)^2\sin(\phi)$
d_{z^2}	$-\frac{1}{4}\sin(\theta)(V_{pd\sigma} + 4\sqrt{3}V_{pd\sigma}\cos(\theta)^2 - 3V_{pd\sigma}(\cos(\theta)^2 - \sin(\theta)^2))$
$d_{x^2-y^2}$	$-\frac{1}{2}(\sqrt{3}V_{pd\sigma} - 2V_{pd\pi})(\cos(\phi)^2 - \sin(\phi)^2)\cos(\theta)^2\sin(\theta)$

TABLE 7.4.: The Slater-Koster matrix elements for the relative angle θ of the normals between orbital μ at site 1 and orbital ν at site 0 for the p_z- and the five d-orbitals.

7.3. Perturbation Theory for Bending of Graphene

In this section, an effective single-orbital tight-binding model is derived in order to describe the occurrence of Rashba-type spin-orbit coupling terms in deformed graphene. The formalism is adapted from [286, 287], where the downfolding of a multi-orbital Hamiltonian in flat graphene is described. An example of a multi-orbital tight-binding Hamiltonian in real space is given in Eq. B.1. Let such single-particle Hamiltonian have closed periodic boundary conditions, such that it can be written compactly as $\hat{H} = \sum_{\langle i,j \rangle, \alpha, \beta} t_{\alpha,\beta}^{ij} \hat{c}_i^{\dagger \alpha} \hat{c}_j^{\beta}$ with annihilation (and creation) operators $\hat{c}_l^{\mu(\dagger)}$ for site l and orbital μ. The orbitals at the different sites are connected by the direction-dependent hopping matrix elements $t_{\alpha,\beta}^{ij}$, which are limited to nearest-neighbor hopping. In this derivation, the orbitals under consideration are the three p-orbitals and the s-orbital. The single-particle wave function that is used as ansatz for solving the Schrödinger equation $\hat{H}\psi = \varepsilon \psi$ with energy ε is obtained by applying the field operator $\hat{\psi}^{\dagger} = \sum_{\mu,l} a_{\mu,l} \hat{c}_l^{\mu \dagger}$ on the vacuum, such that $\psi := \hat{\psi}^{\dagger}|0\rangle$. The energy ε is close to the energy of the p-orbitals ε_p and equations for the coefficients of ψ can be derived from the tight-binding Hamilton operator. The energy of the s-orbitals will be denoted ε_s. Additionally to the hopping, intrinsic spin-orbit coupling among p-orbitals with parameter ξ_p, as given by the $\hat{\vec{L}}\hat{\vec{S}}$-operator, is included in the derivation. Such terms will be considered as perturbation of the single-orbital model. Furthermore, a deformation of graphene induces hopping matrix elements among different orbitals, which are zero in flat graphene, due to symmetry. Non-zero hopping matrix elements in flat graphene are changed in bent graphene, as well. However, for the purpose of the derivation of Rashba-type spin-orbit coupling presented in this section, the terms arising from the bending-induced hopping matrix elements are of primary interest.

The coefficients of the wave function ψ at a specific site 0 are denoted as $a_{\alpha,0}$ and those of the three adjacent sites $n \in \{1, 2, 3\}$ by $a_{\alpha,n}$, where the orbital index $\alpha \in \{s, x, y, z\}$ denotes either the s- or p_x-, p_y- and p_z-orbitals. The coefficients of the next-nearest-neighboring sites of site 0 are denoted as $a_{\alpha,n'}$. The hopping parameters in bent graphene are locally depending on the relative angle θ of the quantization axes at each of the sites, which are parallel to the local surface normals of the deformed graphene plane. For each hopping matrix element, a combined index $\theta_i := (\theta, \phi)_i$ is written, where both the bond angle ϕ and bending angle θ for the respective bond are included. The relative angles between site 0 and site n are denoted θ_n and between each n and n' by $\theta_{n'}$. In the following, a short-hand notation for the matrix elements along these bonds is given. The matrix elements are next labeled by θ_n, such that $t_{\alpha\beta}(\theta_n) := t_{\alpha,\beta}^{0n}$ for hopping form site 0 to n and as $t_{\alpha\beta}(\theta_{n'})$ for the one between n and n'. The Pauli matrices acting on the spin-space are denoted $\hat{s}_x$, etc.

With this, the equations for the coefficients at site 0 and its neighboring sites resulting

from the Schrödinger equation are expressed as

$$(\varepsilon - \varepsilon_p)a_{z,0} = -i\hat{s}_y\xi_p a_{x,0} + i\hat{s}_x\xi_p a_{y,0} + \sum_n t_{zz}(\theta_n)a_{z,n} + \sum_m t_{zx}(\theta_n)a_{x,n}$$
$$+ \sum_n t_{zy}(\theta_n)a_{y,n} + \sum_n t_{zs}(\theta_n)a_{s,n}, \tag{7.1}$$

as well as

$$(\varepsilon - \varepsilon_p)a_{x,0} = i\hat{s}_y\xi_p a_{z,0} - i\hat{s}_z\xi_p a_{y,0} + \sum_n t_{xz}(\theta_n)a_{z,n} + \sum_n t_{xy}(\theta_n)a_{y,n}$$
$$+ \sum_n t_{xx}(\theta_n)a_{x,n} + \sum_n t_{xs}(\theta_n)a_{s,n} \tag{7.2}$$

$$(\varepsilon - \varepsilon_p)a_{y,0} = -i\hat{s}_x\xi_p a_{z,0} + i\hat{s}_z\xi_p a_{x,0} + \sum_n t_{yz}(\theta_n)a_{z,n} + \sum_n t_{yy}(\theta_n)a_{y,n}$$
$$+ \sum_n t_{yx}(\theta_n)a_{x,n} + \sum_n t_{ys}(\theta_n)a_{s,n} \tag{7.3}$$

$$(\varepsilon - \varepsilon_s)a_{s,0} = \sum_n t_{ss}(\theta_n)a_{s,n} + \sum_n t_{sx}(\theta_n)a_{x,n} + \sum_n t_{sy}(\theta_n)a_{y,n} + \sum_n t_{sz}(\theta_n)a_{z,n}. \tag{7.4}$$

In the low-energy approximation, the energy ε in the Schrödinger equation is close to ε_p and can approximated to be identical to it in higher-order processes. This would lead to divergences, but the next-nearest neighbor hopping from the s- to the p_z-orbitals causes an energy shift, due to the offset ε_s from ε, which will remove this issue. By treating the p_x-, p_y- and s-orbitals as virtual states in the second-order perturbation theory, their effect on the p_z-orbitals is considered only effectively. This method describes effective hopping paths [286], which will renormalize the relative energies of the s- and p-orbitals and also the nearest-neighbor hopping. Furthermore, it will introduce a next-nearest neighbor hopping and include the intrinsic spin-orbit coupling as a spin-dependent next-nearest neighbor hopping. In the case of bent graphene, it will also introduce effective Rashba-type spin-orbit coupling terms.

For flat graphene, the matrix element in the single-orbital model for p_z-orbitals is given by $t_{zz}(\theta = 0) = V_{pp\pi}$. The p_x-, p_y- and s-orbitals form sp^2-hybridized states with the non-zero hopping matrix elements t_{xy}, t_{xs}, t_{ys} and t_{ss}. In general, a deformation of graphene leads to the non-zero matrix elements $t_{sz}(\theta_n)$, $t_{xz}(\theta_n)$, and $t_{yz}(\theta_n)$, because of the broken symmetry along the surface normal of the lattice. The resulting Rashba-type spin-orbit coupling terms arising from this perturbation will be shown to depend on the latter matrix elements.

Next, the multi-orbital model is cast into an effective single-orbital model. For this, hopping from one s-orbital to a neighboring one, as it appears in Eq. 7.4, can be neglected, due to their large energy offset from ε [287]. Thus, for the s-component at any site n and its

neighbors n' in Eq. 7.4, it follows that

$$(\varepsilon - \varepsilon_s)a_{s,n} = \sum_{n'} t_{sx}(\theta_{n'})a_{x,n'} + \sum_{n'} t_{sy}(\theta_{n'})a_{y,n'} + \sum_{n'} t_{sz}(\theta_{n'})a_{z,n'}. \qquad (7.5)$$

Next, the equations for the $a_{x,0}$ and $a_{y,0}$ components as in Eq. 7.2 and Eq. 7.3 are rewritten by eliminating the component for the s-orbitals at all sites n via Eq. 7.5. For the first, it follows

$$(\varepsilon - \varepsilon_p)a_{x,0} = i\hat{s}_y\xi_p a_{z,0} - i\hat{s}_z\xi_p a_{y,0} + \sum_n t_{xz}(\theta_n)a_{z,n} + \sum_n t_{xy}(\theta_n)a_{y,n}$$

$$+ \sum_n t_{xx}(\theta_n)a_{x,n} + \sum_n \frac{t_{xs}(\theta_n)}{\varepsilon - \varepsilon_s}\left[\sum_{n'} t_{sx}(\theta_{n'})a_{x,n'} + t_{sy}(\theta_{n'})a_{y,n'} + t_{sz}(\theta_{n'})a_{z,n'}\right].$$

$$(7.6)$$

The same is done for the $a_{x,n}$ component, resulting in

$$(\varepsilon - \varepsilon_p)a_{x,n} = i\hat{s}_y\xi_p a_{z,n} - i\hat{s}_z\xi_p a_{y,n} + \sum_{n'} t_{xz}(\theta_{n'})a_{z,n'} + \sum_{n'} t_{xy}(\theta_{n'})a_{y,n'}$$

$$+ \sum_{n'} t_{xx}(\theta_{n'})a_{x,n'} + \sum_{n'} \frac{t_{xs}(\theta_{n'})}{\varepsilon - \varepsilon_s}\left[\sum_{n''} t_{sx}(\theta_{n''})a_{x,n''} + t_{sy}(\theta_{n''})a_{y,n''} + t_{sz}(\theta_{n''})a_{z,n''}\right].$$

$$(7.7)$$

The next-nearest neighbor terms with index n'' in the brackets in Eq. 7.7 also include the original site 0. The terms for this site can be rewritten as $\varepsilon'a_{x,0}$. This term describes an energy contribution, which shifts the energy ε_p of this orbital at this site. This shift in Eq. 7.7 also occurs in the corresponding equation for $a_{y,n}$. It is of the form $\varepsilon'a_{\alpha,0} = \sum_{n'} \frac{t_{\alpha s}(\theta_{n'})}{\varepsilon-\varepsilon_s}t_{s\alpha}(\theta_{n'})a_{\alpha,0}$, where $\alpha \in \{x, y\}$. It is important that for $\varepsilon \approx \varepsilon_p$ the terms $t_{\alpha s}(\theta_{n'})$ for the p_x- and p_y-orbitals are non-zero, even for flat graphene. This ensures that the energy difference $\varepsilon - \varepsilon_p - \varepsilon'$, which will occur in Eq. 7.7, is non-zero for $\varepsilon \approx \varepsilon_p$ and the seemingly problematic divergence in Eq. 7.1 for zero θ_n is removed. The model presented here is valid in the low energy approximation. Thus, only small deformations will be considered, and therefore the matrix elements in the energy shift ε' will be considered to be approximately identical to those in flat graphene. Thus, $\varepsilon' \approx \frac{3}{4}\frac{V_{sp\sigma}^2}{\varepsilon_p-\varepsilon_s}$ is the energy shift for both p_x- and p_y-orbitals, which is the reduction of energy, when the in-plane p-orbitals couple together with the s-orbital. Next, Eqs. 7.6, 7.7 and the corresponding equations for $a_{y,0}$ and $a_{y,n}$ are inserted into Eq. 7.1, such that the s-orbitals are eliminated from the equations. If the effective hopping is restricted to next-nearest neighbors, Eq. 7.1 can be cast into

$$(\varepsilon - \varepsilon_p - \varepsilon'')a_{z,0} = A_n + B_n + C_n + A_{nn} + B_{nn} + C_{nn} \qquad (7.8)$$

with nearest-neighbor and next-nearest-neighbor terms with index n and nn, respectively. The energy shift ε'' originates from the second-order hopping from site 0 back to itself, similar to how ε' arises and therefore site 0 is excluded from the sums for the next-nearest neighbor terms. It will be zero for a flat system. The expression for ε'' is given below.

The term A_n describes the nearest-neighbor hopping among p_z-orbitals directly via $t_{zz}(\theta_n)$. Due to intrinsic spin-orbit coupling, an on-site transition from a p_z-orbital to either a p_x- or p_y-orbital is also possible, followed by a hopping to a neighboring p_x- or p_y-orbital and a transition back to a p_z-orbital. This results in another nearest-neighbor hopping term. Together, they are given by

$$A_n := \sum_n t_{zz}(\theta_n)a_{z,n} + \left(\frac{\xi_p}{\varepsilon'}\right)^2 \sum_n \left(t_{xx}(\theta_n) + t_{yy}(\theta_n)\right) a_{z,n}. \tag{7.9}$$

Furthermore, the p_z-orbitals are coupled by the bending-induced Rashba-type spin-orbit coupling terms B_n and C_n, which are

$$B_n := \frac{\xi_p}{\varepsilon'} \sum_n \left(i\hat{s}_x t_{yz}(\theta_n) - i\hat{s}_y t_{xz}(\theta_n)\right) a_{z,n}$$

$$- \frac{\xi_p}{\varepsilon'} \sum_n \left(i\hat{s}_x t_{zy}(\theta_n) - i\hat{s}_y t_{zx}(\theta_n)\right) a_{z,n} = 0 \tag{7.10}$$

$$C_n := -2 \left(\frac{\xi_p}{\varepsilon'}\right)^2 \sum_n \left(i\hat{s}_x t_{zy}(\theta_n) - i\hat{s}_y t_{zx}(\theta_n)\right) a_{z,n}. \tag{7.11}$$

Both of these are comprised of hopping matrix elements, which are non-zero only in bent graphene. The term B_n is formally linear in the intrinsic spin-orbit coupling parameter ξ_p. It vanishes, however, due to the symmetries of the matrix elements as given in Tab. 7.1, as $t_{\alpha z}(\theta_n) = t_{z\alpha}(\theta_n)$ for both $\alpha \in \{x, y\}$, due to the parity of the p-orbitals, but it is stated here for completeness. While B_n would describe an on-site transition from a p_z- to either a p_x- or p_y-orbital, followed by a bending-induced hopping to a neighboring p_z-orbital, the term C_n occurs due to two on-site transitions among different p-orbitals. This higher-order term is quadratic in ξ_p. Both processes are depicted in Fig. 7.2. The on-site transition from a p_z- to a p_x- or p_y-orbital causes a spin-flip, while the one from a p_x- to a p_y-orbital does not. This is derived in Eq. 3.23. Consequently, both of these Rashba terms exhibit a similar spin-dependence.

Effective next-nearest neighbor hopping matrix elements are introduced by the deformation

as well, which will be denoted A_{nn} and result in

$$A_{nn} := \sum_{n,n' \neq 0} \left(\frac{\xi_p}{\varepsilon'}\right)^2 \frac{1}{\varepsilon'} \left[t_{zx}(\theta_n)t_{xz}(\theta_{n'}) + t_{zy}(\theta_n)t_{yz}(\theta_{n'})\right] a_{z,n'} \tag{7.12}$$

$$-\frac{1}{\varepsilon_s} \sum_{n,n' \neq 0} t_{zs}(\theta_n)t_{sz}(\theta_{n'}) a_{z,n'} + \frac{1}{\varepsilon'} \sum_{n,n' \neq 0} \left[t_{zx}(\theta_n)t_{xz}(\theta_{n'}) + t_{zy}(\theta_n)t_{yz}(\theta_{n'})\right] a_{z,n'} \tag{7.13}$$

$$-\left(\frac{\xi_p}{\varepsilon'}\right)^2 \frac{1}{\varepsilon_s} \sum_{n,n' \neq 0} \left[t_{xs}(\theta_n)t_{sx}(\theta_{n'}) + t_{ys}(\theta_n)t_{sy}(\theta_{n'})\right] a_{z,n'}. \tag{7.14}$$

The first term is a result of the bending-induced coupling of p_z-orbitals to p_x- and p_y-orbitals, which are shifted from their original energy ε_p by the hybridization energy ε'. The second and third term describe a hopping from a p_z-orbital to either an s-, p_x- or p_y-orbital, followed by a hopping to another p_z-orbital. These terms are dominant compared to the first, as a consequence of the energy shift and the size of the matrix elements - in particular those related to the s-orbitals. The fourth term describes an on-site spin-orbit coupling transition from the p_z-orbitals to the p_x- or p_y-orbitals, followed by two hoppings and a transition back to a p_z-orbital at a next-nearest-neighboring site. Due to the quadratic order in ξ_p, this term is small.

The two spin-dependent next-nearest neighbor terms B_{nn} and C_{nn} denote a higher-order Rashba-type spin-orbit coupling term and the effective intrinsic spin-orbit coupling term, respectively. The latter is different compared to that of flat graphene, however, because the bending changes the isotropy of the lattice. The two terms are given by

$$B_{nn} :=$$

$$i\frac{\xi_p}{(\varepsilon')^2} \sum_{n,n' \neq 0} \left(\hat{s}_y \left[t_{zx}(\theta_n)t_{xx}(\theta_{n'}) + t_{zy}(\theta_n)t_{yx}(\theta_{n'})\right] - \hat{s}_x \left[t_{zx}(\theta_n)t_{xy}(\theta_{n'}) + t_{zy}(\theta_n)t_{yy}(\theta_{n'})\right]\right) a_{z,n'}$$

$$- i\frac{\xi_p}{(\varepsilon')^2} \sum_{n,n' \neq 0} \left(\hat{s}_y \left[t_{xx}(\theta_n)t_{xz}(\theta_{n'}) + t_{xy}(\theta_n)t_{yz}(\theta_{n'})\right] - \hat{s}_x \left[t_{yx}(\theta_n)t_{xz}(\theta_{n'}) + t_{yy}(\theta_n)t_{yz}(\theta_{n'})\right]\right) a_{z,n'}$$

$$\tag{7.15}$$

$$- i\frac{\xi_p}{\varepsilon'\varepsilon_s} \sum_{n,n' \neq 0} \left(\hat{s}_y \left[t_{zs}(\theta_n)t_{sx}(\theta_{n'}) - t_{xs}(\theta_n)t_{sz}(\theta_{n'})\right] - \hat{s}_x \left[t_{zs}(\theta_n)t_{sy}(\theta_{n'}) - t_{ys}(\theta_n)t_{sz}(\theta_{n'})\right]\right) a_{z,n'}$$

$$\tag{7.16}$$

$$C_{nn} := \left(\frac{\xi_p}{\varepsilon'}\right)^2 \frac{i\hat{s}_z}{\varepsilon_p - \varepsilon_s} \sum_{n,n' \neq 0} \left[t_{xs}(\theta_n)t_{sy}(\theta_{n'}) - t_{ys}(\theta_n)t_{sx}(\theta_{n'})\right] a_{z,n'}, \tag{7.17}$$

where higher orders of ξ_p are omitted. The matrix elements entering the intrinsic spin-orbit coupling term C_{nn} stay non-zero even without bending. B_{nn} has a similar effective order as the intrinsic spin-orbit coupling, it describes hopping among next-nearest neighbors, followed

by an on-site spin-flip, resulting in linear order in ξ_p, but quadratic order in the hopping matrix elements. Such process is shown in Fig. 7.2. It is important to note, that the terms in Eq. 7.15 do not cancel each other in general, despite their similar appearance. The same holds true for Eq. 7.16, because the different matrix elements are unequal in case of $\theta_n \neq \theta_{n'}$. For uniaxial deformations this is always the case, due to the different orientations of the bonds in the lattice and the resulting bending, as was discussed in Fig. 7.1. The next-nearest neighbor hopping terms in Eq. 7.14 back to site 0 cause the aforementioned energy shift of the p_z-orbitals

$$
\begin{aligned}
\varepsilon'' \approx {} & \frac{1}{\varepsilon'} \sum_n \left[t_{zx}(\theta_n) t_{xz}(\theta_n) + t_{zy}(\theta_n) t_{yz}(\theta_n) \right] - \frac{1}{\varepsilon_s} \sum_n t_{zs}(\theta_n) t_{sz}(\theta_n) \\
& + 2\frac{\xi_p^2}{\varepsilon'} + \left(\frac{\xi_p}{\varepsilon'} \right)^2 \frac{1}{\varepsilon'} \sum_n \left[t_{zx}(\theta_n) t_{xz}(\theta_n) + t_{zy}(\theta_n) t_{yz}(\theta_n) \right] \\
& - \left(\frac{\xi_p}{\varepsilon'} \right)^2 \frac{1}{\varepsilon_s} \sum_n \left[t_{xs}(\theta_n) t_{sx}(\theta_n) + t_{ys}(\theta_n) t_{sy}(\theta_n) \right],
\end{aligned}
\tag{7.18}
$$

due to the hybridization of the in-plane and out-of-plane orbitals. The first two terms of Eq. 7.18 are very small, because of the quadratic order in ξ_p. The second term is small compared to the dominant third term, but both are small for small deformations, because all of the occurring matrix elements are zero for $\theta = 0$. The last term is also negligible. The energy shift of the edge atoms is largely given by the bending-induced hybridization of p_z- and s-orbitals. If the edge sites of a graphene sample are not passivated with hydrogen atoms, the energy shift is approximately zero. However, the third term in Eq. 7.18 largely overestimates the energy shift for passivated edge atoms by several orders of magnitude. The reason is that the sp^2-hybridization of the hydrogen atoms at the edge sites in case of passivation shifts the energy of the hydrogen s-orbitals, such that the contribution is reduced.

Rashba-type Spin-orbit Coupling Originating from Deformation or Electric Field

The derived bending-induced Rashba terms act on the $\hat{s}_x$- and $\hat{s}_y$-components in a similar way as the Rashba-type spin-orbit coupling originating from an electric field perpendicular to a flat graphene sample, as in Eq. 2.27. However, the interaction in this section contains hopping matrix elements which couple next-nearest neighbors and which are only non-zero in a bent sample. Without Rashba-type spin-orbit coupling, a transition from a p_z-orbital to another p-orbital is only possible with a spin-flip due to intrinsic spin-orbit coupling, but returning to the p_z-orbital reverses the effect. The main similarity of the bending-induced Rashba-type spin-orbit coupling and the one originating from an external electric field perpendicular to a flat graphene sample is the induced transition between orbitals which would otherwise only be coupled by intrinsic spin-orbit coupling. This way, hopping among neighboring and next-nearest-neighboring p_z-orbitals may be facilitated via an intermediate

Lowest order:

Higher order in intrinsic spin-orbit coupling:
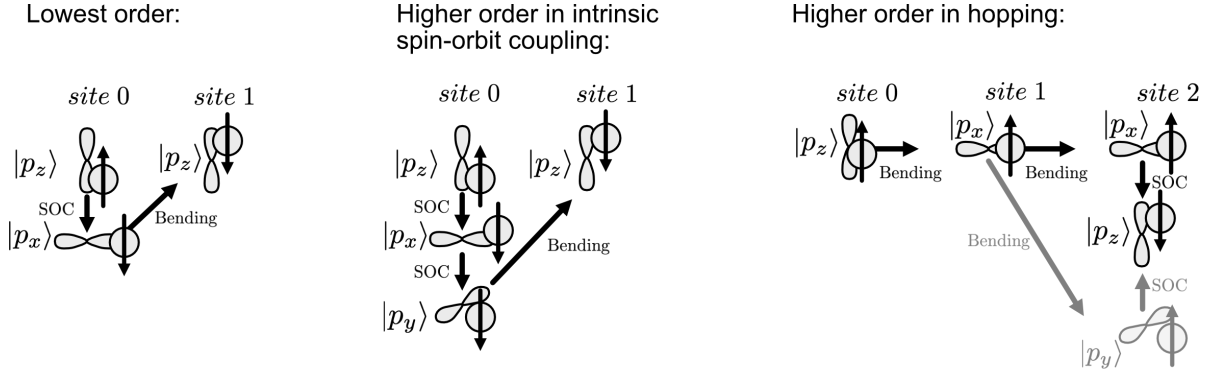
Higher order in hopping:

FIGURE 7.2.: A schematic overview of the different bending-induced Rashba-type spin-orbit coupling effects. The z-component of the real spin is indicated by an arrow at each orbital. The lowest-order term corresponds to the term B_n. Higher-order terms include either a second on-site transition, corresponding to C_n, or a hopping to a next-nearest neighbor, which leads to B_{nn}. The transition from p_x to p_y at site 0 in the middle figure does not include a spin-flip, due to the matrix elements in the $\hat{\vec{L}}\hat{\vec{S}}$-operator. A possible variation of hopping path, also leading to B_{nn}, is depicted in grey.

transition to the sp^2-hybridized orbitals, without reversing the spin-flip of the intrinsic spin-orbit coupling. An external electric field allows for an on-site transition between s- and p_z-orbitals in flat graphene, but a deformation of the sample induces a coupling of neighboring orbitals. Even though the two Rashba-type terms are very similar in their effect on the spin, they have different group theoretical characteristics. The *principal plane mirror asymmetry* (PIA) is used in the literature [124] to denote a spin-flipping next-nearest neighboring term, such as the bending-induced Rashba-type spin-orbit coupling discussed in this work. The Rashba-type spin-orbit coupling originating from an electric field, however, is a spin-flipping nearest-neighbor term.

Numerical Estimations of the Different Spin-orbit Coupling Terms

The different Slater-Koster parameters of the tight-binding model used in this estimation will be given in the next section in greater detail. For a bending angle[1] of $\theta \approx 0.03$, which corresponds to a bending radius of $R = 4\,\text{nm}$, the energy shift of the p_x- and p_y-orbitals due to the hybridization with the s-orbitals in flat graphene is given by $\varepsilon' \approx 2.828\,\text{eV}$. This value deviates only by $2\,\text{meV}$ from that of flat graphene and it is in line with the value $2.79\,\text{eV}$ obtained in [82], which is the band separation of sp^2-hybridized bands and π-bands.

With the above value for θ, the bending-induced Rashba-type term C_n in Eq. 7.11 is on the order of $\left(\frac{\xi_p}{\varepsilon'}\right)^2 (V_{pp\sigma} - V_{pp\pi})\theta \approx 1\,\mu\text{eV}$. The terms in B_{nn}, as in Eqs. 7.15 and 7.16, are on

---

[1]θ is given in rad.

the order of $\frac{\xi_p}{(\varepsilon')^2}(V_{pp\sigma} - V_{pp\pi})V_{pp\pi}\theta \approx 0.6\,\text{meV}$ and $\frac{\xi_p}{\varepsilon'\varepsilon_s}V_{pp\sigma}^2\theta \approx 0.2\,\text{meV}$. The term C_{nn} is on the order of $\left(\frac{\xi_p}{\varepsilon'}\right)^2 \frac{V_{sp\sigma}^2}{\varepsilon_s} \approx 10\,\mu\text{eV}$. In a bent system, the different spin-orbit coupling terms compete for an alignment of the spin along the local axis of quantization or along the bending direction. Their relative magnitude is therefore a good indication of which terms dominate the spin alignment and this will be discussed in detail in the next section. By comparing the different magnitudes discussed here, it is evident that the influence of the deformation on the spin structure is mostly determined by B_{nn}, which is a next-nearest neighbor contribution. The nearest-neighbor Rashba term C_n does not influence the spin alignment at all, while the other nearest-neighbor Rashba term B_n is not even present. The next-nearest neighbor term C_{nn} is very weak in comparison to B_{nn}.

7.4. Multi-orbital Tight-binding Model with σ-Bands

Extension of the Tight-binding Model with s-, p_x- and p_y-orbitals

The multi-orbital tight-binding model described in Sec. 3.2.4 is extended to also include s-, p_x- and p_y-orbitals with the Slater-Koster approximation. The three p-orbitals share the same energy, but the s-orbitals in this model are shifted by approximately $-8.37\,\mathrm{eV}$ relative to the three p-orbitals [80]. The remaining parameters are used as $V_{ss\sigma} = -5.73\,\mathrm{eV}$ and $V_{sp\sigma} = 5.62\,\mathrm{eV}$ [80]. The intrinsic spin-orbit coupling among the p-orbitals is included via Eq. 3.23. The commonly accepted magnitude of the intrinsic spin-orbit coupling in the p-orbitals is given by $\xi_p = 5\,\mathrm{meV}$ [78].

The sp^2-hybridization of the graphene lattice is perturbed, because the lattice has an edge. In the low-energy approximation, which was used to study either the effective single-orbital tight-binding model or the multi-orbital model as in the previous chapters, the energy separation from the p_z- to the in-plane orbitals is large enough, such that the latter can be neglected. The intrinsic spin-orbit coupling effects among p-orbitals could be neglected there as well. In the description of bending on the other hand, the broken symmetry of the lattice will directly affect the edge states, because the dangling bonds of the broken sp^2-hybridization at the edge sites will couple to the p_z-orbitals and affect the edge state dispersion. Therefore the passivation of the edge sites with hydrogen atoms has to be included in the model explicitly. The tight-binding model is extended to have additional sites at the edges, as depicted in Fig. 7.3 a). The hydrogen atoms are only considered to exhibit localized s-orbitals, which are coupled to the four orbitals at each edge site. The parameters for this coupling are different from the bonds among carbon atoms, they will be denoted by an additional index H, and are given by $V_{ss\sigma}^H = -6.84\,\mathrm{eV}$ and $V_{sp\sigma}^H = 7.8\,\mathrm{eV}$. Their energy shift relative to the three p-orbitals of graphene is $-2.49\,\mathrm{eV}$ [78].

Dislocation of Lattice Sites in Deformed Samples

The computation of a Hamiltonian of the tight-binding model for a bent sample presented in this chapter is similar to that of a flat graphene sample from previous considerations. Obtaining the relative displacement vectors of the sites in the bent scenario, however, becomes a central task. For the geometrical determination of the atomic positions, two different directions of deformation are considered, a deformation along and another perpendicular to the zigzag edge. A circular deformation has constant curvature along one cartesian axis and zero curvature along the other. It is characterized by a bending radius R. The atomic sites are first dislocated in space to account for the actual sample shape in the bending computation. From this, the interatomic displacement vectors required for the Slater-Koster approximation are computed. When the relative coordinates of each pair of sites are determined according to a function of the bending radius R, which describes the corresponding deformation, the relative distances of the sites must not change compared to the flat system. For extreme curvatures in real systems on the other hand, the atomic distances in curved space and flat
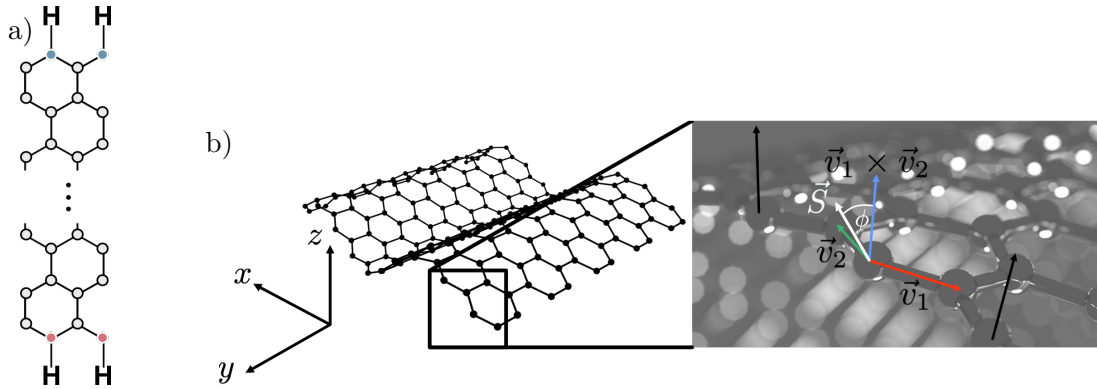
FIGURE 7.3.: a) The graphene carbon atoms at the edges are passivated with hydrogen atoms. One edge state is localized at the red sites, the other at the blue sites. b) An example of the normal vector at an edge of a nanoribbon. The vectors pointing to the two nearest neighbors (red and green) determine to the local normal vector (blue) at a site. The normals at neighboring sites have a different orientation (black). The spin polarization $\vec{S}$ is obtained in site-dependent local coordinates, where the local quantization axis is parallel to the local normal vector.

space may differ significantly. Therefore the computations are only regarded in the small bending regime.

Another type of bending is the sinusoidal deformation, where the curvature varies along the spatial direction. This deformation is characterized by an amplitude and a wavelength.

Local Normal Vectors

In order to describe the spin polarization of the edge atoms, a local quantization axis in curved space is defined. It is taken as the local normal vector of the lattice at the respective edge atom's position, which is depicted in Fig. 7.3 b). For obtaining this normal, two vectors pointing to a nearest neighbor of a site, each, are used. The vector product of the two is then parallel to the local normal vector.

7.5. Deformation Effects

In this section the dispersion relation and spin polarization of the edge states under different deformations of the flat graphene nanoribbon is discussed. For this purpose, the 4-band tight-binding model, which was introduced in the last section, is used to discuss the spin alignment under different circular deformations of the regular graphene lattice. The different lattice symmetries of the deformed samples are shown to lead to different symmetries of the edge state dispersion relations.

7.5.1. Spin-orbit Coupling due to Deformation

For the discussion presented in this section, only uni-directional deformations of the graphene lattice with constant curvature will be considered, which are either taken parallel to the zigzag-direction or perpendicular to it. As was discussed in the previous section, the second term of the spin-dependent next-nearest neighbor hopping B_{nn} in Eq. 7.16 is most relevant for the spin-texture of the graphene sample. The reason is that the p_z-orbitals couple to the s-orbitals only due to the deformation, and therefore the interaction matrix elements are highly-dependent on the bending direction. In contrast, the p_x- and p_y-orbitals couple to the s-orbitals in flat graphene already, which is only slightly changed by the bending.

The different influence of the bending along or perpendicular to the zigzag edge is depicted in Fig. 7.4. If the bending is taken along the x-direction, which is the periodic direction of the sample, the bending will only change the red bonds in a), because the black ones do not have an x-component and are thus left unchanged. This will have great consequences for the magnitude of the matrix elements for the p_z- and s-orbitals. If the bending is taken along the y-direction, as indicated in b), the violet bonds will have a reduced bending contribution of $\theta/2$, compared to the red ones where the angle is θ. In order to discuss the influence of the direction of bending on Eq. 7.16, the next-nearest neighbor hopping is discussed along two specific bonds. Consider a successive hopping along path 1, followed by a hopping along path 2, as depicted in Fig. 7.4 c). As the bending acts as a perturbation, the in-plane directive cosines are approximately those of flat graphene and are thus given by the relative displacement $\boldsymbol{b} \in \{\boldsymbol{\delta}_1, \boldsymbol{\delta}_2, \boldsymbol{\delta}_3\}$ of the neighboring sites, e.g. in Tab. 7.1 $\sin(\phi_n) = b_{n,y}$ and $\cos(\phi_n) = b_{n,x}$. Then, Eq. 7.16 becomes

$$B_{nn} = \frac{i\xi_p}{\varepsilon'\varepsilon_s} V_{sp\sigma}^2 \left(\hat{s}_y \left[\sin(\theta_2)b_{1,x} - \sin(\theta_1)b_{2,x} \right] - \hat{s}_x \left[\sin(\theta_2)b_{1,y} - \sin(\theta_1)b_{2,y} \right] \right), \qquad (7.19)$$

and for circular bending along the x-direction it can be reduced to

$$\begin{aligned} B_{nn}^x &= \frac{i\xi_p}{\varepsilon'\varepsilon_s} V_{sp\sigma}^2 \left(\hat{s}_y \left[\sin(\theta) \cdot 0 - 0 \cdot \sqrt{3}/2 \right] - \hat{s}_x \left[\sin(\theta) \cdot 1 - 0 \cdot 1/2 \right] \right) \\ &= -\frac{i\xi_p}{\varepsilon'\varepsilon_s} V_{sp\sigma}^2 \hat{s}_x \sin(\theta). \end{aligned} \qquad (7.20)$$
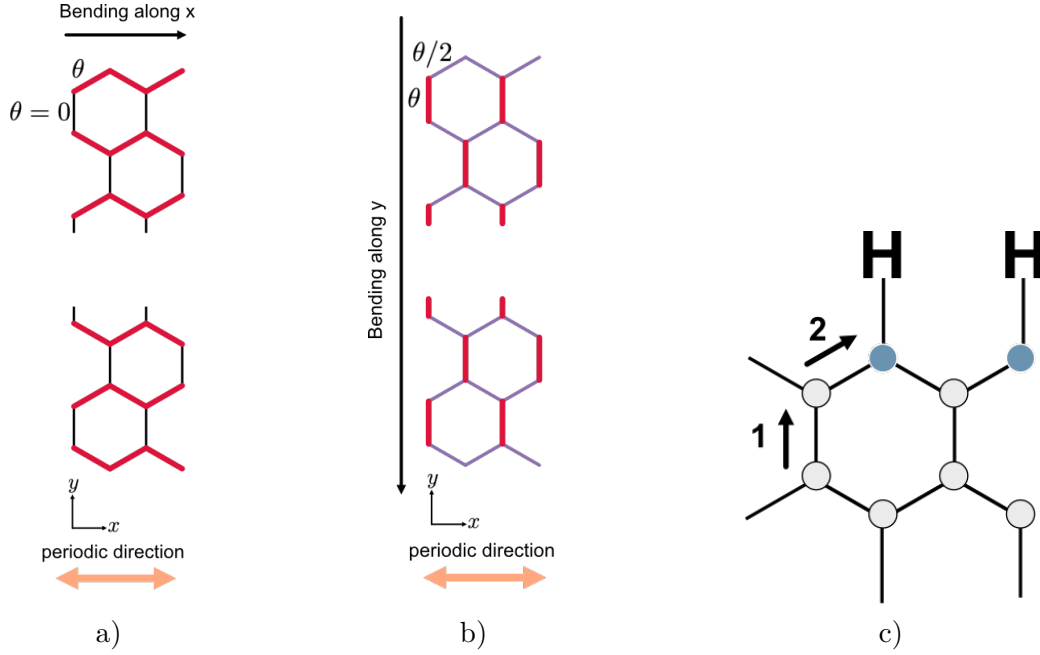
FIGURE 7.4.: a) Schematic of the bonds in the bent graphene cell which change when bending is applied. Black represents the bonds that correspond to that of flat graphene. a) For bending along x only the bonds with a component along the zigzag edge are affected, as indicated in red. b) For bending along y all bonds in the sample have a component along the y-direction, but the horizontal bonds are affected less, indicated by the violet color. c) An illustration of a hopping path required for the computation of the bending-induced Rashba-type spin-orbit coupling term B_{nn}. The edge sites are depicted in blue.

Consequently, for bending parallel to the edge only the x- component of the spin in the Rashba-type term in Eq. 7.20 is present. Due to the symmetry of the matrix elements, this term is zero for hopping along two consecutive zigzag bonds and for any other hopping paths between two next-nearest-neighbors it is identical to Eq. 7.20. When the bending is taken along the y-direction, the symmetry of the lattice results in a similar effect on the spin, with a different direction of spin-polarization. This is shown next, where Eq. 7.19 becomes

$$B_{nn}^{y} = \frac{i\xi_p}{\varepsilon'\varepsilon_s} V_{sp\sigma}^2 \left(\hat{s}_y \left[\sin\left(\theta/2\right) \cdot 0 - \sin\left(\theta\right) \cdot \sqrt{3}/2 \right] - \hat{s}_x \left[\sin\left(\theta/2\right) \cdot 1 - \sin\left(\theta\right) \cdot 1/2 \right] \right). \quad (7.21)$$

The deformations here are only considered for very small angles, and thus $\sin\left(\theta/2\right) \approx \sin\left(\theta\right)/2$. Then the last term in Eq. 7.21 cancels out and the Rashba-type spin-orbit coupling parameter is left with the y-component of the spin, which results in

$$B_{nn}^{y} = -\frac{i\xi_p}{\varepsilon'\varepsilon_s} V_{sp\sigma}^2 \sqrt{3}/2 \hat{s}_y \sin\left(\theta\right). \quad (7.22)$$

The same functional dependencies hold true for any other hopping path in the sample, but for hopping along two consecutive zigzag bonds B_{nn}^{y} will be zero, similar to B_{nn}^{x}. The fact that both Eq. 7.20 and Eq. 7.22 are proportional to $t_{sz}(\theta) = V_{sp\sigma} \sin(\theta)$, is consequence of the symmetry of the Rashba-type term and its dependence on the deformation strength.

For sinusoidal deformations, where the curvature is not constant, the above considerations are not fulfilled, such that one would expect the spin components in the different directions not to cancel. For the deformations with varying curvature along the y-direction considered later in this work, the cancellation of the $\hat{s}_x$-component is still approximately true, however, because the curvature difference on the scale of two neighboring bonds of the lattice is still very small. This will be different for the deformations along the x-direction, because there the curvature variation will be assumed to be larger.

The case of deformation with constant curvature along the x-direction will not be discussed in this work, because it is not possible to construct a tight-binding model with constant curvature along the periodic direction [78].

7.5.2. Energy Degeneracy in Bent Ribbons

In this section, the effect of the different directions of spin alignment on the energy spectrum is discussed. Bending with constant curvature along the zigzag direction of a graphene sample, in combination with the periodicity, is what makes up a single wall carbon nanotube with zigzag configuration. These systems are described by a chiral vector[2], which denotes the principal axis of the tube. In the case presented here, the tube has the configuration $(n, 0)$, where n is even. Such a system is symmetric with respect to inversion, due to its cylindrical structure [288]. Additionally, zigzag nanotubes are symmetric with respect to all group operations of the two-dimensional point group $C_{2\nu}$ [289]. The constant curvature along the zigzag edge causes the spins to align along the principal axis of the nanotube. This situation is illustrated in the top of Fig. 7.5. The inversion symmetry is maintained by the fact that a cylinder is invariant under swapping $\boldsymbol{r}$ with $-\boldsymbol{r}$. As can be seen in the figure, the symmetry of the sample ensures that energies E of the states fulfill

$$E(1, \downarrow, -\mathbf{k}) = E(2, \downarrow, \mathbf{k}) \tag{7.23}$$

$$E(1, \uparrow, \mathbf{k}) = E(2, \uparrow, -\mathbf{k}), \tag{7.24}$$

where the additional parameter denotes edge 1 or 2. These states are labeled by another parameter $\uparrow$ or $\downarrow$, with respect to the local quantization axis in the xz-plane. As was discussed in Sec. 2.2.1, time-reversal symmetry leads to two-fold degeneracy of the energy bands and in conjunction with inversion symmetry to a spin degeneracy of all bands.

For bending perpendicular to the edges, the spins align in the yz-plane, which is oriented perpendicular to the sample edges, see bottom of Fig. 7.5. The z-components of the local

---

[2]The chiral vector $\vec{c} = n\vec{a}_1 + m\vec{a}_2$ with two integers n and m and the lattice vectors of the honeycomb lattice denotes the periodicity of a nanotube and is commonly written as (n, m) [69].
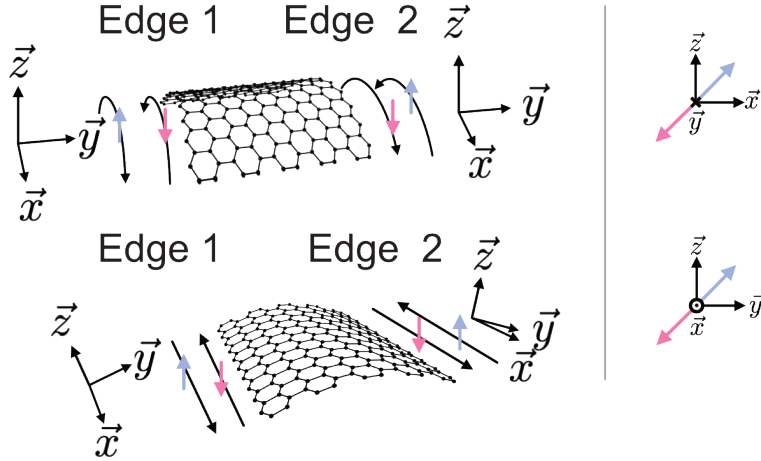
FIGURE 7.5.: Illustration of the spin alignment for a deformation along the zigzag edge (top) and perpendicular to the edges (bottom). In the top case, the spins align in the xz-plane and in the bottom case in the yz-plane. In the bottom picture the z-components of the local quantization axes at each edge are not parallel, as indicated by the tripods.

coordinate systems at each edge are not parallel, which is indicated by the tripods in the figure. Replacing $x \to -x$ and $y \to -y$ are valid symmetry operations of such a sample, but replacing $z \to -z$ is not, and thus the sample is not inversion symmetric, while all operations of the point group $C_{2\nu}$ are still intact. Such a sample only exhibits two-fold degenerate bands, due to Kramers theorem.

7.5.3. Deformation Pseudo Potentials

Using a procedure discussed in [290], the occurrence of a pseudomagnetic field within the sublattice spin space is introduced in the following. Let the single-orbital graphene Hamiltonian for the following discussion be the Hamiltonian in Eq. 3.7 and let the hopping matrix elements be explicitly dependent on the bond direction $\boldsymbol{\delta}_i$ as also discussed in Chapter 3. Let the hopping matrix elements additionally be depending on the position $\boldsymbol{r}$, such that $t = t(\boldsymbol{r}, \boldsymbol{\delta}_i)$. This spatial dependence of the hopping matrix element is responsible for the occurrence of the pseudomagnetic field, as will be shown in the following. It was discussed before, that the nearest-neighbor hopping changes in a deformed sample, according to the first term in Eq. 7.9. Due to this term, $t(\boldsymbol{r}, \boldsymbol{\delta}_i)$ will be assumed to change compared to its non-bent counterpart, such that

$$t(\boldsymbol{r}, \boldsymbol{\delta}_i) \approx t(\boldsymbol{\delta}_i) + \delta t(\boldsymbol{r}, \boldsymbol{\delta}_i)$$
$$= t + \delta t(\boldsymbol{r}, \boldsymbol{\delta}_i) \tag{7.25}$$

For weak deformations where $\delta t(\boldsymbol{r}, \boldsymbol{\delta}_i) \ll |t|$, it is a valid approximation, to only consider the dominant first term in the Fourier expansion of Eq. 3.5 [290]. With this, Eq. 3.7 in the basis

$\{|p_z, A\rangle, |p_z, B\rangle\}$ can be rewritten as

$$
\begin{aligned}
H_{\mathbf{k}} = {} & t(1 + e^{-i\boldsymbol{a}_2\boldsymbol{k}} + e^{-i\boldsymbol{a}_3\boldsymbol{k}})\alpha_{\mathbf{k}}^{\dagger}\beta_{\mathbf{k}} \\
& + (\delta t(\boldsymbol{r}, \boldsymbol{\delta}_1)e^{-i\boldsymbol{a}_2\boldsymbol{k}} + \delta t(\boldsymbol{r}, \boldsymbol{\delta}_2)e^{-i\boldsymbol{a}_3\boldsymbol{k}} + \delta t(\boldsymbol{r}, \boldsymbol{\delta}_3))\alpha_{\mathbf{k}}^{\dagger}\beta_{\mathbf{k}} + \text{h.c..}
\end{aligned}
\tag{7.26}
$$

Next, an expansion around the Dirac points $K^{(')}$ is performed, such that $\boldsymbol{k} \to (\pm\frac{4\pi}{3\sqrt{3}}, 0) + (q_x, q_y)$ and the valley isospin $\tau = \pm 1$ is used to denote the corresponding Dirac point. It follows

$$
H_{\mathbf{k}} = \frac{3ta}{2\hbar}(-\tau q_x + iq_y)\alpha_{\mathbf{k}}^{\dagger}\beta_{\mathbf{k}} + \left(\delta t(\boldsymbol{r}, \boldsymbol{\delta}_1)e^{-\frac{2i\pi\tau}{3}} + \delta t(\boldsymbol{r}, \boldsymbol{\delta}_2)e^{\frac{2i\pi\tau}{3}} + \delta t(\boldsymbol{r}, \boldsymbol{\delta}_3)\right)\alpha_{\mathbf{k}}^{\dagger}\beta_{\mathbf{k}} + \text{h.c..}
\tag{7.27}
$$

The first term is the Hamiltonian for undeformed graphene and the second one describes the pseudopotential due to bending. With $v_F = \frac{3|t|a}{2\hbar}$ and the definition of the pseudopotential

$$
H_{\mathbf{k}} = v_F \begin{pmatrix} 0 & -\tau q_x - iq_y \\ -\tau q_x + iq_y & 0 \end{pmatrix} + v_F \begin{pmatrix} 0 & A_x - i\tau A_y \\ A_x + i\tau A_y & 0 \end{pmatrix},
\tag{7.28}
$$

the two components of the vector potential $\vec{A} = (A_x, A_y)$ are found to be [290]

$$
v_F A_x = \delta t(\boldsymbol{r}, \boldsymbol{\delta}_3) - \frac{1}{2}(\delta t(\boldsymbol{r}, \boldsymbol{\delta}_1) + \delta t(\boldsymbol{r}, \boldsymbol{\delta}_2))
\tag{7.29}
$$

$$
v_F A_y = -\frac{\sqrt{3}}{2}(\delta t(\boldsymbol{r}, \boldsymbol{\delta}_2) - \delta t(\boldsymbol{r}, \boldsymbol{\delta}_1)).
\tag{7.30}
$$

Pseudomagnetic Field

The pseudomagnetic field $\vec{B}$ is only generated if the components of the vector potential change spatially via

$$
B_z(\boldsymbol{r}) = \frac{\partial A_y(\boldsymbol{r})}{\partial x} - \frac{\partial A_x(\boldsymbol{r})}{\partial y},
\tag{7.31}
$$

which is not the case for bending with constant curvature. If the bending is taken with constant curvature parallel to the zigzag edge (along x), then $\delta t(\boldsymbol{r}, \boldsymbol{\delta}_1) = \delta t(\boldsymbol{r}, \boldsymbol{\delta}_2) = const.$ and $\delta t(\boldsymbol{r}, \boldsymbol{\delta}_3) = 0$. Then

$$
v_F A_x = -\delta t(\boldsymbol{r}, \boldsymbol{\delta}_1) = const.
\tag{7.32}
$$

$$
v_F A_y = 0
\tag{7.33}
$$

If the bending is taken perpendicular to the zigzag edge, along the y-direction, then $\delta t(\boldsymbol{r}, \boldsymbol{\delta}_1) = \delta t(\boldsymbol{r}, \boldsymbol{\delta}_2) = const.$ and $\delta t(\boldsymbol{r}, \boldsymbol{\delta}_3) = const. \neq \delta t(\boldsymbol{r}, \boldsymbol{\delta}_1)$. Then

$$v_F A_x = \delta t(\boldsymbol{r}, \boldsymbol{\delta}_3) - \frac{1}{2}(\delta t(\boldsymbol{r}, \boldsymbol{\delta}_1) + \delta t(\boldsymbol{r}, \boldsymbol{\delta}_2)) = const. \tag{7.34}$$

$$v_F A_y = 0, \tag{7.35}$$

which is qualitatively similar to the previous case. If the bending is taken parallel to the zigzag edge, but with sinusoidal deformation, then the vector potential becomes spatially dependent (on x) via $\delta t(x, \boldsymbol{\delta}_1) \neq \delta t(x, \boldsymbol{\delta}_2)$ and $\delta t(x, \boldsymbol{\delta}_3) = 0$, such that

$$v_F A_x = -\frac{1}{2}(\delta t(x, \boldsymbol{\delta}_1) + \delta t(x, \boldsymbol{\delta}_2)) \tag{7.36}$$

$$v_F A_y = -\frac{\sqrt{3}}{2}(\delta t(x, \boldsymbol{\delta}_2) - \delta t(x, \boldsymbol{\delta}_1)). \tag{7.37}$$

This generates a pseudomagnetic field, because

$$B_z(x) = \frac{\partial A_y(x)}{\partial x} - \frac{\partial A_x(x)}{\partial y} = -\frac{\sqrt{3}}{2v_F} \frac{\partial(\delta t(x, \boldsymbol{\delta}_2) - \delta t(x, \boldsymbol{\delta}_1))}{\partial x}. \tag{7.38}$$

The condition $\delta t(x, \boldsymbol{\delta}_1) \neq \delta t(x, \boldsymbol{\delta}_2)$ is fulfilled for curvatures, where the wavelength of the sinusoidal deformation is on the order of the lattice constant. But the derivative of the two deformations $\delta t(x, \boldsymbol{\delta}_1)$ and $\delta t(x, \boldsymbol{\delta}_2)$ will be nearly identical in this case and thus the resulting pseudomagnetic is very small.

Lastly, the case of bending perpendicular to the zigzag edge with sinusoidal deformation is considered. In such a situation, the vector potential is spatially dependent on y, and with $\frac{1}{2}\delta t(y, \boldsymbol{\delta}_3) \approx \delta t(y, \boldsymbol{\delta}_1) = \delta t(y, \boldsymbol{\delta}_2)$ it follows

$$B_z(y) = -\frac{1}{2v_F} \frac{\partial(\delta t(y, \boldsymbol{\delta}_3))}{\partial y}. \tag{7.39}$$

Again, the change of the hopping matrix element is identical for both zigzag bonds, but different for the bonds perpendicular to the zigzag edge, such that a pseudomagnetic field can be generated in this case. The results for different bending types (circular or sinusoidal) are summarized in Tab. 7.5 for both bending directions.

Pseudo Scalar Potential

In addition to the pseudo vector potential $\vec{A}$, a pseudo scalar potential $\Phi(\boldsymbol{r})$ is induced by the deformation, because of the modified next-nearest-neighbor hopping in bent graphene [274]. Such a contribution will add a term to Eq. 3.5 and accounts for hopping from and to sites of identical sublattice via

$$H^{nnn} = t' \sum_{\mathbf{R}} \sum_{i=1}^{3} \left(\hat{a}_{\mathbf{R}}^{\dagger} \hat{a}_{\mathbf{R}+\boldsymbol{a}_i} + \hat{b}_{\mathbf{R}}^{\dagger} \hat{b}_{\mathbf{R}+\boldsymbol{a}_i} \right) + \text{h.c.}, \tag{7.40}$$

direction	type	$\vec{A}$	B_z
$\perp$	circular	$A_x = const., \ A_y = 0$	0
	sinusoidal	$A_x(y) \neq 0, \ A_y(y) = 0$	$B_z(y) \sim \frac{\partial A_x}{\partial y}$
$\parallel$	circular	$A_x = const., \ A_y = 0$	0
	sinusoidal	$A_x(x) \neq 0, \ A_y(x) \neq 0$	$B_z(x) \sim \frac{\partial A_y}{\partial x}$

TABLE 7.5.: Summary of the deformation-induced vector potentials and resulting magnetic fields. The direction of bending is either parallel ($\parallel$) or perpendicular to the zigzag edge ($\perp$) and has either constant curvature (circular) or varying curvature (sinusoidal).

where the next-nearest-neighbor hopping is given by t' and the lattice vector $\boldsymbol{a}_3$ is introduced in addition to those in Eq. 3.1. The next-nearest-neighbor hopping, similar to the nearest-neighbor hopping, becomes spatially-dependent, such that

$$
\begin{aligned}
t'(\boldsymbol{r}, \boldsymbol{a}_i) &\approx t'(\boldsymbol{a}_i) + \delta t'(\boldsymbol{r}, \boldsymbol{a}_i) \\
&= t' + \delta t'(\boldsymbol{r}, \boldsymbol{a}_i).
\end{aligned}
\tag{7.41}
$$

Due to the next-nearest-neighbor matrix elements regarding the σ-band model, it follows that $t' = 0$, while $\delta t'(\boldsymbol{r}, \boldsymbol{a}_i)$ is given by Eq. 7.13. In the case of d-orbitals, $t' \neq 0$ and an additional term is added to $\delta t'(\boldsymbol{r}, \boldsymbol{a}_i)$, which will be discussed in Sec. 7.7. The Fourier transformation of Eq. 7.40 leads to

$$
H_{\mathbf{k}}^{nnn} = 2 \sum_{i=1}^{3} \left(t' + \delta t'(\boldsymbol{r}, \boldsymbol{a}_i) \right) \cos\left(\mathbf{k}\boldsymbol{a}_i \right) \left(\alpha_{\mathbf{k}}^{\dagger} \alpha_{\mathbf{k}} + \beta_{\mathbf{k}}^{\dagger} \beta_{\mathbf{k}} \right) + \text{h.c.}
\tag{7.42}
$$

and the expansion around the Dirac and Γ-points results in

$$
\Phi(\boldsymbol{r})^{K/K'} = -\sum_{i=1}^{3} \delta t'(\boldsymbol{r}, \boldsymbol{a}_i) \qquad\qquad \Phi(\boldsymbol{r})^{\Gamma} = 2 \sum_{i=1}^{3} \delta t'(\boldsymbol{r}, \boldsymbol{a}_i).
\tag{7.43}
$$

7.6. Bent Graphene Nanoribbons with s- and p-orbitals

In the following, the 4-band tight-binding model is used to discuss the effect of deformation on the edge states of graphene nanoribbons. An important influence on the resulting edge state dispersion is the inversion symmetry with respect to the center of the deformed nanoribbon. Different cases of deformation will be discussed, where a circular or a sinusoidal type of bending is applied to the nanoribbons.

7.6.1. Circular Bending Perpendicular to the Edge

As a first step a circular deformation in the direction perpendicular to the zigzag edges is applied to the sample. A schematic illustration of the bending of the sample, which is performed such that the lattice sites are displaced in the yz-plane with a constant radius of curvature, is given in Fig. 7.7 c). The matrix elements are then computed from their relative displacements. Parts of the results presented here have been obtained elsewhere already [78], but are reviewed and extended here for gaining a better understanding of the other types of deformation as well. In Fig. 7.6 a) the dispersion relation of a bent nanoribbon with 16 rows and 4 columns is shown, where the edges are passivated with hydrogen atoms. The bending radius is $R = 30\,\mathrm{nm}$ and the intrinsic spin-orbit coupling parameter of the p-orbitals used here is $\xi_p = 5\,\mathrm{meV}$. In this and in the following sections, the momentum has been rescaled by a factor[3] 4 compared to previous chapters. The edge states cross the band gap, as can be seen in the right of the figure, but due to the deformation, the π-like bands of the edge states exhibit a small energy shift of $\approx 2.6\,\mathrm{meV}$. The broken inversion symmetry of the sample lifts the two-fold spin degeneracy of the states, such that an onset of the trigonal splitting can be observed closer to the Dirac points of the Brillouin zone similar to what was discussed in Chapter 4.5. At the Brillouin zone center, the edges states are localized at their respective edges.

The dispersion of the edge states is governed by the deformation of the ribbon in the vicinity of the edges, which influences the next-nearest-neighbor hopping, mostly by the first term in Eq. 7.13. If however the intrinsic spin-orbit coupling parameter ξ_p were to be increased to larger values, such as $\xi_p = 100\,\mathrm{meV}$, the deformation would not play a significant role at the Brillouin zone center anymore, because it was not the dominant interaction in the system compared to the intrinsic spin-orbit coupling. The onset of the Rashba trigonal warping would still be prominently observable due to the broken inversion symmetry of the system. In Fig. 7.6 b) the expectation values $\langle \hat{s}_x \rangle$, $\langle \hat{s}_y \rangle$ and $\langle \hat{s}_z \rangle$ are shown for the four edge states. The states are clearly spin-polarized and the spin tilts along the y-direction. The amount of spin alignment with respect to the sample plane depends sensitively on the deformation strength and at this point the states are already fully $\langle \hat{s}_y \rangle$-polarized. Therefore

---

[3]An increasing the number of rows in the unit cell of the graphene samples may lead to the occurrence of multiple copies of the band structure in a given k-space interval. Therefore this factor is included to set a relevant interval with only one copy, which has practical reasons.
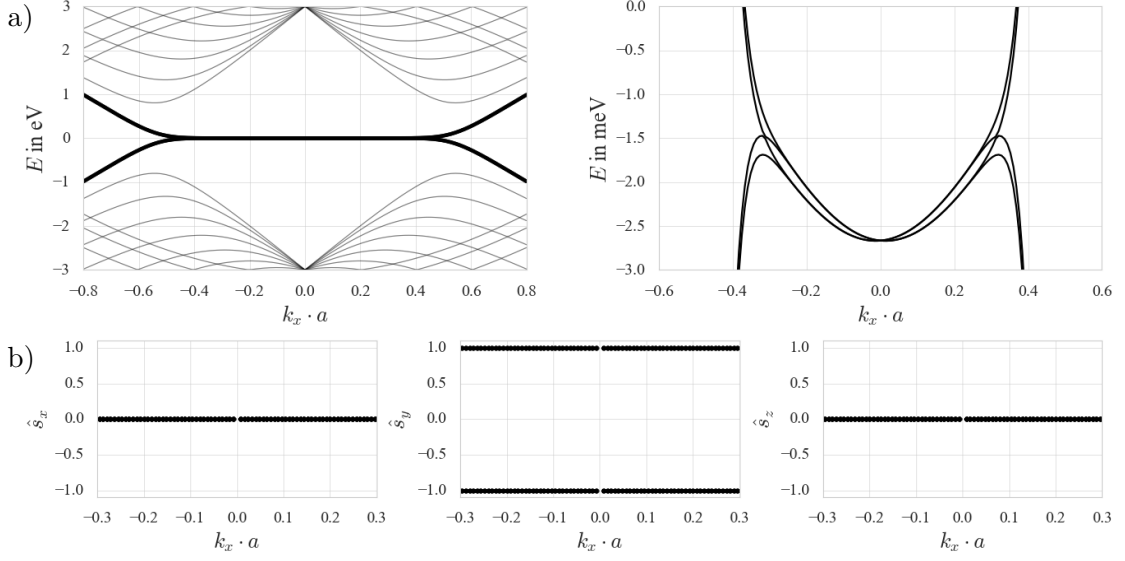
FIGURE 7.6.: a) Band structure of a nanoribbon with a unit cell of 16 rows and 4 columns with $\xi_p = 5\,\text{meV}$. Circular bending perpendicular to the edge with bending radius $R = 30\,\text{nm}$ is applied. On the right is a zoom on the detail features of the edge states bands. b) $\langle\hat{s}_x\rangle$, $\langle\hat{s}_y\rangle$ and $\langle\hat{s}_z\rangle$ expectation values of the four edge states.

there is no $\langle\hat{s}_x\rangle$- or $\langle\hat{s}_z\rangle$-component, which is consistent with the discussion in Sec. 7.5.1. In the following, the analysis will be focused on the competition of the bending-induced in comparison with the intrinsic spin-orbit coupling. Central to this is the direction of spin polarization of the edge states. Therefore, the components of the spin expectation value $\langle\hat{\vec{s}}\rangle$ of an edge atom l is computed via

$$\langle\hat{s}_i(l)\rangle = \sum_{\sigma,\sigma'}\sum_{\mu,\nu} a^\dagger_{l,\mu,\sigma} a_{l,\nu,\sigma'} \hat{s}_i^{\sigma,\sigma'}, \tag{7.44}$$

where the coefficients of the wave function used in Sec. 7.3 are written with an additional spin index σ, which also denotes the components of the spin Pauli matrix. In Eq. 7.44 the basis of wave functions with a set of quantum numbers with respect to the local quantization axis is used. Therefore the projection of the expectation value $\langle\hat{\vec{s}}\rangle$ on the local normal $\vec{n}$ is used to compute the angle ϕ, allowing to quantify the alignment of spin and sample. The projection of the spin will be identical for the sites along each edge and while the quantization axes of the two states at a single edge are identical, their respective axis is not parallel to the quantization axis of the states at the opposite edge, see Sec. 7.5.2. The angle ϕ, which was motivated in Fig. 7.3 b), is shown in Fig. 7.7 a) for $\xi_p = 5\,\text{meV}$ in dependence of the inverse radius of curvature $\frac{1}{R} \sim \theta$. A schematic of the edge sites and the direction of the spin is also shown in c) of the figure. The alignment of the spin is very sensitive to the deformation,
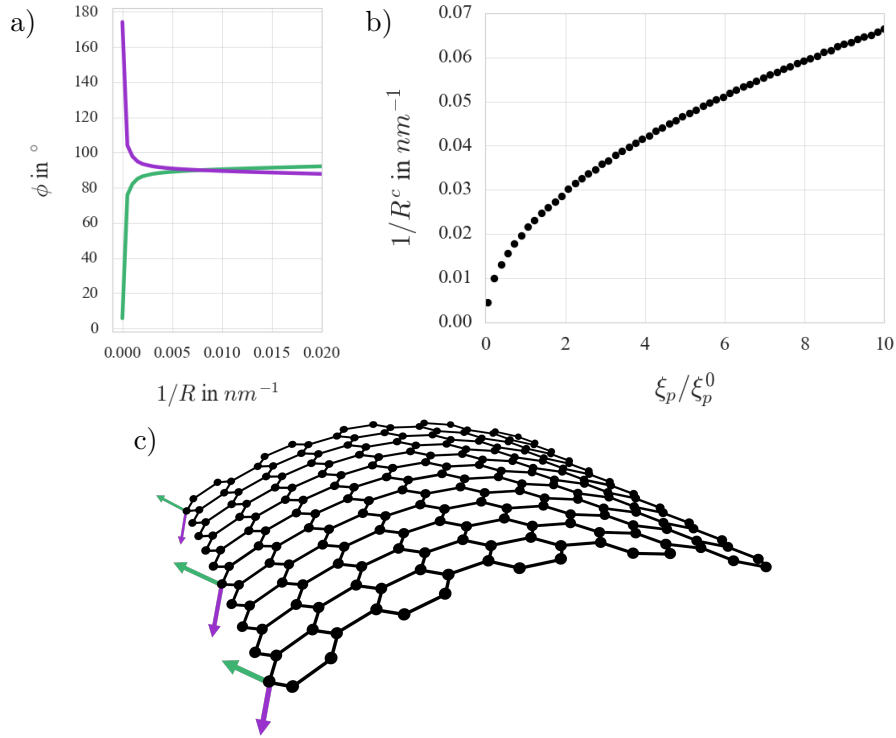
FIGURE 7.7.: a) The angle ϕ of the spin relative to the quantization axis at an edge site of a ribbon with 16 rows and 4 columns for varying $\frac{1}{R}$. b) The critical radius $1/R^c$, where the spins align parallel to the surface normal is plotted against the intrinsic spin-orbit coupling parameter ξ_p in units of $\xi_p^0 = 5\,\mathrm{meV}$. c) d) Schematic of the circular deformation. The spin alignment is indicated by the colors, corresponding to those in a).

as already for $\frac{1}{R} \approx 0.007\,\mathrm{nm}^{-1}$ the two edge states at each edge align their spin completely in-plane, even though the sample is barely deformed. The alignment of $\langle \hat{\vec{s}} \rangle$ with respect to the local normal at the sample edges defines the angle

$$\phi = \arccos \frac{\langle \hat{\vec{s}} \rangle \cdot \vec{v}}{|\langle \hat{\vec{s}} \rangle||\vec{v}|} \approx \frac{\pi}{2} - \langle \hat{s}_z \rangle, \tag{7.45}$$

where $\vec{v} = \vec{v}_1 \times \vec{v}_2$ is given by the normal vector at an edge site l and is obtained from vectors pointing to two of its neighbors, as defined in Fig. 7.3 b). The magnitude of the z-component of the spin is mainly governed by a competition of the terms $|C_{nn}|$ and $|B_{nn}|$, as in Eqs. 7.17 and 7.16. Therefore, a measure of the the spin alignment can be found in

$$\frac{|C_{nn}(\theta)|}{|B_{nn}(\theta)|} = \frac{\xi_p^2 \varepsilon_s \varepsilon' \frac{\sqrt{3}}{2} V_{sp\sigma}^2 \cos(\theta)}{\xi_p(\varepsilon')^2 \varepsilon_s \frac{\sqrt{3}}{2} V_{sp\sigma}^2 \sin(\theta)} \approx \frac{1}{\varepsilon'} \frac{\xi_p}{\theta} \tag{7.46}$$
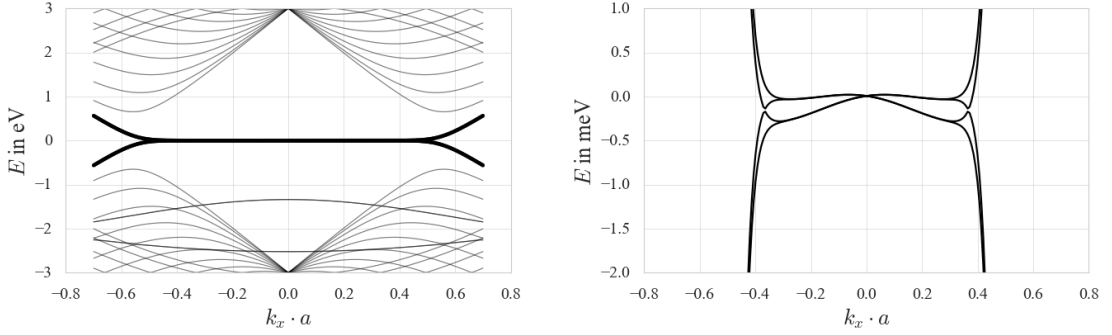
FIGURE 7.8.: Band structure of a nanoribbon with a unit cell with 16 rows and 4 columns with $\xi_p = 5\,\mathrm{meV}$, but no passivation with hydrogen atoms at the edges. The radius of curvature is $R = 30\,\mathrm{nm}$. On the right a detail of the edge states dispersion is depicted.

for small deformations. If this term diverges (or is very large), the spin is (mostly) aligned in z-direction and if it is very small, it is mostly aligned in y-direction. The effective intrinsic spin-orbit coupling term $|C_{nn}|$ scales as $\sim \xi_p^2$, while the bending-induced term scales as $|B_{nn}| \sim \xi_p$ and therefore, an increased ξ_p leads to stronger $\hat{s}_z$-polarization of the edge states.

When the curvature increases, the spins successively align perpendicular to the local axis of quantization, which is clearly seen in the behavior of the angle $\phi \sim \frac{1}{(1/R)}$ in Fig. 7.7 a) and is also found in Eq. 7.46. Thus, the influence of the intrinsic spin-orbit coupling C_{nn} decays as $\frac{1}{(1/R)}$. In other words: The effect of the bending-induced Rashba-type spin-orbit coupling will increase with increased bending angle $\theta \sim \frac{1}{R}$ and is inversely proportional to ξ_p. The point where both edge states exhibit a spin-projection with their local normal of $\phi = 90°$ is mainly given by ξ_p and will be denoted the *critical inverse bending radius* $\frac{1}{R^c}$ in the following. As it is the point where the bending-induced spin-orbit coupling clearly dominates over the intrinsic one, it can be considered a measure of this competition, and it will therefore be central to the discussion in the following.

Let the proportion of B_{nn} and C_{nn} be fixed, such that the spins fully align in the sample plane. Then at any given ξ_p, Eq. 7.46 can be used to compute $\frac{1}{R^c}$, because it directly follows that

$$\frac{1}{R^c} = \frac{|B_{nn,c}|}{|C_{nn,c}|} \frac{\xi_p}{\varepsilon'}, \tag{7.47}$$

which is shown in Fig. 7.7 b) for a ribbon with 16 columns and 4 rows for varying ξ_p. The linear relation of $\frac{1}{R^c}$ on ξ_p is confirmed for larger values, but the approximation becomes inaccurate for smaller ξ_p, due to the neglected terms in Eq. 7.15 and the approximation of relating Eq. 7.46 with ϕ in Eq. 7.45.

Role of Edge Passivation

In a single-orbital model with p_z-orbitals, the low-energy description of graphene is adequate without considering the s-, p_x- and p_y-orbitals, because of their symmetry. If the tight-binding model is extended and these additional orbitals are included, the broken sp^2-hybridization of the sample creates localized states at the edges, due to the dangling bonds. These states are indicated by two doubly degenerate bands in the dispersion relation, shown in the left of Fig. 7.8 at $-1.2\,\mathrm{eV}$ and $-2.5\,\mathrm{eV}$ at the Γ-point. While the occurrence of these states due to the lack of the passivation does not influence the π-bands at the Fermi energy in a flat sample, the passivation becomes relevant, when the sample is deformed. As was shown above, a central aspect of the deformation is the direction-specific coupling of the p_z-orbitals at a given site with the s-orbitals of the neighboring sites. When a sample without passivation of the edge sites with hydrogen atoms is deformed along the direction perpendicular to the edges, the p_z-orbitals at the edges do not have such a target s-orbital, which affects the dispersion relation of the edge states in the unpassivated case compared to a passivated system. In the right of Fig. 7.8, a dispersion of the edge states for an unpassivated sample with a radius of curvature $R = 30\,\mathrm{nm}$ is shown. Compared to the passivated edge state dispersion in Fig. 7.6, the lack of energy shift at the Γ-point is observed. Other than that, the broken symmetry of the lattice at the edges indicates that the dispersion of the edges is described directly by the third term in Eq. 7.18, which is to great extend given by the coupling of the edge sites to the neighboring hydrogen atoms. For higher momenta, the dispersion of the edge states of the passivated and unpassivated cases becomes comparable and an energy splitting of $0.25\,\mathrm{meV}$ at $k_x \cdot a \approx 0.4$ is observed in both cases. An overall shift of the passivated edge band is, however, still not reproduced by the unpassivated case. In the following the passivation of the edge sites will always be assumed.

7.6.2. Sinusoidal Bending Perpendicular to the Edge

The deformation along the y-direction was only considered with constant curvature up to now. This had two major implications. First, the sample does not exhibit inversion symmetry, and second, the edge bands are always hybridized with the s-orbitals of the neighboring atoms, because of the finite overlap due to the bending. Both of these features can be controlled individually, once a variation of curvature in the form of a sinusoidal deformation[4] is considered. Such a sinusoidal deformation $h(y)$ of the lattice sites polarizes p_z- and s-orbitals differently in different parts of the ribbon, depending on the phase of the deformation. If the sample edges are located at the nodes of the sinusoidal deformation, the polarization will be zero and thus the bulk contribution to the edge dispersion is rather flat. When the wavelength of the deformation is changed, such that the edges are located at the hills

---

[4]This function describes the displacement along the z-direction of the sites of a ribbon in dependence of their y-coordinates. It is chosen in such way, that the interatomic distances are kept unchanged from those of the flat ribbon and only the angles change.
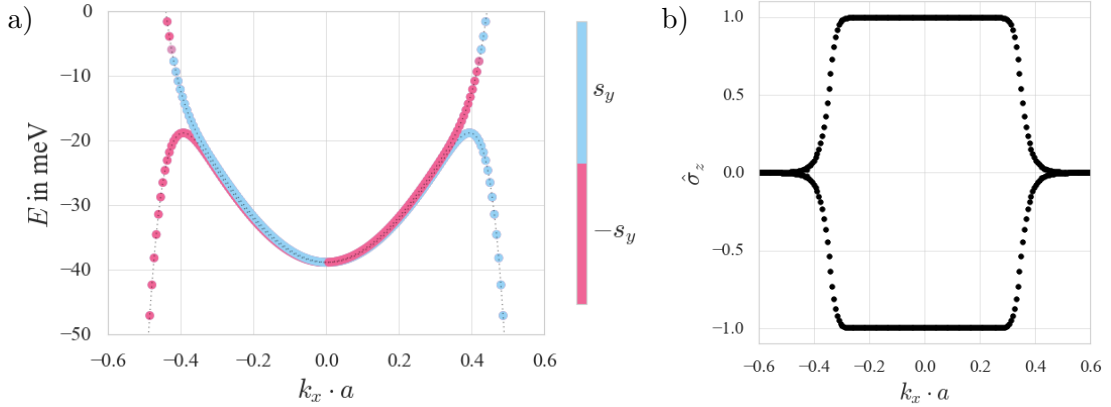
FIGURE 7.9.: a) Dispersion relation of a nanoribbon with 16 rows and 4 columns for $\xi_p = 5\,\text{meV}$, with a sinusoidal deformation of wavelength $\lambda \approx 14.7\,a$ and amplitude $A = a$, where a is the lattice constant. The edge states are colored by $\langle \hat{s}_y \rangle = \pm 1$. b) The sublattice spin expectation values show that in the Brillouin zone center the edge states are complete localized at the edges.

and valleys of $h(y)$, the dispersion becomes stronger, because of the energy shift due to the p_z-s-hybridization at the edges.

In the following the center of the ribbon is always considered to be at a node of $h(y)$ for a sinusoidal deformation, which will enforce inversion symmetry, regardless of amplitude A or wavelength λ of the deformation. If the phase of the deformation is shifted, such that the center of the ribbon is located at a hill or valley of $h(y)$ on the other hand, the inversion symmetry is broken, while a mirror symmetry is still intact. This corresponds to a cosinusoidal deformation. In both cases the center of inversion (or the symmetry axis) is not coinciding with a lattice site. The main difference of the systems arising from this phase shift of the deformation, is the missing energy degeneracy, as was discussed in Sec. 7.5.2. Both of these aspects will be discussed below, but before, the similarities compared to the deformation with constant curvature will be highlighted.

In Fig. 7.9 a) the edge state dispersion of a nanoribbon with a sinusoidal deformation of $\lambda \approx 14.7a$ and an amplitude of $A = a$ is shown. The y-component of the spin expectation value for each of the states is used to color the dispersion, which is polarized to nearly ± 1 and where $\langle \hat{s}_z \rangle \approx 0.05$. There is no x-component, similar to the case with constant curvature. The wavelength is chosen in a way, that the edges are located at two hills of $h(y)$, similar to the case depicted in Fig. 7.10 c). The finite curvature at the edges is responsible for the energy shift of $-38\,\text{meV}$ at the Brillouin zone center. At this particular point the edge states are four-fold degenerate and the $\langle \hat{s}_y \rangle$-polarization indicates a crossing. The states are fully sublattice spin polarized, as can be seen in Fig. 7.9 b).

Next, the impact of the deformation on the edge state dispersion is studied. A nanoribbon with 20 rows is considered, but the wavelength of the deformation is varied, while the

FIGURE 7.10.: Dispersion relations of edge states for sinusoidal deformation with amplitude $A = 0.5a$ for different wavelengths λ, where the center of the sample is always at a node of the deformation, such that it is inversion symmetric. The sample has 20 rows and 4 columns with $\xi_p = 5\,\mathrm{meV}$. a) $\lambda \approx 47.9\,\mathrm{a}$, b) $\lambda \approx 23.8\,\mathrm{a}$, c) $\lambda \approx 15.7\,\mathrm{a}$, d) $\lambda \approx 11.6\,\mathrm{a}$, e) $\lambda \approx 9.0\,\mathrm{a}$.

amplitude is kept constant at $A = 0.5a$. The center of the ribbon is always at a node of the deformation, such that mirror symmetry is ensured. The results are depicted in Fig. 7.10.

In a) $\lambda \approx 47.9\,\mathrm{a}$ is chosen, such that both edges are located at a valley of $h(y)$ and $\lambda/2$ fits in the length of the ribbon. This deformation is similar in appearance as the circular deformation, but here the local quantization axes of the edge states are collinear, ensuring
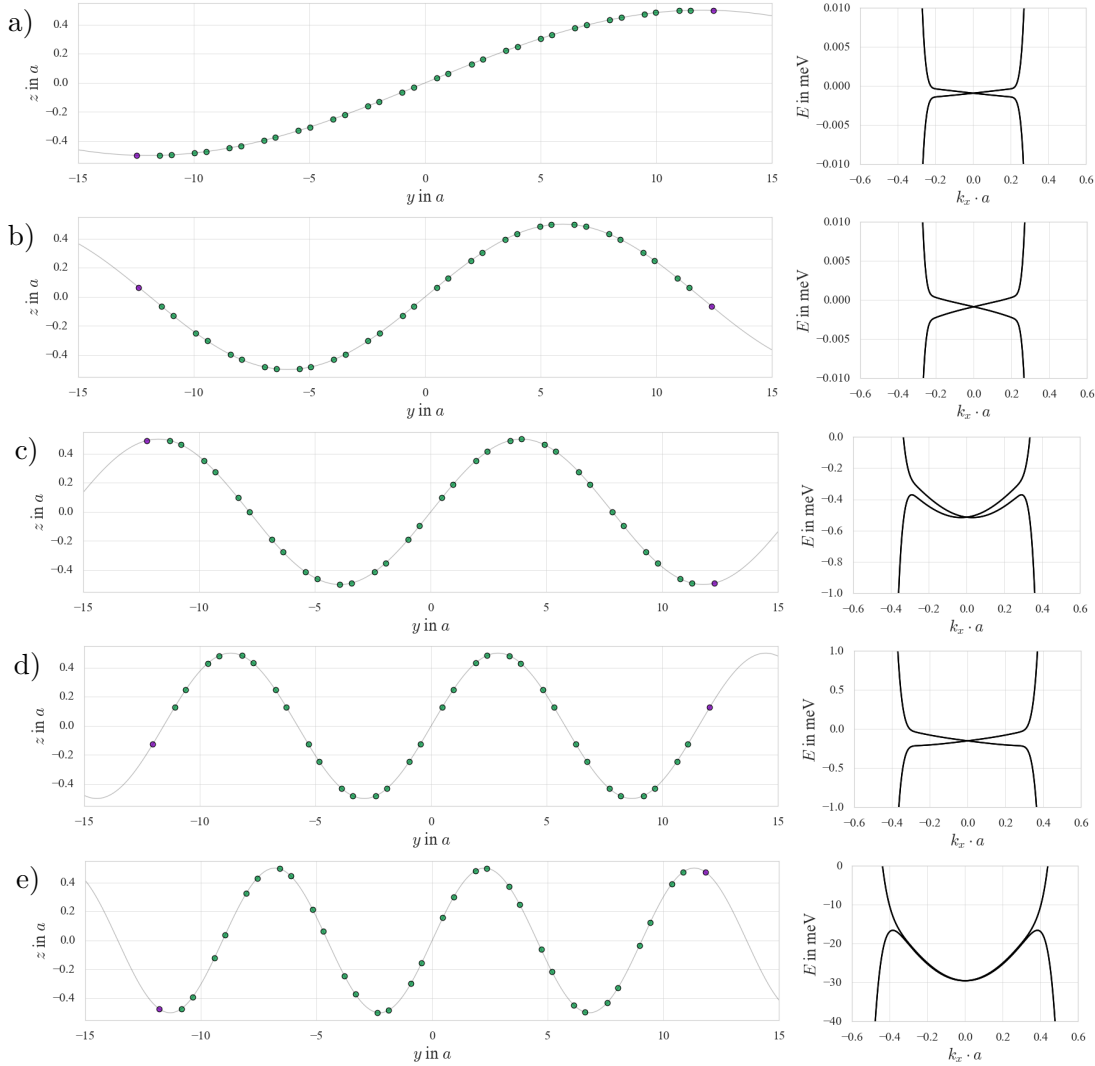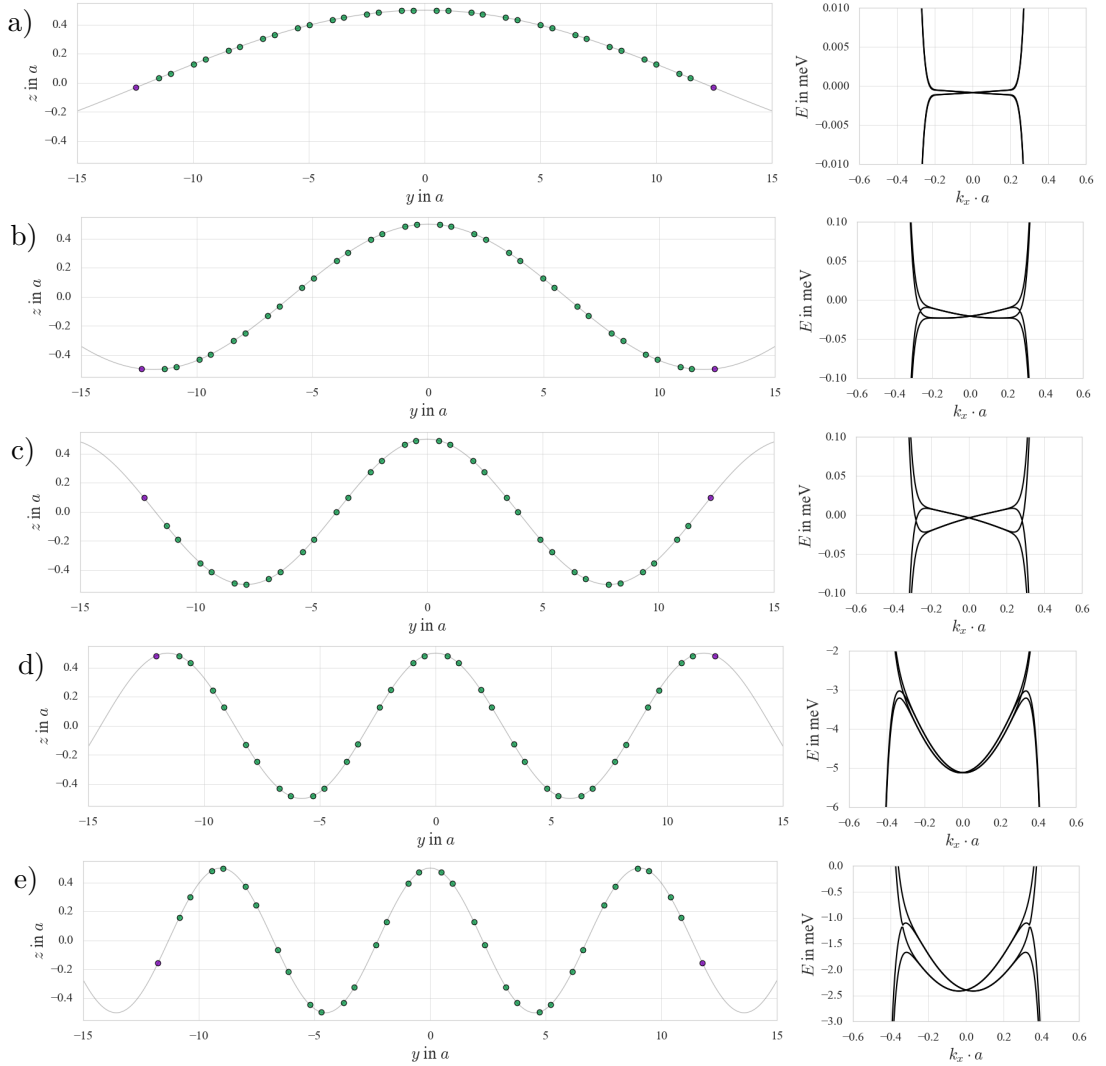
FIGURE 7.11.: Dispersion relations of edge states for sinusoidal deformation with amplitude $A = 0.5a$ for different wavelengths λ, where the center of the sample is always at a valley of the deformation. The sample does not exhibit inversion symmetry, it has 20 rows and 4 columns with $\xi_p = 5\,\text{meV}$. a) $\lambda \approx 47.9\,\text{a}$, b) $\lambda \approx 23.8\,\text{a}$, c) $\lambda \approx 15.7\,\text{a}$, d) $\lambda \approx 11.6\,\text{a}$, e) $\lambda \approx 9.0\,\text{a}$.

two-fold degeneracy with respect to the ↑- and ↓-spin-projections on this axis. The almost flat dispersion of the edge states is a result of the very small curvature at the edges. The states exhibit a small energy shift away from $E = 0$ and a small slope, due to the energy splitting $\sim 1\,\mu\text{eV}$ away from the Brillouin zone center, as a result of the intrinsic spin-orbit coupling. In Fig. 7.10 b) the sample exhibits one full oscillation of $h(y)$ and both edges

are located at nodes of the sinusoidal deformation. This case is qualitatively similar to a), because the curvature at the edge sites is zero and the influence of the bulk does not have a significant impact. For higher momenta, the energy splitting of the edge states has doubled compared to a). In c) λ is 2/3 of the ribbon length and the edges are located at the valleys of the deformation. The curvature is large enough, such that a comparable dispersion relation of the circular deformation can be observed.

In d) λ is 1/2 of the ribbon length and the dispersion of the edge states is again almost flat. This indicates, that the lack of p_z-s-hybridization of the edges is responsible for the lack of edge dispersion, despite the deformation with larger curvature in the bulk. An increased overall energy shift of $\sim 0.1\,\mathrm{meV}$, compared to a) is observed. In e) the much higher curvature causes a strong dispersion of the edges and a larger shift across the whole Brillouin zone, which reaches $\sim 30\,\mathrm{meV}$ at the center.

As a next step, the procedure is repeated for the cosinusoidal deformation, which breaks the inversion symmetry of the ribbon, by shifting the center of the ribbon from a node to a hill of $h(y)$. The same ribbons with a deformation of amplitude $A = 0.5a$ are considered and the same wavelengths are chosen, which results in the dispersions relations depicted in Fig. 7.11. Similar to the previous figure, the cases in a)-c) show very little influence on the dispersion of the edge states, due to the small curvature of $h(y)$. The broken inversion symmetry leads to similar results as in the previous section with circular deformation but in a) the weak energy splitting is not visible on the scale of the figure. In Fig. 7.11 d), the curvature at the edges becomes dominant over the energy splitting, similar to the previous Fig. 7.10 e), because in both cases the edges are located at valley and are thus subject to the maximum curvature induced by the deformation. The energy shifts of both cases differ, because of their different wavelengths. In Fig. 7.11 e) the curvature of the deformation is strong enough to noticeably deform the dispersion relation, even though the edges are located at the nodes of $h(y)$ and thus not subject to p_z-s-hybridization. The overlap of the the edge states with the bulk sites lead to curvature effects, because of the bending-induced next-nearest-neighbor hopping.

The results obtained in this subsection can be related to the band splitting dispersions of the FM and AFM magnetic phases, which were discussed in Sec. 6.1. The missing $z \leftrightarrow -z$ symmetry of the FM phase has a similar degeneracy lifting effect on the bands as the ribbons in Fig. 7.11, while the intact symmetry of the AFM phase relates to those in Fig. 7.10.

7.6.3. Bending Parallel to the Edge

In this section, a deformation parallel to the periodic direction is considered. An example of a graphene nanoribbon with one-dimensional periodic boundary condition and constant curvature along this direction is a single wall carbon nanotube. Discussed in Sec. 7.5.2, the spins at the edges in this case align parallel to the edges for increased curvature. If the curvature in this case was to be non-constant, the Rashba-type spin-orbit coupling due to the varying bending angle results in a spin polarization with components along all three directions. In this discussion, a nanoribbon with 16 rows and 8 columns is considered, in

order to have enough sites along the periodic direction for one full oscillation of $\lambda = 6.15\,a$ with an amplitude of $A = 0.5\,a$. A schematic of the edge is shown in Fig. 7.12 f), where the sites of the unit cell are shown in purple and the atoms of the neighboring unit cell in yellow. A schematic of the sinusoidal deformation of the sample along the zigzag direction is depicted in Fig. 7.3 b). The dispersion relation is shown in Fig. 7.12 a), where $\xi_p = 50\,\text{meV}$. Also, a detail of the edge states is depicted on the right of the figure.

The dispersion of the edge states exhibits a different slope compared to the bending perpendicular to the periodic direction. The sign of the slope has changed compared to bending along the y-direction, because of the second term in Eq. 7.14. The varying bending angle as a result of the varying curvature along the edge causes a variation of the sign of the next-nearest-neighbor contribution, which changes to an effective positive next-nearest-neighbor hopping t'. A shift of $-1.3\,\text{meV}$ at the Brillouin zone center is found.

The spin expectation values of the edge states are given in Fig. 7.12 b). The spin aligns mostly in the xz-plane, but exhibits a finite $\hat{s}_y$-component, as opposed to the previous deformations, where no spin component perpendicular to the deformation direction was induced. In Fig. 7.12 c) the energies of the edge states are colored by edge and spin expectation value. As in previous cases, the helicity of the states is conserved and the states cross according to their $\langle \hat{\sigma}_z \cdot \hat{s}_z \rangle$-expectation values. In addition, the states are fully sublattice-spin polarized, as can be seen in Fig. 7.12 d). In e), a nanoribbon with 22 rows and 8 columns is considered with $\lambda = 4.17\,a$ and $A = 0.8\,a$. The wider unit cell introduces additional bulk bands and the deformation perturbs the translational symmetry of the flat edge states strongly. It thereby causes band folding around the Dirac cones.

136
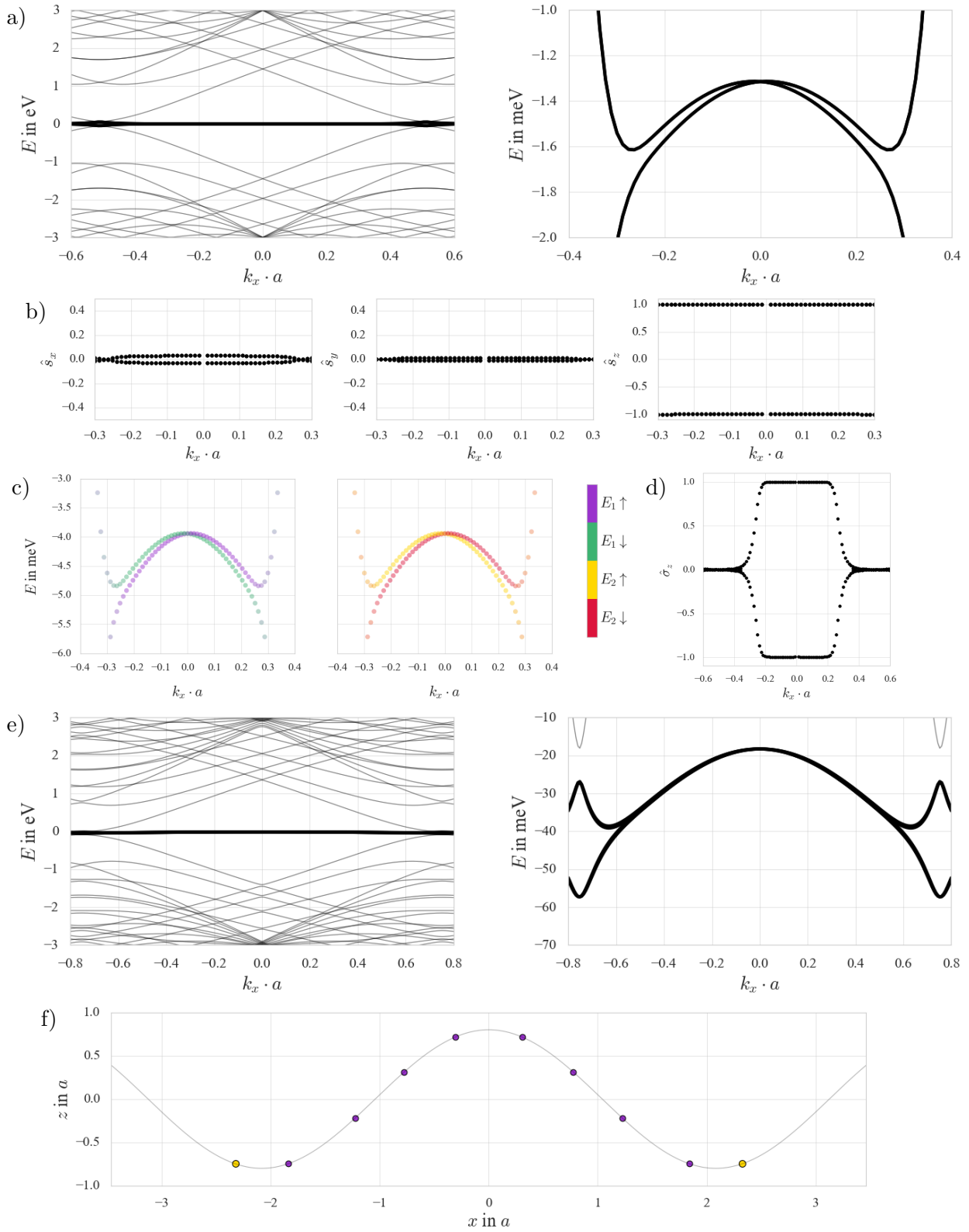
FIGURE 7.12.: a) Dispersion relation of the nanoribbon with 16 rows and 8 columns with $\xi_p = 50\,\text{meV}$ with a sinusoidal deformation of $A = 0.5\,\text{a}$ and $\lambda = 6.15\,\text{a}$. b) The spin expectation values of the edge states. c) Edge state dispersion colored by edge and $\hat{s}_z$ expectation value. d) The sublattice spin expectation value of the edge states. e) Dispersion relation, where 22 rows and 8 columns and $\xi_p = 50\,\text{meV}$ with $A = 0.8\,\text{a}$ and $\lambda = 4.17\,\text{a}$. f) A schematic of the deformation. The purple sites belong to the same unit cell and the yellow ones to neighboring unit cells.

7.7. Localized States in Bent Nanoribbons

In this section, the occurrence of bulk localized states is discussed, which arise due to bending-induced gauge potentials. These potentials have different sources, such as the nearest- and next-nearest-neighbor hopping matrix elements, which may lead to a vector potential, causing a pseudomagnetic field and a scalar gauge potential.

In general, a pseudomagnetic field in localized highly-curved regions of graphene nanoribbons leads to sublattice spin-polarized states, confined to these regions [281, 290]. In Eq. 7.39 the generation of a pseudomagnetic field as a result of the spatially-dependent nearest-neighbor hopping was discussed. For bending along the direction perpendicular to the zigzag edges, the pseudo vector potential causes a pseudomagnetic field, whenever the curvature varies along the bending direction. In the case of a sinusoidal deformation $h(y)$, the curvature $\kappa(y) = \frac{\partial^2 h(y)}{\partial y^2} / \sqrt{1 + \frac{\partial h}{\partial y}^2}^3$ is zero at the nodes, while it increases closer to a valley. Directly at a valley, the curvature reaches a maximum, and it decays again when the next node is approached. Thus the derivative of the curvature $\frac{\partial \kappa(y)}{\partial y}$ changes sign at the valleys of the sinusoidal deformation.

Using a relation of the curvature and its bending angle $\theta(y) = a \cdot \kappa(y)$ [187], with the lattice constant a, it is straight-forward to show that the pseudomagnetic field in Eq. 7.39 as a result of the variation $V_{pp\pi} - t_{zz}(\theta)$ in the nearest-neighbor hopping in the term A_n in Eq. 7.9, is given by

$$B_z = \frac{2\hbar a}{3} \left(1 - \frac{V_{pp\sigma}}{V_{pp\pi}} \right) \kappa(y) \frac{\partial \kappa(y)}{\partial y}. \tag{7.48}$$

The pseudomagnetic field can be used to explain the nearly-flat dispersion of the localized states around points of extremal curvature in the ribbon. This mechanism works on basis of the same principle as the localization of states at zigzag edges of flat graphene nanoribbons, which was discussed in previous chapters. The sample edges exhibit a sublattice-spin polarizing potential, which is caused by a change of the topological constant at the sample boundaries and leads to localized states with flat dispersion.

In the bulk, the generation of localized states is facilitated by a change of sign of the pseudomagnetic field as a consequence of a variation of the vector potential $A(y)$. If this effect is very strong, sublattice-spin polarized localized states are created, which have exponentially small occupation of nearby bulk sites [290]. Similar to the gap-crossing edge states, these bulk states show a flat energy dispersion around the Brillouin zone center. Thus, a strong deformation of a sample may have an effect similar to that of an actual edge, where the regular sample lattice is terminated.

In addition to the vector potential $A(y)$, another gauge potential, the scalar potential $\Phi(y)$, occurs for sinusoidal deformation perpendicular to the sample edges. By doing an analysis
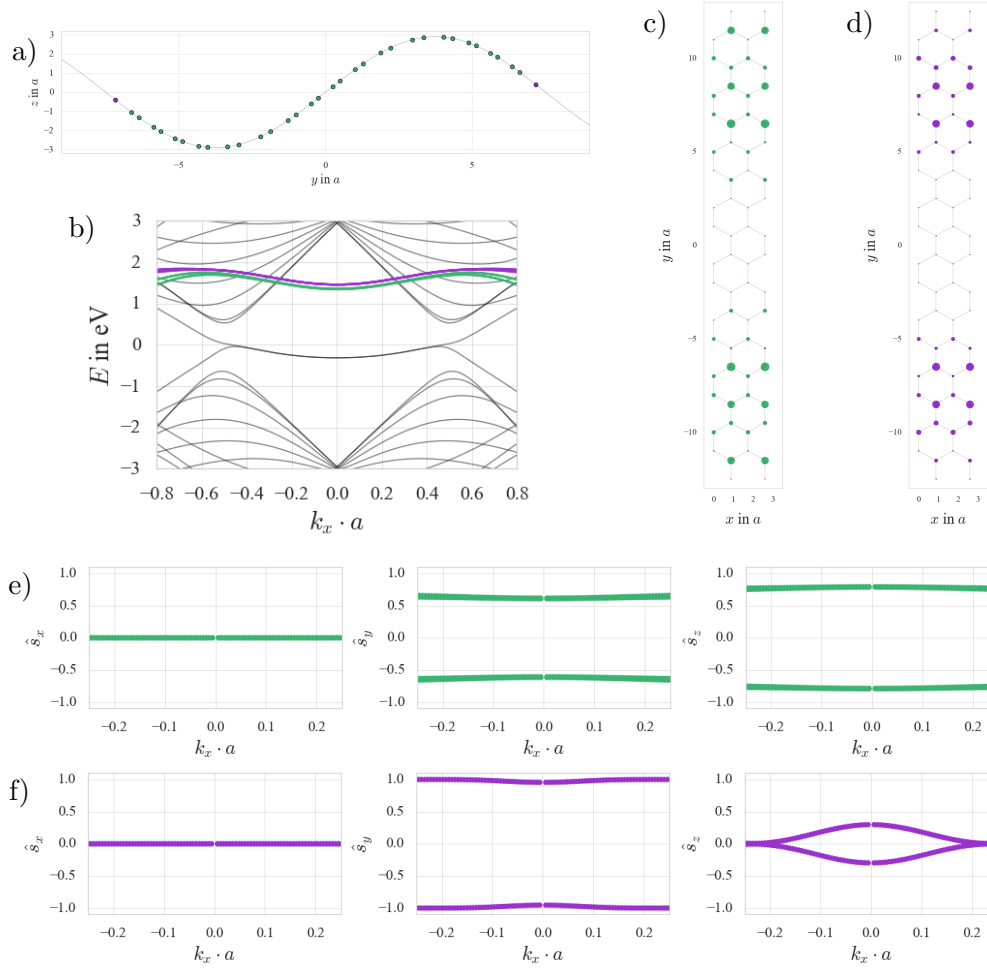
FIGURE 7.13.: a) A schematic overview of the bent nanoribbon with amplitude $A = 2.9a$ and wavelength $\lambda = 15\,a$. b) Dispersion of a bent ribbon with 16 rows, 4 columns and $\xi_p = 5\,\text{meV}$. Several bulk bands are highlighted. c) and d) Spatial distribution of the states color-coded by the bands from a). Spin expectation values of the four bulk states from the green bands e) and of the four bulk states from the purple bands f) as given in a).

of the energy shift ε'', the dominant terms in Eq. 7.18 lead to the scalar potential

$$\Phi(y) = -\frac{1}{\varepsilon_s}V_{sp\sigma}^2 a^2 \kappa(y)^2 + \frac{1}{\varepsilon'}(V_{pp\sigma} - V_{pp\pi})^2 \frac{1}{2}a^2\kappa(y)^2. \tag{7.49}$$

Since it arises from a variation of the next-nearest-neighbor hopping, $\Phi(y)$ stabilizes the sublattice polarization, because it enhances the interaction with the pseudomagnetic field as a consequence of the stronger confinement to states belonging to either sublattice [290].

For an inversion-symmetric sinusoidal deformation with $A = 2.9a$ and a wavelength of

FIGURE 7.14.: a) The pseudomagnetic field B changes sign and b) the scalar potential $\Phi(y)$ exhibits minima at points of extremal deformation.

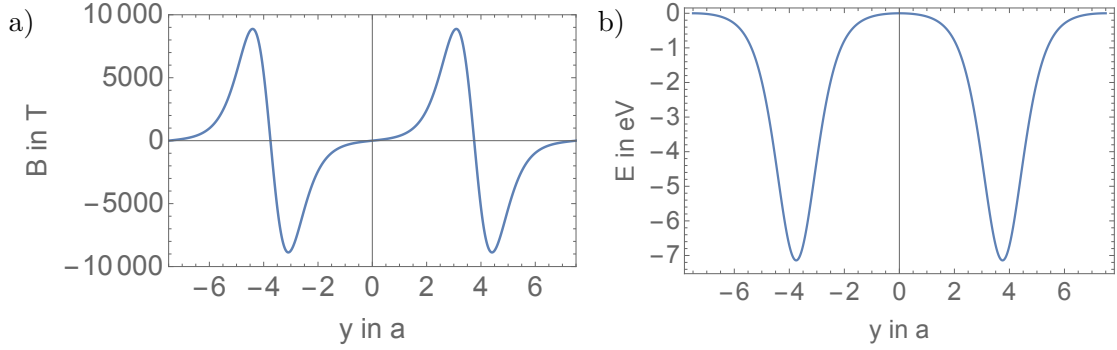$\lambda = 15\,\text{a}$, a nanoribbon with 16 rows and 4 columns is considered, where $\xi_p = 5\,\text{meV}$. This is schematically depicted in Fig. 7.13 a). The edges are located at nodes of the deformation. In b) the dispersion relation of this ribbon is shown, which is similar in appearance to previous dispersions relations for such bending, with the exception of two prominent bands, depicted in green and purple. These bands are comparably flat, similar to the edge states and shifted by $1.3\,\text{eV}$ and $1.5\,\text{eV}$ from the Fermi energy. There are two green bands with nearly identical spatial distribution. The site occupation of one of them is shown in Fig. 7.13 c)[5]. Each of the two bands is two-fold spin-degenerate. The other four purple bands are also doubly-energy degenerate and have a slightly different spatial distribution, which can be seen in Fig. 7.13 d). The $\langle \hat{s}_i \rangle$-expectation values shown in Figs. 7.13 e) and f) indicate that the states are polarized in the yz-plane, similar to the edge states. The findings confirm those regarding the direction-dependent spin-alignment from previous section also for these bulk states.

The states of the purple bands are localized around the hills of the deformation a little more than the green states and the ratio of their spin expectation values is slightly different. The states cannot be separated in states localized around only one of the two areas and they are completely real spin-, but not fully sublattice spin-polarized, such that all states exhibit a finite occupation at both sides of the ribbon. The lack of total sublattice-spin polarization of these localized bulk states is an indicator for the contribution of the pseudomagnetic field in Eq. 7.48 to their localization and that the scalar potential in Eq. 7.49 also has a large influence. In Fig. 7.14 a) the pseudomagnetic field $|B_z(y)|$ is shown. The sign change of $B_z(y)$ at points of extremal curvature is visible, as well as the large magnitude of approximately $B \sim 10^4\,\text{T}$, causing the weak sublattice polarization, observable in Figs 7.13 c) and d). This result is in good agreement with the value of $10^5\,\text{T}$ expected for the occurrence of fully sublattice spin polarized edge states obtained by Sasaki et al. [290].

---

[5]Both spatial distributions are given schematically in coordinates for a flat ribbon, because using the curved ribbon coordinates would lead to a deformed projection. Thus the y-coordinates in the two spatial distributions actually range from $-7a$ to $+7a$ as indicated by the y-coordinates in Fig. 7.13 a).

In Fig. 7.14 b) the scalar potential $\Phi(y)$ is shown. It is observable that the points of lowest potential energy coincide with the points where $B_z(y)$ changes sign. The scalar potential is negative everywhere in the sample.

In a next step, the amplitude and wavelength of the deformation is reduced, in order to keep the curvature at the valleys and hills constant, but include more oscillations in the ribbon. The result is shown in Fig. 7.15 for a deformed nanoribbon with 16 rows, where $A = 1.5\,a$ and $\lambda = 7.5\,a$. In the dispersion relation, shown in ii), there are six flat bands observable. These correspond to four states each and are labelled A-F. The edge states of the system are at $-1\,eV$. The states still cross the band gap despite the deformation, which is indicated by the black circle in ii) and are well localized at the edges, as shown in a), where the spatial distribution at $k_x = 0$ is depicted. The four states of the B band split into two bands away from the Γ-point of the Brillouin zone, as can be seen from the green circle in ii). The spatial distribution of two states from B is shown in b), and the comparable features indicate that the four states are very similar, despite their energy separation. The states are localized close to the edges, but with a dominant occupation of the sites around at the nearby hill and valley of the deformation. The states C-F, shown in c)-f), have also a significant localization on sites belonging to the points of extremal curvature. This is particularly noticeable in E and F. The former consists of states, which are located at only four sites directly at an area with maximum curvature. The latter has dominant contribution at all the four valleys and hills.

In addition to the states presented here, there are many more flat bands in the dispersion relation for this nanoribbon, higher in energy. While it is possible to use different deformations, to bring the energy of such states closer to $E = 0$, the energy of the edge states (A) will also shift as a result. For the deformation strengths applied in this work, no other flat bands could be observed energetically close to the edge states.

To summarize, the curvature of the deformation leads to a variation of the nearest- and next-nearest-neighbor hopping. This variation is shown to lead to sublattice spin-polarizing pseudomagnetic fields and stabilizing scalar potentials. Together, they may facilitate the creation of localized bulk states with nearly flat dispersion. While the curvature required for the existence of perfectly localized and sublattice spin-polarized states might be very strong, moderate deformations, on the order of the lattice constant a are already enough to create the gauge potentials required for localized bulk states. It is possible for these deformation strengths to occur in experiments and they may not always be fully eliminated. Thus, the analysis provided in this section may serve as an estimate of the charge inhomogeneities introduced by bending of graphene nanoribbons.
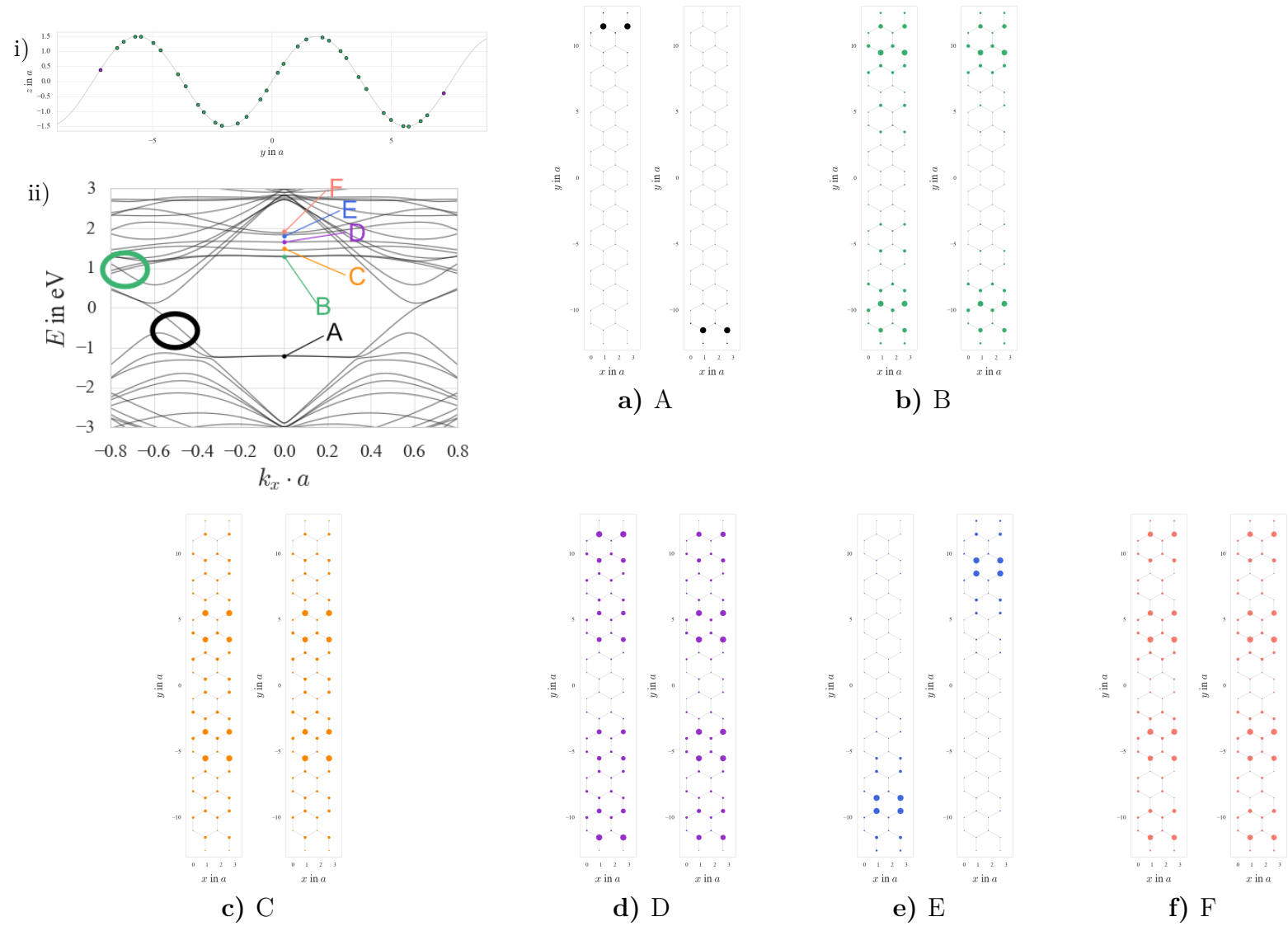
FIGURE 7.15.: A deformed nanoribbon with 16 rows, where $\xi_p = 5\,\text{meV}$, $A = 1.45\,\text{a}$ and $\lambda = 7.5\,\text{a}$. i) The sites of the sample. ii) The dispersion relation features several flat bands. The black circle shows the gap crossing states and the green circle a splitting of the band B. a)-f) corresponds to the spatial distribution states at $k_x = 0$ where the bands are labeled A-F.

7.8. Perturbation Theory for Bending of Graphene with s-, p- and d-orbitals

Previous considerations have only treated s- and p-orbitals and their effect on the spin structure of graphene under deformations. Similar to the tight-binding model for the description of d-orbitals in flat graphene [286, 287], the additional bending-induced interactions from d- to p-orbitals also lead to the occurrence of Rashba-type spin-orbit coupling, a potential shift and an effective next-nearest-neighbor hopping term. Thus, in order to correctly derive the spin-orbit coupling interactions in bent graphene nanoribbons, the coupling of d- to p-orbitals must be accounted for as well.

The d-orbitals are separated from the p-orbitals by the energy ε_d and the d-band atomic spin-orbit interaction is given by the parameter ξ_d. While the energy separation of the s- and d-orbitals is $\sim 20\,\mathrm{eV}$, such that the s-d-coupling can be neglected in very good approximation, bending induces transitions between the in-plane p-orbitals and the in- and out-of-plane d-orbitals in general.

Before a full 9-orbital model is used to derive the Rashba-type spin-orbit coupling, a reduced 5-orbital model with p_x-, p_y- and p_z- and only two of the five d-orbitals, the d_{xz}- and d_{yz}-orbitals, is used to derive an effective term arising due to the d-orbital atomic spin-orbit coupling. Since the s-p-coupling was already derived and analyzed in the previous sections, the p-d-interactions are examined first, before a study of the full interplay of all terms in the 9-orbital model is undertaken. Due to the symmetry of the atomic orbitals, an effective description for understanding the nature of these interactions does not require all five d-orbitals, because the d_{xz}- and d_{yz}-orbitals are the dominant contributions. For understanding this 5-orbital model, the equations for each of the orbitals, similar to Eqs. 7.1 to 7.3 are rewritten to account for the interactions to the other orbitals. This results in the set of equations

$$(\varepsilon - \varepsilon_p)a_{\alpha,0} = \sum_{\alpha' \in \{x,y,z\}} \Lambda_\alpha^{\alpha'} a_{\alpha',0} + \sum_{n,\alpha' \in \{x,y,z\}} t_{\alpha,\alpha'}(\theta_n)a_{\alpha',n} + \sum_n \sum_{\beta \in \{xz,yz\}} t_{\alpha,\beta}(\theta_n)a_{\beta,n}$$

$$(7.50)$$

$$(\varepsilon - \varepsilon_d)a_{\beta,0} = \sum_{\beta' \in \{xz,yz\}} \Upsilon_\beta^{\beta'} a_{\beta',0} + \sum_{n,\alpha' \in \{x,y,z\}} t_{\beta,\alpha'}(\theta_n)a_{\alpha',n} + \sum_n \sum_{\beta' \in \{xz,yz\}} t_{\beta,\beta'}(\theta_n)a_{\beta',n},$$

$$(7.51)$$

where the index $\alpha \in \{x,y,z\}$ denotes the p-orbitals and the index $\beta \in \{xz,yz\}$ the d-orbitals. Thus, the last two terms in Eqs. 7.50 and 7.51 denote the hopping to neighboring p- and d-orbitals. The matrix elements Λ_ν^μ and Υ_ν^μ denote the p-orbital intrinsic spin-orbit coupling given in Eq. 3.23 and the d-orbital spin-orbit coupling in Eq. 3.24, respectively. The p-d-matrix elements are given in Tabs. 7.2, 7.3 and 7.4. The required matrix elements for the coupling of the occurring d-orbitals are stated in Tab 7.6 for completeness. By a similar

μ_1/ν_0	d_{xz}	d_{yz}
d_{xz}	$\sin{(\phi)}^2(V_{dd\delta} + (V_{dd\pi} - V_{dd\delta})\sin{(\theta)}^2)$ $+\frac{1}{8}(V_{dd\delta} + 4V_{dd\pi} + 3V_{dd\sigma}$ $-(V_{dd\delta} - 4V_{dd\pi} + 3V_{dd\sigma})\cos{(4\theta)})\cos{(\phi)}^2$	$-\frac{1}{4}\cos{(\theta)}^2(V_{dd\delta} + 2V_{dd\pi} - 3V_{dd\sigma}$ $+(V_{dd\delta} - 4V_{dd\pi} + 3V_{dd\sigma})(\cos{(\theta)}^2 - \sin{(\theta)}^2))\times$ $2\sin{(\phi)}\cos{(\phi)}$
d_{yz}	$-\frac{1}{4}\cos{(\theta)}^2(V_{dd\delta} + 2V_{dd\pi} - 3V_{dd\sigma}$ $+(V_{dd\delta} - 4V_{dd\pi} + 3V_{dd\sigma})(\cos{(\theta)}^2 - \sin{(\theta)}^2))\times$ $2\sin{(\phi)}\cos{(\phi)}$	$\cos{(\phi)}^2(V_{dd\delta} + (V_{dd\pi} - V_{dd\delta})\sin{(\theta)}^2)$ $+\frac{1}{8}(V_{dd\delta} + 4V_{dd\pi} + 3V_{dd\sigma}$ $-(V_{dd\delta} - 4V_{dd\pi} + 3V_{dd\sigma})\cos{(4\theta)})\sin{(\phi)}^2$

TABLE 7.6.: The Slater-Koster matrix elements for the relative angle θ of the normals between the d_{xz}- and d_{yz}-orbitals. They are denoted μ_1 and ν_0, where the indices 1 and 0 label corresponding sites.

procedure as in Sec. 7.3, the orbitals of neighboring sites are expressed as p_z-orbitals of next-nearest-neighboring sites. The terms obtained in the 5-orbital model, can later be added to the previous 4-model, because the s-d-interaction is neglected. As a result, the effective hopping for the p_z-orbitals of the 4-orbital model in Eq. 7.8 can be modified to

$$(\varepsilon - \varepsilon_p - \varepsilon'' - \varepsilon''_d)a_{z,0} = A_n + B_n + C_n + A_{nn} + B_{nn} + C_{nn} + A_{nn}^D + B_{nn}^D + C_{nn}^D, \quad (7.52)$$

with the additional terms A_{nn}^D, B_{nn}^D and C_{nn}^D. The effective contributions are a next-nearest-neighbor hopping

$$A_{nn}^D = \frac{1}{\varepsilon - \varepsilon_d} \sum_{n,n'\neq 0} [t_{z,xz}(\theta_n)\, t_{xz,z}(\theta_{n'}) + t_{z,yz}(\theta_n)\, t_{yz,z}(\theta_{n'})]\, a_{z,n'}, \quad (7.53)$$

and the effective intrinsic spin-orbit coupling

$$C_{nn}^D = -\frac{i\xi_d \hat{s}_z}{\varepsilon_d^2} \sum_{n,n'\neq 0} [t_{z,yz}(\theta_n)\, t_{xz,z}(\theta_{n'}) - t_{z,xz}(\theta_n)\, t_{yz,z}(\theta_{n'})]\, a_{z,n'}. \quad (7.54)$$

Due to the coupling of the p_z- and d-orbitals, an additional energy shift is obtained

$$\varepsilon''_d = \frac{1}{\varepsilon_d} \sum_n [t_{z,xz}(\theta_n)\, t_{xz,z}(\theta_n) + t_{z,yz}(\theta_n)\, t_{yz,z}(\theta_n)] \approx \frac{3V_{pd\pi}^2}{\varepsilon_d}. \quad (7.55)$$

While the dispersion relation of the edge states of a multi-orbital tight-binding model for flat ribbons has already been discussed briefly in Sec. 4.4, the dispersion in Fig. 4.2 can directly be attributed to the term A_{nn}^D. The coupling of the p_z- with the d_{xz}- and d_{yz}-orbitals leads to an effective next-nearest-neighbor model with a corresponding intra-lattice hopping $t'_d > 0$. This is in contrast to the effective bending-induced hopping parameter $t'_p < 0$ among

s- and p-orbitals, which leads to a different band dispersion and is observable in Fig. 7.6 a). Furthermore, t'_d occurs in flat graphene, while t'_p does not and thus $|t'_d| > |t'_p|$ for moderate deformations. The term A^D_{nn} is at least an order of magnitude larger than the corresponding one A_{nn}, even for very strong deformations. Thus the edge state dispersion of the effective 5-orbital model is only slightly deviating from that of a flat graphene sample with p_z-, d_{xz}- and d_{yz}-orbitals. There also occurs a Rashba-type spin-orbit coupling contribution

$$
\begin{aligned}
B^{D,0}_{nn} = -\frac{i\xi_p}{\varepsilon'\varepsilon_d} \sum_{n,n'\neq 0} & \left(\hat{s}_y \left[t_{x,xz}\left(\theta_n\right)t_{xz,z}\left(\theta_{n'}\right) + t_{x,yz}\left(\theta_n\right)t_{yz,z}\left(\theta_{n'}\right)\right] \right. \\
& \left. -\hat{s}_x \left[t_{y,xz}\left(\theta_n\right)t_{xz,z}\left(\theta_{n'}\right) + t_{y,yz}\left(\theta_n\right)t_{yz,z}\left(\theta_{n'}\right)\right]\right) a_{z,n'}.
\end{aligned}
\tag{7.56}
$$

Surprisingly, the Rashba contribution does not depend on the intrinsic spin-orbit coupling parameter ξ_d of the d-orbitals, but that of the p-orbitals. The reason is, that the hopping from the p-orbitals to the d-orbitals is dominant, compared to the hopping among d-orbitals. The terms in Eq. 7.56 do not have the correct symmetry to describe general deformations, however. This is indicated by the fact that the deformation-induced spin-polarization is not reflected correctly, because of the broken angular momentum conservation in the reduced 5-orbital model for arbitrary deformations. This is only possible if all five d-orbitals are considered. Therefore, an extended multi-orbital model is described next, which leads to the full interaction. As discussed above, the following derivation is stated without the s-orbitals. Because the dominant contribution to the atomic d-orbital spin-orbit coupling is given by Eq. 7.54 already, only the term B^D_{nn} in Eq. 7.52 will be modified by this approach. Otherwise the full 9-orbital model is also given by Eq. 7.52.

The equations for any site n and any neighboring sites n' are rewritten as in Eq. 7.6 for the p- and d-orbitals, such that

$$
(\varepsilon - \varepsilon_p)a_{\alpha,n} = \sum_{\alpha'} \Lambda^{\alpha'}_{\alpha} a_{\alpha',n} + \sum_{n',\alpha'} t_{\alpha,\alpha'}(\theta_{n'})a_{\alpha',n'} + \sum_{n'}\sum_{\beta} t_{\alpha,\beta}(\theta_{n'})a_{\beta,n'}
\tag{7.57}
$$

$$
(\varepsilon - \varepsilon_d)a_{\beta,n} = \sum_{\beta'} \Upsilon^{\beta'}_{\beta} a_{\beta',n} + \sum_{n',\alpha'} t_{\beta,\alpha'}(\theta_{n'})a_{\alpha',n'} + \sum_{n'}\sum_{\beta'} t_{\beta,\beta'}(\theta_{n'})a_{\beta',n'},
\tag{7.58}
$$

where the index $\alpha \in \{x, y, z\}$ again denotes the p-orbitals and the index $\beta \in \{xy, xz, yz, x^2 - y^2, z^2\}$ all five d-orbitals. The equations Eq. 7.57 and 7.58 can the be used analogously to Eq. 7.1 to find an effective next-nearest-neighbor hopping from a p_z-orbital at site 0 to a

p_z-orbital at its next-nearest-neighboring sites n'. This leads to

$$
(\varepsilon - \varepsilon_p)a_{z,0} = \sum_{\alpha} \Lambda_z^{\alpha} \frac{1}{\varepsilon'} \left(\sum_{\alpha'} \Lambda_{\alpha}^{\alpha'} a_{\alpha',0} + \sum_{n}\sum_{\alpha'} t_{\alpha,\alpha'}(\theta_n)a_{\alpha',n} + \sum_{n}\sum_{\beta} t_{\alpha,\beta}(\theta_n)a_{\beta,n} \right)
$$
$$
+ \sum_{\alpha}\sum_{n} t_{z,\alpha}(\theta_n)\frac{1}{\varepsilon'} \left(\sum_{\alpha'} \Lambda_{\alpha}^{\alpha'} a_{\alpha',0} + \sum_{n'}\sum_{\alpha'} t_{\alpha,\alpha'}(\theta_{n'})a_{\alpha',n'} + \sum_{n'}\sum_{\beta} t_{\alpha,\beta}(\theta_{n'})a_{\beta,n'} \right)
$$
$$
+ \sum_{\beta}\sum_{n} t_{z,\beta}(\theta_n)\frac{1}{\varepsilon - \varepsilon_d} \left(\sum_{\beta'} \Upsilon_{\beta}^{\beta'} a_{\beta',n} + \sum_{n'}\sum_{\alpha} t_{\beta,\alpha}(\theta_{n'})a_{\alpha,n'} + \sum_{n'}\sum_{\beta'} t_{\beta,\beta'}(\theta_{n'})a_{\beta',n'}. \right)
$$
$$\tag{7.59}$$

The third term in the first line of Eq. 7.59 leads to the Rashba-type spin-orbit coupling. It also describes terms of third order in either the intrinsic spin-orbit coupling or the hopping. Those will not be considered in this perturbation theory. The eighth term, in the last line, leads to the effective next-nearest-neighbor hopping, which has an effective form as in Eq. 7.53 due to the dominant matrix elements of p_z-, d_{xz}- and d_{yz}-orbitals. Due to the p-orbital intrinsic spin-orbit coupling it follows for the effective Rashba-type spin-orbit coupling term $B_{nn}^{D,1}$ that

$$
B_{nn}^{D,1} = \sum_{\alpha} \Lambda_z^{\alpha} \frac{1}{\varepsilon'} \sum_{n}\sum_{\beta} t_{\alpha,\beta}(\theta_n)\frac{1}{\varepsilon_d} \sum_{n'\neq 0} t_{\beta,z}(\theta_{n'})a_{z,n'}. \tag{7.60}
$$

Using Eq. 3.23, $\Lambda_z^{x} = -i\hat{s}_y\xi_p$, $\Lambda_z^{y} = i\hat{s}_x\xi_p$ and $\Lambda_z^{z} = 0$ are obtained. Thus, the effective Rashba-type contribution becomes

$$
B_{nn}^{D,1} = -\frac{i\xi_p}{\varepsilon'\varepsilon_d} \sum_{n,n'\neq 0} \left[\hat{s}_y \left(\sum_{\beta} t_{x,\beta}(\theta_n)t_{\beta,z}(\theta_{n'}) \right) - \hat{s}_x \left(\sum_{\beta} t_{y,\beta}(\theta_n)t_{\beta,z}(\theta_{n'}) \right) \right] a_{z,n'}. \tag{7.61}
$$

It is straightforward to show, that Eq. 7.56 is contained in this full expression. There is another bending-induced Rashba-type term, which arises due to the intrinsic spin-orbit coupling in the d-orbitals. It is contained in the seventh term, in the last line of Eq. 7.59, which can be rewritten as

$$
C_{nn}^{D} + B_{nn}^{D,2} = \sum_{\beta}\sum_{n} t_{z,\beta}(\theta_n)\frac{1}{(\varepsilon - \varepsilon_d)^2} \sum_{\beta'} \Upsilon_{\beta}^{\beta'} \sum_{n'\neq 0} t_{\beta',z}(\theta_{n'})a_{z,n'}, \tag{7.62}
$$

and is given by

$$
B_{nn}^{D,2} = -\frac{i\xi_d}{\varepsilon_d^2} \sum_{n,n'\neq 0} \sum_{l=1}^{3} v(l) \left[\hat{s}_y \left(t_{z,p(l,1)}(\theta_n)t_{p(l,2),z}(\theta_{n'}) - t_{z,p(l,2)}(\theta_n)t_{p(l,1),z}(\theta_{n'}) \right) \right.
$$
$$
\left. - \hat{s}_x \left(t_{z,q(l,1)}(\theta_n)t_{q(l,2),z}(\theta_{n'}) - t_{z,q(l,2)}(\theta_n)t_{q(l,1),z}(\theta_{n'}) \right) \right] a_{z,n'} \tag{7.63}
$$

and

$$C_{nn}^D = -\frac{i\xi_d \hat{s}_z}{\varepsilon_d^2} \sum_{n,n'\neq 0} \sum_{l=1}^{2} w(l) \left[t_{z,r(l,1)}(\theta_n) t_{r(l,2),z}(\theta_{n'}) - t_{z,r(l,2)}(\theta_n) t_{r(l,1),z}(\theta_{n'}) \right] a_{z,n'}. \quad (7.64)$$

For this notation,

$$(p(l,1), p(l,2)) \in \{(xz, xy), (x^2 - y^2, yz), (z^2, yz)\} \quad (7.65)$$

$$(q(l,1), q(l,2)) \in \{(xz, z^2), (x^2 - y^2, xz), (xy, yz)\} \quad (7.66)$$

$$(r(l,1), r(l,2)) \in \{(xz, yz), (xy, x^2 - y^2)\} \quad (7.67)$$

are introduced, which denote all of the pairs of orbitals relevant in the respective terms. The factors $v(l) \in \{1, 1, \sqrt{3}\}$ and $w(l) \in \{1, 2\}$ arise due to the numerical factors in the intrinsic spin-orbit coupling operator Eq. 3.24. The bending-induced d-orbital spin-orbit coupling in Eq. 7.63 is small, due to the second-order process in the energetically separate d-orbitals and because the bending-induced hopping matrix elements are small for small θ. It is important however, that $B_{nn}^{D,2} \sim \xi_d$, which will be of relevance in the following section. The effective form of the intrinsic spin-orbit coupling in Eq. 7.64, contains a dominant contribution, given by Eq. 7.54. Although C_{nn}^D has the same appearance as $B_{nn}^{D,2}$, the contribution to the spin alignment of the former is much more relevant, because the matrix elements $t_{xz,z}(\theta)$ and $t_{yz,z}(\theta)$ are much larger than $t_{xy,z}(\theta)$ or $t_{x^2-y^2,z}(\theta)$. The full bending-induced d-orbital Rashba-type spin-orbit coupling for the effective 9-orbital model in Eq. 7.52 is given by $B_{nn}^D = B_{nn}^{D,1} + B_{nn}^{D,2}$. A schematic overview of these terms is given in Fig. 7.17.

7.8.1. Bending in a Multi-orbital Tight-binding Model with s-, p- and d-orbitals

The central aspects of the dispersion relation of a multi-band tight-binding model with d_{xz}- and d_{yz}-orbitals in addition to the p_z-orbitals has already been discussed in Sec. 4.4. The addition of $d_{x^2-y^2}$-, d_{xy}- and d_{z^2}-orbitals alone have little impact on the dispersion relation of the edge states in bent graphene, because of the weak coupling due to the large energy separation and weak coupling of p_z- and d-orbitals. This changes dramatically, when the other p-orbitals are included. As was motivated in the previous section, the interplay of p_x-, p_y- and d-orbitals in a bent sample is of central importance, such that in this section a 9-orbital tight-binding model is used to obtain numerical results. The dispersion relation of a ribbon with 16 rows and 4 columns is depicted in Fig. 7.16 a), where a deformation perpendicular to the edges with a radius of $R = 10\,\mathrm{nm}$ is applied. It is $\xi_p = 5\,\mathrm{meV}$ and $\xi_d = 0.9\,\mathrm{meV}$. The dispersion of the edge states is dominated by the slope introduced by the coupling of p_z-, d_{xz}- and d_{yz}-orbitals, which is also occurring in flat graphene and is only slightly modified in the deformed case, whereas the additional d-orbitals contribute very little. A shift of $151\,\mathrm{meV}$ is observed, as well as the $\langle \hat{s}_y \rangle$-polarization, which is shown in Fig. 7.16 b). Due to the broken inversion symmetry of the system, the bands exhibit a spin-splitting of

$\sim 0.5\,\text{meV}$ at $k_x \cdot a \approx 0.4$, similar to previous findings for circular deformations perpendicular to the edges.

In order to illustrate the influence of the atomic spin-orbit coupling on the band dispersion, the energy difference of the edge bands with and without spin-orbit coupling is plotted in Fig. 7.16 c). On the left figure, the difference

$$\Delta E(k) = E(k, \xi_p, \xi_d) - E(k, \xi_p = 0, \xi_d = 0) \tag{7.68}$$

is depicted for the 9-orbital model. This result is numerically identical to that of the 4-orbital model with only s- and p-orbitals at the scale of this figure, despite the different dispersion of the bands. A band crossing is observable, because the spin-orbit coupling lifts the four-fold energy degeneracy, as a result of the broken symmetry, compared to the case without intrinsic spin-orbit coupling. These findings are qualitatively similar to what was reported in [78]. In the right figure, the difference

$$\Delta E(k) = E(k, \xi_p, \xi_d) - E(k, \xi_p, \xi_d = 0) \tag{7.69}$$

is shown. It is on the order of μeV and thus the influence of the d-orbital intrinsic spin-orbit coupling on the bending-induced energy splitting is only marginal compared to that of the p-orbitals. An energy splitting is nearly completely absent in bent ribbons when only p_z- and d-orbitals are considered. Next, the effect of the different effective spin-orbit coupling terms will be discussed and extended upon those of the 4-orbital model from Sec. 7.3.

In a 6-orbital model consisting of only p_z- and the five d-orbitals the spin alignment among d- and p_z-orbitals alone is extremely weak, compared to that in Sec. 7.3. In this model, the alignment is determined by the competition of the bending-induced d-orbital spin-orbit coupling $B_{nn}^{D,2}$ and intrinsic d-orbital spin-orbit coupling C_{nn}^D. Both are shown schematically in Fig. 7.17. Geometrical factors arising from the in-plane directive cosines can be neglected for an estimate of the order of magnitude. Furthermore, the influence of the term $B_{nn}^{D,2}$ is very weak, compared to the term $B_{nn}^{D,1}$. Then

$$\frac{|C_{nn}^D|}{|B_{nn}^{D,2}|} \approx \frac{\varepsilon_d^2}{\xi_d V_{pd\pi}^2} \frac{\xi_d V_{pd\sigma}^2}{\varepsilon_d^2} \frac{1}{\theta} = \frac{V_{pd\sigma}^2}{V_{pd\pi}^2} \frac{1}{\theta} \approx 10^3, \tag{7.70}$$

when the usual bending angle of $\theta \approx 0.03$ is assumed. The very large value resulting from Eq. 7.70 indicates that the bending-induced d-orbital Rashba-type spin-orbit coupling $B_{nn}^{D,2}$ does not play a significant role, compared to the intrinsic spin-orbit coupling C_{nn}^D. Apart from this, the spin alignment in Eq. 7.70 is independent of the intrinsic spin-orbit coupling parameter ξ_d. This is verified by computing the angle ϕ of the edge spin alignment with the local normal for the 6-orbital model, which is shown in Fig. 7.18 a). In this figure, a nanoribbon with 16 rows and $\xi_d = 5 \cdot \xi_d^0 = 4\,\text{meV}$, where $\xi_d^0 = 0.8\,\text{meV}$, is considered without edge passivation. A very weak influence of the bending-induced Rashba-type spin-orbit coupling is observed. Increasing the intrinsic d-orbital spin-orbit coupling parameter to $\xi_d = 100 \cdot \xi_d^0$ does not lead
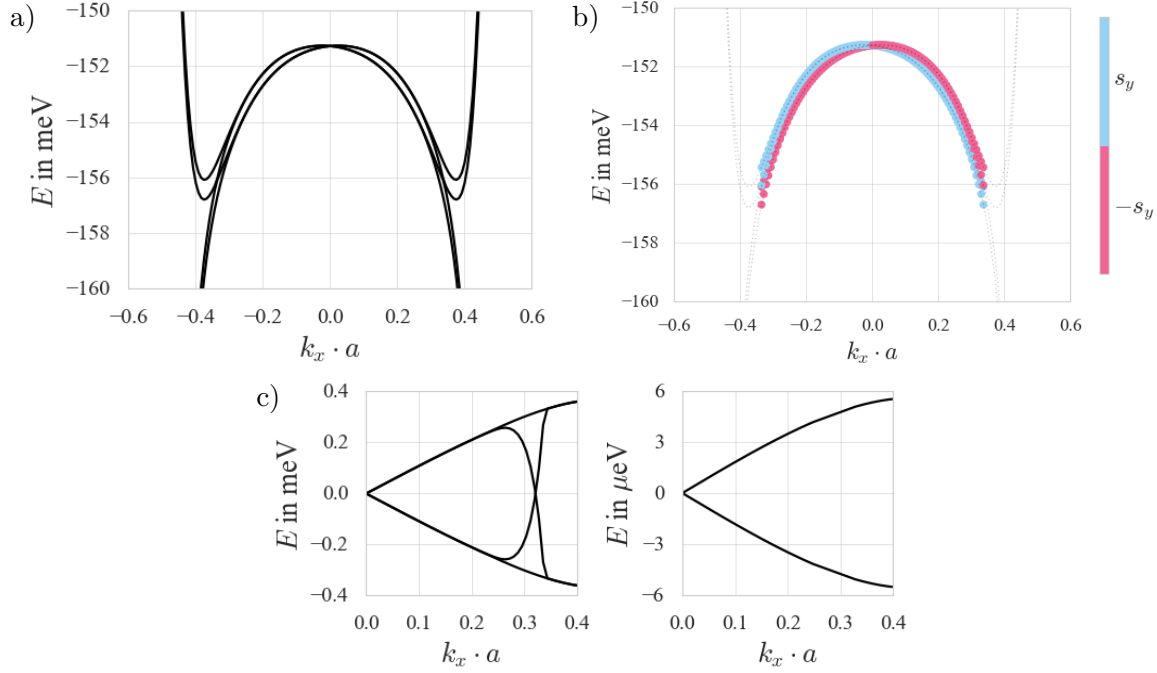
FIGURE 7.16.: a) Dispersion relation of a ribbon with 16 rows and 4 columns $R = 10\,\text{nm}$, where $\xi_p = 5\,\text{meV}$ and $\xi_d = 0.9\,\text{meV}$. b) The states are colored by their $\langle \hat{s}_y \rangle$-polarisation ± 1. c) The energy difference of the edge states where $\xi_p = 5\,\text{meV}$, $\xi_d = 0.9\,\text{meV}$ is compared with $\xi_p = 0$, $\xi_d = 0$ (left) and $\xi_p = 5\,\text{meV}$, $\xi_d = 0.9\,\text{meV}$ is compared with $\xi_p = 5\,\text{meV}$, $\xi_d = 0$ (right).

to an observable difference of the results in Fig. 7.18 a), suggesting the independency of the competitions of the different spin-orbit coupling types of ξ_d. As a comparison, the 4-orbital model with s- and p-orbitals, from Eq. 7.46, results in $\frac{|C_{nn}|}{|B_{nn}|} \approx 5 \times 10^{-2}$ for the same parameters. This shows that the predictions of both multi-orbital tight-binding models differ by at least 4 orders of magnitude. The comparison suggests that both models tend to over- or underestimate the spin-orbit coupling contributions either in favor of the bending-induced Rashba-type spin-orbit coupling or in favor of the intrinsic spin-orbit coupling. In order to give a realistic estimation of the bending-induced spin alignment at the graphene edge, the dominant terms of each of the two models are compared to each other. This competition of the dominant spin-orbit coupling terms in the effective 9-orbital model in Eq. 7.71 is given by the two different p-d-Rashba-type spin-orbit coupling terms, as well as the s-p-Rashba-type and both effective intrinsic p- and d-orbital spin-orbit coupling terms. This consideration leads to

$$\frac{|C_{nn} + C_{nn}^D|}{|B_{nn} + B_{nn}^{D,1} + B_{nn}^{D,2}|}(\xi_p, \xi_d) \sim \left(\frac{a_0 \xi_p^2}{a_1 \xi_p + a_2 \xi_d} + \frac{b_0 \xi_d}{a_1 \xi_p + a_2 \xi_d} \right) \frac{1}{\theta}, \qquad (7.71)$$
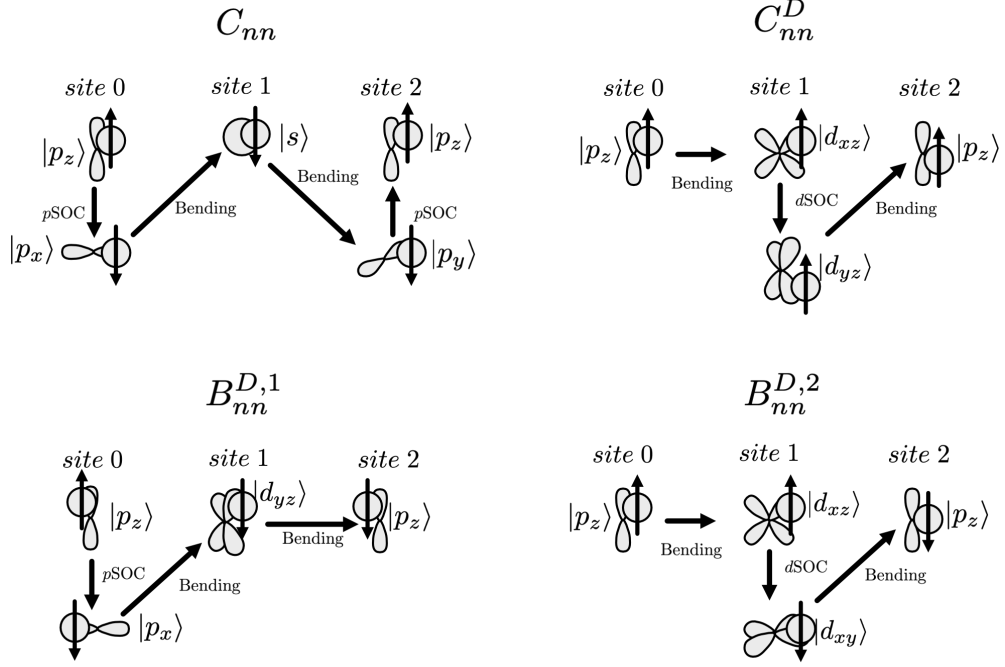
149

FIGURE 7.17.: Examples of different hopping paths which result in the different effective spin-orbit coupling terms C_{nn}, C_{nn}^D, $B_{nn}^{D,1}$ and $B_{nn}^{D,2}$. The intrinsic p-orbital spin-orbit coupling is denoted pSOC and that of the d-orbitals dSOC. The terms C_{nn}^D and $B_{nn}^{D,2}$ are identical except for the dSOC transition at site 1, where there is no spin flip induced in the former case, but in the latter.

where the constants[6] a_0, a_1, a_2 and b_0 contain the Slater-Koster parameters $V_{pd\pi}$, $V_{pd\sigma}$, as well as $V_{sp\sigma}$ and numerical factors, due to the $t_{ij}(\theta_n)t_{i'j'}(\theta_{n'})$ and the different ε. Additionally, $a_0 \sim \frac{1}{\text{eV}}$, while a_1, a_2 and b_0 are unitless. Eq. 7.71 evaluates to 0.15 for $\theta = 0.03$ and is in between the two extreme values of the reduced models. The contribution of B_{nn} is a larger than $B_{nn}^{D,1}$ and both are vastly larger than $B_{nn}^{D,2}$. When ξ_p is varied, such that $\xi_p^0 \ll \xi_p$, it is also $\xi_d^0 \ll \xi_p$. Here $|C_{nn}| \ll |B_{nn}|$ and therefore $\frac{a_0 \xi_p}{a_1} \ll 1$. Also $a_2 \ll a_1$, because $|B_{nn}|$ is the dominant bending-induced contribution. Since $|C_{nn}| < |C_{nn}^D|$ in general, the first term in Eq. 7.71 is smaller than the second, but it becomes relevant at large ξ_p. For varying ξ_p and constant $\xi_d = \xi_d^0$, Eq. 7.71 is approximately

$$\frac{|C_{nn} + C_{nn}^D|}{|B_{nn} + B_{nn}^{D,1} + B_{nn}^{D,2}|}(\xi_p, \xi_d^0) \sim \left(\frac{a_0}{a_1}\xi_p + \frac{1}{\frac{a_1}{b_0 \xi_d^0}\xi_p + \frac{a_2}{b_0}} \right) \frac{1}{\theta} \sim \frac{1}{\xi_p \theta}. \qquad (7.72)$$

---

[6]These constants can be worked out in detail from the different spin-orbit coupling terms in Eq. 7.71, but are chosen here to only represent the general functional dependency in terms of ξ_p, ξ_d and θ. Their full expression is not important for the discussion here and a more detailed treatment is out of the scope of this work.

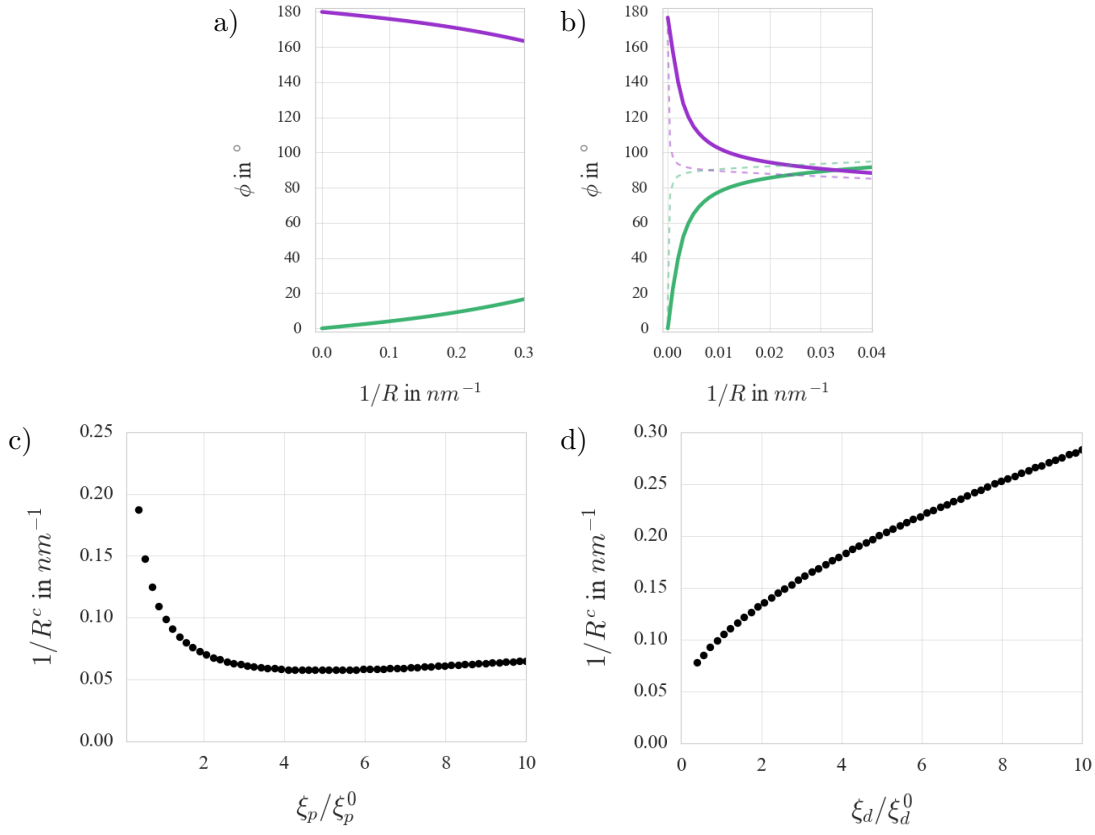FIGURE 7.18.: The angle ϕ between the spin-polarization and the local normal of a 20 row nanoribbon with $\xi_d = 4\,\text{meV}$ computed with a 6-orbital tight-binding model including p_z- and the five d-orbitals in a) and with the 9-orbital model in b). Here the spin alignment of the full 9-orbital model (solid) and the reduced 4-orbital model (dashed) is depicted for a ribbon with 16 rows. The critical inverse radius of curvature $1/R^c$ in the 9-orbital model for the same ribbon when c) ξ_p and d) ξ_d is varied. Here $\xi_p^0 = 5\,\text{meV}$ and $\xi_d^0 = 0.8\,\text{meV}$.

The nearly constant offset, observable where $\xi_p \approx \sqrt{\frac{b_0 \xi_d^0}{a_0}}$, corresponding to $\xi_p/\xi_p^0 \approx 5$, is $\frac{2a_0}{a_1}\sqrt{\frac{b_0 \xi_d^0}{a_0}}$. When ξ_d is varied, with the same approximations as in the previous case, it follows from the second term of Eq. 7.71 that

$$\frac{|C_{nn} + C_{nn}^D|}{|B_{nn} + B_{nn}^{D,1} + B_{nn}^{D,2}|}(\xi_p^0, \xi_d) \sim \frac{\xi_d}{\theta}. \tag{7.73}$$

Here the spin alignment offset for $\xi_d/\xi_d^0 = 0$ is $\frac{a_0}{a_1}\xi_p^0$.

A numerical evaluation of the 9-orbital model for an $N = 16$ nanoribbon under circular bending along the y-direction leads to a spin-alignment comparable to the case of the 4-

orbital model. Again the critical inverse radius of curvature is computed, where the two edge spins completely align inplane, such that $\phi = 90°$. The result is depicted in Fig. 7.18 b). As before in the 4-orbital model (dashed curve), the spin alignment is $\sim (1/R^c)^{-1}$. However, the result for the 9-orbital model (solid) indicates a larger bending required to align the edge spin in the graphene plane.

Furthermore, when ξ_p is varied, which is shown in Fig. 7.18 c), a completely different picture compared to the 4-orbital model is observed. While $\frac{1}{R^c} \sim \xi_p$ in the previous case, now $\frac{1}{R^c} \sim \xi_p^{-1}$, but with an offset. The d-orbital intrinsic spin-orbit coupling on the other hand, shows $\frac{1}{R^c} \sim \xi_d$ - also with an offset, as depicted in Fig. 7.18 d). Both of these results are in line with the consideration in Eqs. 7.72 and 7.73, as the resulting function can be used to fit the data very well with appropriate choice of constants in both cases.

This finding is a strong indication that the effect of deformation and introduction of bending-induced spin-orbit coupling requires a multi-orbital tight-binding model, which includes both σ- and d-bands in addition to the p_z-orbitals in order to correctly describe the effect on the edge states.

For the understanding this behavior in the scope of this model, the influence of the different orbitals on the p_z-orbitals is most important. The deformation of graphene leads to a very strong effect on the spin-alignment of the edge states, attributed to the bending-induced coupling of the s- and p-orbitals. The intrinsic spin-orbit coupling of the d-orbitals on the other hand diminishes the effect of the bending on the alignment - much more than that of the p-orbitals. Due to the bending, the s-, p_x- and p_y-orbitals couple only $\sim \theta$ to the p_z-orbitals, whereas the d_{xz}- and d_{yz}-orbitals couple due to the lattice symmetry, which is already the case in flat graphene. Therefore, the intrinsic d-orbital intrinsic spin-orbit coupling has a much stronger influence on the π-bands, than the intrinsic p-orbital spin-orbit coupling. For the deformation-induced spin-orbit coupling, the roles are reversed. The large energy difference of the d-orbitals from the p_z-orbitals reduces the influence of the bending-induced coupling of the d-orbitals to a minimum. The s-, p_x- and p_y-orbitals on the other hand are energetically much closer to the p_z-orbitals and thus even small deformations have a larger impact on the π-bands. As a result the interplay of intrinsic and bending-induced spin-orbit coupling originating from all additional orbitals is needed in order to correctly model spin-alignment of the edge states in deformed nanoribbons.

7.8.2. Localized States

For the same parameters used in the 4-orbital model in Fig. 7.13 a), the effect of the sinusoidal deformation on the bulk states in the 9-orbital model is computed. The resulting dispersion relation is depicted in Fig. 7.19. On the left of the figure, several bulk bands are observed, which are not found in the results for the 4-orbital model. One band (denoted B) is particularly close to the edge state bands (A). Around the Γ-point, the dispersion relation of the edge states is qualitatively similar to that of the 4-orbital model for bent ribbons. Since the sinusoidal deformation with amplitude $A = 2.9\,\text{a}$ introduces a strong dispersion of the
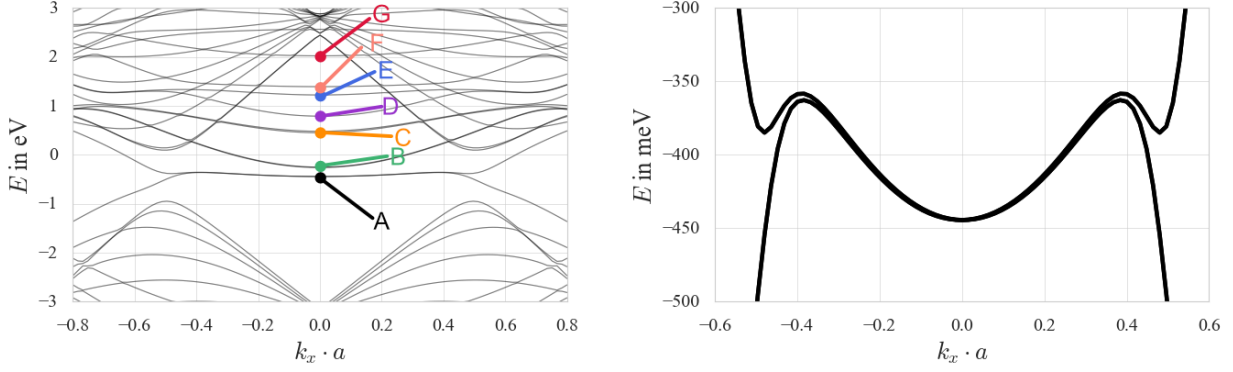
FIGURE 7.19.: left: Dispersion relation of a deformed nanoribbon with 16 rows, where $\xi_p = 5\,\text{meV}$, $\xi_d = 0.9\,\text{meV}$, $A = 2.9\,\text{a}$ and $\lambda = 15\,\text{a}$, computed with the 9-orbital model. right: Detail of the edge state dispersion relation.

edge states, on the order of $100\,\text{meV}$, the dispersion due to the *d*-orbitals of approximately $5\,\text{meV}$ is insignificant. The spatial distribution of the different states is depicted in Fig. 7.20 a-f) and labelled accordingly. The four states B are localized around points of maximal curvature. C are two pairs of states with nearly identical spatial distribution, as well as two pairs denoted D and two pairs denoted E. In F and G two sets of two-fold degenerate states are shown, which are localized only at either side of the ribbon. As before in the 4-orbital model, the sign change of the pseudomagnetic field leads to localized states. This was argued to be mostly the case, when the pseudomagnetic field switches between large positive and large negative values in a very small spatial region. Due to the additional orbitals, however, more localized state are observed, which are also more sensitive to the pseudomagnetic field. As a result, the sign change at $y = 0$ in Fig. 7.14 a) also leads to localized states, which can be seen in Fig. 7.20 in D and E.

a) left: A right: B   **b)** C   **c)** D

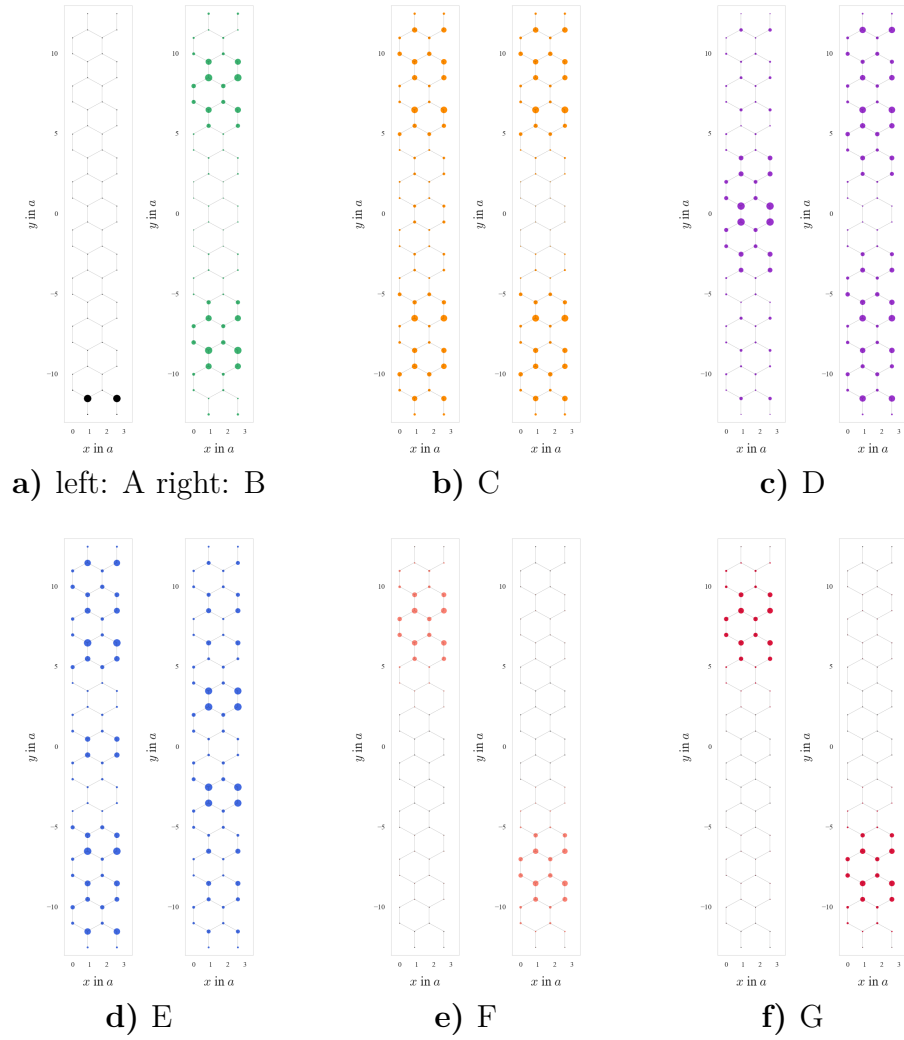**d)** E   **e)** F   **f)** G

FIGURE 7.20.: A deformed nanoribbon with 16 rows, where $\xi_p = 5\,\text{meV}$, $\xi_d = 0.9\,\text{meV}$, $A = 2.9\,\text{a}$ and $\lambda = 15\,\text{a}$, computed with the 9-orbital model. i) The sites of the sample. ii) The dispersion relation of the ribbon. a)-f) corresponds to the spatial distribution of states at $k_x = 0$, where the bands are labeled A-G.

7.9. Summary of Deformations of Graphene

In this chapter, different deformations have been discussed and their effect on the edge spin direction of narrow graphene nanoribbons has been analyzed. For this purpose, a 4-orbital tight-binding model has been derived analytically, which was then used to obtain effective bending-induced spin-orbit coupling terms. These terms were then analyzed with respect to the symmetry breaking of circular deformations perpendicular to and along the zigzag edge of the nanoribbons. Then the spin alignment of the edge states in bent nanoribbons was computed numerically with different curvatures. It was found both analytically and numerically that increased intrinsic spin-orbit coupling strength leads to stronger tendency for the edge spins to align along their local quantization axis. In that case stronger curvature is needed to align the spins along the graphene plane.

Following this, various sinusoidal deformations along and perpendicular to the zigzag edge of the nanoribbons were computed numerically. In the deformation perpendicular to the edges, the edge state dispersion is only affected, when the deformation exhibits a finite curvature close to the edges of the sample. For the deformation parallel to the edges, not only a y-component of the edge spins was observed, as in the previous case, but also an x-component occurs, as consequence of the varying curvature along the deformation direction.

Using the sinusoidal deformation perpendicular to the edges, with large deformation amplitude and thus with large curvature, localized states were observed. These states are energetically closer to the edge states than other bulk states and have a strong localization around points with extremal curvature.

In a next step, the analytical 4-orbital tight-binding model was extended to also include the 5 d-orbitals, leading to an effective 9-orbital tight-binding model. The additional bending-induced effective spin-orbit coupling terms were derived and analyzed. Due to the d-orbital intrinsic spin-orbit coupling, a stronger bending was required to align the edge spins in-plane, than what was predicted by the 4-orbital model. The analytical results were confirmed by the numerical computations and a dominant effect of the intrinsic d-orbital spin-orbit coupling compared to the p-orbital spin-orbit coupling was found.

Lastly, the 9-orbital model was used to compute localized bulk states in strongly bent ribbons. Due to the additional orbitals, more localized states, which come energetically close to the edge state dispersion, with stronger sensitivity to the deformation-induced pseudo-magnetic field were observed.

8. Summary And Outlook

The contribution of this thesis is a better understanding of the gap crossing edge states of graphene nanoribbons with zigzag edges under intrinsic and extrinsic spin-orbit coupling and electronic interactions with particular attention turned to their topological properties. The edge magnetic phases discussed in this thesis have different characteristics and electric properties, exhibiting insulating, half-metallic or conducting behavior. These phases were previously discussed in the literature [291], but a concise discussion of the nanoribbon size and its influence on the different edge magnetic phases was lacking. The non-magnetic phase was only mentioned for small doping [213, 260], but the strong doping case was not touched. Additionally, the discussion of the edge magnetic phases has been widened to an extended Hubbard model, containing the higher-in-energy d-orbitals [80] and Coulomb interactions therein. While it was previously well known, that the deformation of a planar graphene sample leads to different types of spin-orbit coupling [78], previous discussions were limited to the effect of the σ-bands on the π-band dispersion. It was found that the intrinsic d-orbital rather than the intrinsic p-orbital spin-orbit coupling competes with the deformation-induced Rashba-type spin-orbit coupling of the s- and p-orbitals for the spin-alignment of the edge states.

   In the following, the results of this thesis are summarized and it is discussed how the insights on the spin-orbit coupling and electronic interactions lead to a better understanding of the topological phase of zigzag edge carbon nanoribbons. Lastly, an outlook is given, which proposes a direction for further research.

Summary

Chapter 1 provides an introduction to the topic of topological insulators and motivates the new classification of *topological phases*. The advantages of using a multi-orbital tight-binding model in this projects are highlighted and the flexibility of the model is emphasized in prospect of using an on-site Hubbard interaction in the mean-field approximation for considering electronic interactions.

   Special attention is given to the description of spin-orbit coupling in Chapter 2. The occurrence of spin-orbit coupling is discussed, as it arises from the motion of the charge carriers in an electric field, originating from either an atomic nucleus, the crystal geometry or other external sources. Two prominent examples are the Rashba- and Dresselhaus-type spin-orbit coupling. Symmetry properties of terms in the low-energy approximation of a Hamiltonian are discussed. The intrinsic spin-orbit coupling in graphene is particularly weak, such that

an overview is given on the current experimental status regarding its measurement. Additionally, various efforts to increase the spin-orbit coupling via external factors are discussed.

Details regarding the construction of a tight-binding model are given in Chapter 3. The Slater-Koster approximation is used to define the interaction matrix element for a nearest-neighbor hopping in the tight-binding model. As a first result, the trigonal warping effect at the Dirac points of bulk graphene is analyzed, as it originates from Rashba-type spin-orbit coupling. For this, the x- and y-expectation values of the sublattice spin of the conduction and valence bands around each of the Dirac points and the corresponding winding numbers are computed. The trigonal warping is found to split each Dirac cone into four distinct ones, each with its own winding number. However, the total winding number is found to be equal to the sum of the four numbers, which is a consequence of the topological nature of these winding numbers. Such a winding number relates to the topologically insulating or trivial phase of graphene, because the chirality of each of the Dirac cones leads to a phase between the two components of the wave functions for each of the sublattices, which in turn affects the winding numbers in sublattice spin space. A 2×2-model is derived in the $\{\psi_{A\uparrow}, \psi_{B\downarrow}\}$-subspace and it is shown how the sublattice spin expectation values for the lower conduction and upper valence band can be computed analytically with this model in very good approximation.

Following the computational details of the model in the previous chapters, the properties of graphene as a topological insulator are stated in Chapter 4. Special emphasis is laid on the topological edge states and their dispersion relation in the multi-orbital tight-binding model. The effects of Rashba-type spin orbit coupling on the gap crossing of the edge states is discussed by real and sublattice spin expectation values. It is found that the resulting system remains topologically non-trivial, provided that the intrinsic spin-orbit coupling is large enough, which is rooted in the fact that the edge states in such a time-reversal invariant topological insulator are topologically protected [41]. While a magnetic field explicitly breaks time-reversal symmetry, graphene in a magnetic field becomes a Weyl semimetal [226, 227], because at each edge states with both types of spin occur, such that for each spin component, the states still cross the energy gap. If however the time-reversal symmetry required for the topological insulator is broken, and also the inversion symmetry is lifted, the edge states do not cross the band gap and the material becomes topologically trivial. This result is obtained when both a magnetic field and Rashba-type spin-orbit coupling were considered at the same time.

A treatment of electronic interactions in a multi-orbital Hubbard model is the topic of Chapter 5. A Hamilton operator for electronic interaction is formulated in terms of the p- and d-orbitals, which is then transformed into the mean-field approximation. The self-consistent field method for solving such problem is laid out.

In Chapter 6, the non-magnetic phase is described, which is topologically similar to the non-interacting system, but has a density accumulation on the edge sites. Two magnetic phases are also analyzed. First, the ferromagnetic edge phase (FM) is discussed, which exhibits gap crossing edge state, and after that the topologically trivial antiferromagnetic

edge phase (AFM) is treated, which does exhibit a band gap. The energy splittings of the two magnetic phases are examined in terms of the nanoribbon length and the exponentially decreasing overlap of the edge states is discussed in terms of increasing p_z-orbital repulsion. A systematic study of the single-orbital model with respect to the ribbon length and interaction parameter reveals that the AFM phase is always the magnetic ground state, in agreement with Lieb's theorem.

Then the energy dependency of the non-magnetic phase on the filling factor is analyzed. A small and a large doping regime are found, where in the first regime only the different edge bands and in the second also the bulk bands become filled. This leads to a different scaling behavior of the energy in the two regimes and an energetic minimum is found, which defines an energetically preferred doping strength at the transition point from one regime into the other. It is argued that the occurrence of the non-magnetic phase could be the reason why the experimental verification of magnetic edges in graphene ribbons is still elusive, by relating it to the possible hole doping effects of a substrate [270].

In the multi-orbital model, the magnetic ground state remains the AFM phase for all parameter choices, even attractive electronic interactions in the d-orbitals. However, the occupation of the higher energy d-orbitals as a consequence of the attractive forces is shown to have a significant impact on the energy difference between the two magnetic phases nonetheless. The d-orbital occupation can also be increased, by lowering the energy separation between p_z- and d-orbitals, which diminishes the energy gap between the magnetic ground state and first exited state, but does not create a magnetic ground state with finite spin magnetic moment. In a last step, the energy of the non-magnetic phase in terms of doping is analyzed, where in a multi-orbital tight-binding model, the finite d-state population has to be accounted for. In order to find an effective model for discussing the energy-dependence of the doping, the d-orbital occupation for different electronic interaction strengths is computed numerically.

The topic of deformation of a flat graphene sample is discussed in Chapter 7. The deformation breaks the inversion symmetry with respect to the normal of the graphene plane. Therefore transition matrix elements between sp^2-hybridized orbitals and π-bands become finite, leading to a deformation-induced Rashba-type spin-orbit coupling. It is found that for the circular bending perpendicular to the edges at strong curvature the edge states acquire a non-zero $\hat{s}_y$-component, which lifts their two-fold $\hat{s}_z$-degeneracy. The alignment of the local spin polarization of the edge atoms in bent ribbons with constant curvature relative to the local surface normals indicates that the deformation-induced spin-orbit coupling from the d-orbitals is affecting the in-plane spin polarization less than that of the sp^2-orbitals. The influence of the intrinsic spin-orbit coupling of the d-orbitals, however, is found to be much more relevant for the spin-polarization along the local surface normal than that of the p-orbitals. Altogether the direction of spin-polarization is mostly given by a competition of intrinsic d-orbital spin-orbit coupling and deformation-induced spin-orbit coupling arising from the coupling of π- and σ-bands. This leads to a formulation of a 9-orbital tight-binding model, where this is shown by numerically computing the spin alignment and its dependency
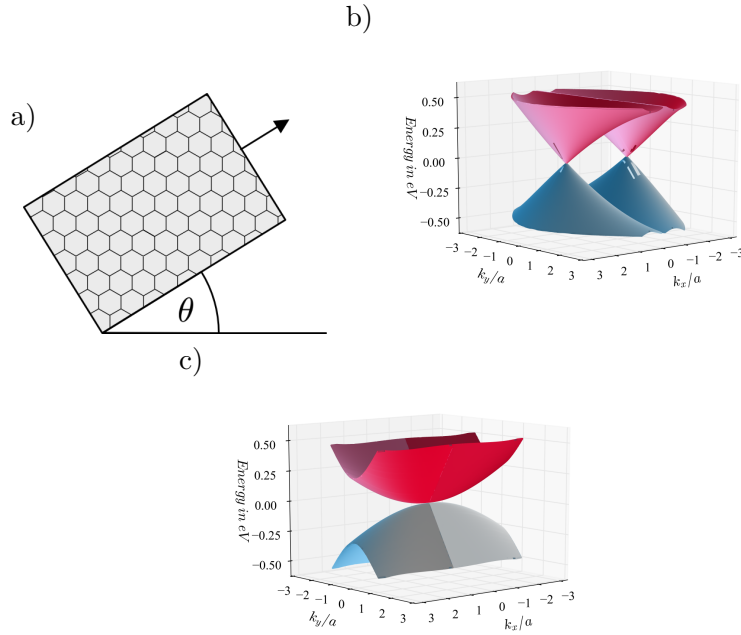
FIGURE 8.1.: a) The angle θ where uniaxial strain is applied to the graphene plane. b) Dispersion relation with the two Dirac cones and strain along the y direction, corresponding to $\theta = \frac{\pi}{2}$, does not lead to Dirac cone merging. c) Strain with $\theta = 0$ causes a merging of the Dirac cones.

on the different spin-orbit coupling strengths. Analytical expressions for the spin-dependent next-nearest-neighbor hoppings in this model are derived, with which the numerical results are underpinned.

Furthermore, bent nanoribbons with sinusoidal deformation perpendicular to the zigzag edges are examined in a tight-binding model with only s- and p-orbitals. Here localized states are found with predominant occupation of lattice sites around areas of the ribbon with extremal curvature. This is repeated for the 9-orbital model, with similar results. Nanoribbons bent along the zigzag edge with sinusoidal curvature are also analyzed. The varying curvature leads to a spin-polarization with components in all three spatial directions.

Outlook

A model used in the literature, which allows the analysis of the interplay of intrinsic spin-orbit coupling and Hubbard interaction with respect to the topological state of a system with hexagonal lattice, is the Kane-Mele-Hubbard (KMH) model [292]. This model combines the Kane-Mele model in Eq. 4.7 with an additional Hubbard term and leads to a rich phase diagram [293, 294]. The ground state of bulk graphene with the parameter choices for the

interaction and spin-orbit coupling strengths similar to this work is found to be topologically insulating. A magnetically ordered state is reached for strong interactions larger than what is considered here [295]. Including a sublattice potential into the KMH model allows for the occurrence of a spin-polarized quantum Hall insulating phase, which is caused by the Coulomb interaction in a system with broken sublattice symmetry [296].

The KMH model can be extended to also include Rashba-type spin-orbit coupling [297]. This addition is found to alter the result of the KMH model only for very strong Rashba-type interaction, where collinear magnetic states are less favorable and magnetism with in-plane spin alignment occurs [292].

While the above considerations deal with two-dimensional graphene, the finite coupling of the edge states in zigzag ribbons, leads to the energy gap in the antiferromagnetic ground state [110, 291, 298], which was discussed in detail in this work. Therefore, the results obtained, among those reported by others [50, 110], could be regarded as a step towards applying the KMH model to systems with finite size and realistic parameter choices.

In planar graphene, the alignment of the real spin polarization parallel to the sample plane, together with Coulomb interactions, leads to spin mixing and results in a gap opening in the edge magnetic phases of graphene nanoribbons [299]. Such an effect is also expected, when the curvature-induced Rashba-type spin-orbit coupling affects the spin alignment. The correct inclusion of Rashba-type spin-orbit coupling via deformations or external electric fields in this case requires the spin-rotational invariance in the mean-field Hamiltonian in Eq. 5.22.

Therefore, an interesting direction for further research might be the inclusion of Coulomb interaction in the sp^2-hybridized orbitals of graphene used to describe deformations, because this would lead to a multi-orbital tight-binding model with sensitivity for the geometric distortions of the lattice. This is particularly interesting, because it would allow to further understand the occurrence of magnetic edges in graphene ribbons under realistic experimental conditions.

Furthermore, the transport properties of the edge states in graphene nanoribbons are strongly affected by the edge shape [224, 300]. As a result small deviation from the regular zigzag geometry, due to a vacant site or passivation with an atom of large electro-negativity [301], may change the effect of Coulomb interactions or that of bending on the edge states dispersion entirely [263].

Strain along one direction, shown in Fig. 8.1 a) introduces a spatial modification of the hopping in the graphene lattice. This modifies the shape of the Brillouin zone, as shown in Fig. 8.1 b), which can ultimately lead to a merging of the two Dirac cones, depicted in c). With focus on electronic interactions, further studying the magnetic ground state in strained graphene nanoribbons could also lead to many insights. Restoring the topologically non-trivial state by this method has already been theorized [302] and could also help to further understand experimental results.

Appendices

A. Spin-orbit Coupling Symmetries

A.1. Computing the Transformation Behavior of Spin-orbit Coupling Operators

In this section, the derivation of the transformation behavior of real space and reciprocal space coordinates and of real spin and sublattice spin operators is presented. For this, the effect of symmetry operations on the respective coordinates or spins is compared to character tables. By doing so, similar transformation behavior is obtained, which makes these operators and products comparable.

A.1.1. Sublattice Spin Transformation Behavior

At first the sublattice spin transformation behavior is discussed. It is shown in Fig. A.1, how the two sublattices transform according to different symmetry transformations of the point group $C_{2\nu}$. The mirroring operation σ_{xz} swaps sublattices, while the other mirroring operation σ_{yz} leaves them invariant. The rotation C_2 also swaps the sublattices, while the identity element E does not. Hence these operations can be represented by a two-dimensional matrix acting on a vector in the sublattice spin basis, where the x-component of the vector denotes $\uparrow$ and the y-component $\downarrow$ in the sublattice basis. The respective representation of the group elements is listed in Table A.1. For establishing how products of sublattice and reciprocal space vectors transform, the transformations of momentum vectors need also be related to the group $C_{2\nu}$. For that their transformation behavior is expressed as a transformation in real space. A mirroring or rotation in real space may also affect the orientation of reciprocal space. An operation in real space that interchanges the sublattices (flips the sublattice spin), such as σ_{xz} in Table A.1, changes the valley in reciprocal space. This means that the valley isospin τ_z is flipped. As a consequence the valley isospin changes in the same way as the sublattice spin changes. And thus, for each non-diagonal matrix in Tab. A.1, τ_z obtains a

$$
E = \begin{pmatrix} 1 & 0 \\ 0 & 1 \end{pmatrix} \quad C_2 = \begin{pmatrix} 0 & 1 \\ 1 & 0 \end{pmatrix} \quad \sigma_{xz} = \begin{pmatrix} 0 & 1 \\ 1 & 0 \end{pmatrix} \quad \sigma_{yz} = \begin{pmatrix} 1 & 0 \\ 0 & 1 \end{pmatrix}
$$

TABLE A.1.: The operations of the point group $C_{2\nu}$ in the basis of the sublattices A and B.
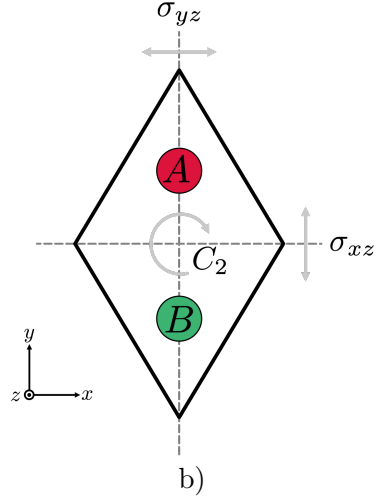
162

FIGURE A.1.: The group operations of $C_{2\nu}$. The unit cell of graphene with coordinate system and symmetry operations. The atom at position A is associated with sublattice spin *up*, i.e. $|\uparrow\rangle$, and the one with at position B with *down*, that is $|\downarrow\rangle$. The mirror operation σ_{xz}, as well as a rotation by the angle π, interchange the sublattices.

$$E = \begin{pmatrix} 1 & 0 \\ 0 & 1 \end{pmatrix} \quad C_2 = \begin{pmatrix} -1 & 0 \\ 0 & -1 \end{pmatrix} \quad \sigma_{xz} = \begin{pmatrix} 1 & 0 \\ 0 & -1 \end{pmatrix} \quad \sigma_{yz} = \begin{pmatrix} -1 & 0 \\ 0 & 1 \end{pmatrix}$$

TABLE A.2.: The operations of the point group $C_{2\nu}$ in the basis of the the real space coordinates x and y.

sign, such that

$$E : \hat{\tau}_z \rightarrow \hat{\tau}_z \tag{A.1}$$

$$C_2 : \hat{\tau}_z \rightarrow -\hat{\tau}_z \tag{A.2}$$

$$\sigma_{xz} : \hat{\tau}_z \rightarrow -\hat{\tau}_z \tag{A.3}$$

$$\sigma_{yz} : \hat{\tau}_z \rightarrow \hat{\tau}_z. \tag{A.4}$$

In order to find the transformation of the momenta k_x and k_y, the effect of the operations given in Tab. A.1 are computed by using $k_i \sim \frac{\partial}{\partial x_i}$. Hence the reciprocal coordinates transform identical as their real space counterparts x and y. However, also the valley isospin has to be transformed for the correct coordinates in the low-energy description for graphene. A representation of the operations in Tab. A.1 on the real space (and thus reciprocal space) coordinates is given in Tab. A.2. Together with the transformation behavior of the valley isospin from Eqs. A.1-A.4 and the reciprocal space vectors in Tab. A.2 in place, the sublattice spin transformation behavior can be related to reciprocal space. Now products of the

$\mathbf{C}_{2\nu}$	$\hat{\sigma}_x$	$\hat{\sigma}_y$	$\hat{\sigma}_z$	$\hat{\tau}_z$	k_x	k_y
E	+1	+1	+1	+1	+1	+1
C_2	+1	−1	−1	−1	−1	−1
σ_{xz}	+1	−1	−1	+1	+1	−1
σ_{yz}	+1	+1	+1	−1	−1	+1

TABLE A.3.: The effect of the group actions of $C_{2\nu}$ on sublattice spin and crystal momenta.

two can be constructed via Tab. A.3 and related to basis functions in Tab. A.7. From Tab. A.3 it can be seen, that $\hat{\sigma}_y$ transforms as k_y, but $\hat{\sigma}_x$ does not transform as k_x. The reason is that in the reciprocal space the valleys of the K and K'-points transform identically, but in the sublattice spin space they do not. Hence the valley isospin τ_z needs to be included when sublattice spin and momentum are interchanged, and thus the pairs $\{\hat{\sigma}_x, \hat{\sigma}_y\} \sim \{\hat{\tau}_z k_x, k_y\}$ are identical in their transformation behavior. This is also the reason, why the Hamiltonian for graphene differs from the actual Dirac Hamiltonian when the formulation of the sublattice spin is compared to that of the real spin.

A.1.2. Real Spin Transformation Behavior

The real spin transformation behavior is different than that of the real space and sublattice spin, because the Pauli matrices span SU(2), the complex spinor space. A representation of the group O(3) on the Pauli matrices is [148]

$$U_n = \cos\frac{\phi}{2}\hat{s}_0 + i\vec{n}\hat{\vec{s}}\sin\frac{\phi}{2},\tag{A.5}$$

where $\hat{\vec{s}}$ is the direction of the spin vector spanned by the Pauli matrices. These correspond to rotations in a plane with normal vector $\vec{n}$ by the angle ϕ. A reflection on a plane with normal vector $\vec{n}$ is represented by

$$\Sigma_\alpha = -i\vec{n}\hat{\vec{s}}.\tag{A.6}$$

A group symmetry on the real spin matrices $\hat{s}_i$ is applied by

$$D\left(g\right)\hat{s}_i D\left(g\right)^\dagger = \pm\hat{s}_j,\tag{A.7}$$

where $D\left(g\right)$ is the representation of the group action in spinor space defined by a group element g. Therefore the operations of the groups under discussion here are made up of operations of the type given in Eq. A.5 and Eq. A.6. For instance a roto-inversion, e.g. S_4^1,

is made up of a rotation around $\frac{\pi}{2}$ and a consecutive mirroring in the plane perpendicular to the z axis. The resulting operation is given by

$$S_4^1 = \frac{-i}{\sqrt{2}}\hat{s}_z - \frac{1}{\sqrt{2}}\hat{s}_0. \tag{A.8}$$

For the group $C_{2\nu}$ only the group elements E, C_2, $\sigma_{xz} = C_2'$ and $\sigma_{yz} = C_2''$ are required. When applying these to $\hat{s}_x$, $\hat{s}_y$ and $\hat{s}_z$, they affect only the signs of the spin operators, since $C_{2\nu}$ has only one-dimensional irreducible representations. The result of applying the group elements of $C_{2\nu}$ to the real spin matrices is given in Tab. A.4. In this table the signs of the individual group operations of $C_{2\nu}$ on the Pauli matrices can be related to the irreducible representations for the group encoded in the respective character table, Tab. A.7. One can deduce for instance, that $\hat{s}_x$ transforms like the irreducible representation B_2. Thus it can be represented by one of its basis functions. A basis function comprised of real space coordinates for the same irreducible representation would be yz. In this way the transformation behavior of the real space coordinates x,y and z is made comparable and therefore products of real space, reciprocal space, real spin and sublattice spin can be analyzed according to their symmetries. For a more complicated group, the same procedure can be used and the transformation behavior established. A two-dimensional representation of the group D_{2d} acting on the group elements of SU(2) is given in Tab. A.5. If the basis $\{\hat{s}_x, \hat{s}_y\}$ is chosen, the elements of group D_{2d} produce the representation in Tab. A.6, which coincide with the representation for the real space coordinates x and y. By consulting the character table of D_{2d}, Tab. A.9, it is established, that for the two-dimensional irreducible representation E, the spin matrices for this group behave as $\hat{s}_y \sim xz$ and $\hat{s}_x \sim yz$, similar to what was previously discussed for $C_{2\nu}$. That concludes the discussion on transformation behaviors of these operators under point group symmetry elements.

E	C_2	σ_{xz}	σ_{yz}	$\hat{s}_i$
1	-1	-1	1	$\hat{s}_x$
1	-1	1	-1	$\hat{s}_y$
1	1	-1	-1	$\hat{s}_z$

TABLE A.4.: The irreducible representations of the group $C_{2\nu}$ applied to $\hat{s}_x$, $\hat{s}_y$ and $\hat{s}_z$. The rows correspond a specific Pauli matrix , where the elements in the different columns are applied according to Eqs. A.5 and A.6.

$$E = \hat{s}_0 \qquad\qquad E^{-1} = \hat{s}_0$$

$$C_2 = -i\hat{s}_z \qquad\qquad (C_2)^{-1} = i\hat{s}_z$$

$$S_4^1 = \tfrac{-i}{\sqrt{2}}\hat{s}_z - \tfrac{1}{\sqrt{2}}\hat{s}_0 \qquad (S_4^1)^{-1} = \tfrac{i}{\sqrt{2}}\hat{s}_z - \tfrac{1}{\sqrt{2}}\hat{s}_0$$

$$S_4^2 = \tfrac{-i}{\sqrt{2}}\hat{s}_z + \tfrac{1}{\sqrt{2}}\hat{s}_0 \qquad (S_4^2)^{-1} = \tfrac{i}{\sqrt{2}}\hat{s}_z + \tfrac{1}{\sqrt{2}}\hat{s}_0$$

$$C_2' = -i\hat{s}_x \qquad\qquad (C_2')^{-1} = i\hat{s}_x$$

$$C_2'' = -i\hat{s}_y \qquad\qquad (C_2'')^{-1} = i\hat{s}_y$$

$$\sigma_d^1 = -i\tfrac{\hat{s}_x - \hat{s}_y}{\sqrt{2}} \qquad (\sigma_d^1)^{-1} = i\tfrac{\hat{s}_x - \hat{s}_y}{\sqrt{2}}$$

$$\sigma_d^2 = -i\tfrac{\hat{s}_x + \hat{s}_y}{\sqrt{2}} \qquad (\sigma_d^2)^{-1} = i\tfrac{\hat{s}_x + \hat{s}_y}{\sqrt{2}}$$

TABLE A.5.: The transformation matrices of the group D_{2d} on the SU(2) group elements. Here $\hat{s}_0$ represents the identity matrix in two-dimensions.

$$E = \begin{pmatrix} 1 & 0 \\ 0 & 1 \end{pmatrix} \qquad C_2 = \begin{pmatrix} -1 & 0 \\ 0 & -1 \end{pmatrix} \qquad \sigma_d^1 = \begin{pmatrix} 0 & -1 \\ -1 & 0 \end{pmatrix} \qquad \sigma_d^2 = \begin{pmatrix} 0 & 1 \\ 1 & 0 \end{pmatrix}$$

$$C_2'^1 = \begin{pmatrix} 1 & 0 \\ 0 & -1 \end{pmatrix} \qquad C_2'^2 = \begin{pmatrix} -1 & 0 \\ 0 & 1 \end{pmatrix} \qquad S_4^1 = \begin{pmatrix} 0 & -1 \\ 1 & 0 \end{pmatrix} \qquad S_4^2 = \begin{pmatrix} 0 & 1 \\ -1 & 0 \end{pmatrix}$$

TABLE A.6.: The operations of the point group D_{2d} in the basis of the spatial coordinates x and y.

A.2. Character Tables

$\mathbf{C}_{2\nu}$	E	C_2	$\sigma_v\,(xz)$	$\sigma_v\,(yz)$	linear order	quadratic order	cubic order
A_1	$+1$	$+1$	$+1$	$+1$	z	x^2, y^2, z^2	x^2z, y^2z
A_2	$+1$	$+1$	-1	-1		xy	xyz
B_1	$+1$	-1	$+1$	-1	x	xz	
B_2	$+1$	-1	-1	$+1$	y	yz	

TABLE A.7.: The character table for the point group $C_{2\nu}$ [114].

$\mathbf{C}_{4\nu}$	E	$2C_4$	C_2	$2\sigma_v$	$2\sigma_d$	linear order	quadratic order	cubic order
A_1	$+1$	$+1$	$+1$	$+1$	$+1$	z	$x^2 + y^2$	$z\left(x^2 + y^2\right)$
A_2	$+1$	$+1$	$+1$	-1	-1			
B_1	$+1$	-1	$+1$	$+1$	-1		$x^2 - y^2$	$z\left(x^2 - y^2\right)$
B_2	$+1$	-1	$+1$	-1	$+1$			xyz
E	$+2$	0	-2	0	0	(x, y)	(xz, yz)	

TABLE A.8.: The character table for the point group $C_{4\nu}$ [114].

$\mathbf{D}_{2\mathbf{d}}$	E	$2S_4$	C_2	$2C_2'$	$2\sigma_d$	linear order	quadratic order	cubic order
A_1	$+1$	$+1$	$+1$	$+1$	$+1$		$x^2 + y^2$	xyz
A_2	$+1$	$+1$	$+1$	-1	-1			$z\left(x^2 - y^2\right)$
B_1	$+1$	-1	$+1$	$+1$	-1		$x^2 - y^2$	
B_2	$+1$	-1	$+1$	-1	$+1$	z	xy	$z\left(x^2 + y^2\right)$
E	$+2$	0	-2	0	0	(x, y)	(xz, yz)	

TABLE A.9.: The character table for the point group D_{2d} [114].

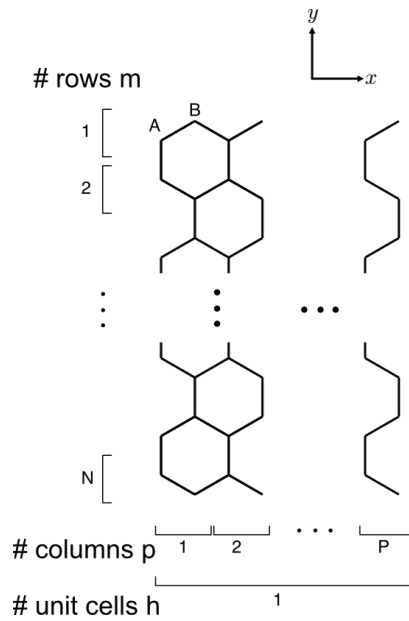# B. Multi-orbital Tight-binding Model With Zigzag Edges

FIGURE B.1.: Definition of the multi-orbital tight-binding model with zigzag edges, periodic in the x-direction. The sites A and B are labeled accordingly.

The definition of the multi-orbital tight-binding model with zigzag edges is performed in analogy to the single-orbital models presented in [50, 150]. A tight-binding model is defined with periodic boundary conditions in the x-direction and terminated by zigzag edges along y. The unit cell of the model consists of P columns, labelled with the index p and N rows, marked by the index m. Each primitive cell contains 2 sites, named A and B. Due to the geometry of the lattice, see Fig. B.1, the definition of the tight-binding model must distinguish between rows of odd and even m. The periodicity is then given by the index h, which is the periodic index used in the Fourier transformation into reciprocal space. Additionally, the index s is added for the spin and the indices μ and ν for the other orbitals

at each site. The real space Hamiltonian is then given by

$$
\begin{aligned}
H^{\mu\nu s} =& \sum_h \sum_{m \text{ odd}}^N \left(-t^{\mu\nu}(\vec{\delta}_1/a) \sum_{p=1}^P \hat{b}_{hmp}^{\dagger\mu s} \hat{a}_{hmp}^{\nu s} - t^{\mu\nu}(-\vec{\delta}_2/a) \sum_{p=1}^{P-1} \hat{a}_{hm(p+1)}^{\dagger\mu s} \hat{b}_{hmp}^{\nu s} \right) \\
&+ \sum_h \sum_{m \text{ even}}^N \left(-t^{\mu\nu}(\vec{\delta}_1/a) \sum_{p=1}^{P-1} \hat{b}_{hm(p+1)}^{\dagger\mu s} \hat{a}_{hmp}^{\nu s} - t^{\mu\nu}(-\vec{\delta}_2/a) \sum_{p=1}^P \hat{a}_{hmp}^{\dagger\mu s} \hat{b}_{hmp}^{\nu s} \right) \\
&+ \sum_h \sum_{m \text{ odd}}^N -t^{\mu\nu}(-\vec{\delta}_2/a) \hat{a}_{(h+1)m1}^{\dagger\mu s} \hat{b}_{hmP}^{\nu s} + \sum_h \sum_{m \text{ even}}^N -t^{\mu\nu}(\vec{\delta}_1/a) \hat{b}_{(h+1)m1}^{\dagger\mu s} \hat{a}_{hmP}^{\nu s} \\
&+ \sum_h \sum_{m=1}^{N-1} -t^{\mu\nu}(\vec{\delta}_3/a) \sum_{p=1}^P \hat{a}_{hmp}^{\dagger\mu s} \hat{b}_{h(m+1)p}^{\nu s} \\
&+ \sum_h \sum_{m=1}^N \sum_{p=1}^P \left(\hat{a}_{hmp}^{\dagger\mu s} \hat{a}_{hmp}^{\nu s} + \hat{b}_{hmp}^{\dagger\mu s} \hat{b}_{hmp}^{\nu s} \right) E_{\mu,\nu} + \text{h.c..}
\end{aligned}
\tag{B.1}
$$

In this Hamiltonian, the first two lines describe the vertical hopping along the zigzag direction for odd row numbers and the second line that for even row numbers. The third line includes the periodic boundary condition for the transition from one unit cell h to the next $h+1$ and the fourth line describes the vertical hopping between different rows and the last the energy shift of different orbital types. Here it is defined $E_{\mu,\nu} = E_d$ if $\mu = \nu \in \{d\}$ and $E_{\mu,\nu} = 0$ otherwise. In a next step the ladder operators are Fourier transformed by

$$
\hat{a}_{hmp}^{\mu s} = \frac{1}{\sqrt{H}} \sum_{k_x} e^{ik_x x_{hmp}^A} \hat{\alpha}_{k_x mp}^{\mu s} \qquad\qquad \hat{b}_{hmp}^{\mu s} = \frac{1}{\sqrt{H}} \sum_{k_x} e^{ik_x x_{hmp}^B} \hat{\beta}_{k_x mp}^{\mu s},
\tag{B.2}
$$

with H being the number of unit cells. The complex conjugate of these operators is defined analogously. x_{hmp}^A and x_{hmp}^B are the x-coordinates of the A and B atoms in the primitive cell in column p and row m in unit cell h. This leads to the multi-orbital tight-binding

Hamiltonian

$$
\begin{aligned}
H_{k_x}^{\mu\nu s} = & \sum_{m \text{ odd}}^{N} \left(-t^{\mu\nu}(\vec{\delta}_1/a) \sum_{p=1}^{P} \hat{\beta}_{k_x mp}^{\dagger\mu s} \hat{\alpha}_{k_x mp}^{\nu s} e^{-ik_x \delta_1^x} - t^{\mu\nu}(-\vec{\delta}_2/a) \sum_{p=1}^{P-1} \hat{\alpha}_{k_x mp+1}^{\dagger\mu s} \hat{\beta}_{k_x mp}^{\nu s} e^{-ik_x \delta_2^x} \right) \\
& + \sum_{m \text{ even}}^{N} \left(-t^{\mu\nu}(\vec{\delta}_1/a) \sum_{p=1}^{P-1} \hat{\beta}_{k_x mp+1}^{\dagger\mu s} \hat{\alpha}_{k_x mp}^{\nu s} e^{-ik_x \delta_1^x} - t^{\mu\nu}(-\vec{\delta}_2/a) \sum_{p=1}^{P} \hat{\alpha}_{k_x mp}^{\dagger\mu s} \hat{\beta}_{k_x mp}^{\nu s} e^{-ik_x \delta_2^x} \right) \\
& + \sum_{m \text{ odd}}^{N} -t^{\mu\nu}(-\vec{\delta}_2/a) \hat{\alpha}_{k_x m1}^{\dagger\mu s} \hat{\beta}_{k_x mP}^{\nu s} e^{-ik_x \delta_2^x} e^{-ik_x P \cdot a_1^x} \\
& + \sum_{m \text{ even}}^{N} -t^{\mu\nu}(\vec{\delta}_1/a) \hat{\beta}_{k_x m1}^{\dagger\mu s} \hat{\alpha}_{k_x mP}^{\nu s} e^{ik_x \delta_1^x} e^{-ik_x P \cdot a_1^x} \\
& + \sum_{m=1}^{N-1} -t^{\mu\nu}(\vec{\delta}_3/a) \sum_{p=1}^{P} \hat{\alpha}_{k_x mp}^{\dagger\mu s} \hat{\beta}_{k_x m+1p}^{\nu s} \\
& + \sum_{m=1}^{N} \sum_{p=1}^{P} \left(\hat{\alpha}_{k_x mp}^{\dagger\mu s} \hat{\alpha}_{k_x mp}^{\nu s} + \hat{\beta}_{k_x mp}^{\dagger\mu s} \hat{\beta}_{k_x mp}^{\nu s} \right) E_{\mu,\nu} + \text{h.c..} \qquad\qquad (B.3)
\end{aligned}
$$

The x-components of the $\boldsymbol{\delta}_1$ and $\boldsymbol{\delta}_2$ vectors (labelled δ_1^x and δ_2^x) are identical up to a sign. Thus, terms of the form $e^{\pm ik_x \delta_{1/2}^x/2}$ can be absorbed into the ladder operators. If periodic boundary conditions along y are additionally included in Eq. B.3, the description can be simplified by setting $H = 1$, $N = 1$ and $P = 1$. This will result in the Hamiltonian Eq. 3.14 given in Chapter 3.

C. Multi-orbital Mean-field Hamiltonian With Spin-rotational Invariance

The full Hamiltonian in the mean-field approximation for the multi-orbital Hubbard model including terms for conserving spin-rotational invariance is given by

$$
\begin{aligned}
H_{pd} \approx & \frac{U_p}{2}\left(\hat{n}_p\langle\hat{n}_p\rangle - 4\vec{S}_p\langle\vec{S}_p\rangle - \frac{\langle\hat{n}_p\rangle^2}{2} + 2\langle\vec{S}_p\rangle^2\right) \\
& + \sum_n \Bigg[V_n\Big(\langle\hat{n}_{p\uparrow}\rangle\hat{n}_{n\downarrow} + \langle\hat{n}_{n\downarrow}\rangle\hat{n}_{p\uparrow} - \langle\hat{n}_{p\uparrow}\rangle\langle\hat{n}_{n\downarrow}\rangle - \langle\hat{c}^\dagger_{p\uparrow}\hat{c}_{n\downarrow}\rangle\hat{c}^\dagger_{n\downarrow}\hat{c}_{p\uparrow} - \langle\hat{c}^\dagger_{n\downarrow}\hat{c}_{p\uparrow}\rangle\hat{c}^\dagger_{p\uparrow}\hat{c}_{n\downarrow} + \langle\hat{c}^\dagger_{n\downarrow}\hat{c}_{p\uparrow}\rangle\langle\hat{c}^\dagger_{p\uparrow}\hat{c}_{n\downarrow}\rangle\Big) \\
& \qquad + V_n\Big(\langle\hat{n}_{p\downarrow}\rangle\hat{n}_{n\uparrow} + \langle\hat{n}_{n\uparrow}\rangle\hat{n}_{p\downarrow} - \langle\hat{n}_{p\downarrow}\rangle\langle\hat{n}_{n\uparrow}\rangle - \langle\hat{c}^\dagger_{p\downarrow}\hat{c}_{n\uparrow}\rangle\hat{c}^\dagger_{n\uparrow}\hat{c}_{p\downarrow} - \langle\hat{c}^\dagger_{n\uparrow}\hat{c}_{p\downarrow}\rangle\hat{c}^\dagger_{p\downarrow}\hat{c}_{n\uparrow} + \langle\hat{c}^\dagger_{n\uparrow}\hat{c}_{p\downarrow}\rangle\langle\hat{c}^\dagger_{p\downarrow}\hat{c}_{n\uparrow}\rangle\Big) \\
& \qquad + J_n\Big(-\langle\hat{S}^\dagger_p\rangle\hat{S}^-_n - \langle\hat{S}^-_n\rangle\hat{S}^\dagger_p + \langle\hat{c}^\dagger_{n\downarrow}\hat{c}_{p\downarrow}\rangle\hat{c}^\dagger_{p\uparrow}\hat{c}_{n\uparrow} + \langle\hat{c}^\dagger_{p\uparrow}\hat{c}_{n\uparrow}\rangle\hat{c}^\dagger_{n\downarrow}\hat{c}_{p\downarrow} - \langle\hat{c}^\dagger_{p\uparrow}\hat{c}_{n\uparrow}\rangle\langle\hat{c}^\dagger_{n\downarrow}\hat{c}_{p\downarrow}\rangle + \langle\hat{S}^\dagger_p\rangle\langle\hat{S}^-_n\rangle\Big) \\
& \qquad + J_n\Big(-\langle\hat{S}^-_p\rangle\hat{S}^\dagger_n - \langle\hat{S}^\dagger_n\rangle\hat{S}^-_p + \langle\hat{c}^\dagger_{p\downarrow}\hat{c}_{n\uparrow}\rangle\hat{c}^\dagger_{n\uparrow}\hat{c}_{p\uparrow} + \langle\hat{c}^\dagger_{n\uparrow}\hat{c}_{p\uparrow}\rangle\hat{c}^\dagger_{p\downarrow}\hat{c}_{n\downarrow} - \langle\hat{c}^\dagger_{n\uparrow}\hat{c}_{p\uparrow}\rangle\langle\hat{c}^\dagger_{p\downarrow}\hat{c}_{n\downarrow}\rangle + \langle\hat{S}^-_p\rangle\langle\hat{S}^\dagger_n\rangle\Big) \\
& \qquad + (V_n - J_n)\Big(\langle\hat{n}_{p\uparrow}\rangle\hat{n}_{n\uparrow} + \langle\hat{n}_{n\uparrow}\rangle\hat{n}_{p\uparrow} - \langle\hat{n}_{n\uparrow}\rangle\langle\hat{n}_{p\uparrow}\rangle - \langle\hat{c}^\dagger_{p\uparrow}\hat{c}_{n\uparrow}\rangle\hat{c}^\dagger_{n\uparrow}\hat{c}_{p\uparrow} - \langle\hat{c}^\dagger_{n\uparrow}\hat{c}_{p\uparrow}\rangle\hat{c}^\dagger_{p\uparrow}\hat{c}_{n\uparrow} + \langle\hat{c}^\dagger_{n\uparrow}\hat{c}_{p\uparrow}\rangle\langle\hat{c}^\dagger_{p\uparrow}\hat{c}_{n\uparrow}\rangle\Big) \\
& \qquad + (V_n - J_n)\Big(\langle\hat{n}_{p\downarrow}\rangle\hat{n}_{n\downarrow} + \langle\hat{n}_{n\downarrow}\rangle\hat{n}_{p\downarrow} - \langle\hat{n}_{n\downarrow}\rangle\langle\hat{n}_{p\downarrow}\rangle - \langle\hat{c}^\dagger_{p\downarrow}\hat{c}_{n\downarrow}\rangle\hat{c}^\dagger_{n\downarrow}\hat{c}_{p\downarrow} - \langle\hat{c}^\dagger_{n\downarrow}\hat{c}_{p\downarrow}\rangle\hat{c}^\dagger_{p\downarrow}\hat{c}_{n\downarrow} + \langle\hat{c}^\dagger_{n\downarrow}\hat{c}_{p\downarrow}\rangle\langle\hat{c}^\dagger_{p\downarrow}\hat{c}_{n\downarrow}\rangle\Big)\Bigg].
\end{aligned} \tag{C.1}
$$

D. Rotation of the Transition Matrix Elements in the Slater-Koster Approximation

Various different approaches for computing the two-center approximation integrals can be found in the literature [303, 304]. For specific purposes, some are more suitable than others. In opposition to the one presented in Chapter 3 for highlighting the computation of the polynomials in the Slater-Koster paper [182], an approach by Elena and Meister [303] is discussed here, which can be used to obtain the transition matrix elements when rotated with respect to each other, which is particularly useful in bending computations. A similar treatment also used in this section is found elsewhere [305, 306]. Using a representation of the Wigner d-function

$$d^l_{mm'}(\beta) = 2^{-l}(-1)^{l-m'} \left[(l+m)!(l-m)!(l+m')!(l-m')! \right]^{1/2}$$
$$\times \sum_{k=k_>}^{k_<} \frac{(-1)^k(1-\cos\beta)^{l-k-(m+m')/2}(1+\cos\beta)^{k+(m+m')/2}}{k!(l-m-k)!(l-m'-k)!(m+m'+k)!}, \quad \text{(D.1)}$$

with $k_< = \min(l-m, l-m')$, $k_> = \max(0, -m-m')$ and $l_< = \min(l_1, l_2)$ the following matrix elements yield the two-center integrals in dependence of the polar angle θ and azimuthal angle φ

$$\langle l_1 m_1 | H | l_2 m_2 \rangle (\varphi, \theta)$$
$$= \sum_{m'=1}^{l_<} \left[S^{l_1}_{m_1 m'}(\varphi, \theta) S^{l_2}_{m_2 m'}(\varphi, \theta) + T^{l_1}_{m_1 m'}(\varphi, \theta) T^{l_2}_{m_2 m'}(\varphi, \theta) \right] (l_1 l_2 | m' |)$$
$$+ 2 A_{m_1}(\varphi) A_{m_2}(\varphi) d^{l_1}_{|m_1|0}(\theta) d^{l_2}_{|m_2|0}(\theta) (l_1 l_2 0). \quad \text{(D.2)}$$

Here the material-specific parameters $(l_1 l_2 0)$ and $(l_1 l_2 | m' |)$ are the usual Slater-Koster parameters, e.g. $V_{ss\sigma}$ in the former and $V_{pp\pi}$ in the latter case. For the compact notation in Eq. D.2 the following two functions are introduced,

$$S^l_{mm'} := A_m \left[(-1)^{m'} d^l_{|m||m'|} + d^l_{|m|-m'} \right] \quad \text{(D.3)}$$

and

$$T^l_{mm'} := B_m(1-\delta_{m0}) \left[(-1)^{m'} d^l_{|m||m'|} - d^l_{|m|-m'} \right], \quad \text{(D.4)}$$
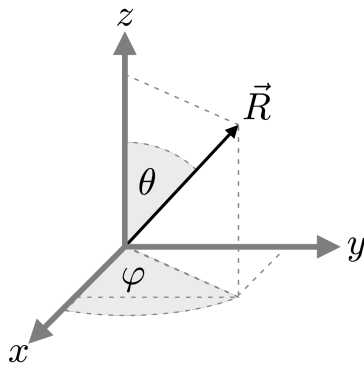
172

FIGURE D.1.: The definition of the azimuthal and polar angle in the Slater-Koster approximation.

making use of

$$A_m(\varphi) = \begin{cases} (-1)^m [\tau(m) \cos(|m|\varphi) + \tau(-m) \sin(|m|\varphi)] & \text{if } m \neq 0 \\ \frac{1}{\sqrt{2}} & \text{if } m = 0 \end{cases} \tag{D.5}$$

and

$$B_m(\varphi) = \begin{cases} (-1)^m [\tau(-m) \cos(|m|\varphi) - \tau(m) \sin(|m|\varphi)] & \text{if } m \neq 0 \\ 0 & \text{if } m = 0 \end{cases} \tag{D.6}$$

with the Heaviside function

$$\tau(m) = \begin{cases} 1 & \text{if } m \geq 0 \\ 0 & \text{if } m < 0 \end{cases}. \tag{D.7}$$

Bibliography

1. Charles Kittel. *Introduction to Solid State Physics* (John Wiley & Sons, 2004).

2. Heisenberg, W. *Die Physikalischen Prinzipien Der Quantentheorie* (Hirzel,S. Verlag, 2008).

3. Dirac, P. A. M. *The Principles of Quantum Mechanics* (Oxford University Press, Jan. 1981).

4. von Neumann, J. *Mathematical Foundations of Quantum Mechanics* (Princeton University Press, 2018).

5. Hunklinger, S. *Festkörperphysik* (de Gruyter, Berlin, Boston, 2017).

6. Hirsch, J., Maple, M. & Marsiglio, F. Superconducting Materials Classes: Introduction and Overview. *Superconducting Materials: Conventional, Unconventional and Undetermined* **514,** 1–8 (2015).

7. Yu, P. & Cardona, M. *Fundamentals of Semiconductors: Physics and Materials Properties* Fourth (Springer-Verlag Berlin Heidelberg, 2010).

8. Grundmann, M. *The Physics of Semiconductors* Third (Springer International Publishing, 2016).

9. Baimuratov, A. S. & Högele, A. Valley-Selective Energy Transfer between Quantum Dots in Atomically Thin Semiconductors. *Scientific Reports* **10,** 16971 (2020).

10. Winiarski, M. J. & Kowalska, D. A. Crystal Structure of Rare Earth and Group III Nitride Alloys by Ab Initio Calculations. *Scientific Reports* **10,** 16414 (2020).

11. Jin, W. *et al.* Observation of the Polaronic Character of Excitons in a Two-Dimensional Semiconducting Magnet CrI_3. *Nature Communications* **11,** 4780 (2020).

12. Davidovikj, D. *et al.* Ultrathin Complex Oxide Nanomechanical Resonators. *Communications Physics* **3,** 163 (2020).

13. He, M. *et al.* Symmetry Breaking in Twisted Double Bilayer Graphene. *Nature Physics,* 26–30 (2020).

14. Jeong, H., Song, J. H., Jeong, S. & Chang, W. S. Graphene/PbS Quantum Dot Hybrid Structure for Application in near-Infrared Photodetectors. *Scientific Reports* **10,** 12475 (2020).

15. Patri, A. S., Khait, I. & Kim, Y. B. Emergent Non-Fermi-Liquid Phenomena in Multipolar Quantum Impurity Systems. *Physical Review Research* **2,** 013257 (2020).

16. Snider, E. *et al.* Room-Temperature Superconductivity in a Carbonaceous Sulfur Hydride. *Nature* **586,** 373–377 (2020).

17. Ashcroft, N. W. & Wagner, N. D. *Solid State Physics* (Cengage Learning, 1976).

18. Flores-Livas, J. A. *et al.* Emergence of Superconductivity in Doped H_2O Ice at High Pressure. *Scientific Reports* **7,** 6825 (2017).

19. Kawashima, K. *et al.* Superconductivity in a 122-Type Fe-Based Compound $(La,Na,K)Fe_2As_2$. *Scientific Reports* **8,** 16827 (2018).

20. Bernevig, B. A. & Hughes, T. L. *Topological Insulators and Topological Superconductors* (Princeton University Press, 2013).

21. Jänich, K. *Topologie* (Springer, Berlin, Heidelberg, 2005).

22. Kühnel, W. *Differentialgeometrie: Kurven - Flächen - Mannigfaltigkeiten* Sixth (Springer Spektrum, 2013).

23. Hasan, M. Z. & Kane, C. L. Colloquium: Topological Insulators. *Reviews of Modern Physics* **82,** 3045–3067 (2010).

24. Gehring, P. & Burghard, M. Topologische Isolatoren. *Physik in unserer Zeit* **45,** 299–305 (2014).

25. Thouless, D. J., Kohmoto, M., Nightingale, M. P. & den Nijs, M. Quantized Hall Conductance in a Two-Dimensional Periodic Potential. *Physical Review Letters* **49,** 405–408 (1982).

26. Kane, C. L. & Mele, E. J. Z_2 Topological Order and the Quantum Spin Hall Effect. *Physical Review Letters* **95,** 146802 (2005).

27. Landau, L. D. On the Theory of Phase Transitions. *Journal of Experimental and Theoretical Physics* **7,** 19–32 (1937).

28. Hall, E. H. On a New Action of the Magnet on Electric Currents. *American Journal of Mathematics* **2,** 287–292 (1879).

29. V. Klitzing, K., Dorda, G. & Pepper, M. New Method for High-Accuracy Determination of the Fine-Structure Constant Based on Quantized Hall Resistance. *Physical Review Letters* **45,** 494–497 (1980).

30. Avron, J. E., Osadchy, D. & Seiler, R. A Topological Look at the Quantum Hall Effect. *Physics Today* **56,** 38–42 (2003).

31. Haldane, F. D. M. Model for a Quantum Hall Effect without Landau Levels: Condensed-Matter Realization of the "Parity Anomaly". *Physical Review Letters* **61,** 2015–2018 (1988).

32. Chang, R.-A. & Chang, C.-R. Chern Insulator in a Ferromagnetic Two-Dimensional Electron System with Dresselhaus Spin–Orbit Coupling. *New Journal of Physics* **21,** 103019 (2019).

33. Wen, X.-G. Theory of the Edge States in Fractional Quantum Hall Effects. *International Journal of Modern Physics B* **06,** 1711–1762 (1992).

34. Asbóth, J. K., Oroszlány, L. & Pályi, A. *A Short Introduction to Topological Insulators* (Springer International Publishing, 2016).

35. Murakami, S., Nagaosa, N. & Zhang, S.-C. Dissipationless Quantum Spin Current at Room Temperature. *Science* **301,** 1348 (2003).

36. Sinova, J. *et al.* Universal Intrinsic Spin Hall Effect. *Physical Review Letters* **92,** 126603 (2004).

37. Jungwirth, T., Wunderlich, J. & Olejník, K. Spin Hall Effect Devices. *Nature Materials* **11,** 382–390 (2012).

38. Kato, Y. K., Myers, R. C., Gossard, A. C. & Awschalom, D. D. Observation of the Spin Hall Effect in Semiconductors. *Science* **306,** 1910 (2004).

39. Qi, X.-L. & Zhang, S.-C. The Quantum Spin Hall Effect and Topological Insulators. *Physics Today* **63,** 33 (2010).

40. Murakami, S. Two-Dimensional Topological Insulators and Their Edge States. *Journal of Physics: Conference Series* **302,** 012019 (2011).

41. Kane, C. L. & Mele, E. J. Quantum Spin Hall Effect in Graphene. *Physical Review Letters* **95,** 226801 (2005).

42. Moore, J. E. The Birth of Topological Insulators. *Nature* **464,** 194–198 (2010).

43. Yang, Y. *et al.* Time-Reversal-Symmetry-Broken Quantum Spin Hall Effect. *Physical Review Letters* **107,** 066602 (2011).

44. Bernevig, B. A. & Zhang, S.-C. Quantum Spin Hall Effect. *Physical Review Letters* **96,** 106802 (2006).

45. Bernevig, B. A., Hughes, T. L. & Zhang, S.-C. Quantum Spin Hall Effect and Topological Phase Transition in HgTe Quantum Wells. *Science* **314,** 1757–1761 (2006).

46. Thouless, D. J. *Topological Quantum Numbers in Nonrelativistic Physics* (World Scientific, 1998).

47. Li, Y. Y., Chen, M. X., Weinert, M. & Li, L. Direct Experimental Determination of Onset of Electron–Electron Interactions in Gap Opening of Zigzag Graphene Nanoribbons. *Nature Communications* **5,** 4311 (2014).

48. Goerbig, M. O. From Fractional Chern Insulators to a Fractional Quantum Spin Hall Effect. *The European Physical Journal B* **85,** 15 (2012).

49. Yazyev, O. V. Emergence of Magnetism in Graphene Materials and Nanostructures. *Reports on Progress in Physics* **73,** 056501 (2010).

50. Wakabayashi, K., Sasaki, K.-i., Nakanishi, T. & Enoki, T. Electronic States of Graphene Nanoribbons and Analytical Solutions. *Science and Technology of Advanced Materials* **11,** 054504 (2010).

51. König, M. *et al.* Quantum Spin Hall Insulator State in HgTe Quantum Wells. *Science* **318,** 766 (2007).

52. Hsieh, D. *et al.* A Topological Dirac Insulator in a Quantum Spin Hall Phase. *Nature* **452,** 970–974 (2008).

53. Hasan, M. Z. & Moore, J. E. Three-Dimensional Topological Insulators. *Annual Review of Condensed Matter Physics* **2,** 55–78 (2011).

54. Zhang, Y. Experimental Techniques Used in Topological Insulators and Realization of Quantum Spin Hall Effect. *IOP Conference Series: Materials Science and Engineering* **563,** 022033 (2019).

55. Kou, L., Ma, Y., Sun, Z., Heine, T. & Chen, C. Two-Dimensional Topological Insulators: Progress and Prospects. *The Journal of Physical Chemistry Letters* **8,** 1905–1919 (2017).

56. Khanikaev, A. B. *et al.* Photonic Topological Insulators. *Nature Materials* **12,** 233–239 (2013).

57. Lustig, E. *et al.* Photonic Topological Insulator in Synthetic Dimensions. *Nature* **567,** 356–360 (2019).

58. Rechtsman, M. C. *et al.* Photonic Floquet Topological Insulators. *Nature* **496,** 196–200 (2013).

59. Liu, W. *et al.* Z_2 Photonic Topological Insulators in the Visible Wavelength Range for Robust Nanoscale Photonics. *Nano Letters* **20,** 1329–1335 (2020).

60. Klembt, S. *et al.* Exciton-Polariton Topological Insulator. *Nature* **562,** 552–556 (2018).

61. Otrokov, M. M. *et al.* Prediction and Observation of an Antiferromagnetic Topological Insulator. *Nature* **576,** 416–422 (2019).

62. Pesin, D. & MacDonald, A. H. Spintronics and Pseudospintronics in Graphene and Topological Insulators. *Nature Materials* **11,** 409–416 (2012).

63. Hirohata, A. *et al.* Review on Spintronics: Principles and Device Applications. *Journal of Magnetism and Magnetic Materials* **509,** 166711 (2020).

64. Lu, J. W., Chen, E., Kabir, M., Stan, M. R. & Wolf, S. A. Spintronics Technology: Past, Present and Future. *International Materials Reviews* **61,** 456–472 (2016).

65. Zegeye, S. M. A Review Paper on Spintronics and Its Role to Improve Electronic Devies. *American Journal of Quantum Chemistry and Molecular Spectroscopy* **3,** 41–47 (2019).

66. Baughman, R. H., Zakhidov, A. A. & de Heer, W. A. Carbon Nanotubes - the Route Toward Applications. *Science* **297,** 787–792 (2002).

67. C. D. Dimitrakopoulos & D. J. Mascaro. Organic Thin-Film Transistors: A Review of Recent Advances. *IBM Journal of Research and Development* **45,** 11–27 (2001).

68. Reich, S., Thomsen, C. & Maultzsch, J. *Carbon Nanotubes: Basic Concepts and Physical Properties* (Addison-Wiley, 2004).

69. Saito, R., Dresselhaus, G. & Dresselhaus, M. S. *Physical Properties of Carbon Nanotubes* (World Scientific, 1998).

70. Wallace, P. R. The Band Theory of Graphite. *Physical Review* **71,** 622–634 (1947).

71. McClure, J. W. Diamagnetism of Graphite. *Physical Review* **104,** 666–671 (1956).

72. Slonczewski, J. C. & Weiss, P. R. Band Structure of Graphite. *Physical Review* **109,** 272–279 (1958).

73. Novoselov, K. S. *et al.* Electric Field Effect in Atomically Thin Carbon Films. *Science* **306,** 666–669 (2004).

74. Novoselov, K. S. *et al.* Two-Dimensional Atomic Crystals. *Proceedings of the National Academy of Sciences of the United States of America* **102,** 10451 (2005).

75. Katsnelson, M. I., Novoselov, K. S. & Geim, A. K. Chiral Tunnelling and the Klein Paradox in Graphene. *Nature Physics* **2,** 620–625 (2006).

76. Katsnelson, M. I. Graphene: Carbon in Two Dimensions. *Materials Today* **10,** 20–27 (2007).

77. Brey, L. & Fertig, H. A. Edge States and the Quantized Hall Effect in Graphene. *Physical Review B* **73,** 195408 (2006).

78. Gosálbez-Martínez, D., Palacios, J. J. & Fernández-Rossier, J. Spin-Orbit Interaction in Curved Graphene Ribbons. *Physical Review B* **83,** 115436 (2011).

79. Goldman, N., Beugeling, W. & Smith, C. M. Topological Phase Transitions between Chiral and Helical Spin Textures in a Lattice with Spin-Orbit Coupling and a Magnetic Field. *Europhysics Letters Association* **97,** 23003 (2012).

80. Konschuh, S., Gmitra, M. & Fabian, J. Tight-Binding Theory of the Spin-Orbit Coupling in Graphene. *Physical Review B* **82,** 245412 (2010).

81. Min, H. *et al.* Intrinsic and Rashba Spin-Orbit Interactions in Graphene Sheets. *Physical Review B* **74,** 165310 (2006).

82. Huertas-Hernando, D., Guinea, F. & Brataas, A. Spin-Orbit Coupling in Curved Graphene, Fullerenes, Nanotubes, and Nanotube Caps. *Physical Review B* **74,** 155426 (2006).

83. Balakrishnan, J., Kok Wai Koon, G., Jaiswal, M., Castro Neto, A. H. & Özyilmaz, B. Colossal Enhancement of Spin–Orbit Coupling in Weakly Hydrogenated Graphene. *Nature Physics* **9,** 284–287 (2013).

84. Zhou, J., Liang, Q. & Dong, J. Enhanced Spin–Orbit Coupling in Hydrogenated and Fluorinated Graphene. *Carbon* **48,** 1405–1409 (2010).

85. Ciattoni, A., Rizza, C., Lee, H. W. H., Conti, C. & Marini, A. Plasmon-Enhanced Spin–Orbit Interaction of Light in Graphene. *Laser & Photonics Reviews* **12,** 1800140 (2018).

86. Wakamura, T. *et al.* Spin-Orbit Interaction Induced in Graphene by Transition Metal Dichalcogenides. *Physical Review B* **99,** 245402 (2019).

87. Wang, Z. *et al.* Strong Interface-Induced Spin–Orbit Interaction in Graphene on WS_2. *Nature Communications* **6,** 8339 (2015).

88. Reich, S., Maultzsch, J., Thomsen, C. & Ordejón, P. Tight-Binding Description of Graphene. *Physical Review B* **66,** 035412 (2002).

89. Georges, A., Kotliar, G., Krauth, W. & Rozenberg, M. J. Dynamical Mean-Field Theory of Strongly Correlated Fermion Systems and the Limit of Infinite Dimensions. *Reviews of Modern Physics* **68,** 13–125 (1996).

90. Burke, K. Perspective on Density Functional Theory. *The Journal of Chemical Physics* **136,** 150901 (2012).

91. Polini, M., Tomadin, A., Asgari, R. & MacDonald, A. H. Density Functional Theory of Graphene Sheets. *Physical Review B* **78,** 115426 (2008).

92. Lewenkopf, C. H. & Mucciolo, E. R. The Recursive Green's Function Method for Graphene. *Journal of Computational Electronics* **12,** 203–231 (2013).

93. Czycholl, G. *Theoretische Festkörperphysik Band 1* (Springer Spektrum, 2016).

94. Premasiri, K. & Gao, X. P. A. Tuning Spin–Orbit Coupling in 2D Materials for Spintronics: A Topical Review. *Journal of Physics: Condensed Matter* **31,** 193001 (2019).

95. Dresselhaus, G. Spin-Orbit Coupling Effects in Zinc Blende Structures. *Physical Review* **100,** 580–586 (1955).

96. Rashba, E. I. & Sheka, V. I. Symmetry of Energy Bands in Crystals of Wurtzite Type II. Symmetry of Bands with Spin-Orbit Interaction Included. *New Journal of Physics* **17,** 050202 (2015).

97. Meschede, D. *Gerthsen Physik* (Springer Spektrum, 2015).

98. Nolting, W. *Grundkurs Theoretische Physik 5/2* (Springer Spektrum, 2015).

99. Goldstein, H. *Classical Mechanics* (Addison-Wesley, 2002).

100. Mayer-Kuckuk, T. *Atomphysik* (Vieweg+Teubner Verlag, 1997).

101. Farago, P. S. Derivation of the Spin-Orbit Interaction. *American Journal of Physics* **35,** 246–249 (1967).

102. Lew Yan Voon, L. C. & Willatzen, M. *The k·p Method* (Springer-Verlag Berlin Heidelberg, 2009).

103. Löwdin, P.-O. A Note on the Quantum Mechanical Perturbation Theory. *The Journal of Chemical Physics* **19,** 1396–1401 (1951).

104. Winkler, R. *Spin-Orbit Coupling Effects in Two-Dimensional Electron and Hole Systems* (Springer-Verlag Berlin Heidelberg, 2003).

105. Glasser, M. Symmetry Properties of the Wurtzite Structure. *Journal of Physics and Chemistry of Solids* **10,** 229–241 (1959).

106. Rashba, E. I. Graphene with Structure-Induced Spin-Orbit Coupling: Spin-Polarized States, Spin Zero Modes, and Quantum Hall Effect. *Physical Review B* **79,** 161409 (2009).

107. Petersen, L. & Hedegård, P. A Simple Tight-Binding Model of Spin–Orbit Splitting of sp -Derived Surface States. *Surface Science* **459,** 49–56 (2000).

108. Messiah, A. *Quantenmechanik 2* (de Gruyter, 1990).

109. Herring, C. Effect of Time-Reversal Symmetry on Energy Bands of Crystals. *Physical Review* **52,** 361–365 (1937).

110. Lado, J., García-Martínez, N. & Fernández-Rossier, J. Edge States in Graphene-like Systems. *Synthetic Metals* **210,** 56–67 (2015).

111. Dresselhaus, M. S. & Dresselhaus, G. *Group Theory* (Springer, 2008).

112. Fischer, G. *Lineare Algebra* (Springer Spektrum, 2010).

113. Koster, G. in *Solid State Physics* (eds Seitz, F. & Turnbull, D.) 173–256 (Academic Press, 1957).

114. Koster, G. *Properties of the 32 Point Groups* (MIT Press, 1963).

115. Kogan, E. & Nazarov, V. U. Symmetry Classification of Energy Bands in Graphene. *Physical Review B* **85,** 115418 (2012).

116. Wigner, E. P. *Gruppentheorie Und Ihre Anwendung Auf Die Quantenmechanik Der Atomspektren* (Springer Vieweg, 1931).

117. Seitz, F. On the Reduction of Space Groups. *Annals of Mathematics* **37,** 17–28 (1936).

118. Cvetkovic, V. & Vafek, O. Space Group Symmetry, Spin-Orbit Coupling, and the Low-Energy Effective Hamiltonian for Iron-Based Superconductors. *Physical Review B* **88,** 134510 (2013).

119. Fabian, J., Matos-Abiague, A., Ertler, C., Stano, P. & Žutić, I. Semiconductor Spintronics. *Acta Physica Slovaca. Reviews and Tutorials* **57** (2007).

120. Foreman, B. A. Effective-Mass Hamiltonian and Boundary Conditions for the Valence Bands of Semiconductor Microstructures. *Physical Review B* **48,** 4964–4967 (1993).

121. Kittel, C. & Mitchell, A. H. Theory of Donor and Acceptor States in Silicon and Germanium. *Physical Review* **96,** 1488–1493 (1954).

122. Elliott, R. J. Theory of the Effect of Spin-Orbit Coupling on Magnetic Resonance in Some Semiconductors. *Physical Review* **96,** 266–279 (1954).

123. Elliott, R. J. Spin-Orbit Coupling in Band Theory—Character Tables for Some "Double" Space Groups. *Physical Review* **96,** 280–287 (1954).

124. Kochan, D., Irmer, S. & Fabian, J. Model Spin-Orbit Coupling Hamiltonians for Graphene Systems. *Physical Review B* **95,** 165415 (2017).

125. Kurpas, M., Faria Junior, P. E., Gmitra, M. & Fabian, J. Spin-Orbit Coupling in Elemental Two-Dimensional Materials. *Physical Review B* **100,** 125422 (2019).

126. Dresselhaus, G., Kip, A. F. & Kittel, C. Cyclotron Resonance of Electrons and Holes in Silicon and Germanium Crystals. *Physical Review* **98,** 368–384 (1955).

127. Galeriu, C. k·p *Theory of Semiconductor Nanostructures* PhD Thesis (Worcester Polytechnic Institute, 2005).

128. Kane, E. O. Band Structure of Indium Antimonide. *Journal of Physics and Chemistry of Solids* **1,** 249–261 (1957).

129. Luttinger, J. M. & Kohn, W. Motion of Electrons and Holes in Perturbed Periodic Fields. *Physical Review* **97,** 869–883 (1955).

130. Kane, E. O. Energy Band Structure in P-Type Germanium and Silicon. *Journal of Physics and Chemistry of Solids* **1,** 82–99 (1956).

131. Kane, E. O. The Semi-Empirical Approach to Band Structure. *Journal of Physics and Chemistry of Solids* **8,** 38–44 (1959).

132. Chuang, S. L. & Chang, C. S. *k·p* Method for Strained Wurtzite Semiconductors. *Physical Review B* **54,** 2491–2504 (1996).

133. Rössler, U. Nonparabolicity and Warping in the Conduction Band of GaAs. *Solid State Communications* **49,** 943–947 (1984).

134. Malard, L. M., Guimarães, M. H. D., Mafra, D. L., Mazzoni, M. S. C. & Jorio, A. Group-Theory Analysis of Electrons and Phonons in N-Layer Graphene Systems. *Physical Review B* **79,** 125426 (2009).

135. Vaughan, M. P. & Rorison, J. M. Modeling Spin Relaxation in Semiconductor Quantum Wells: Modifying the Elliot Process. *Semiconductor Science and Technology* **33,** 094003 (2018).

136. Ganichev, S. D. & Golub, L. E. Interplay of Rashba/ Dresselhaus Spin Splittings Probed by Photogalvanic Spectroscopy – A Review. *Phys. Status Solidi B* **251,** 1801–1823 (2014).

137. Gmitra, M. & Fabian, J. Graphene on Transition-Metal Dichalcogenides: A Platform for Proximity Spin-Orbit Physics and Optospintronics. *Physical Review B* **92,** 155403 (2015).

138. Gmitra, M. & Fabian, J. First-Principles Studies of Orbital and Spin-Orbit Properties of GaAs, GaSb, InAs, and InSb Zinc-Blende and Wurtzite Semiconductors. *Physical Review B* **94,** 165202 (2016).

139. Gmitra, M., Kochan, D., Högl, P. & Fabian, J. Trivial and Inverted Dirac Bands and the Emergence of Quantum Spin Hall States in Graphene on Transition-Metal Dichalcogenides. *Physical Review B* **93,** 155104 (2016).

140. Hao, Y. F. Rashba and Dresselhaus Spin-Orbit Interaction in Semiconductor Quantum Wells. *The European Physical Journal B* **85,** 84 (2012).

141. Bihlmayer, G., Rader, O. & Winkler, R. Focus on the Rashba Effect. *New Journal of Physics* **17,** 050202 (2015).

142. Bychkov, Y. A. & Rashba, E. I. Properties of a 2D Electron Gas with Lifted Spectral Degeneracy. *JETP Letters* **39,** 78 (1984).

143. Bihlmayer, G. & Blügel, S. *Electronic Structure of Matter* in *Lecture Notes f the 47th IFF Spring School 2016 "Memristive Phenomena - From Fundamental Physics to Neuromorphic Computing"* (eds Waser, R. & Wuttig, M.) **113** (2016).

144. Shanavas, K. V. & Satpathy, S. Electric Field Tuning of the Rashba Effect in the Polar Perovskite Structures. *Physical Review Letters* **112,** 086802 (2014).

145. Shanavas, K. V., Popović, Z. S. & Satpathy, S. Theoretical Model for Rashba Spin-Orbit Interaction in d-Electrons. *Physical Review B* **90,** 165108 (2014).

146. Ast, C. R. & Gierz, I. Sp-Band Tight-Binding Model for the Bychkov-Rashba Effect in a Two-Dimensional Electron System Including Nearest-Neighbor Contributions from an Electric Field. *Physical Review B* **86,** 085105 (2012).

147. Berche, B., Mireles, F. & Medina, E. Rashba Spin-Orbit Interaction Enhanced by Graphene in-Plane Deformations. *Condensed Matter Physics* **20,** 13702 (2017).

148. Landau, L. & Lifshitz, E. *Quantum Mechnics* (Pergamon Press, 1977).

149. Nestoklon, M. O. Electric Field Effect on Electron Spin Splitting in SiGe/Si Quantum Wells. *Phys. Rev. B* **77,** 155328 (2008).

150. van Gelderen, R. & Morais-Smith, C. Rashba and Intrinsic Spin-Orbit Interactions in Biased Bilayer Graphene. *Physical Review B* **81,** 125435 (2010).

151. Sichau, J. *et al.* Resonance Microwave Measurements of an Intrinsic Spin-Orbit Coupling Gap in Graphene: A Possible Indication of a Topological State. *Physical Review Letters* **122,** 046403 (2019).

152. Sichau, J. *Electron Spin Resonance Studies on Spin-Orbit Interactions in Graphene* English. PhD Thesis (Universität Hamburg, Hamburg, Germany, 2019).

153. Mani, R. G., Hankinson, J., Berger, C. & de Heer, W. A. Observation of Resistively Detected Hole Spin Resonance and Zero-Field Pseudo-Spin Splitting in Epitaxial Graphene. *Nature Communications* **3,** 996 (2012).

154. Wang, Z. *et al.* Origin and Magnitude of 'Designer' Spin-Orbit Interaction in Graphene on Semiconducting Transition Metal Dichalcogenides. *Physical Review X* **6,** 041020 (2016).

155. Yang, B. *et al.* Tunable Spin–Orbit Coupling and Symmetry-Protected Edge States in Graphene/ WS$_2$. *2D Materials* **3,** 031012 (2016).

156. Yang, B. *et al.* Strong Electron-Hole Symmetric Rashba Spin-Orbit Coupling in Graphene/ Monolayer Transition Metal Dichalcogenide Heterostructures. *Physical Review B* **96,** 041409 (2017).

157. Hikami, S., Larkin, A. I. & Nagaoka, Y. Spin-Orbit Interaction and Magnetoresistance in the Two Dimensional Random System. *Progress of Theoretical Physics* **63,** 707–710 (1980).

158. Tikhonenko, F., Kozikov, A., Savchenko, A. & Gorbachev, R. Transition between Electron Localization and Antilocalization in Graphene. *Physical Review Letters* **103,** 226801 (2009).

159. Novoselov, K. S. *et al.* Two-Dimensional Gas of Massless Dirac Fermions in Graphene. *Nature* **438,** 197–200 (2005).

160. Datta, S. *Electronic Transport in Mesoscopic Systems* (Cambridge University Press, 1995).

161. Beenakker, C. & van Houten, H. in *Solid State Physics* (eds Ehrenreich, H. & Turnbull, D.) 1–228 (Academic Press, 1991).

162. Wang, D. *et al.* Quantum Hall Effect Measurement of Spin–Orbit Coupling Strengths in Ultraclean Bilayer Graphene/WSe$_2$ Heterostructures. *Nano Letters* **19,** 7028–7034 (2019).

163. Hsu, Y.-T., Vaezi, A., Fischer, M. H. & Kim, E.-A. Topological Superconductivity in Monolayer Transition Metal Dichalcogenides. *Nature Communications* **8,** 14985 (2017).

164. Lu, J. M. *et al.* Evidence for Two-Dimensional Ising Superconductivity in Gated MoS$_2$. *Science* **350,** 1353 (2015).

165. Afzal, A. M., Min, K. H., Ko, B. M. & Eom, J. Observation of Giant Spin–Orbit Interaction in Graphene and Heavy Metal Heterostructures. *RSC Advances* **9,** 31797–31805 (2019).

166. Otrokov, M. M. *et al.* Evidence of Large Spin-Orbit Coupling Effects in Quasi-Free-Standing Graphene on Pb/Ir(1 1 1). *2D Materials* **5,** 035029 (2018).

167. Balakrishnan, J. *et al.* Giant Spin Hall Effect in Graphene Grown by Chemical Vapour Deposition. *Nature Communications* **5,** 4748 (2014).

168. Avsar, A., Lee, J. H., Koon, G. K. W. & Özyilmaz, B. Enhanced Spin–Orbit Coupling in Dilute Fluorinated Graphene. *2D Materials* **2,** 044009 (Nov. 2015).

169. Yao, Y., Ye, F., Qi, X.-L., Zhang, S.-C. & Fang, Z. Spin-Orbit Gap of Graphene: First-Principles Calculations. *Physical Review B* **75,** 041401 (2007).

170. Boettger, J. C. Scalar-Relativistic Linear Combinations of Gaussian-Type-Orbitals Technique for Crystalline Solids. *Physical Review B* **57,** 8743–8746 (1998).

171. Boettger, J. C. & Trickey, S. B. First-Principles Calculation of the Spin-Orbit Splitting in Graphene. *Physical Review B* **75,** 121402 (2007).

172. Irmer, S. *et al.* Spin-Orbit Coupling in Fluorinated Graphene. *Physical Review B* **91,** 115141 (2015).

173. Martin, R. M. *Electronic Structure: Basic Theory and Practical Methods* (Cambridge University Press, Cambridge, 2004).

174. Lawlor, J. A. & Ferreira, M. S. Green Functions of Graphene: An Analytic Approach. *Physica B: Condensed Matter* **463,** 48–53 (2015).

175. Boykin, T. B. & Klimeck, G. Practical Application of Zone-Folding Concepts in Tight-Binding Calculations. *Physical Review B* **71,** 115215 (2005).

176. Carvalho, A. R. A. *Edge Magnetization in Chiral Graphene Nanoribbons and Quantum Anomalous Hall Effect Interfaces in Graphene* PhD Thesis (Universidade Federal Fluminense, Rio de Janeiro, Brazil, 2016).

177. Kunstmann, J., Özdoğğan, C., Quandt, A. & Fehske, H. Stability of Edge States and Edge Magnetism in Graphene Nanoribbons. *Physical Review B* **83,** 045414 (2011).

178. Wang, L., Sofer, Z. & Pumera, M. Will Any Crap We Put into Graphene Increase Its Electrocatalytic Effect? *ACS Nano* **14,** 21–25 (2020).

179. Feldner, H. *et al.* Magnetism of Finite Graphene Samples: Mean-Field Theory Compared with Exact Diagonalization and Quantum Monte Carlo Simulations. *Physical Review B* **81,** 115416 (2010).

180. Mecklenburg, M. & Regan, B. C. Spin and the Honeycomb Lattice: Lessons from Graphene. *Physical Review Letters* **106,** 116803 (2011).

184

181. Chisholm, C. D. H. *Group Theoretical Techniques in Quantum Chemistry* (London New York Academic Press, 1976).

182. Slater, J. C. & Koster, G. F. Simplified LCAO Method for the Periodic Potential Problem. *Physical Review* **94,** 1498–1524 (1954).

183. Lendi, K. Extension of the Slater-Koster Tables for Tight-Binding Calculations to f-Electrons. *Physical Review B* **9,** 2433–2440 (1974).

184. Claveau, Y., Arnaud, B. & Matteo, S. D. Mean-Field Solution of the Hubbard Model: The Magnetic Phase Diagram. *European Journal of Physics* **35,** 035023 (2014).

185. Condon, E. & Shortley, G. *The Theory of Atomic Spectra* (Cambridge University Press, 1935).

186. Edmonds, A. R. *Angular Momentum in Quantum Mechanics* (Princeton University Press, 1957).

187. Bronstein, I. N., Mühlig, H., Musiol, G. & Semendjajew, K. A. *Taschenbuch Der Mathematik* (Edition Harri Deutsch, 2016).

188. Shankar, R. *Principles of Quantum Mechanics* (Springer, 2011).

189. *Memristive Phenomena – From Fundamental Physics to Neuromorphic Computing 47th IFF Spring School, Jülich* (eds Waser, R. & Wuttig, M.) (Forschungszentrum Jülich GmbH Zentralbibliothek Verlag Jülich, Jülich, 2016).

190. Shanavas, K. V. Theoretical Study of the Cubic Rashba Effect at the $SrTiO_3$ (001) Surfaces. *Physical Review B* **93,** 045108 (2016).

191. Rakyta, P., Kormányos, A. & Cserti, J. Trigonal Warping and Anisotropic Band Splitting in Monolayer Graphene Due to Rashba Spin-Orbit Coupling. *Physical Review B* **82,** 113405 (2010).

192. Goerbig, M. O. & Montambaux, G. Dirac Fermions in Condensed Matter and Beyond. *arXiv:1410.4098* (2014).

193. Kazankin-Berg, A. *Characterization of Sublattice Spin in Bi-Partite Lattices at the Example of the Low-Energy Description of Graphene* Bachelor Thesis (Universität Hamburg, Hamburg, Germany, 2020).

194. Fuchs, J.-N. Dirac Fermions in Graphene and Analogues: Magnetic Field and Topological Properties. *arXiv:1306.0380* (2013).

195. Aharonov, Y. & Bohm, D. Significance of Electromagnetic Potentials in the Quantum Theory. *Physical Review* **115,** 485–491 (1959).

196. Peierls, R. Zur Theorie Des Diamagnetismus von Leitungselektronen. *Zeitschrift für Physik* **80,** 763–791 (1933).

197. Roth, L. Theory of Bloch Electrons in a Magnetic Field. *Journal of Physics and Chemistry of Solids* **23,** 433–446 (1962).

198. Aidelsburger, M. *Artificial Gauge Fields with Ultracold Atoms in Optical Lattices* PhD Thesis (Ludwig-Maximilians-Universität, Munich, Germany, 2016).

199. Feynman, R. P., Leighton, R. B. & Sands, M. *The Feynman Lectures on Physics Vol. 2: Mainly Electromagnetism and Matter* (Basic Books; New Millennium ed. Edition, 2011).

200. Harper, P. G. The General Motion of Conduction Electrons in a Uniform Magnetic Field, with Application to the Diamagnetism of Metals. *Proceedings of the Physical Society. Section A* **68,** 879–892 (1955).

201. Eliashvili, M., Tsitsishvili, G. & Japaridze, G. The Quantum Group and Harper Equation on a Honeycomb Lattice. en. *Journal of Mathematical Sciences* **216,** 522–526 (2016).

202. Langbein, D. The Tight-Binding and the Nearly-Free-Electron Approach to Lattice Electrons in External Magnetic Fields. *Physical Review* **180,** 633–648 (1969).

203. Hofstadter, D. R. Energy Levels and Wave Functions of Bloch Electrons in Rational and Irrational Magnetic Fields. *Physical Review B* **14,** 2239–2249 (1976).

204. Rössler, U. & Suhrke, M. *Bloch Electrons in a Magnetic Field: Hofstadter's Butterfly* in *Advances in Solid State Physics 40* (ed Kramer, B.) (Springer Berlin Heidelberg, Berlin, Heidelberg, 2000), 35–50.

205. Skomski, R. *Simple Models of Magnetism* (Oxford University Press, Oxford, 2008).

206. Haken, H. & Wolf, H. *Atom- Und Quantenphysik: Einführung in Die Experimentellen Und Theoretischen Grundlagen* (Springer Berlin Heidelberg, 2013).

207. Yao, W., Yang, S. A. & Niu, Q. Edge States in Graphene: From Gapped Flat-Band to Gapless Chiral Modes. *Physical Review Letters* **102,** 096801 (2009).

208. Zhao, X., Li, L. & Zhao, M. Lattice Match and Lattice Mismatch Models of Graphene on Hexagonal Boron Nitride from First Principles. *Journal of Physics: Condensed Matter* **26,** 095002 (2014).

209. Fruchart, M. & Carpentier, D. An Introduction to Topological Insulators. *Comptes Rendus Physique* **14,** 779–815 (2013).

210. Brey, L. & Fertig, H. A. Electronic States of Graphene Nanoribbons Studied with the Dirac Equation. *Physical Review B* **73,** 235411 (2006).

211. König, M. *et al.* The Quantum Spin Hall Effect: Theory and Experiment. *Journal of the Physical Society of Japan* **77,** 031007 (2008).

212. Qiao, Z. *et al.* Quantum Anomalous Hall Effect in Graphene from Rashba and Exchange Effects. *Physical Review B* **82,** 161414 (2010).

213. Gosálbez-Martínez, D., Soriano, D., Palacios, J. & Fernández-Rossier, J. Spin-Filtered Edge States in Graphene. *Solid State Communications* **152,** 1469–1476 (2012).

214. Altland, A. & Zirnbauer, M. R. Nonstandard Symmetry Classes in Mesoscopic Normal-Superconducting Hybrid Structures. *Physical Review B* **55,** 1142–1161 (1997).

215. Zirnbauer, M. R. Riemannian Symmetric Superspaces and Their Origin in Random-matrix Theory. *Journal of Mathematical Physics* **37,** 4986–5018 (1996).

216. Ryu, S., Schnyder, A. P., Furusaki, A. & Ludwig, A. W. W. Topological Insulators and Superconductors: Tenfold Way and Dimensional Hierarchy. *New Journal of Physics* **12,** 065010 (2010).

217. Liu, Y., Bian, G., Miller, T. & Chiang, T.-C. Visualizing Electronic Chirality and Berry Phases in Graphene Systems Using Photoemission with Circularly Polarized Light. *Physical Review Letters* **107,** 166803 (2011).

218. Drozdov, I. K. *et al.* One-Dimensional Topological Edge States of Bismuth Bilayers. *Nature Physics* **10,** 664–669 (2014).

219. Hou, J.-M. & Chen, W. Hidden Symmetry and Protection of Dirac Points on the Honeycomb Lattice. *Scientific Reports* **5,** 17571 (2015).

220. Mikitik, G. P. & Sharlai, Y. V. Manifestation of Berry's Phase in Metal Physics. *Physical Review Letters* **82,** 2147–2150 (1999).

221. Xiao, D., Chang, M.-C. & Niu, Q. Berry Phase Effects on Electronic Properties. en. *Reviews of Modern Physics* **82,** 1959–2007 (2010).

222. Shen, S.-Q. *Topological Insulators* (Springer Singapore, 2017).

223. Mong, R. S. K. & Shivamoggi, V. Edge States and the Bulk-Boundary Correspondence in Dirac Hamiltonians. *Physical Review B* **83,** 125109 (2011).

224. Nakada, K., Fujita, M., Dresselhaus, G. & Dresselhaus, M. S. Edge State in Graphene Ribbons: Nanometer Size Effect and Edge Shape Dependence. *Physical Review B* **54,** 17954–17961 (1996).

225. Winkler, R. & Deshpande, H. Effective Hamiltonian for Protected Edge States in Graphene. *Physical Review B* **95,** 235312 (2017).

226. Huang, S.-M. *et al.* A Weyl Fermion Semimetal with Surface Fermi Arcs in the Transition Metal Monopnictide TaAs Class. eng. *Nature communications* **6,** 7373–7373 (2015).

227. Wan, X., Turner, A. M., Vishwanath, A. & Savrasov, S. Y. Topological Semimetal and Fermi-Arc Surface States in the Electronic Structure of Pyrochlore Iridates. *Physical Review B* **83,** 205101 (2011).

228. Kobayashi, Y., Fukui, K.-i., Enoki, T., Kusakabe, K. & Kaburagi, Y. Observation of Zigzag and Armchair Edges of Graphite Using Scanning Tunneling Microscopy and Spectroscopy. *Physical Review B* **71,** 193406 (2005).

229. Tao, C. *et al.* Spatially Resolving Edge States of Chiral Graphene Nanoribbons. *Nature Physics* **7,** 616–620 (2011).

230. Magda, G. Z. *et al.* Room-Temperature Magnetic Order on Zigzag Edges of Narrow Graphene Nanoribbons. *Nature* **514,** 608–611 (2014).

231. Shibayama, Y., Sato, H., Enoki, T. & Endo, M. Disordered Magnetism at the Metal-Insulator Threshold in Nano-Graphite-Based Carbon Materials. *Physical Review Letters* **84,** 1744–1747 (2000).

232. Joly, V. L. J. *et al.* Observation of Magnetic Edge State in Graphene Nanoribbons. *Physical Review B* **81,** 245428 (2010).

233. Luis, F. & Coronado, E. Spinning on the Edge of Graphene. *Nature* **557,** 645–647 (2018).

234. Hubbard, J. & Flowers, B. H. Electron Correlations in Narrow Energy Bands. *Proceedings of the Royal Society of London. Series A. Mathematical and Physical Sciences* **276,** 238–257 (1963).

235. Hubbard, J. & Flowers, B. H. Electron Correlations in Narrow Energy Bands. II. The Degenerate Band Case. *Proceedings of the Royal Society of London. Series A. Mathematical and Physical Sciences* **277,** 237–259 (1964).

236. Hubbard, J. & Flowers, B. H. Electron Correlations in Narrow Energy Bands III. An Improved Solution. *Proceedings of the Royal Society of London. Series A. Mathematical and Physical Sciences* **281,** 401–419 (1964).

237. Fazekas, P. *Lecture Notes on Electron Correlation and Magnetism* English (World Scientific, Singapore, New Jersey, London, Hong Kong, 1999).

238. Peltonen, T. J., Ojajärvi, R. & Heikkilä, T. T. Mean-Field Theory for Superconductivity in Twisted Bilayer Graphene. en. *Physical Review B* **98,** 220504 (2018).

239. Correa, J. H., Pezo, A. & Figueira, M. S. Braiding of Edge States in Narrow Zigzag Graphene Nanoribbons: Effects of Third-Neighbor Hopping on Transport and Magnetic Properties. *Physical Review B* **98,** 045419 (2018).

240. Peter Mohn. *Magnetism in the Solid State - An Introduction* (Springer-Verlag Berlin Heidelberg, 2003).

241. Wakabayashi, K., Sigrist, M. & Fujita, M. Spin Wave Mode of Edge-Localized Magnetic States in Nanographite Zigzag Ribbons. *Journal of the Physical Society of Japan* **67,** 2089–2093 (1998).

242. Lieb, E. H. Two Theorems on the Hubbard Model. *Physical Review Letters* **62,** 1201–1204 (1989).

243. Jung, J., Pereg-Barnea, T. & MacDonald, A. H. Theory of Interedge Superexchange in Zigzag Edge Magnetism. *Physical Review Letters* **102,** 227205 (2009).

244. Altland, A. & Simons, B. D. *Condensed Matter Field Theory* (Cambridge University Press, Cambridge, 2010).

245. *The LDA+DMFT Approach to Strongly Correlated Materials* (eds Pavarini, E., Koch, E., Lichtenstein, A. & Vollhardt, D.) (Forschungszentrum Jülich GmbH Institute for Advanced Simulations, 2011).

246. van Loon, E. G. C. P. & Katsnelson, M. I. The Extended Hubbard Model with Attractive Interactions. *Journal of Physics: Conference Series* **1136,** 012006 (2018).

247. Laad, M. S. & Ghosh, D. K. Extended Hubbard Model in Two Dimensions. *Journal of Physics: Condensed Matter* **3,** 9723–9732 (1991).

248. Schüler, M., van Loon, E. G. C. P., Katsnelson, M. I. & Wehling, T. O. First-Order Metal-Insulator Transitions in the Extended Hubbard Model Due to Self-Consistent Screening of the Effective Interaction. *Physical Review B* **97,** 165135 (2018).

249. Auerbach, Assa. *Interacting Electrons and Quantum Magnetism* PhD Thesis (Springer-Verlag New York, 1994).

250. Hoshino, S. & Werner, P. Electronic Orders in Multiorbital Hubbard Models with Lifted Orbital Degeneracy. *Physical Review B* **93,** 155161 (2016).

251. Imada, M., Fujimori, A. & Tokura, Y. Metal-Insulator Transitions. *Reviews of Modern Physics* **70,** 1039–1263 (1998).

252. Kim, A. J., Jeschke, H. O., Werner, P. & Valentí, R. **J** Freezing and Hund's Rules in Spin-Orbit-Coupled Multiorbital Hubbard Models. *Physical Review Letters* **118,** 086401 (2017).

253. Sun, Q. *et al.* PySCF: The Python-Based Simulations of Chemistry Framework. *Wiley Interdisciplinary Reviews: Computational Molecular Science* **8,** e1340 (2018).

254. Hadipour, H. *et al.* Screening of Long-Range Coulomb Interaction in Graphene Nanoribbons: Armchair versus Zigzag Edges. *Physical Review B* **98,** 205123 (2018).

255. Kim, M. *et al.* Control of Electron-Electron Interaction in Graphene by Proximity Screening. *Nature Communications* **11,** 2339 (2020).

256. Pisani, L., Chan, J. A., Montanari, B. & Harrison, N. M. Electronic Structure and Magnetic Properties of Graphitic Ribbons. *Physical Review B* **75,** 064418 (2007).

257. Kuroda, S.-i. & Shirakawa, H. Electron-Nuclear Double-Resonance Evidence for the Soliton Wave Function in Polyacetylene. *Physical Review B* **35,** 9380–9382 (1987).

258. Neilson, D., Perali, A. & Zarenia, M. Many-Body Electron Correlations in Graphene. *Journal of Physics: Conference Series* **702,** 012008 (2016).

259. Szabo, A. & Ostlund, N. S. *Modern Quantum Chemistry: Introduction to Advanced Electronic Structure Theory* (Dover Publications Inc., Mineola, New York, 1982).

260. Jung, J. & MacDonald, A. H. Carrier Density and Magnetism in Graphene Zigzag Nanoribbons. *Physical Review B* **79,** 235433 (2009).

261. Sawada, K., Ishii, F., Saito, M., Okada, S. & Kawai, T. Phase Control of Graphene Nanoribbon by Carrier Doping: Appearance of Noncollinear Magnetism. *Nano Letters* **9,** 269–272 (2009).

262. Veyrat, L. *et al.* Helical Quantum Hall Phase in Graphene on $SrTiO_3$. *Science* **367,** 781–786 (2020).

263. Yazyev, O. V. & Katsnelson, M. I. Magnetic Correlations at Graphene Edges: Basis for Novel Spintronics Devices. *Physical Review Letters* **100,** 047209 (2008).

264. Pitaevskii, L. & Stringari, S. Uncertainty Principle, Quantum Fluctuations, and Broken Symmetries. *Journal of Low Temperature Physics* **85,** 377–388 (1991).

265. Ganguly, S., Kabir, M. & Saha-Dasgupta, T. Magnetic and Electronic Crossovers in Graphene Nanoflakes. *Physical Review B* **95,** 174419 (2017).

266. Son, Y.-W., Cohen, M. L. & Louie, S. G. Energy Gaps in Graphene Nanoribbons. *Physical Review Letters* **97,** 216803 (2006).

267. Fernández-Rossier, J. Prediction of Hidden Multiferroic Order in Graphene Zigzag Ribbons. *Physical Review B* **77,** 075430 (2008).

268. Eckle, Hans-Peter. *Models of Quantum Matter: A First Course on Integrability and the Bethe Ansatz* (Oxford Graduate Texts, July 2019).

269. Kim, S. *et al.* Direct Measurement of the Fermi Energy in Graphene Using a Double-Layer Heterostructure. *Physical Review Letters* **108,** 116404 (2012).

270. Fan, X. F., Zheng, W. T., Chihaia, V., Shen, Z. X. & Kuo, J.-L. Interaction between Graphene and the Surface of SiO2. *Journal of Physics: Condensed Matter* **24,** 305004 (2012).

271. Pearce, A. J., Mariani, E. & Burkard, G. Tight-Binding Approach to Strain and Curvature in Monolayer Transition-Metal Dichalcogenides. en. *Physical Review B* **94,** 155416 (2016).

272. Rostami, H., Roldán, R., Cappelluti, E., Asgari, R. & Guinea, F. Theory of Strain in Single-Layer Transition Metal Dichalcogenides. *Physical Review B* **92,** 195402 (2015).

273. Steele, G. *et al.* Large Spin-Orbit Coupling in Carbon Nanotubes. *Nature Communications* **4,** 1573 (2013).

274. Isacsson, A., Jonsson, L. M., Kinaret, J. M. & Jonson, M. Electronic Superlattices in Corrugated Graphene. *Physical Review B* **77,** 035423 (2008).

275. Kim, E.-A. & Castro Neto, A. H. Graphene as an Electronic Membrane. *Europhysics Letters* **84,** 57007 (2008).

276. Goerbig, M. O. Electronic Properties of Graphene in a Strong Magnetic Field. en. *Reviews of Modern Physics* **83,** 1193–1243 (2011).

277. Pereira, V. M., Castro Neto, A. H. & Peres, N. M. R. Tight-Binding Approach to Uniaxial Strain in Graphene. *Physical Review B* **80,** 045401 (2009).

278. Guinea, F., Katsnelson, M. I. & Vozmediano, M. A. H. Midgap States and Charge Inhomogeneities in Corrugated Graphene. *Physical Review B* **77,** 075422 (2008).

279. de Juan, F., Sturla, M. & Vozmediano, M. A. H. Space Dependent Fermi Velocity in Strained Graphene. *Physical Review Letters* **108,** 227205 (2012).

280. Castro-Villarreal, P. & Ruiz-Sánchez, R. Pseudomagnetic Field in Curved Graphene. *Physical Review B* **95,** 125432 (2017).

281. Vozmediano, M. A. H., de Juan, F. & Cortijo, A. Gauge Fields and Curvature in Graphene. *Journal of Physics: Conference Series* **129,** 012001 (2008).

282. Stegmann, T. & Szpak, N. Current Flow Paths in Deformed Graphene: From Quantum Transport to Classical Trajectories in Curved Space. *New Journal of Physics* **18,** 053016 (2016).

283. Son, Y.-W., Cohen, M. L. & Louie, S. G. Half-Metallic Graphene Nanoribbons. *Nature* **444,** 347–349 (2006).

284. Ribeiro, R. M., Pereira, V. M., Peres, N. M. R., Briddon, P. R. & Castro Neto, A. H. Strained Graphene: Tight-Binding and Density Functional Calculations. *New Journal of Physics* **11,** 115002 (2009).

285. Jeong, J.-S., Shin, J. & Lee, H.-W. Curvature-Induced Spin-Orbit Coupling and Spin Relaxation in a Chemically Clean Single-Layer Graphene. *Physical Review B* **84,** 195457 (2011).

286. Konschuh, S., Gmitra, M., Kochan, D. & Fabian, J. Theory of Spin-Orbit Coupling in Bilayer Graphene. *Physical Review B* **85,** 115423 (2012).

287. Konschuh, S. *Spin-Orbit Coupling Effects: From Graphene to Graphite* PhD thesis (University Regensburg, Regensburg, 2011).

288. Santos, H., Latgé, A., Alvarellos, J. E. & Chico, L. All-Electrical Production of Spin-Polarized Currents in Carbon Nanotubes: Rashba Spin-Orbit Interaction. *Physical Review B* **93,** 165424 (2016).

289. Avramenko, M. V., Rochal, S. B. & Yuzyuk, Y. I. Symmetry of the Carbon Nanotube Modes and Their Origin from the Phonon Branches of Graphene. *Physical Review B* **87,** 035407 (2013).

290. Sasaki, K.-i., Murakami, S. & Saito, R. Gauge Field for Edge State in Graphene. *Journal of the Physical Society of Japan* **75,** 074713 (2006).

291. Soriano, D. & Fernández-Rossier, J. Spontaneous Persistent Currents in a Quantum Spin Hall Insulator. *Physical Review B* **82,** 161302 (2010).

292. Rachel, S. Interacting Topological Insulators: A Review. *Reports on Progress in Physics* **81,** 116501 (2018).

293. Zheng, D., Zhang, G.-M. & Wu, C. Particle-Hole Symmetry and Interaction Effects in the Kane-Mele-Hubbard Model. *Physical Review B* **84,** 205121 (2011).

294. Hohenadler, M., Parisen Toldin, F., Herbut, I. F. & Assaad, F. F. Phase Diagram of the Kane-Mele-Coulomb Model. *Physical Review B* **90,** 085146 (2014).

295. Rachel, S. & Le Hur, K. Topological Insulators and Mott Physics from the Hubbard Interaction. *Physical Review B* **82,** 075106 (2010).

296. Cao, J. & Xiong, S.-J. Topological Phase Transition in a Graphene System with a Coexistence of Coulomb Interaction, Staggered Potential, and Intrinsic Spin-Orbit Coupling. *Physical Review B* **88,** 085409 (2013).

297. Laubach, M., Reuther, J., Thomale, R. & Rachel, S. Rashba Spin-Orbit Coupling in the Kane-Mele-Hubbard Model. *Physical Review B* **90,** 165136 (2014).

298. Luo, M. Topological Edge States of a Graphene Zigzag Nanoribbon with Spontaneous Edge Magnetism. *Physical Review B* **102,** 075421 (2020).

299. Lado, J. L. & Fernández-Rossier, J. Magnetic Edge Anisotropy in Graphenelike Honeycomb Crystals. *Physical Review Letters* **113,** 027203 (2014).

300. Sun, L., Wei, P., Wei, J., Sanvito, S. & Hou, S. From Zigzag to Armchair: The Energetic Stability, Electronic and Magnetic Properties of Chiral Graphene Nanoribbons with Hydrogen-Terminated Edges. *Journal of Physics: Condensed Matter* **23,** 425301 (2011).

301. Saloriutta, K. *et al.* Electron Transport in Edge-Disordered Graphene Nanoribbons. *Physical Review B* **83,** 205125 (2011).

302. Abanin, D. A. & Pesin, D. A. Interaction-Induced Topological Insulator States in Strained Graphene. *Physical Review Letters* **109,** 066802 (2012).

303. Elena, A. M. & Meister, M. Automatic Generation of Matrix Element Derivatives for Tight Binding Models. *Physical Review B* **72,** 165107 (2005).

304. Sharma, R. R. General Expressions for Reducing the Slater-Koster Linear Combination of Atomic Orbitals Integrals to the Two-Center Approximation. *Physical Review B* **19,** 2813–2823 (1979).

305. Podolskiy, A. V. & Vogl, P. Compact Expression for the Angular Dependence of Tight-Binding Hamiltonian Matrix Elements. *Physical Review B* **69,** 233101 (2004).

306. Urban, A. *Environment-Dependent Crystal-Field Tight-Binding Based on Density-Functional Theory* PhD Thesis (Friedrich-Alexander-Universität Erlangen-Nürnberg (FAU), Erlangen, Nuremberg, Germany, 2012).

Acknowledgements

I would like to thank my friends, my family and the members of the group *Quantentheorie der Kondensierten Materie*, as well as many members of the *I. Institut für theoretische Physik.*

I am very thankful to Daniela Pfannkuche who advised me during my dissertation. She helped me to find new angles for tackling problems and motivated me throughout my thesis. A number of discussions have helped me to understand underlying connections in physical laws and mathematical principles, which led to many insights that greatly enriched my physical abilities.

I would also like Marta Prada who also advised me during my thesis and who provided the original research idea when my project was first planned. In her, I have found a mentor who helped me to develop myself as a researcher and in the later stages of my project a scientist who provided valuable feedback that allowed me to critically think about my results.

Also I would like to thank Michael Potthoff for providing help in finding the direction of my project in the early stages and for reviewing my thesis.

I thank Robert Blick to be part of the examination committee during the defense of my thesis and I also thank Robin Santra for being a member of this committee, as well as for chairing my defense.

My project would not have been the adventure it was, without the other members of our research group. They deserve my sincerest thanks for countless scientific discussions and above all great personal experiences that made my project certainly one of the most interesting periods of my life.

Frederik Bartelmann has helped me to not loose my mind with many struggles during my research project and allowed me to learn many insightful things in lengthy discussions. This has been invaluable, especially during the pandemic, which overshadowed the later stages of my research project. Lars-Hendrik Frahm, who allowed me to learn from him what it means to be a doctoral student in the early stages of my project, also enlighted me by showing me the qualities of rice pudding in our local mensa. The two of us were probably responsible that all members of a certain conference in a certain hotel near the Baltic sea had rice pudding for dessert.

I would like to thank Daniel Duarte Ruiz for many opportunities to talk about different aspects of physics, which were not always closely related to our projects. I thank Milad Behrooz and Motilal Jana for having a great time in our office and for a lot of spontaneous discussions over the rims of our monitors. Alexander Chudnovskiy has helped me a lot with giving me a different angle on my research results and pointed me into the right direction, when I struggled with my project.